

Growth and Characterisation of Pentacene Thin Films on Clean and Modified Metal Surfaces

Oisín McDonald (B.Sc.)
School of Physical Sciences
Dublin City University

A thesis submitted to



For the degree of
Doctor of Philosophy

Research Supervisor
Prof. Greg Hughes

August 2006

Declaration

I hereby certify that this material, which I now submit for assessment on the programme of study leading to the award of Doctor of Philosophy, is entirely my own work and has not been taken from the work of others save and to the extent that such work has been cited and acknowledged within the text of my own work.

Signed: Clive McDonald

ID Number: 98337963

Date: 25/9/06

Contents

Title page	i
Declaration	ii
Contents	iii
Abstract	vii
Acknowledgements	viii
Chapter 1 Introduction	1
<i>Chapter 1 References</i>	<i>7</i>
Chapter 2 Theoretical Background	8
2.1 Photoelectron Emission Spectroscopy	9
2.1.1 Photoelectron Emission Theory.....	9
2.1.2 Core Level Spectroscopy.....	12
2.1.3 Analysis of Core Level Spectra.....	12
2.1.4 Origin of Peak Shifts.....	14
2.1.5 Valence Band Spectroscopy.....	16
2.1.6 Evaluating Valence Band Spectra.....	17
2.1.7 Workfunction Measurements.....	19
2.1.8 Interface Dipole Formation.....	19
2.2 Group Theory	21
2.2.1 Selection Rules.....	24
2.3 Near Edge X-ray Absorption Fine Structure	25
2.3.1 NEXAFS Theory.....	26
2.4 Surface Sensitivity	29
2.5 Scanning Tunnelling Microscopy	31
2.5.1 Tunnelling Theory.....	32
2.6 Growth Modes	35
2.7 Low Energy Electron Diffraction	36

2.7.1	Diffraction/LEED Theory.....	37
2.7.2	Elements of LEED Theory	39
2.8	<i>Summary</i>	40
	<i>Chapter 2 References</i>	40
Chapter 3	Experimental Details	43
3.1	<i>Photoelectron Emission Spectroscopy</i>	44
3.1.1	Synchrotron Radiation.....	44
3.1.2	Monochromater and Grating.....	45
3.1.3	Experimental Setup	47
3.1.4	The Electron Energy Analyser.....	48
3.2	<i>Near Edge X-ray Absorption Fine Structure</i>	49
3.2.1	Modes of Detection	49
3.2.2	Experimental Setup	52
3.3	<i>Scanning Tunnelling Microscopy</i>	53
3.3.1	Experimental Setup	53
3.3.2	Piezo Scanner	54
3.3.3	Vibrational Isolation System	54
3.3.4	Scanning Modes.....	56
3.3.5	Feedback Mechanism	56
3.3.6	UHV system.....	58
3.4	<i>Low Energy Electron Diffraction</i>	59
3.4.1	LEED Experimental Setup	59
3.5	<i>Evaporators</i>	60
3.5.1	Pentacene Evaporator	60
3.5.2	Sodium Evaporator.....	61
3.5.3	Sulphur Evaporator	62
3.6	<i>Summary</i>	63
	<i>Chapter 3 References</i>	63

Chapter 4	Pentacene on Cu(110)	64
4.1	<i>Introduction</i>	65
4.1.1	Previous studies of the pentacene/Cu(110) interface	65
4.2	<i>Experimental Details</i>	66
4.3	<i>Pentacene on Cu(110) – Untemplated Film Growth</i>	67
4.3.1	Workfunction analysis	67
4.3.2	C1s core level analysis	69
4.3.3	Cu3p core level analysis	71
4.3.4	Valence band and group theory analysis	73
4.4	<i>Pentacene on Cu(110) – Templated Film Growth</i>	89
4.4.1	C1s core level analysis	89
4.4.2	Cu3p core level analysis	91
4.4.3	Valence band analysis	92
4.5	<i>Molecular energy level diagram</i>	94
4.6	<i>Summary</i>	95
	<i>Chapter 4 References</i>	96
Chapter 5	Pentacene on Au(100)	98
5.1	<i>Introduction</i>	99
5.2	<i>Experiment</i>	100
5.3	<i>Photoelectron Emission Spectroscopy Results</i>	101
5.3.1	Workfunction measurements	101
5.3.2	Au4f _{7/2} core level analysis	102
5.3.3	C1s core level analysis	104
5.3.4	Valence band and group theory analysis	105
5.3.5	Molecular energy level diagram	113
5.4	<i>NEXAFS results</i>	114
5.5	<i>STM and LEED</i>	119
5.5.1	Clean Au(100)-(hex)	119
5.5.2	Pentacene on Au(100)	122
5.6	<i>Summary</i>	127
	<i>Chapter 5 References</i>	128

Chapter 6 Organic Film Modification131

6.1	<i>Introduction</i>	132
6.2	<i>Experiment</i>	133
6.3	<i>Alkali metal doping of pentacene films</i>	134
6.3.1	Na doping of untemplated pentacene film on Cu(110).....	134
6.3.2	Na doping of templated pentacene film on Cu(110).....	140
6.3.3	Summary.....	147
6.4	<i>Pentacene deposited on O/Cu(110)-(2×1)</i>	148
6.4.1	O/Cu(110)-(2×1).....	148
6.4.2	Workfunction measurements.....	150
6.4.3	C1s core level analysis.....	152
6.4.4	Substrate signal analysis.....	153
6.4.5	Valence band analysis.....	155
6.4.6	Molecular energy level diagram.....	158
6.4.7	Summary.....	159
6.5	<i>Pentacene deposited on sulphur terminated Au(100)</i>	160
6.5.1	Workfunction analysis.....	160
6.5.2	Substrate signal analysis.....	161
6.5.3	Valence band analysis.....	163
6.5.4	Summary.....	166
	<i>Chapter 6 References</i>	167

Chapter 7 Conclusion and Future Work170

List of Publications	178
List of Tables	179
List of Figures	180

Abstract

The primary focus of this PhD is the investigation of pentacene thin films grown on metal substrates. Numerous techniques have been used to investigate these films including synchrotron based photoelectron emission spectroscopy (PES) and near edge x-ray absorption fine structure (NEXAFS) techniques in addition to scanning tunnelling microscopy (STM) and low energy electron diffraction (LEED) techniques. The two primary experimental systems that have been studied are the pentacene/Au(100) and the pentacene/Cu(110) systems. In both pentacene/metal systems the molecules were found to bond flat, or nearly flat to the substrate, with a significantly stronger bond observed between the pentacene and Cu(110) substrate.

In addition to these studies, secondary studies involving the manipulation of the properties of pentacene films have been investigated. This investigation has been carried out through the use of interlayers and film doping. Interfacial layers of sulphur and oxygen were deposited on the Au(100) and Cu(110) substrates respectively prior to the deposition of pentacene in order to investigate changes in the interfacial interaction of the pentacene and underlying substrate. These studies were carried out using PES. Additional PES experiments were carried out to investigate the alkali metal doping of the pentacene/Cu(110) system using sodium in order to alter the injection characteristics of the organic/metal system. The effects of different levels of ordering in the molecular film were found to influence the doping of the molecular film.

Acknowledgements

For help, encouragement, and infectious enthusiasm for surface science over the past four years, I am indebted to Prof. Greg Hughes, whose door was always open, whether for advice, or simply for a chat.

Sincerest thanks also to Dr. Tony Cafolla for help over the past number of years.

To my parents, Bernard and Finola, much love and thanks is due for the constant love, support, and encouragement over the past 26 years. It's very much appreciated, and always has been.

To my loving girlfriend, Mary-Jane, to whom I owe a huge debt of gratitude for all the love, support, and understanding you have given me. Everything's always better with you by my side. Thanks couldn't possibly capture it properly. My turn now!

To my sisters, Ciara and Aoife, who have come to see me as an eternal student, who works with lasers, and interprets carpet samples, many thanks also. Time to get a job now I think!

To all the friends I have gained in the office and the department in my time here. You have helped make the experience much more than just an educational one. Special mention to Darren, Ian (sorry about the knee), Kev Kav, Steve, and Barry. Additional mention to Eoin, Phil, Eilish, Claire, Grainne, the football crew, the CoD crew, and the rest of the gang. It's been great craic!

Finally, I would like to acknowledge the financial help and support from the Higher Education Authority (HEA) under the PRTLTI programme for PhD funding. Additional acknowledgement is also given to funding from the European Union Access to Research Infrastructure (EUARI) in order to undertake synchrotron radiation studies at the ASTRID synchrotron in Aarhus, Denmark.

Chapter 1 Introduction

In the past 20 years there has been a growing interest in the area of science known as 'organic molecular electronics'. There are two main driving forces behind this growth, one of which is a demand for a bottom up approach to fabricating electronic devices and the other is the invention of the Scanning Tunnelling Microscope (STM)^{1, 2,}

3

The demand for a bottom up approach to the fabrication of electronic devices comes at a time when computer chip manufacturers are struggling to keep up with Moore's Law⁴. Moore's Law originated from a 1965 paper, in which Moore observed that there had been an exponential growth pattern in the number of transistors that could be manufactured on an individual silicon wafer, and he predicted that this growth would continue with the development of microelectronics. This increase in the number of transistors on a silicon wafer was facilitated by the ever-decreasing size of transistors. The smaller transistor size allowed for quicker switching speeds and it is this increase in switching speeds that the microelectronic industry is seeking to sustain. The current method of device fabrication is a top down approach whereby the device is created by a multiple step etch and deposition sequence. However, this approach will reach its limit in the near future as lithographic methods of pattern generation hit fundamental limits, which are extremely difficult to surpass. Intensive research efforts are underway to extend the top down fabrication method for as long as possible because of the historic success of this technology and the financial investments already made, however, there is increasing interest in a fundamental change of direction in terms of device fabrication, and it is here that 'organic molecular electronics' has shown excellent potential.

On a very simple level, the use of molecules to create structures on the nanometre scale should provide engineers with a level of control not available with current technologies. The comparison between top-down based technologies currently employed for microelectronic fabrication and possible future bottom-up molecular based fabrication techniques is analogous to creating a building by carving it from solid rock as opposed to building it from the foundations up using blocks. In essence, it is hoped that molecules can eventually be used as the building blocks to create the nanometre scale microelectronic devices of the future. While the ultimate aim of 'molecular electronics' is to create a functioning transistor using a single molecule, a less ambitious but more readily obtainable goal is the fabrication of electronic devices using monolayer and multilayers of organic semiconductors.

However, before this aim can be achieved and the potential of molecular based technologies can be fully realised, it is essential that the critical aspects of molecular

interactions, with each other and with a substrate, on the nanometre scale are fully understood. After all, silicon based technologies have had a 35 year head start on molecular based devices in order to reach the scale and speed of devices currently available. So while there has been extensive research carried out aimed at controlling the properties of silicon over the past 35 years, there has been relatively little carried out on thin molecular films until recently.

Much of the work that would allow for the possible replacement of solid-state semiconductor devices with molecular based devices would not have been possible without the invention of the STM, which has become an essential tool for organic semiconductor research. The STM facilitated for the first time the observation of interactions at surfaces on the atomic scale allowing for a much greater understanding and investigation of thin molecular films.

Currently the focus of the investigation into 'organic molecular electronics' falls broadly into two categories. The first category is research that is being carried out on a macroscopic scale and involves the fabrication and optimisation of simple molecular based devices. Organic Field Effect Transistors⁵ (OFETs) have thus far been fabricated with room temperature mobilities in the range of $1.5\text{cm}^2/\text{Vs}$ indicating the potential that organic semiconductors could have for the future production of electronic devices. Similarly, the optimisation of Organic Light Emitting Diodes^{6, 7, 8, 9} (OLEDs) through the use of doping has allowed for greater control of the luminescence of these devices along with improved device stability. The second category of research involves the investigation of the properties of ultrathin molecular films on a microscopic, and more fundamental level. Studies of devices have shown for example, that grain boundaries and defects can have a large role to play in determining the electronic properties of these devices^{5, 10}. For device optimisation, it is imperative that a greater understanding of the properties of molecular films is obtained. In order to achieve this, studies at a more fundamental level are required into the chemical and electronic properties of thin organic films and their interfaces with various substrates.

One group of molecules that has attracted a significant amount of interest are the acenes, which are molecules consisting of differing numbers of aromatic, six membered rings bonded in a linear geometry^{11, 12}. The acene molecular group consist of benzene, naphthalene, anthracene, tetracene and pentacene, which consist of one to five aromatic rings respectively. Of the acenes, pentacene has attracted the most attention recently for a number of different reasons. The acenes in general have relatively high charge carrier mobilities, and pentacene thin film transistors with room temperature mobilities as high

as $1.5\text{cm}^2/\text{Vs}$ have been fabricated⁵ to date, making this a very promising molecule in terms of electronic properties.

Pentacene has also been observed to exhibit short and long range ordering on a variety of different surfaces including Ag/Si(111)-($\sqrt{3} \times \sqrt{3}$) R30^{13, 14}, Cu(110)^{15, 16, 17, 18}, Au(110)¹⁹, and Ag(110)²⁰. This is the basis for the formation of self-assembled monolayers (SAMs), which are of utmost importance for the optimisation of molecular electronic devices.

In addition to this, the planar nature of the pentacene molecule allows for the investigation of the interaction between ideal π -conjugated molecules and metallic surfaces. The growth and orientation of molecular thin films depends primarily on the subtle competition between the intermolecular and molecular-substrate interactions, primarily those occurring in the first few monolayers (MLs). It has been shown that in many cases the intermolecular forces, which determine the relative orientation of the molecules in the bulk, are very different to those experienced by molecules bonded to metal surfaces. It is therefore evident that studies of the organic/metal interfaces are key in terms of future development optimisation of more complex 'organic molecular electronic' devices.

In the course of this work synchrotron radiation based photoelectron emission spectroscopy (PES), near edge x-ray absorption fine structure (NEXAFS) in addition to STM and low energy electron diffraction (LEED) have been used in the study of two primary systems, the pentacene/Cu(110) and pentacene/Au(100) systems. In addition to these primary systems, studies have also focussed on attempts to control the molecular order at the organic/substrate interface. These further studies have included the use of interface layers, namely sulphur on Au(110) and a half monolayer of oxygen on Cu(110), to modify the interaction of the initial monolayer of organic molecules with the metal substrate. The modification of the injection characteristics of pentacene thin films on Cu(110) have also been carried out through the use of alkali metal doping.

Chapter 2 describes the theory behind the different experimental techniques used in the course of this work. Section 2.1 deals with the theory behind the PES technique, in addition to an in-depth discussion of the features observed in the PES spectra and their significance. Section 2.2 introduces the theory behind the application of group theory to PES analysis, which was used in an attempt to determine molecular orientation. This discussion begins with operator assignments and point group identification and follows with an introduction to the theory that is used for the formulation of the selection rules used in PES analysis in chapters 4 and 5.

Section 2.3 deals with the theory behind the NEXAFS technique, including a brief derivation of the formulae associated with investigation of the angular orientation of the molecule. Section 2.4 discusses the origin of the surface sensitivity of the PES and NEXAFS experimental techniques.

Section 2.5 describes the tunnelling theory behind the operation of STM. Section 2.6 consists of a brief discussion of the different growth modes associated with the adsorption of organic molecules on different surfaces and the origin of the different growth modes. Section 2.7 introduces the theoretical background associated with the LEED technique. Diffraction theory and reciprocal space are introduced to help explain the operation of the LEED system.

Chapter 3 introduces the experimental details associated with the techniques discussed in the previous chapter. Section 3.1 gives a brief introduction to the origin of synchrotron radiation, followed by a discussion of the equipment associated with extracting useful radiation from the synchrotron source. Additional discussion centres on the UHV chamber used in the PES experiments and the electron analyser used to acquire the PES spectra.

Section 3.2 introduces the different detection modes used to carry out NEXAFS experiments, in addition to a description of the UHV chamber used in the NEXAFS experiments. Section 3.3 discusses the different equipment associated with the STM technique, which includes the piezo scanner, vibrational isolation system, the feedback mechanism and the UHV system used in the course of the STM experiments. Additional discussion on the different scanning modes possible in STM is also presented.

Section 3.4 details the equipment associated with the LEED technique and section 3.5 describes the operation of the pentacene, Na and S evaporators used in the course of the work presented in chapters 4, 5 and 6.

Chapter 4 describes the deposition of pentacene on Cu(110) by organic molecular-beam deposition (OMBD) under ultra high vacuum conditions. Synchrotron based PES is used to investigate pentacene thin films grown with and without the use of an annealed monolayer to template further film growth. Carbon and copper core level analysis is used to gain insight into both the interfacial bonding between the pentacene and the Cu(110) substrate, and the growth mode of the deposited pentacene film. The application of group theory presented in section 2.2, allows for the formation of selection rules to predict which molecular orbitals should be observed in the valence band spectra. This group theory analysis is then applied to the valence band spectra in order to extract molecular orientational information from the valence band spectra.

Chapter 5 describes the deposition of pentacene on Au(100) by OMBD under ultra high vacuum conditions. Characterisation of the pentacene thin film is carried out using synchrotron based PES and NEXAFS, in addition to STM and LEED. PES core level analysis is used to investigate the interfacial bonding between the pentacene and the Au(100) substrate. A selection rules analysis of the valence band spectra is carried out to extract molecular orientational information. Valence band analysis additionally allows for the calculation of the hole and electron injection characteristics of the film. The NEXAFS technique is used to complement the molecular orientational information obtained from the selection rules analysis of the valence band spectra. The STM technique is used to image both the clean substrate and the pentacene covered surface, in order to investigate the ordering in the molecular film, and additionally to find the pentacene unit cell parameters. The LEED technique is used as a further method of investigating the ordering in the molecular film, on a more global scale than that investigated with STM.

Chapter 6 presents work carried out on the modification of the characteristics of pentacene/metal films. This was carried out using two different methods. The first method involves the use of alkali metals to dope the pentacene films, in an effort to modify the electron and hole injection characteristics of the pentacene film. The effect of the degree of ordering in the molecular film on the doping process is also examined in this section. PES is used to investigate the doping process by examining the valence band region of the spectrum, the secondary electron cutoff, and the core levels of the substrate, the pentacene, and the Na dopant.

The second method of organic film property modification is carried out via the introduction of interlayers between the metal substrate and the pentacene overlayer. Studies on the effects of interlayers were carried out by terminating the Cu(110) surface with a half monolayer of oxygen, and the Au(100) substrate with an annealed sulphur layer, prior to the deposition of pentacene. PES is used as a means of investigating the effect of the different interlayers on the subsequent pentacene film growth in both cases.

Finally, Chapter 7 reviews the results, and looks at some possible future directions for this field of research.

Chapter 1 References

- ¹ G. Binnig, H. Rohrer, Ch. Gerber, E. Weidel, *Phys Rev Lett*, 49, (1982) 57.
- ² G. Binnig, H. Rohrer, *Helv. Phys. Acta*, 55 (1982) 726.
- ³ G. Binnig, H. Rohrer, Ch. Gerber, E. Weidel, *Phys. Rev. Lett.* 40 (1982) 178.
- ⁴ G. E. Moore, *Electronics* 38 (1965) 8.
- ⁵ N. Karl, *Synth. Met.* 133-134 (2003) 649.
- ⁶ C.W. Tang, S.A. VanSlyke, C.H. Chen, *J. Appl. Phys.* 65 (1989) 3610.
- ⁷ J. Kido, K. Hongawa, K. Okyama, K. Nagai, *Appl. Phys. Lett.* 64 (1994) 815.
- ⁸ A. Yamamori, C. Adachi, T. Koyama, Y. Taniguchi, *Appl. Phys. Lett.* 72 (1998) 2147.
- ⁹ H. Fujii, T. Sano, Y. Hamada, K. Shibata, *Macromol. Symp.* 125 (1997) 77.
- ¹⁰ T. W. Kelley and C. D. Frisbie, *J. Phys. Chem. B* 105 (2001) 4538.
- ¹¹ N. O. Lipari, C. B. Duke, *J. Chem. Phys.* 63 (1975) 1768.
- ¹² P. A. Clark, F. Brogli, E. Heilbronner, *Helv. Chim. Acta.* 55 (1972) 1415.
- ¹³ Ph. Guaino, D. Carty, G. Hughes, P. Moriarty, A. A. Cafolla, *Appl. Surf. Sci.* 212-213 (2003) 537.
- ¹⁴ Ph. Guaino, A. A. Cafolla, D. Carty, G. Sheerin, G. Hughes, *Surf. Sci.* 540 (2003) 107.
- ¹⁵ S. Sönchen, S. Lukas, G. Witte, *J. Chem. Phys.* 121 (2004) 525.
- ¹⁶ S. Lukas, G. Witte, Ch. Woll, *Phys. Rev. Lett.* 88 (2002) 028301.
- ¹⁷ S. Lukas, S. Sönchen, G. Witte, Ch. Woll, *ChemPhysChem.* 5 (2004) 266.
- ¹⁸ Q. Chen, A. J. McDowall, N. V. Richardson. *Langmuir* 19 (2003) 10164.
- ¹⁹ Ph. Guaino, D. Carty, G. Hughes, O. McDonald, and A. A. Cafolla, *Appl. Phys. Lett.* 85 (2004) 2777.
- ²⁰ Y. L. Wang, W. Ji, D. X. Shi, S. X. Du, C. Seidel, Y. G. Ma, H.-J. Gao, L. F. Chi, H. Fuchs, *Phys. Rev. B.* 69 (2004) 075408.

Chapter 2 Theoretical Background

2.1 Photoelectron Emission Spectroscopy

The technique of photoelectron emission spectroscopy (PES) in its modern form was predominantly developed in the 1950s and 1960s as an analytical tool for the study of chemical and electronic properties of solids. It was found that accurate measurement of the electronic binding energies could provide information about the elemental composition of the sample in addition to information regarding the chemical environments of the elements present. The technique itself came about as a result of the breakthroughs in quantum physics around the start of the 20th century but due to poor equipment, it was not fully developed until the 50s and 60s. It was Kai Siegbahn¹ who developed much of the instrumentation and theory that is the basis for the modern analytical technique of PES, and in 1981 he was awarded the Nobel Prize in physics for his contributions to the development of the technique.

One of the qualities that makes synchrotron radiation PES such a valuable tool in chemical composition analysis of samples is that through the use of different incident photon energies, different depths in the sample can be probed. Section 2.4 will show that by correct choice of experimental setup, PES can be optimised in such a manner that the technique becomes extremely surface sensitive. This is achieved by altering the incident photon energy such that the resultant kinetic energy (KE) of the emitted electron falls within the 30-50eV range, which yields a minimum in the inelastic mean free path (IMFP) of the emitted electrons, which is a distinctive length that the electron can travel without an energy loss due to a collision. Although conventional X-ray photoelectron spectroscopy (XPS) and ultraviolet photoelectron spectroscopy (UPS) sources have fixed incident photon energies, many modern day high-resolution PES experiments make use of synchrotron radiation sources², which provide a continuous range of photon energies that can be tuned to a desirable photon energy for a given experiment. PES studies focus on two main regions of the spectrum (a) core levels (b) valence bands.

2.1.1 Photoelectron Emission Theory

The basic physics behind PES can be described by the Einstein equation³, which states:

$$E_B = h\nu - KE \quad (2.1)$$

where E_B is the binding energy of the electron in the atom and of the chemical environment in which it resides, $h\nu$ is the incident photon energy and KE is the kinetic energy of the emitted electron. It is therefore evident that the quantity E_B can be easily obtained from the known value for $h\nu$, and the measured value of KE.

The origin of the E_B of the electron must now be considered. Conceptually the E_B of an emitted photoelectron is simply the energy difference between the (n-1)-electron final state and the n-electron initial state, which can be summarised by the following:

$$E_B = E_f(n-1) - E_i(n) \quad (2.2)$$

An approximation of the E_B can be obtained from Koopmans' Theorem⁴ by assuming no rearrangement of the other electrons in the atom or material during the photoelectron emission process. The result is that the E_B of the electron is simply equal to the negative orbital energy, $-\epsilon_k$, summarised as:

$$E_B \approx -\epsilon_k \quad (2.3)$$

This approximation typically yields values that are within 10-30eV of the experimentally obtained values for E_B . However, this simple approximation does not account for all the contributions to the E_B of the electron. One of the main omissions in this equation is a result of the assumption that the other electrons in the atom do not respond to the emission of the photoelectron. In reality, the creation of a core hole will result in the other electrons in the atom rearranging in order to minimise the energy of the ionised atom. This final state effect, represented by $E_r(k)$ in equation 2.4, occurs both in the newly ionised atom and in the surrounding atoms. Further corrections to equation 2.3 occur due to electron correlation ($\delta\epsilon_{corr}$) and relativistic ($\delta\epsilon_{rel}$) effects. The addition of these amendments results in the following equation:

$$E_B = -\epsilon_k - E_r(k) - \delta\epsilon_{corr} - \delta\epsilon_{rel} \quad (2.4)$$

Typically the correlation and relativistic effects are small in magnitude however, and are frequently neglected in the calculation of the binding energy. Figure 2.1 shows a typical photoelectron emission process whereby the incident photon transfers all its energy to a core level electron with the resulting emission of a photoelectron. It can be seen from the diagram that Einstein's equation 2.1 does not take into account the workfunction of the sample ϕ_s . The workfunction of a sample is the minimum energy that an emitted photoelectron must possess before it will be able to leave the sample. By

taking this into account, a more accurate representation of the photoelectron emission process is therefore given by:

$$E_B = h\nu - KE - \phi_s \quad (2.5)$$

For a sample that is in electrical contact with the spectrometer (i.e. both grounded) the measured KE of the electron is reduced by $\phi_{sp} - \phi_s$, yielding the following equation for E_B as measured by the spectrometer:

$$E_B = h\nu - KE - \phi_{sp} \quad (2.6)$$

It is clear that in order to accurately calculate the E_B of a sample core level using equation 2.6, it is necessary to first know ϕ_{sp} , the workfunction of the spectrometer. Alternatively, the position of the Fermi Level (E_f) at a given incident photon energy can be used as a reference point. The energy separation between the core level and the Fermi Level can then be used to calculate the E_B of the core level without needing to calculate the workfunction of the spectrometer.

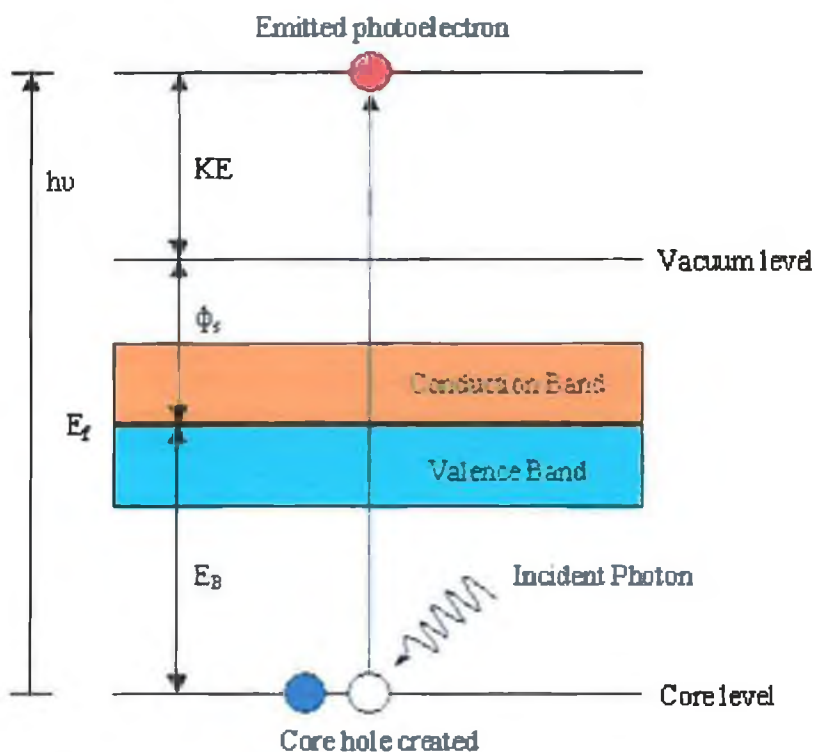


Figure 2.1 An example of a photoelectron emission process, where an incident photon transfers all its energy to a core level electron.

2.1.2 Core Level Spectroscopy

Core level spectra are obtained when electrons from deep lying atomic orbitals are excited by incident photons, which result in the emission of a photoelectron. The spectra are made up of both electrons that have been elastically scattered within the sample and from electrons that have been inelastically scattered within the sample. The inelastically scattered electrons give rise to the spectrum background, which increases on the low kinetic energy side of the peak, while the electrons that have been elastically scattered give rise to the sharp intense PES peaks. The differing internal orbital structure of all elements results in a unique PES spectrum for each element and serves as a fingerprint for the identification of constituent elements in a sample. In addition to identification of constituent elements, shifts in core level positions can be used to give information on the chemical environment of atoms in a sample

2.1.3 Analysis of Core Level Spectra

The peak width due to the core hole lifetime is Lorentzian in nature and can be calculated from the Heisenberg's uncertainty relationship³:

$$\Gamma = \frac{h}{\tau} \quad (2.7)$$

where Γ is the intrinsic width of the peak in eV, h is Planck's constant in eV-seconds and τ is the core hole lifetime in seconds. Since the lifetime of the core hole is dictated by how quickly another electron can fill the hole, it is evident that the core hole lifetime of inner shell electrons in general will be shorter than those of more loosely bound electrons, due to a greater probability of an electron from an outer shell electron falling to fill the core hole. Additionally core holes formed in atoms with a larger number of shells have a shorter lifetime due to increased probability of an outer shell electron falling to fill the core hole. It is evident from equation 2.7 that there is a reciprocal relationship between the lifetime of the core hole created, and the width of the observed PES peak.

In practice the overall shape of the PES peak is a convolution of the intrinsic Lorentzian lineshape of the core level and a Gaussian component, which takes instrumental broadening of the Lorentzian component into account. The main contributions to the Gaussian component are due to the energy spread of the incident radiation and the resolution of the analyser. In the case of conventional XPS studies, the energy spread of the incident X-rays result in the instrumental broadening dominating

over the intrinsic Lorentzian lineshape of the peaks, and the peaks become essentially Gaussian in nature. However, the much narrower intrinsic lineshape of the incident radiation obtained from synchrotron light sources allows for much higher resolution studies of surfaces by greatly reducing the Gaussian component in the measured lineshape. For synchrotron radiation based studies both the Lorentzian and Gaussian components to the lineshape must be considered⁵ for accurate fitting of the data. This convolution of a Lorentzian component and a Gaussian component is known as a Voigt lineshape.

The WinSpec⁶ fitting program was used to fit the core level spectra for the PES experiments in the thesis. The program allowed the user to input multiple peaks of various different types in addition to a choice of different backgrounds in order to fit the experimentally obtained lineshapes. In all core levels examined in this thesis, the lineshape of the core levels were fitted with Lorentzian peaks given by equation 2.8, which were Gaussian broadened by a unit area Gaussian curve. It should be noted that this fitting procedure is merely a computational approximation of a Voigt lineshape, as there was no actual convolution of Lorentzian and Gaussian components carried out by the program. The instrumental broadening was calculated in each case for a given incident photon energy, pass energy, and slit width, and was inputted as a fixed value in each case. The Lorentzian component was then calculated using:

$$L(x) = \frac{h}{1 + 4\left(\frac{x - x_0}{w}\right)^2} \quad (2.8)$$

where h is the peak intensity, x_0 is the peak position, and w is the Full Width at Half Maximum (FWHM) of the peak. The program utilised multiple iterations to minimise the difference between the inputted data spectrum and the computationally obtained fit of the spectrum.

If we now consider atoms at the surface of a sample, it is evident that they are unique in that the way that they are bonded to their neighbours differs from that of atoms in the sample bulk. This is due to the missing next atomic layer and results in a differing chemical environment than that experienced by atoms in the bulk. It is evident that atoms at the outermost layers have unsaturated bonds due to a lack of additional binding partners. In many cases the surface atoms will rearrange and form bonds with other surface atoms in order to minimise their potential energy. As mentioned previously, one of the strengths of the PES technique is its ability to identify atoms in

differing chemical environments by their energy shifted spectral components. In core level spectra of atomically clean surfaces it is common for two components to be observed, one which is attributed to the bulk atoms, and one which is attributed to the surface atoms^{7,8}.

2.1.4 Origin of Peak Shifts

Correct interpretation of core level peak shifts is essential for maximisation of the potential of PES as an analytical tool. As mentioned in section 2.1.3, surface reconstructions frequently result in the introduction of a new component to the PES spectra. However, there are many other effects that result in the emergence of new core level components, which must also be considered for correct interpretation of data.

(a) Initial state effects

Equation 2.2 shows that both the initial and final states effects contribute to the observed E_B of a core level. The initial state is simply the ground state of the atom prior to the emission of a photoelectron. It can be seen that a change in the initial state energy $E_i(n)$ will result in a change in the E_B of the core level. The initial state energy of an atom is changed by the formation of chemical bonds with other atoms. It is found that for many samples, the final state effects have similar magnitudes irrespective of the initial state energy. In these cases it can be shown that the change in the E_B of the core level is equal to the change in magnitude of the orbital energy ϵ_k yielding the formula:

$$\Delta E_B = -\Delta \epsilon_k \quad (2.9)$$

In summary, the formation of a bond that results in negative charge transfer from the investigated atom to its bonding partner will result in an increase in the E_B of the atom relative to its unbonded state, while negative charge transfer from the bonding partner to the investigated atom will result in a decrease in the E_B relative to its unbonded state.

(b) Final state effects

Within an individual atom involved in the PES process, the predominant final state effect in evidence is known as relaxation effects. As discussed briefly in section 2.1.1, the formation of a core hole in an atom by the emission of a photoelectron will result in a rearrangement of the remaining electrons in order to minimise the energy of the ionised atom. This results in all cases in the reduction of the E_B of the measured

photoelectron. Additional extra-atomic relaxation is also observed in many cases as the surrounding atoms contribute to the minimisation of the energy of the ionised atom.

This extra-atomic contribution to the effective screening of a core hole can be observed with the deposition of an adsorbate onto a metallic surface. The formation of a core hole in the adsorbate by the photoelectron emission process will result in a screening effect, which reduces the measured E_B of the core level from which the electron was emitted. Extra-atomic screening effects by metallic surfaces have been observed for the physisorption of xenon on Au(110)⁹ and additionally for organic molecules deposited on metal surfaces.

An alternative way to look at the extra-atomic screening process is as follows. In order to explain this effect we must initially consider an adsorbate molecule and a metallic surface separated sufficiently such that the molecule can be considered to be in its gas phase. If an electron is now removed from the core level of the molecule to an infinite distance from the molecule, the energy required is equal to the E_B of the core level. If this molecular cation is now moved towards the metal surface, it will experience an attractive force due to the electrostatic image force and it will lose potential energy. When at rest on the metal surface, the change in the potential energy of the hole can be calculated as $e^2/4r$, where r is the estimated distance of the positive charge from the metal surface.

If a neutral molecule on the surface is now considered, the energy required to remove an electron from a core level to infinity is equal to the gas phase binding energy of the adsorbate core level minus the change in potential energy mentioned above. The effect of this screening by the metal substrate is therefore to reduce the E_B of the core hole formed and so increases the kinetic energy of the emitted electron associated with the core hole.

Due to the fact that this screening effect is an electrostatic effect and so diminishes as $e^2/4r$, it is thought to only affect the initial monolayer of adsorbate. Therefore electrons emitted from the initial interfacial layer of adsorbate are affected by the final state screening effect and their kinetic energy is increased. In subsequent adsorbate layers, the screening effect is greatly diminished and so electrons emitted from the core levels of these molecules will have a lower kinetic energy than those from the interfacial layer.

While relaxation or screening effects are the final state effects that are observed to dominate on both the atomic and inter-atomic scales, additional atomic level final

state effects are also commonly observed in PES. The two main additional effects are multiplet splitting, which results from the interaction of the core hole with unpaired electrons in its outer orbitals, and shakeup satellites, which arise from the outgoing photoelectron losing part of its kinetic energy to excite a valence electron into an unoccupied orbital. These effects result in the loss of kinetic energy of the outgoing electron, which is observed as an increase in the E_B of the investigated core level.

(c) *Fermi level shifts*

The Fermi level in a metal is the energy above which no electrons are found at a temperature of 0K. It can be visualised as a step, where the probability of finding an electron goes from 1 to 0 across the step. At temperatures above 0K, thermal effects result in the broadening of this step and the Fermi level now becomes the statistical position at which the probability of finding an electron at a temperature above 0K is 0.5. This statistical definition of the position of the Fermi level can be applied to organic semiconductors.

The doping process in a semiconductor involves the addition of either holes or electrons to the sample depending on the desired doping effect. The addition of electrons to conduction band by doping the semiconductor with an electron donor will result in a movement of the Fermi level up the bandgap towards lowest unoccupied molecular orbital (LUMO). In PES this effective shift in the Fermi level will manifest itself as a shift in the adsorbate related core level and valence band peaks to higher binding energy.

2.1.5 Valence Band Spectroscopy

As stated in section 2.1.2, the core level spectra result from photoelectron emission from deep lying energy levels, which generally result in the observation of a well-defined PES peak. As schematically shown in figure 2.1, the valence band region of the PES spectrum is the region close in energy to the Fermi level, and therefore corresponds to emission from outer atomic orbitals with relatively low E_B . However, this region of the spectrum is of great interest because the orbitals that make up this region are the atomic orbitals generally involved in bond formation and in dictating the electronic behaviour of the material. It is therefore evident that a large amount of information can be deduced from valence band investigations of samples.

Studies of the valence band region are essential for investigation of the electronic and interface properties of samples, such as the valence band offset. In terms of organic/metal interface studies, information regarding the injection characteristics of the interface can be inferred from observation of the position of the highest occupied molecular orbital (HOMO) of the organic molecule relative to the Fermi level position. Additional essential information regarding band bending and the formation of interface dipoles can be obtained via measurement of the position of the secondary electron cutoff⁸.

2.1.6 Evaluating Valence Band Spectra

While core level studies are essential for building up a picture of the elements present in given sample, in addition to information regarding the chemical environment of the different elements present, valence band analysis provides information that cannot be obtained via a core level study and so is essential for a thorough investigation of molecular thin films. Molecular orientational information can be obtained from the molecular orbitals present in the valence band spectra, which cannot be obtained via a core level study. The application of group theory is used to extract pentacene orientational information in chapters 4 and 5 for pentacene thin films deposited on the Cu(110) and Au(100) substrates.

Additional information regarding surface states, molecular orbitals and the formation of interface states can also be extracted from valence band analysis. A large body of work by Corradini et al^{10, 11, 12, 13, 14, 15, 16} allows for the formation of simple guidelines for full analysis and interpretation of features in the valence band region of the PES spectrum of pentacene thin films deposited on atomically clean metal surfaces and is therefore summarised below.

(a) *Surface States*

These are identified as metal substrate related features that are fully quenched with the deposition of the initial monolayer of adsorbate. The quenching of these features should differ from the overall attenuation in the substrate related valence band features as a result of increasing overlayer thickness.

(b) Molecular Orbitals

Molecular orbitals can be identified by comparison with adsorbate related features observed for either a thick molecular film or a molecular film grown while maintaining a low substrate temperature. The features should be observed to grow from sub-monolayer coverages up to the formation of a thick molecular film. However, upon application of group theory, as described in section 2.2, this statement is observed to be fully correct only in circumstances where the orientation of the organic molecule remains constant with respect to the substrate throughout the entire molecular film. A molecular rearrangement or a change in molecular orientation at different film thicknesses can result in the suppression of some molecular orbital features despite an increasing film thickness.

(c) Interface States

Interface states are identified as features that are observed to increase in intensity up until the completion of the initial monolayer of adsorbate, and are subsequently attenuated with film growth in excess of the initial monolayer. They are due to bonding between the molecular orbitals of the adsorbate and the valence band orbitals of the substrate and can be either substrate or molecular related in character. A comparative study of two different π -conjugated molecules on the same metallic substrate can aid in the identification of interface states. The growth of identically positioned new features in both valence band studies cannot be attributed to molecular orbitals, as the position and character of molecular orbitals would differ for both molecules. New features observed in the valence bands can therefore be unequivocally identified as interface states.

The use of varying photoionisation cross section with changing incident photon energy can be used to probe the character of the identified interface state. An example of this can be seen in the bonding of a π -conjugated molecule to an Au substrate, studied using the HeI and HeII lines of the helium lamp, which have incident energies of 20.2eV and 40.4eV respectively. An increase in the Au5d photoionisation cross section by a factor of 1.5 between the energies of the HeI and HeII lines allows for the identification of Au 5d substrate related character in interface states that have a greater intensity in the valence band spectra obtained using the HeII line. Similarly, the molecular π -levels follow the photoionisation cross-section of the C2p peak, which diminished by a factor of 3 from HeI to HeII excitations. Therefore interface states that

are observed to decrease in intensity between the HeI and HeII valence band spectra are identified as having strong π character¹².

2.1.7 Workfunction measurements

Theoretically the workfunction consists of contributions from a bulk component and a surface component given by:

$$\phi_{tot} = \phi_{bulk} + \phi_{surf} \quad (2.10)$$

The bulk component depends exclusively on the bulk properties of the material and is not altered by adsorption of molecules on the surface. At the surface, the presence of asymmetric forces lead to a spill-out of the electron gas, which results in an asymmetric charge distribution or dipole layer on the surface¹⁷. The surface component of the workfunction is due to the difference in the electrostatic potential inside and outside the metal surface.

Experimentally the workfunction of the sample can be calculated from the energy position of the secondary electron tail and is usually obtained in conjunction with the valence band studies for organic/metal interfaces. However, in order to separate the workfunction of the sample from that of the analyser the sample is usually biased negatively. For systems with an observable Fermi edge, the workfunction of the sample can then be calculated from the width of the spectrum (accounting for the negative bias) and the incident photon energy as given by the formula:

$$\phi = h\nu - (E_F - E_{co}) \quad (2.11)$$

where E_F is the measured kinetic energy of the Fermi level of the grounded sample and E_{co} is the cutoff position, found by subtracting the sample bias from the kinetic energy position of the biased secondary electron cutoff. In organic/metal studies, measurement of the workfunction is essential as it provides valuable information regarding the magnitude of the interface dipole formed upon adsorption of the organic molecules.

2.1.8 Interface dipole formation

According to the Schottky model, when a semiconductor is brought into contact with a metal electrode, the Fermi levels of the two components line up, and the result is band bending in the semiconductor¹⁸. It was therefore also assumed that when an organic semiconductor was deposited on a metal substrate, band bending in the organic

semiconductor would result. Indeed this explanation was used up until relatively recently to explain the shift in the vacuum level of the sample in the transition from a clean substrate to a thin organic molecular film¹⁹. However, it was noted in many cases that the shift in the vacuum level was completed with the deposition of the initial monolayer of adsorbate. The calculated free carrier concentration required to account for the observed vacuum level shift purely in terms of band bending in the molecular film was found to be many orders of magnitude in excess of that measured for the organic semiconductors²⁰. It was therefore evident that the band-bending model used to explain the interaction at the interface of solid-state semiconductors and metals could not be applied to accurately explain the interaction at organic/metal interfaces.

The explanation for the vacuum level shift that is most favoured currently involves the formation of an interface dipole at the surface. While the idea of interface dipole formation is widely accepted, the origin of the vacuum level shift has remained relatively elusive until the past few years. One puzzling aspect of the interface dipole model was the magnitude of the interface dipole formed. For example, the adsorption of a completed saturated inert alkane on gold results in the formation of an interface dipole of magnitude 1.0eV^{21} , which is comparable in magnitude and direction to the vacuum level shift observed with the deposition of alkali metals on gold. While negative charge transfer from the alkali metal to the substrate can be used to explain the vacuum level shift observed for the deposition of an alkali metal on gold, the origin of the vacuum level shift involved with the formation of an organic/metal interface is less clear.

Using *ab initio* calculations, Witte et al²² have shown that the interface dipole is due partially to a chemical interaction between the molecule and the substrate, but the predominant contribution arises from the physical electron repulsion process, described as a “cushion” effect, associated with bringing the molecule ‘into contact’ with the metal surface. For physisorption of the molecule to the metal surface, Van der Waals forces pull the molecule towards the surface, with the molecular charge pushing aside the surface metal charge due to electron repulsion. As mentioned in section 2.1.7, the surface component of the workfunction is due to the difference in electrostatic potential outside the metal and in the sample. The repulsion of the spill-out of electrons from the metal by the electrons in the molecule results in a lowering of the electrostatic potential outside the metal. The difference in the electrostatic potential outside the metal and in the metal is now reduced, resulting in a lowering of the surface component of the workfunction of the metal, and hence a reduction in the overall workfunction. This

study found that the molecule acts as the “hard” partner in the interaction in terms of electron repulsion and the metal substrate acts as the “soft” partner.

For the case of chemisorption of the molecule, an additional interface dipole component due to negative charge transfer between the molecule and the surface is observed in addition to the charge repulsion effect. In the literature it has frequently been reported that the completion of the interface dipole is observed to occur with the deposition of the interfacial organic monolayer²⁰, although other groups have reported a contribution to the total dipole by the deposition of the second and third monolayers of adsorbate²³.

2.2 Group Theory

The physical and chemical applications of group theory are usually based on the geometric symmetries of atoms, molecules and crystals. By using these symmetry relations it is possible to form a connection between the molecular orientation of the pentacene molecule and the observed spectroscopy results.

In order to further our discussion on the application of group theory it is necessary to introduce the idea of “point groups” at this time. A point group classifies the type and number of symmetry operations that can be carried out on the molecule as shown in table 2.1²⁴.

Symmetry Operators		Symmetry Operations
Symbol	Description	
E	Identity	No change
σ_v	Plane of symmetry	Reflection through vertical plane
σ_h	Plane of symmetry	Reflection through horizontal plane
i	Center of symmetry – inversion	Inversion through the centre
C_n	Axis of Rotation	Rotation about the axis by $360^\circ/n$
S_n	Improper Rotation – rotation-reflection axis of symmetry	Rotation about the axis by $360^\circ/n$ followed by reflection through the plane

Table 2.1 Symmetry elements and symmetry operations²⁴.

In this section group theory is used to determine the point group and associated selection rules for a pentacene molecule, shown in figure 2.2. Each of the above symmetry elements listed in table 2.1 can be applied to the molecule. All the symmetry operations that can be performed on the pentacene molecule are shown in figure 2.2. For example a rotation about the C_2 y-axis of the pentacene molecule causes the molecule to rotate about the y-axis by 180° , therefore the displacement x vector points in the negative x-direction and the displacement z vector points in the negative z-direction. This result can be written as²⁴:

$$C_y(T_y) = (-1)(T_y) \quad (2.12)$$

It is helpful to summarise the symmetry properties of a molecule or point group in the form of a “character table”. These are formulated by application of all the symmetry operators to a point group with the result being given as either a “1” or “-1” in the character table.

The pentacene molecule is found to belong to the D_{2h} point group due to its symmetry. It is found to have three C_2 axes, a single C_2 axis along the z-direction and perpendicular to the σ_{xy} plane and two further C_2 axes along the x and y-axes. It also has a horizontal plane σ_h . The character table for the D_{2h} symmetry group and therefore the pentacene molecule is shown in table 2.2²⁴.

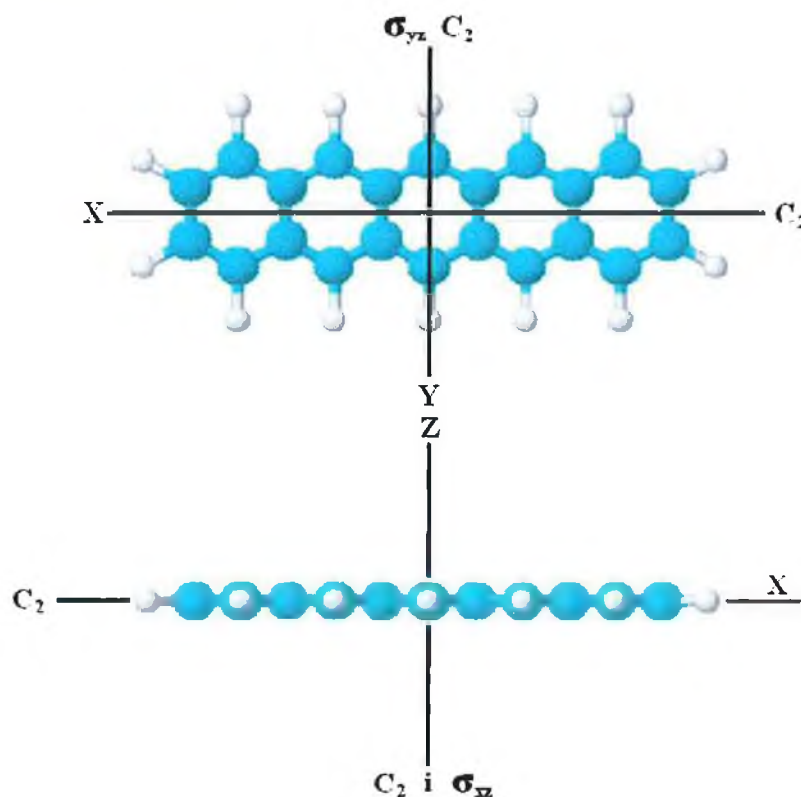


Figure 2.2 Diagram of pentacene molecule showing all the operations on the molecule.

D_{2h}	E	$C_2(x)$	$C_2(y)$	$C_2(z)$	i	$\sigma(xy)$	$\sigma(xz)$	$\sigma(yz)$		
A_g	1	1	1	1	1	1	1	1		x^2, y^2, z^2
B_{1g}	1	1	-1	-1	1	1	-1	-1	R_z	xy
B_{2g}	1	-1	1	-1	1	-1	1	-1	R_y	xz
B_{3g}	1	-1	-1	1	1	-1	-1	1	R_x	yz
A_u	1	1	1	1	-1	-1	-1	-1		
B_{1u}	1	1	-1	-1	-1	-1	1	1	z	
B_{2u}	1	-1	1	-1	-1	1	-1	1	y	
B_{3u}	1	-1	-1	1	-1	1	1	-1	x	

Table 2.2 Character table for D_{2h} symmetry²⁴.

Conventionally, the letters A, B, E and T are used in the left column of table 2.2. A and B are one-dimensional, E is two-dimensional and T is three-dimensional. The dimension of the irreducible representation is the dimension of any of its matrices. The subscript which may appear with A, B, E or T are arbitrary labels, with the subscript u represents antisymmetric with respect to inversion, and the subscript g represents symmetric with respect to inversion. The two columns on the right of the table contain the basis functions for the irreducible representations. These basis functions have the same symmetry properties as the atomic orbitals, which bear the same names.

Upon adsorption of the pentacene molecule on a substrate, the symmetry of the molecule can be reduced from the D_{2h} of the free molecule to C_{2v} symmetry. The C_{2v} symmetry is found to have only one C_2 axis along the z-direction, and has only two symmetry planes along the x and y-axes. Table 2.3 shows the character table for the C_{2v} symmetry.

C_{2v}	E	$C_2(z)$	σ_x	σ_y		
A_1	1	1	1	1	z	x^2, y^2, z^2
A_2	1	1	-1	-1	R_z	xy
B_1	1	-1	-1	1	x, R_y	zx
B_2	1	-1	1	-1	y, R_x	yz

Table 2.3 Character table for C_{2v} symmetry²⁴.

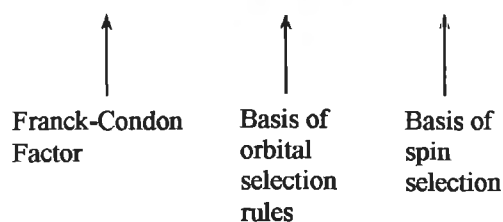
2.2.1 Selection Rules

It is found that symmetry constraints have a large role to play in dictating which transitions between energy levels are possible. For example, it can be shown that a molecule may not be able to absorb light, even if that light has precisely the correct energy to cause a transition between two energy levels of the molecule, if the symmetry conditions for the transition are not met. The symmetries of the states involved must be compatible in order for the transition to be possible. The selection rules which dictate which transitions are allowed and which are forbidden is one of the most important uses of symmetry.

The selection rules governing the uv-photoelectron emission process from the clean and pentacene covered Cu(110) and the Au(100) surfaces as a consequence of the symmetry properties of the system will be discussed.

Using a simplified one-dimensional model, it can be shown that the probability that a transition between two states will be induced by the oscillating electric field of a light wave is proportional to the square of the transition moment integral. For an electronic transition, the transition moment integral has the form²⁵

$$M = \int \psi_v^* \psi_v d\tau_n \int \psi_e^* \hat{\mu} \psi_e d\tau_e \int \psi_s^* \psi_s d\tau_s \quad (2.13)$$



Equation 2.13 is the basis of the electronic selection rules and is composed of three parts. The vibrational integral is labeled the Franck-Condon principle in equation 2.14, and is found to represent the overlap of vibrational wavefunctions between the ground and excited electronic states. The spin integral is also shown in equation 2.13. The orbital selection rules integral part of the equation is generally used on its own for calculating the electronic transitions.

Table 2.2 shows that the dipole moment operator of light in the x, y, and z direction with respect to the molecule are denoted by the symmetry operators B_{1u} , B_{2u} and B_{3u} respectively²⁵. For the reduced C_{2v} symmetry the dipole moment operator of light in the x, y and z directions with respect to the molecule are denoted the symmetry operators B_1 , B_2 and A_1 respectively²⁶. By using the operators it is possible to calculate

the allowed final state for a given initial state, which in essence is a calculation of

$$\int \psi_e^* \hat{\mu} \psi_e d\tau_e$$
 from equation 2.13.

In chapters 4 and 5, the selection rules governing the electronic transitions of the D_{2h} molecule are calculated and related to observed transitions in the valence band spectra in order to determine the molecular orientation of the molecule on the two surfaces.

2.3 Near Edge X-ray Absorption Fine Structure²⁷

The near edge X-ray absorption fine structure (NEXAFS) technique was developed in the 1980s with the goal of investigating the structure of molecules bonded to surfaces, and in particular low-Z molecules. The term “low-Z molecules” refers to the Z-number of the main constituent atoms in a molecule and so primarily refers to organic molecules containing carbon, oxygen, fluorine, and nitrogen. Prior to the development of NEXAFS, much of the molecular orientation studies would have been carried out using the LEED technique, which is described in section 2.7.

While the development of NEXAFS has only occurred from the 1980s onwards, the basis of the technique has been in use since the 1920s, when X-ray absorption spectroscopy was first used for the structural investigations of matter. The absorption structure was primarily divided into two sections, the fine structure near the absorption edges, known as “Kossel structure” for many years, after it was first explained in general terms by a theory of Kossel²⁸, and the structure extending for hundreds of electron volts past the absorption edge, known as the “Kronig structure”²⁹. The study of the “Kronig structure” became the basis for the technique of extended X-ray absorption fine structure (EXAFS).

The study of EXAFS was the precursor to NEXAFS, as the development of EXAFS as a powerful structural analysis tool in the 1970s inadvertently involved the acquisition of the NEXAFS spectrum with every EXAFS spectrum acquired. In most cases the NEXAFS part of the absorption spectrum was discarded as it was thought to be too complicated. It was noted however, that the near edge structure of low-Z molecules could be excited by electron energy loss spectroscopy. It was from these inner shell electron energy loss spectroscopy (ISEELS) studies that the first calculations of the near edge structure of molecules was carried out by Dehmer and Dill³⁰ and the technique of NEXAFS was born.

2.3.1 NEXAFS Theory

NEXAFS utilises the absorption of synchrotron radiation as a means of investigating the orientation of molecules on surfaces. The absorption process occurs in two steps, firstly by exciting electrons from a core level into an unoccupied molecular state above the Fermi level. Core hole annihilation then occurs, which involves the filling of the created core hole by a valence electron, with the surplus energy being released via the emission of either (a) an Auger electron or (b) a fluorescent photon as shown in figure 2.3.

It is evident that by varying the energy used to excite the core level electrons it is possible to promote the electrons into unoccupied states with different energies above the Fermi level. For low Z organic molecules, the unoccupied states closest to the Fermi level are found to be π in nature while those energetically separated from the Fermi level are σ in nature²⁷.

The probability of excitation of an electron from a core level to an unoccupied molecular orbital is given by equation 2.14.

$$I \propto \left| \langle f | e \cdot p | i \rangle \right|^2 \propto \frac{1}{|E|^2} \left| \langle f | E \cdot p | i \rangle \right|^2 \propto \frac{1}{|E|^2} \left| E \cdot \langle f | p | i \rangle \right|^2 \quad (2.14)$$

where i and f represent the initial and final states of the investigated transition, p is the sum of the linear momentum operators of the electron, and e is the unit vector of the plane electromagnetic wave.

For a $1s$ initial state and a vector final state orbital (i.e. a π^* state), the matrix element $\langle f | p | i \rangle$ points in the direction of maximum orbital amplitude. This means that the probability of excitation is at a maximum when the electric field vector E , is pointing in the same direction as the direction of the final state and is given by:

$$\left| e \cdot \langle f | p | i \rangle \right|_v^2 \propto I_v = \cos^2 \delta \quad (2.15)$$

where δ is the angle between the E -field vector and the vector direction of the final state orbital.

Similarly it can be shown that the transition probability between a $1s$ initial state and a planar molecular orbital (i.e. a σ^* state) is given by:

$$\left| \langle f | e \cdot p | i \rangle \right|_p^2 \propto I_p = \sin^2 \varepsilon \quad (2.16)$$

where ϵ is the angle between the E-field vector and normal to the plane of the final state orbital. It should be noted that for pentacene the π^* molecular orbitals are perpendicular to the molecular plane and the σ^* molecular orbitals are in the plane of the molecule so the angles δ and ϵ in equations 2.15 and 2.16 respectively are equivalent.

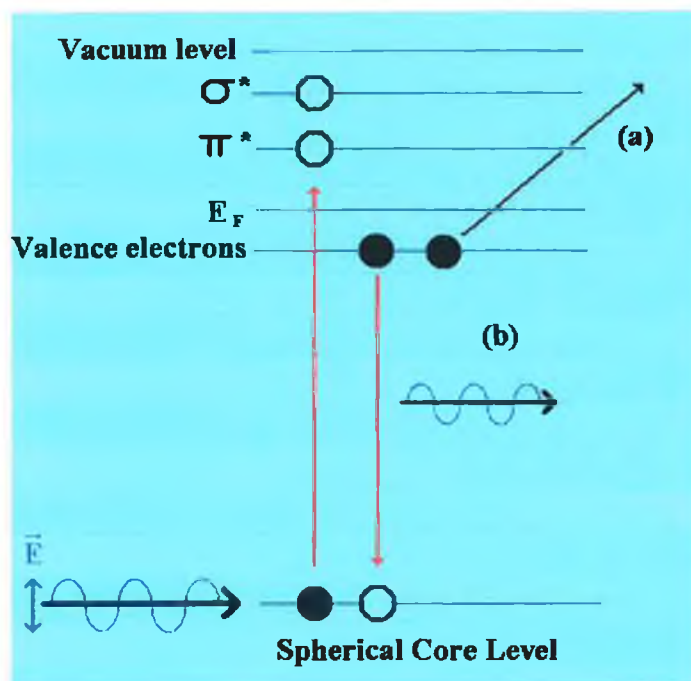


Figure 2.3 Two-step process that forms the basis for NEXAFS studies. The first step involves excitation of core level electrons into π^* and σ^* unoccupied levels. The core hole left by the excitation process is then filled by a valence electron with the surplus energy resulting in either the emission of (a) an Auger electron or (b) a fluorescent photon.

The cases stated by equations 2.15 and 2.16 are for the interaction of a unidirectional E-field with π^* and σ^* molecular orbitals. For synchrotron radiation obtained from a bending magnet source it is found that the electric field vector has two phase-related, orthogonal components of different magnitude that must be considered. The larger component lies in the horizontal orbital plane of the storage ring and the smaller component is vertical. If the coordinate system is oriented such that the X-rays propagate down the z-axis and the x- and y- axes with unit vectors e^{\parallel} and e^{\perp} lie in the horizontal and vertical planes respectively, the electric field E can then be described by:

$$E = E^{\parallel} \cos(kz - \omega t) + E^{\perp} \sin(kz - \omega t) \quad (2.17)$$

where k is the momentum of the X-rays and ω is the frequency of the electromagnetic wave.

Equation 2.14 must now be altered to account for the perpendicularly oriented E-field vectors with the resultant equation of the form:

$$I \propto \frac{\left| \langle f | E^{\parallel} \cdot p | i \rangle \right|^2 + \left| \langle f | E^{\perp} \cdot p | i \rangle \right|^2}{|E^{\parallel}|^2 + |E^{\perp}|^2} \quad (2.18)$$

It is helpful at this point to introduce a quantity known as the polarisation factor P , which characterises the degree of linearly polarised light as a function of the total light and is given by:

$$P = \frac{|E^{\parallel}|^2}{|E^{\parallel}|^2 + |E^{\perp}|^2} \quad (2.19)$$

Using equation 2.19, equation 2.18 can now be represented by:

$$I \propto P \left| \langle f | e^{\parallel} \cdot p | i \rangle \right|^2 + (1 - P) \left| \langle f | e^{\perp} \cdot p | i \rangle \right|^2 \quad (2.20)$$

where e^{\parallel} and e^{\perp} are the unit length vectors in the direction of E^{\parallel} and E^{\perp} .

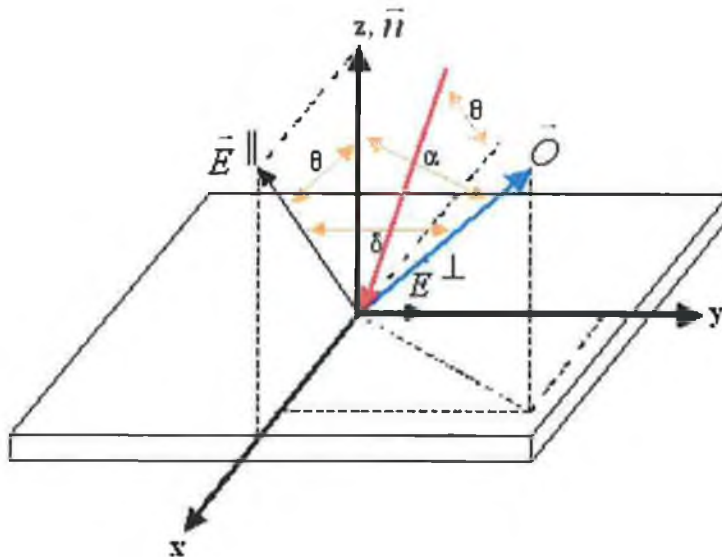


Figure 2.4 Coordinate system defining the geometry of a π^* vector orbital, denoted by \vec{O} , with respect to the sample surface and the incident synchrotron radiation.

Figure 2.4 shows a coordinate system defining the geometry of a π^* vector orbital, denoted by \vec{O} , with respect to the incident E-field vectors \vec{E}^{\parallel} and \vec{E}^{\perp} . θ denotes the angle between the incident synchrotron radiation and the plane of the surface, α denotes the angle between the surface normal and the vector orbital \vec{O} , and δ denotes the angle between the projections of \vec{O} and \vec{E}^{\parallel} onto the surface plane.

Using the coordinate system defined by figure 2.4, equation 2.20 can be redefined in terms of the angles θ , α and δ . It can be shown that for a surface exhibiting twofold symmetry the intensity of the π^* emission can be given by:

$$I \propto P \left(\cos^2 \theta \cos^2 \alpha + \sin^2 \theta \sin^2 \alpha \cos^2 \delta \right) + (1 - P) \left(\sin^2 \alpha \sin^2 \delta \right) \quad (2.21)$$

For threefold or higher symmetry, the $\cos^2 \delta$ averages to $\frac{1}{2}$ and the intensity variance of the π^* emission can be given by:

$$I \propto P \left(\cos^2 \theta \cos^2 \alpha + \frac{1}{2} \sin^2 \theta \sin^2 \alpha \right) + (1 - P) \left(\frac{1}{2} \sin^2 \alpha \right) \quad (2.22)$$

Using equations 2.21 and 2.22 it is therefore possible to deduce the orientation of the unoccupied molecular orbital with respect to the incident synchrotron radiation, and consequently with respect to the substrate.

2.4 Surface Sensitivity

As mentioned previously, the surface sensitivity of PES as an analytical technique is inextricably linked to the kinetic energy of the emitted electrons. Because the NEXAFS technique used measures the Auger peak in the PES spectrum in order to form NEXAFS spectra, the sampling depth is also found to be dependent on the kinetic energy of the emitted Auger electrons.

The inherent electric charge on electrons results a much greater interaction with matter than that observed for photons of similar energy. So while the incident photons in PES are found to penetrate deep into the sample, the measured photoelectrons that make up the PES peak (i.e. those that have not been inelastically scattered within the sample) can be shown to come from a region that is much closer to the surface. Photoelectrons emitted from deeper in the sample may escape and be collected by the analyser but in propagating to the surface they will have collided with other atoms or

electrons and lost energy through inelastic collisions. These electrons constitute the background signal observed in the PES spectrum.

An electron travelling through a solid with a well defined kinetic energy will have a certain inelastic mean free path (IMFP) as calculated using equation 2.23, which is a distinctive length that the electron can travel without an energy loss due to a collision. Emitted photoelectrons with a kinetic energy in the range 40-150eV are found to be particularly surface sensitive, as shown in figure 2.5.

There appears to be two competing mechanisms³¹ at work that influence the IMFP of the emitted electrons. At very low kinetic energies the electrons are unable to excite any of the loss mechanisms and therefore the IMFP is very long. These loss mechanisms include plasmon excitations and electron-hole pair formation. Plasmon excitations are collective oscillations of the free electron gas, and can occur either at the sample surface or within the sample. At very high energies the cross section for these losses is again low and the IMFP is long.

$$\text{IMFP} = \lambda_d = 49\text{KE}^{-2} + 0.11\text{KE}^{0.5} \quad (2.23)$$

The mean free path for increasing electron kinetic energy in a pentacene film shown in figure 2.6 was calculated using the Tanuma, Powell, and Penn formula in the program electron inelastic-mean-free-path v.1.1, provided by the National Institute of Standards and Technology, NIST³¹.

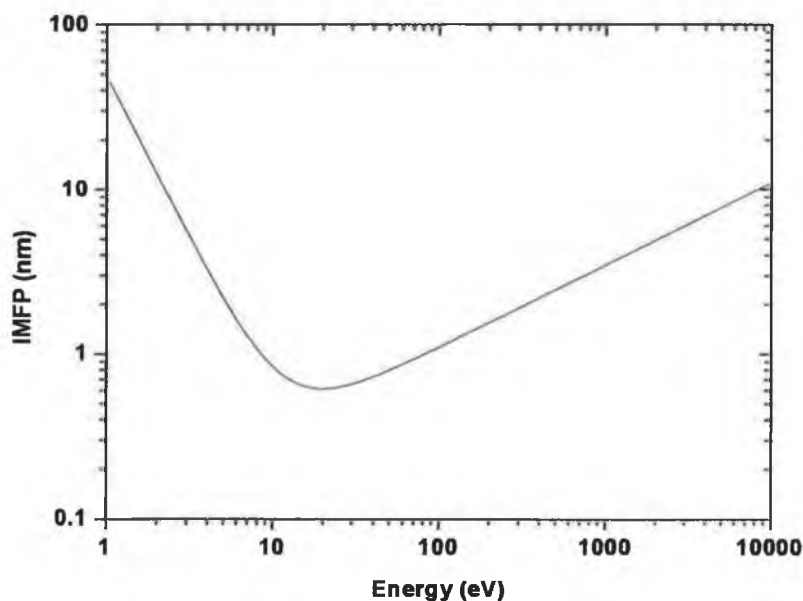


Figure 2.5 Universal Inelastic Mean Free Path versus electron kinetic energy for organic thin films calculated using equation 2.23³¹.

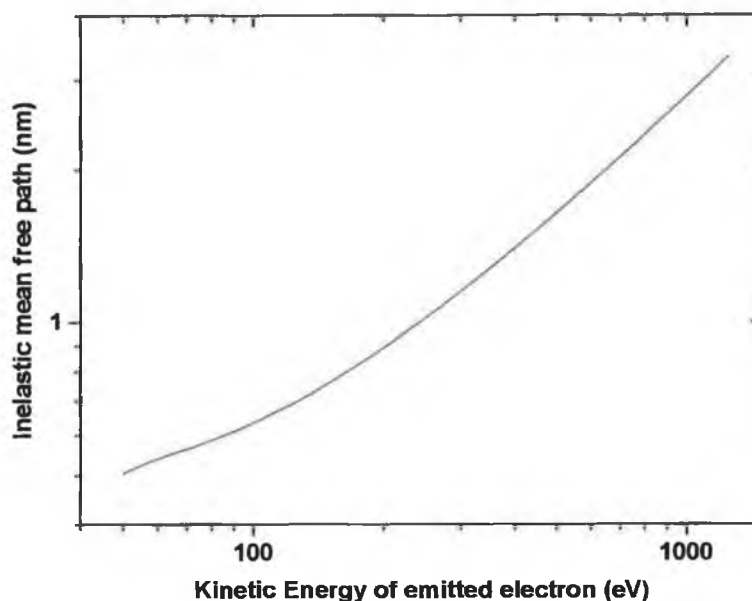


Figure 2.6 Inelastic Mean Free Path versus electron kinetic energy for electrons propagating through a pentacene overlayer³².

It should be noted that the program does not allow for the calculation of the IMFP of electrons emitted with a kinetic energy of less than 50eV, therefore the increase in the IMFP of electrons of kinetic energy less than 20eV is not observed in this diagram. It should also be noted that since the program takes the pentacene film density into account in the calculation of the IMFP values, it is assumed that the calculated IMFP values are more accurate than those calculated using equation 2.23, which is a general formula for organic films. The sampling depth, which is defined as the depth from which 95% of the elastically scattered electrons are found to come from, is calculated as three times the IMFP at a given electron kinetic energy.

2.5 Scanning Tunnelling Microscopy

Scanning tunnelling microscopy (STM) is a technique that has revolutionised the study of surfaces in the 25 years since its invention. Indeed such was the revolutionising effect of the STM that its inventors, G. Binnig and H. Rohrer, were awarded a Nobel Prize a mere five years after its invention. The STM was invented by G. Binnig and H. Rohrer, along with co-workers at the IBM Zurich Research Laboratory in March 1981^{33, 34, 35}. The operational concept of the STM is relatively simple. A metal tip is positioned in very close proximity to a conducting sample surface, so close that the wave functions of the closest atom in the tip and the surface

atom overlap. If a potential is now applied between the tip and the surface, a tunnel current will be observed flow. By varying the potential between the tip and the surface, the local density of states can be probed. By scanning the tip across the surface an image of the surface topography can be formed from either variations in the observed tunnelling current or from variations in the tip height necessary to maintain a constant tunnelling current and therefore constant tip-surface separation.

One of the first applications of STM, and certainly one that caused the most impact was the solution to the problem of the atomic arrangement of the reconstructed (7×7) surface on silicon (111)³⁶ over which there had been much debate.

2.5.1 Tunnelling Theory

By considering the solution to the Schrödinger equation for a one-dimensional square barrier of height V_0 shown in figure 2.7, it is possible to understand the theory behind the tunnelling observed for STM operation.

In classical mechanics, the energy E of an electron moving in a potential $U(z)$ with momentum p is given by:

$$\frac{p_z^2}{2m} + U(z) = E \quad (2.24)$$

where m is the mass of the electron. The electron has a nonzero momentum and can move in regions where $E > U(z)$ but cannot penetrate into any region where $E < U(z)$, i.e. a potential barrier.

The equivalent quantum mechanical expression for the state of the same electron is Schrödinger's equation, where the electron is described by a wavefunction $\psi(z)$, which satisfies Schrödinger's equation³⁷,

$$-\frac{\hbar^2}{2m} \frac{d^2}{dz^2} \psi(z) + U(z)\psi(z) = E\psi(z) \quad (2.25)$$

where $\hbar = h/2\pi$ and h is Planck's constant. Consider the case of a piecewise constant potential, as shown in figure 2.7. In the classically allowed region, $E > U$, the electron is represented by a traveling wave and equation 2.25 has solutions³⁷

$$\psi(z) = \psi(0)e^{\pm ikz} \quad (2.26)$$

where

$$k = \frac{\sqrt{2m(E - U)}}{\hbar}$$

is the wave vector. The electron is moving (in either the positive or the negative direction) with a constant momentum $p_z = \hbar k = [2m(E - U)]^{1/2}$, or a constant velocity $v_z = p_z/m$, the same as the classical case. In the classically forbidden barrier region, $E < U$ (region 2 in figure 2.7) the wavefunction is a decaying exponential³⁸

$$\psi(z) = \psi(0)e^{-\kappa z} \quad (2.27)$$

where

$$\kappa = \frac{\sqrt{2m(U - E)}}{\hbar}$$

is the decay constant. The probability density of observing an electron near a point z is proportional to³⁸

$$|\psi(0)|^2 e^{-2\kappa z} \quad (2.28)$$

which has a nonzero value in the barrier region.

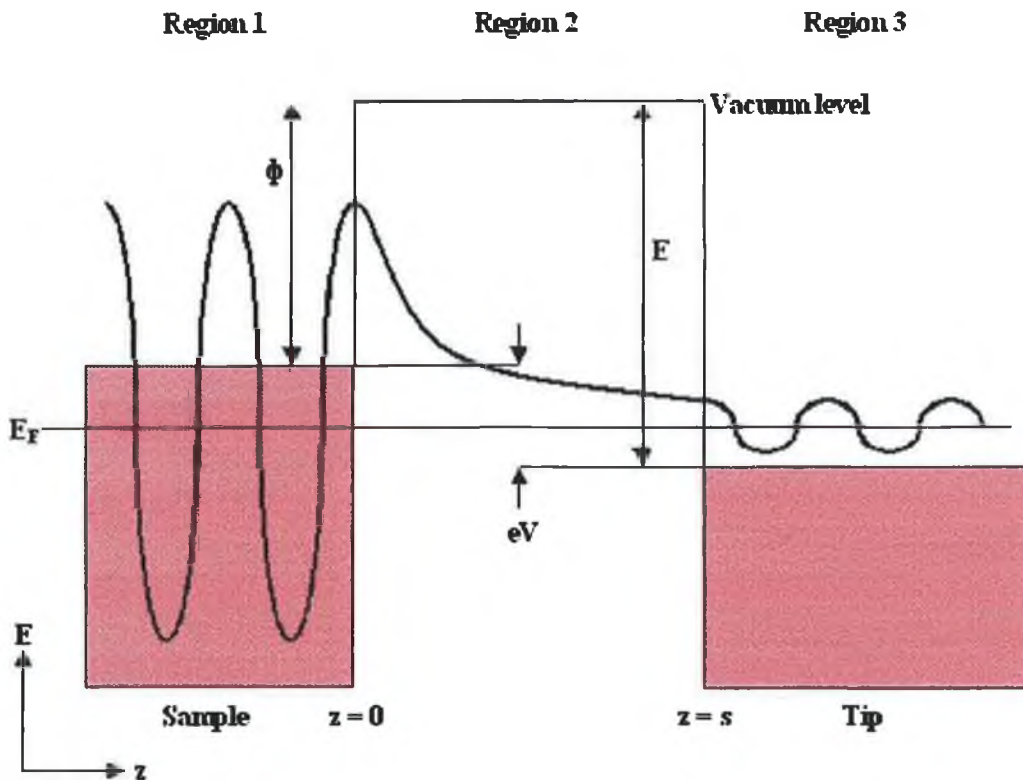


Figure 2.7 One-dimensional metal-vacuum-metal tunnelling junction. The bias voltage V is assumed to be small ($eV \ll \phi$) and the workfunctions of both electrodes are identical so the vacuum level is effectively the same for both electrodes.

From this elementary model, some basic features of metal-vacuum-metal tunneling can be explained. If the vacuum level is taken as the zero point for energy, then the Fermi level is $E_F = -\phi$, where ϕ is the workfunction, i.e. the energy required to remove an electron from the surface of a metal^{37, 38, 39}. The workfunctions of the two

electrodes are assumed to be equal. For materials commonly encountered in STM experiments, typical values of the workfunction lie between 4.0 and 5.5eV. By applying a bias V to the junction, a net tunneling current can flow due to tunneling from states between $E_F - eV$ and E_F . For small bias voltages ($eV \ll \phi$), the energy levels of the tunneling states are approximately equal to the Fermi energy. Thus, the energy of the n^{th} tunneling state E_n can be approximated by $E_n \approx -\phi$ and the probability P of an electron from this state reaching the tip can be written as^{37, 38}

$$P \propto |\psi(s)|^2 = |\psi(0)|^2 e^{-2\kappa s} \quad (2.29)$$

where

$$\kappa = \frac{\sqrt{2m\phi}}{\hbar}$$

is the decay constant of a sample near the Fermi level in the barrier region, and s is the gap between the electrodes, as shown in figure 2.7. Using eV as the unit of the workfunction, and \AA^{-1} as the unit of the decay constant, the numerical value of κ is

$$\kappa = 0.51\sqrt{\phi(\text{eV})} \text{\AA}^{-1} \quad (2.30)$$

For a typical workfunction value of 4eV, this implies that $\kappa = 1.025 \text{\AA}^{-1}$ so the current will fall by a factor of $e^{2\kappa} \approx 7.75$ times if the gap width is increased by 1 \AA . The total tunneling current I , reaching the tip, can be calculated by summing over all the states between $E_F - eV$ and E_F ³⁸.

$$I(V) \propto \sum_{E_n=E_F-eV}^{E_F} |\psi_n(0)|^2 e^{-2\kappa s} \quad (2.31)$$

For small bias voltages, the density of states of a metal is constant between $E_F - eV$ and E_F and the current can be written in terms of the local density of states (LDOS) of the sample at the Fermi level. At a location z and energy E , the LDOS $\rho_s(z=0, E = E_F)$ of the sample is defined as³⁸

$$\rho(z, E) \equiv \lim_{\epsilon \rightarrow 0} \frac{1}{\epsilon} \sum_{E_n=E-\epsilon}^E |\psi_n(z)|^2 \quad (2.32)$$

for a sufficiently small energy, ϵ . The tunneling current at the tip can then be written in terms of the LDOS of the sample as³⁸

$$I(V) \propto V \rho_s(0, E_F) e^{-2\kappa s} \quad (2.33)$$

2.6 Growth Modes⁴⁰

Due to scientific and technological interest, many studies are concerned with growth modes of adsorbates on metal and semiconductor substrates. Temperature, deposition rate and defects of both the substrate and of the growing film can influence the growth modes on metals and semiconductors. In the case of single crystal substrates, the lattice mismatch must also be accommodated during growth by the formation of either epitaxial or overlayer structures or surface alloy structures. However, the adsorption of organic molecules on metal substrates does not result in the formation of alloy structures and so the discussion will focus on epitaxial growth.

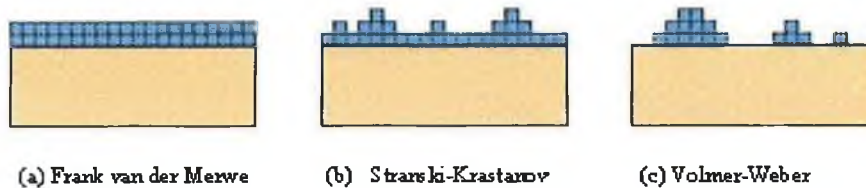


Figure 2.8 Epitaxial Growth Modes: (a) Frank van der Merwe, (b) Stranski-Krastanov; and (c) Volmer Weber.

The term epitaxial growth describes an ordered overlayer structure formed on a single crystal surface. In many cases, such as the adsorption of organic molecules on metal or semiconductor surfaces, the adsorption does not terminate upon the completion of a single monolayer and multilayer structures may be formed.

Epitaxial growth is broadly classified into three different growth modes, based on their original investigators, namely, (i) Frank-van der Merwe, (ii) Volmer Weber (VW) and (iii) Stranski-Krastanov (SK) modes as shown in figure 2.8. These growth modes are governed by the surface free energies of the deposited adatoms (γ_A), the substrate (γ_S) and the interface (γ_{A-S}) according to the parameter:

$$\Delta\gamma = \gamma_A + \gamma_{A-S} - \gamma_S \quad (2.34)$$

(i) *Frank van der Merwe (FM): monolayer-by-monolayer growth*

$$\Delta\gamma \leq 0$$

If there is a large difference between the two surface free energies then the parameters γ_A and γ_S will strongly influence the growth mechanism. In FM growth, the adatoms are more strongly bound to the substrate than to each other. The initial adatoms condense to form a complete monolayer. Then a less tightly bound second

layer covers this. If the decrease in bonding energy is monotonic towards the value of the bulk crystal, then layer-by-layer growth may occur. Whether FM growth continues to high coverages is strongly dependent on the strain energy, that is the lattice mismatch between the substrate and the adsorbate atoms. If its mismatch is large (typically >0-4%) then continued FM growth is unlikely, however it is possible in systems with large lattice mismatch provided that the strain can be relieved, usually by a defect mechanism.

(ii) *Volmer-Webber (VW): Island Growth*

$$\Delta\gamma > 0$$

In this mode adatoms grow as three-dimensional islands. The adatoms are more strongly bound to each other than to the substrate and small clusters nucleate directly on the surface as adsorbate growth continues.

(iii) *Stranski-Krastanov (SK): Monolayer plus Islanding Growth*

$$\Delta\gamma < 0$$

SK growth refers to growth of islands following the deposition of one or more complete monolayers. Any factor that disrupts the monotonic decrease in bonding energy with coverage, thereby resulting in high free energy of the adlayer surface, may cause layer growth to become unfavourable. The bonding energies of a system, large lattice mismatches and the method of adsorbate growth are the major influences on the development of a SK growth mode.

2.7 Low Energy Electron Diffraction

Low energy electron diffraction (LEED) is a technique that uses electron diffractions as a means to probe the crystal structure of a sample. The electron diffraction technique is separated into two general energy regions, a low energy region that spans the energy range 10-500 eV, and high-energy range spanning 10-20 keV. The wavelength of the electron is related to its energy using the simple equation:

$$\lambda = \left(\frac{150.6}{E(eV)} \right) \text{ \AA} \quad (2.35)$$

where E is the electron beam energy. This equation yields wavelength values in the range of approximately 1.0-0.1Å for the low energy electrons. Since these values are on

the scale of the interatomic spacing in crystals, diffraction is possible. Nearly all of the elastic collisions that lead to diffraction peaks take place in the one or two atomic layers close to the surface ensuring that this technique is extremely surface sensitive.

The elastically scattered electrons produce a diffraction pattern, which allows the two-dimensional surface periodicity to be calculated. Unit cell sizes can be calculated from the observed diffraction pattern and therefore adsorption-induced changes in the unit cell can be measured. By measuring the variations in the spot intensities with beam energy, a technique referred to as IV-LEED, can be used to determine the complete surface geometry of a sample.

2.7.1 Diffraction/LEED Theory

Any plane of atoms in a crystal structure can be defined by three coordinates known as Miller Indices, (h, k, l). These Miller indices are obtained by calculating the intercepts of a plane with the a, b, c, axes as a fraction of a, b, c, then taking reciprocals of these numbers, and expressing the result in the form of the smallest whole numbers.

The Miller indices of a plane bear a reciprocal relationship to the real intercepts of the plane with the axes; in the same way the wavelength of an x-ray beam (a real distance) bears a reciprocal relationship to the wavevector, k , of the beam, whose magnitude is defined as³:

$$|\mathbf{k}| = 2\pi/\lambda \quad (2.36)$$

The wavevector is a measure of the momentum of the incident and diffracted beams. The change in the wavevector of a beam scattering from a plane of atoms will determine the wavevector of any emergent diffracted beams. A diffracted beam of electrons emerges from a crystal whenever constructive interference occurs between electrons scattered from successive planes of atoms in the real lattice. By applying the law of conservation of momentum to a reciprocal lattice, where the distances are directly proportional to momentum, it is possible to find where constructive interference occurs. The geometrical construction employed is known as the Ewald sphere construction. Figure 2.9 shows the reciprocal space diagram for a cubic lattice, with the distance between adjacent lattice points is $2\pi/d$, where d is the distance between points in the real lattice. A wavevector \mathbf{k}_0 , representing the wavevector of the incident electron beam, is drawn on the diagram with its tip pointing towards (000), the origin of

reciprocal space. A sphere is drawn with radius $|k_0|$, with the origin at point P. This is the Ewald sphere³.

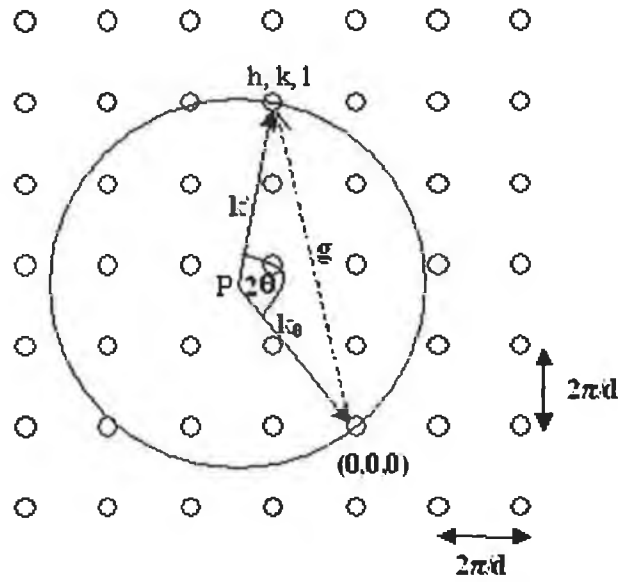


Figure 2.9 Ewald sphere construction for a cubic lattice. (hkl) are the Miller indices of the point on the Ewald sphere.

If the sphere intersects any of the reciprocal lattice points, the condition for elastic scattering is satisfied (i.e. there is a change in momentum of the beam but there is no change in energy) with the scattered beam having a wavevector k' . By conservation of momentum³:

$$k_0 = k' + g \quad (2.37)$$

where the change in momentum on scattering is represented by the reciprocal lattice vector g . For elastic scattering $|k_0| = |k'|$. From figure 2.9 it can be seen that³:

$$\sin \theta = \frac{|g|/2}{|k_0|} \quad (2.38)$$

Pythagoras' theorem in three dimensions gives us the result that:

$$|g| = (h^2 + k^2 + l^2)^{1/2} 2\pi/d \quad (2.39)$$

Using equation 2.38 it can be shown that:

$$\sin \theta = (h^2 + k^2 + l^2)^{1/2} \lambda / 2d \quad (2.40)$$

where λ is the deBroglie wavelength of the electron. It can be shown that equation 2.40 constitutes the familiar Bragg condition for diffraction given by:

$$n\lambda = 2d \sin \theta \quad (2.41)$$

where $n = (h^2 + k^2 + l^2)^{1/2}$, known as the order of diffraction. By relating the interplanar spacing, d , in equation 2.40 to the unit cell lengths, a , b and c , the angles at which diffraction occurs can be used to calculate the unit cell size.

2.7.2 Elements of LEED Theory

The construction of an Ewald sphere in two dimensions differs slightly from that of the three dimensional case. It can be shown that instead of showing reciprocal lattice points in three-dimensions, a diagram would show reciprocal lattice rods. This arises because if the surface forms a completely two-dimensional net the periodic repeat distance normal to the surface is infinite. In the previous section, the distance between adjacent points in three dimensions in a reciprocal lattice is inversely proportional to the corresponding distance in the real space. Therefore in two-dimensions the reciprocal lattice points normal to the surface are infinitely dense, forming rods. The diffraction condition is satisfied for every beam that emerges in a direction along which the sphere intersects a reciprocal rod⁴¹ as shown in figure 2.10. ψ denotes the exit angle, θ denotes the diffraction angle and ϕ denotes the angle of incidence in figure 2.10.

In LEED experiments, diffracted beams may occur at all energies, provided the corresponding rod lies within the Ewald sphere. Changing the incident beam energy will change the radius of the sphere, $|k_0|$, and the number and directions of scattered beams will vary. It is therefore evident that the LEED spots tend towards the specularly (0,0) reflected beam as the incident electron beam energy is increased.

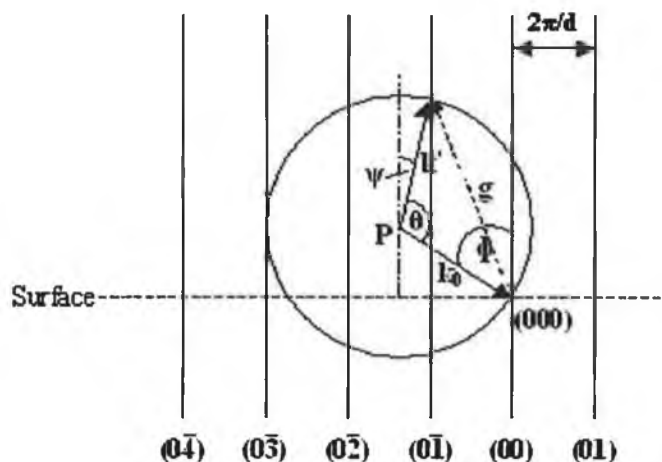


Figure 2.10 Two-dimensional Ewald sphere construction³.

2.8 Summary

Section 2.1 describes in detail the theory behind the PES technique in addition to an in-depth discussion of the features observed in the PES spectra and the significance of observed changes in these features.

Section 2.2 introduces the theory behind the application of group theory to PES analysis. This discussion begins with operator assignments and point group identification and follows with an introduction to the theory that is used for the formulation of the selection rules used in PES analysis in chapters 4 and 5.

Section 2.3 deals with the theory behind the NEXAFS technique, including a brief derivation of the formulae associated with investigation of the angular orientation of the molecule. Section 2.4 discusses the origin of the surface sensitivity of the PES and NEXAFS experimental techniques.

Section 2.5 describes the theory behind the operation of STM. This section uses a quantum mechanical approach to derive equations relating to the tunnelling current observed between two closely spaced surfaces. It was found that the tunnelling current decreases exponentially with an increase in the surface spacing. This effect is utilised in STM to image the atomic structure of the surface under investigation.

Section 2.6 consists of a brief discussion of the different growth modes associated with the adsorption of organic molecules on different surfaces and the origin of the different growth modes. Section 2.7 introduces the theory associated with the LEED technique. Diffraction theory and reciprocal space are introduced to help explain the operation of the LEED system.

Chapter 2 References

-
- ¹ K. Siegbahn, *Science*, 217, (1982), 111
 - ² G. Margaritondo, *Introduction to Synchrotron Radiation*, Oxford University Press, 1988.
 - ³ J. C. Vickerman, *Surface Analysis – The Principal Techniques*, J. Wiley and Sons, 1997.
 - ⁴ T. S. Koopman, *Physica*, 1, (1934) 104-113.
 - ⁵ J.J. Joyce, M. Del Giudice, J.H. Weaver, *J. Electron Spectroscopy and Related Phenomena*, 49, (1989) 31.
 - ⁶ Winspec ver 2.08, Laboratoire Interdisciplinaire de Spectroscopie Electronique, Facultés Universitaires Notre-Dame de la Paix, Belgium.

- ⁷ L. Ley, M. Cardona, *Topics in Applied Physics Vol 27, Photoemission in Solids I and II*, Springer-Verlag 1979.
- ⁸ E.W. Plummer, W. Eberhardt, *Advances in Chem. Phys.* 49, (1982) 533.
- ⁹ K. Horn, K. H. Frank, J. A. Wilder, *Phys. Rev. Lett.* 57 (1986) 1064.
- ¹⁰ V. Corradini, C. Menozzi, M. Cavallini, F. Biscarini, M. G. Betti, C. Mariani, *Surf. Sci.* 532–535 (2003) 249.
- ¹¹ C. Menozzi, V. Corradini, M. Cavallini, F. Biscarini, M. G. Betti, C. Mariani, *Thin Solid Films* 428 (2003) 227.
- ¹² C. Baldacchini, M. G. Betti, V. Corradini, C. Mariani, *Surf. Sci.* 566–568 (2004) 613.
- ¹³ F. Evangelista, A. Ruocco, D. Pasca, C. Baldacchini, M. G. Betti, V. Corradini, C. Mariani, *Surf. Sci.* 566–568 (2004) 79.
- ¹⁴ F. Evangelista, A. Ruocco, V. Corradini, M.P. Donzello, C. Mariani, M. G. Betti, *Surf. Sci.* 531 (2003) 123.
- ¹⁵ V. Di Castro, F. Allegretti, C. Baldacchini, M. G. Betti, G. Contini, V. Corradini, F. Lamastra, C. Mariani, *Surf. Sci.* 507–510 (2002) 7.
- ¹⁶ F. Bussolotti, V. Corradini, V. Di Castro, M. G. Betti, C. Mariani, *Surf. Sci.* 566–568 (2004) 591.
- ¹⁷ X. Crispin, *Sol. Energ. Mat. Sol. C.* 83 (2004) 147.
- ¹⁸ E. H. Rhoderick and R. H. Williams, *Metal-semiconductor contacts*, Oxford University Press, 1988
- ¹⁹ K. Seki, N. Hayashi, H. Oji, E. Ito, Y. Ouchi, H. Ishii, *Thin Solid Films* 393 (2001) 298.
- ²⁰ I. G. Hill, A. J. Mäkinen, Z. H. Kafafi, *J. Appl. Phys.* 88 (2000) 889.
- ²¹ E. Ito, H. Oji, H. Ishii, K. Oichi, Y. Ouchi, and K. Seki, *Chem. Phys. Lett.* 287 (1998) 137.
- ²² G. Witte, S. Lukas, P. Bagus, Ch. Wöll, *Appl. Phys. Lett.* 87 (2005) 263502.
- ²³ G. Koller, R. I. R. Blyth, S. A. Sardar, F. P. Netzer, M. G. Ramsey, *Appl. Phys. Lett.* 76 (2000) 927.
- ²⁴ A. Vincent, *Molecular Symmetry and Group Theory: A programmed Introduction to Chemical Applications*, J. Wiley and Sons, (1977).
- ²⁵ D.C. Harris, M.D. Bertolucci, *Symmetry and Spectroscopy: An Introduction to Vibrational and Electronic Spectroscopy*, Dover Publications Inc., 1978.
- ²⁶ S. L. Altmann, P. Herzig, *Point-group theory tables*, Oxford University Press, 1984.
- ²⁷ J. Stöhr, *NEXAFS Spectroscopy*, Springer-Verlag 2003.

- ²⁸ W. Kossel, *Z. Phys.* 1 (1920) 119; *ibid.* 2 (1920) 470.
- ²⁹ R. de L. Kronig, *Z. Phys.* 70 (1931) 317; *ibid.* 75 (1932) 468.
- ³⁰ J. L. Dehmer, D. Dill, *Phys. Rev. Lett.* 35 (1975) 213; *J. Chem. Phys.* 65 (1976) 5327.
- ³¹ M.P. Seah, W.A. Dench, *Surf. Interface, Anal.* 1, 2-11, (1979).
- ³² The mean free paths were calculated by using the Tanuma, Powell and Penn formula in the program electron inelastic-mean-free-path v.1.1 provided by the National Institute of Standards and Technology, NIST.
- ³³ G. Binnig, H. Rohrer, Ch. Gerber, E. Weidel, *Phys. Rev. Lett.* 49, (1982) 57.
- ³⁴ G. Binnig, H. Rohrer, *Helv. Phys. Acta*, 55 (1982) 726.
- ³⁵ G. Binnig, H. Rohrer, Ch. Gerber, E. Weidel, *Phys. Rev. Lett.* 40 (1982) 178.
- ³⁶ R.M. Tromp, R.J. Hamers, J.E. Demuth, *Phys. Rev. B*, 34 (1986) 1388.
- ³⁷ H. C. O'Hanian, *Modern Physics, Second Edition*, Prentice Hall International Editions, 1987.
- ³⁸ R. Weisendanger, *Scanning Probe Microscopy and Spectroscopy, Methods and Applications*, Cambridge University Press, 1994.
- ³⁹ C. J. Chen, *Introduction to Scanning Tunnelling Microscopy*, Oxford University Press, 1993.
- ⁴⁰ E. Mc. Loughlin, *Structural Investigations of Metal and Semiconductor Interfaces*, Phd Thesis, 2000.
- ⁴¹ C. Barnes, G. Attard, *Surfaces*, New York: Oxford University Press (1998).

Chapter 3 Experimental Details

3.1 Photoelectron Emission Spectroscopy

3.1.1 Synchrotron Radiation¹

Synchrotron radiation is emitted when charged particles moving at relativistic speeds are forced to follow curved trajectories. The first visual observation of Synchrotron Radiation was in 1948 from the General Electric synchrotron in the USA during investigations into the design and construction of accelerators suitable for the production of very high-energy electrons. Over the next 50 years, an explosive growth in the building of accelerators optimised for synchrotron radiation production has turned this interesting radiative energy loss into a valuable research tool.

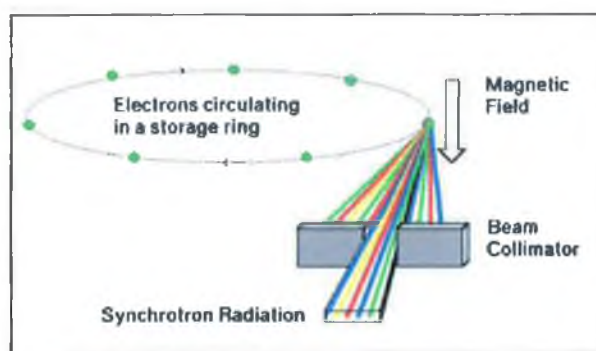


Figure 3.1 Diagram showing the extraction of synchrotron radiation from accelerated electrons.

The radiation emitted is extremely intense and extends over a broad wavelength range from the infrared through the visible and ultraviolet, and into the soft and hard x-ray regions of the electromagnetic spectrum. Synchrotron radiation sources produce x-ray radiation which is of the order of 10^6 times more intense than that from conventional sources and are in addition, continuously tuneable. A schematic diagram of the synchrotron radiation source used in these studies is shown in figure 3.2.

Although the storage ring itself is under high vacuum, electrons are removed by collisions with gas molecules, so the beam current decays with time. At Aarhus, a new beam is injected every 24 hours during normal operation. The radiation frequency required is selected using a monochromator. The broad range of frequencies available means that synchrotron radiation is suitable for a wide variety of experiments^{1,2}. Finally, synchrotron radiation has in addition to its high intensity and collimation two other desirable characteristics.

1. The radiation is almost linearly polarised in the plane of the storage ring in contrast to the unpolarised light from conventional ultraviolet and X-ray sources, allowing for orientational experiments such as NEXAFS.
2. Since the electrons in the ring are “bunched” the radiation will come as short (of the order 10^{-9} s) pulses, which is useful for timing experiments.

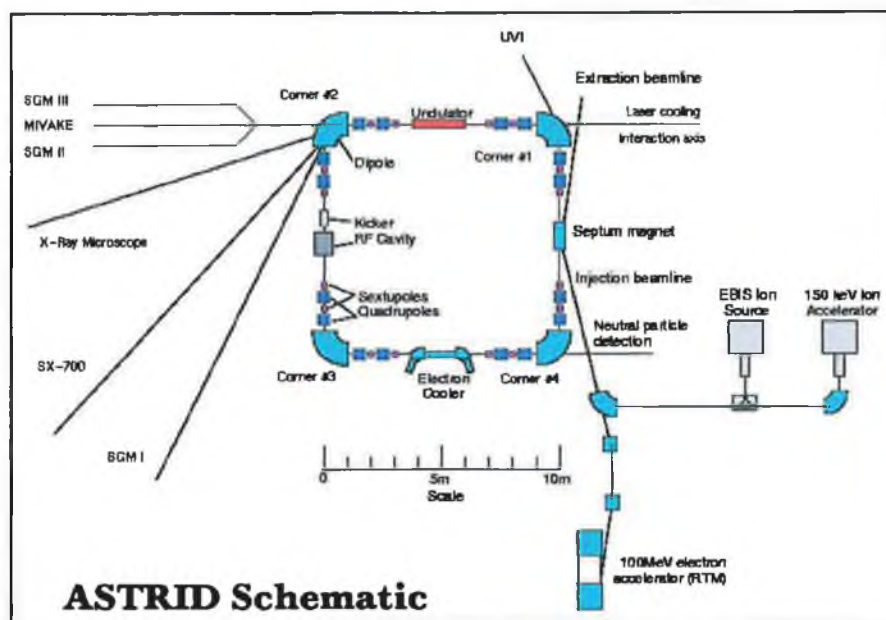


Figure 3.2 Schematic diagram of ASTRID Synchrotron¹.

3.1.2 Monochromator and Grating

One of the major benefits that synchrotron radiation has over conventional XPS, is that a continuous range of photon energies are available in the soft x-ray region of the spectrum. The radiation that comes from the synchrotron is essentially “white” in nature in that it contains a large range of photon energies. It is evident that prior to its use as an excitation source the “white” radiation from ASTRID must be monochromatised so ideally a very small spread in photon energy is obtained.

The SGM1 beamline combines a spherical grating monochromator containing three gratings. The SCIENTA electron energy analyser permits fast acquisition of spectra with high-energy resolution, typically 40 meV. This energy resolution is a significant improvement over that available with conventional laboratory based XPS sources.

The SGM monochromator used in the photoemission studies has a usable photon energy range from 30 eV to 400 eV. Typical flux values are $\geq 10^{10}$ photons/second at

130 eV with 50 μm slits and are $\geq 10^9$ photons/second at 350 eV with the 100 μm slits. The resolution of the three gratings operating with 50 μm slits is shown in figure 3.3¹.

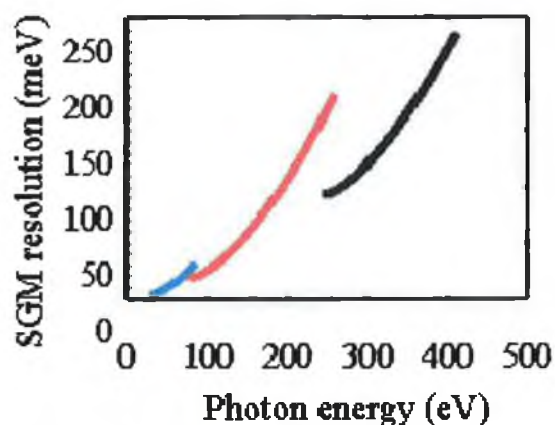


Figure 3.3 Resolution of the SGM1 monochromator with a typical working setting of slits at 50 μm ¹.

The main component of a monochromator is the diffraction grating, which is shown in the schematic drawing of the SGM1 in figure 3.4 to operate at grazing angles of incidence. A reflection diffraction grating consists of a reflecting surface with a periodic array of lines separated by a distance d . If polychromatic light is incident on the grating at an angle of incidence α , and the exit slit is located at an angle β to the grating, the grating equation

$$n\lambda = d(\cos \alpha - \cos \beta) \quad (3.12)$$

determines the wavelength passing through the slit. The first order light ($n=1$) is more intense than the higher order components and is therefore mostly used in experiments, although in the course of our work second order light features were observed in some cases.

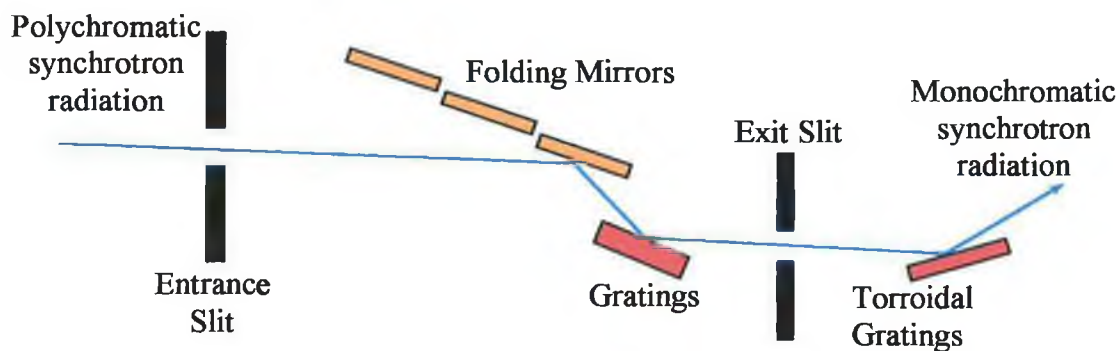


Figure 3.4 SGM1 monochromater.

3.1.3 Experimental Setup

The photoelectron spectroscopy experiments described in this thesis were carried out on the SGM1 beamline at Astrid in Aarhus, Denmark. The experimental station is used primarily for surface science experiments due to the 30-400eV energy range, which makes more bulk analysis prohibitive. The layout of the chamber is presented in figure 3.5.

The chamber consists of two mu-metal chambers mounted on top of each other. The upper chamber is separated from the lower chamber through the use of a gate valve and is used for sample preparation. The lower chamber is connected to the synchrotron via a gate valve and is used as the analysis chamber. A base pressure of 10^{-10} mbar is readily achieved in the analysis chamber after a 24-hour bake of the system.

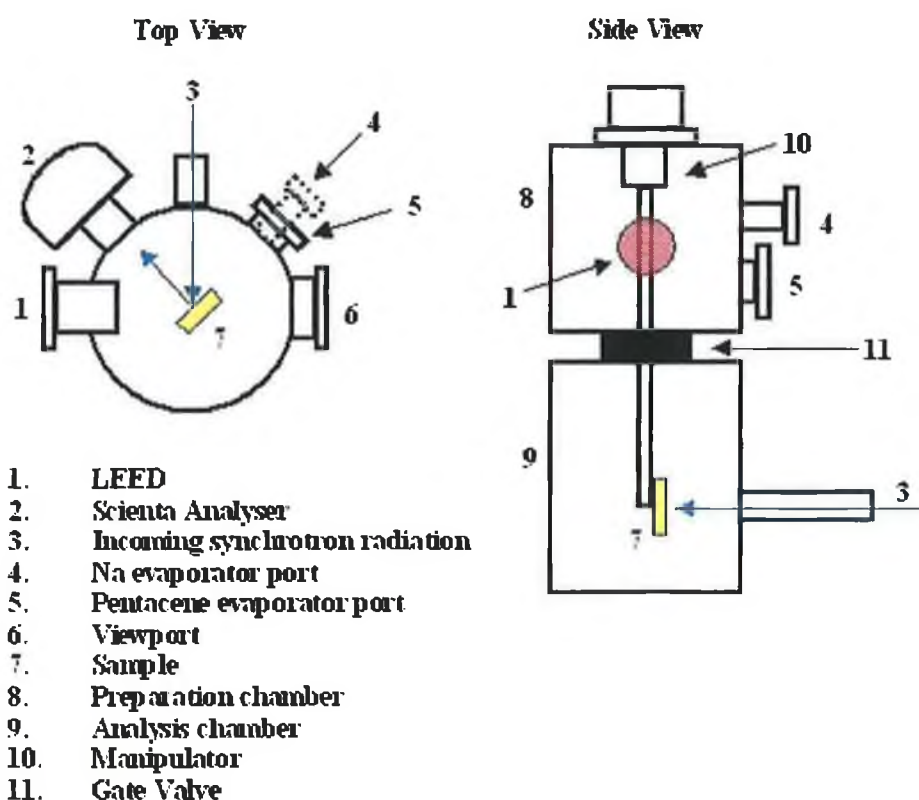


Figure 3.5 Chamber schematic for the SGM1 beamline at the Astrid synchrotron used for photoemission studies.

The preparation chamber is equipped with an Ar^+ gas sputter gun, LEED optics, a mass spectrometer, a quartz crystal monitor, and a gas inlet system. At present there are two sample holders, one with direct current heating (up to 20 A) for thin (~ 0.5 mm) wafers, and one with electron bombardment heating. Both can be cooled via a LN_2 flow cryostat. The sample manipulator has x, y, z movement as well as polar and azimuthal

rotations. A Knudsen cell operating at 150°C was mounted on the chamber for pentacene evaporation in addition to the SAES Na evaporator for alkali metal doping experiments.

The two sample positions that were used in the course of the valence band PES investigations of the pentacene/Cu(110) and pentacene/Au(100) systems are shown in figure 3.6 and are denoted as (a) normal emission (NE) and (b) s-polarised sample positions. In the normal emission sample position the surface normal pointed in the direction of the analyser and the incident synchrotron radiation made an angle of 35° with the surface normal. In the s-polarised sample position the incident synchrotron radiation was along the surface normal and the observed electrons were emitted at an angle of 35° to the analyser.

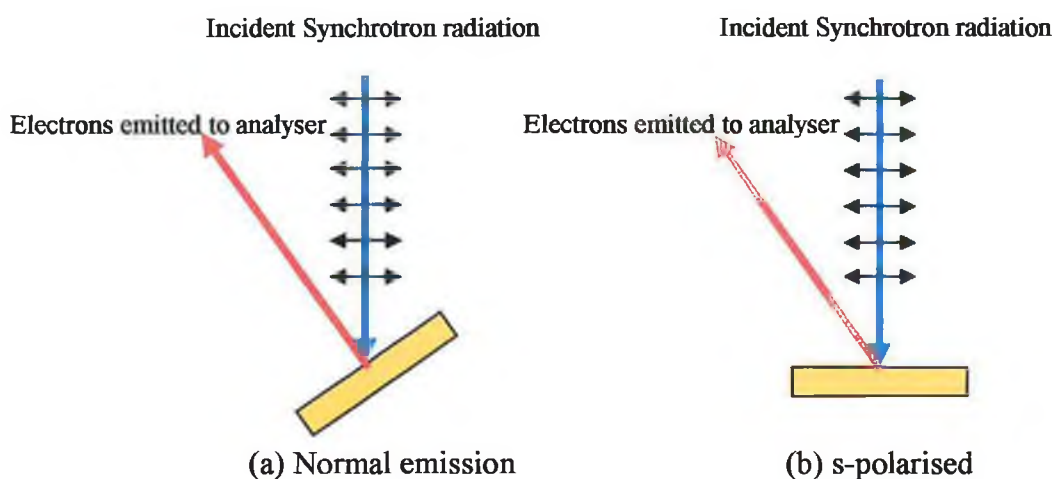


Figure 3.6 Sample positions for valence band photoemission studies.

3.1.4 The Electron Energy Analyser

The vacuum system is equipped with a 200 mm mean radius spherical electron analyser (SCIENTA) with a video based multichannel detector system, shown in figure 3.6. A resolution of 5meV has been demonstrated, whereas a typical working resolution is about 40 meV.

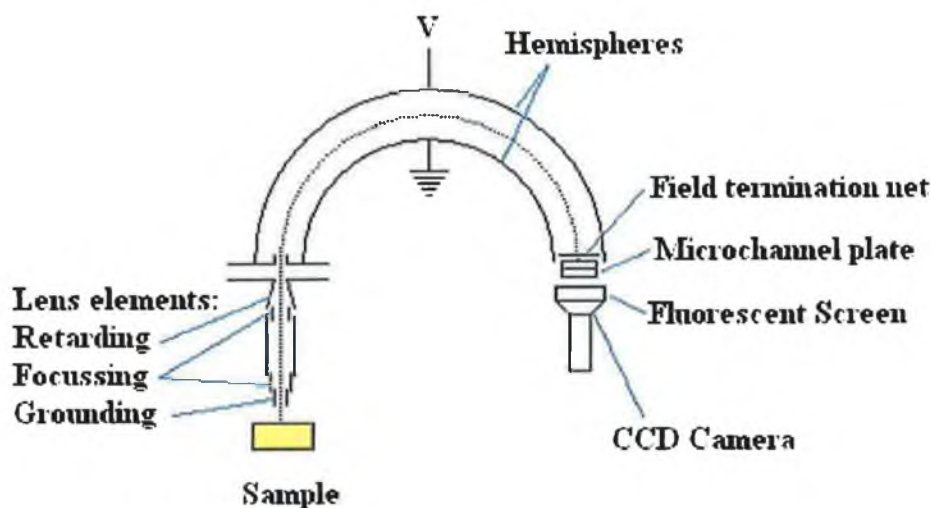


Figure 3.7 Diagram of SCIENTA electron analyser.

3.2 Near Edge X-ray Absorption Fine Structure

3.2.1 Modes of Detection

So far discussion of the NEXAFS technique has centred on the formulation of a model for predicting the transition probability for the excitation of a core level to an unoccupied orbital, which can be represented by a vector, as a function of the incident E-field. No discussion has been carried out on the investigative methods used to measure this transition. A simple diagram of the two-step process by which an absorption event occurs is presented in figure 2.3. The first step involves a core level electron absorbing the energy of the incident photon and being excited into an unoccupied state above the Fermi level. However, because the unoccupied energy levels are below the vacuum level, they constitute bound states and so cannot be measured directly by photoemission. The secondary processes must therefore be examined as a method of indirectly measuring the frequency of primary transition.

The second step of the process involves core hole annihilation, whereby a valence electron falls to fill the core hole created in the initial step, with the resultant surplus energy causing the emission of either a fluorescent photon or an Auger electron. Fluorescent photon emission is known as a radiative event and Auger photon emission is known as a nonradiative event. The fractions of the radiative and nonradiative decay rates as a function of the total decay rate are given by the formula:

$$\omega_a + \omega_f = 1 \quad (3.24)$$

where ω_a is the Auger yield and ω_f is the fluorescent yield. For the K-shell excitation of low-Z atoms, the Auger event occurs over a shorter timescale and so is found to dominate³.

NEXAFS experimental studies using the Auger emission are more common in literature and so this analysis method will be discussed in greater detail. Figure 3.8 shows an energy level diagram and photoemission spectra at three different photon energies for a sample containing atoms with core levels A and B and a valence band VB. In this case atom A is the adsorbate and atom B is the substrate.

In figure 3.8 (a) the incident photon energy $h\nu_1$ is not sufficient to excite the core level electron of atom A above the Fermi level, and therefore the photoemission spectrum is comprised solely of emission from the core level of atom B and the valence bands of both atoms.

In figure 3.8 (b) the incident photon energy has been increased to $h\nu_2$, which is sufficient to excite the core level electron of atom A above the Fermi level and into an unoccupied molecular orbital. Because this state is below the vacuum level it is essentially a bound state and so no corresponding peak will be observed in the photoemission spectrum. However, as described in section 2.3.1, this photon absorption event results in core hole annihilation and the emission of either an Auger electron or a fluorescent photon. The emission of an Auger electron is accompanied by the emergence of the corresponding peak in the photoemission spectrum in addition to the increase in the lower kinetic energy background due to scattered Auger electrons. The shaded region in the photoemission spectrum is used to denote the elastically and inelastically scattered Auger electrons.

In figure 3.8 (c), the photon energy is increased beyond the photoemission threshold energy for atom A and a photoemission peak due to emission from the core level is observed in the photoemission spectrum in addition to the Auger emission corresponding to the core hole annihilation. As with figure 3.8 (b) the shaded region in the photoemission spectrum is used to denote the elastically and inelastically scattered Auger electrons. The yield window setting for the three types of data acquisition are shown on the bottom of figure 3.8 (c).

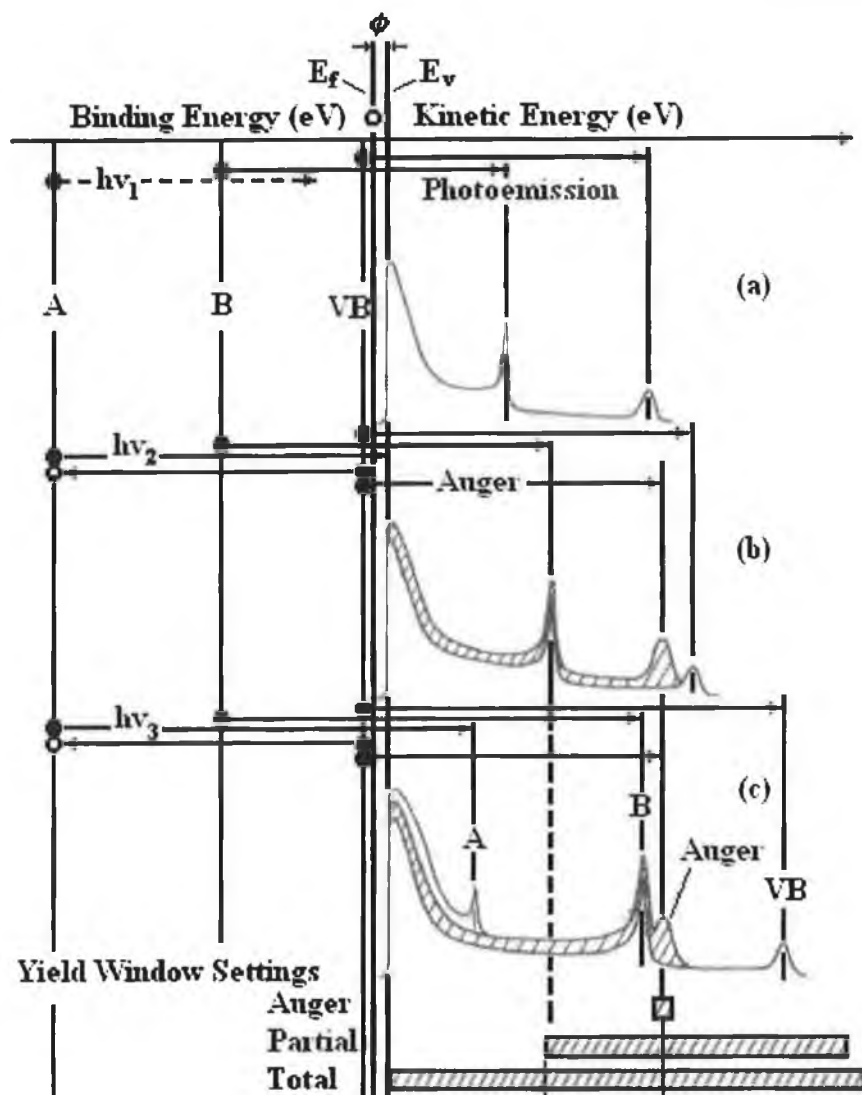


Figure 3.8 Energy level diagram and schematic photoemission spectra at different photon energies for a sample containing atoms with two core levels A and B and a valence band VB⁴.

(a) *Auger Yield Method*

In the Auger yield method the detector is set to measure electrons that have a kinetic energy corresponding to the energy of the Auger peak. Since the energy of the Auger emission is independent of the incident photon energy the position of the peak does not change with increasing photon energy. It is therefore possible to step through the incident photon energies so that the core level electron can be used to probe the states above the Fermi level. The Auger peak intensity will change depending on the absorption probability, which itself is dependent on the orientation of the molecular orbital with respect to the E-field of the incident radiation. By plotting the Auger counts against the incident $h\nu$ photon energy a NEXAFS spectrum can be generated and the orientation of the molecular orbitals can be probed.

(b) Partial Yield Method

The basis of the partial yield method is the use of a retarding voltage to accept electrons that have a kinetic energy exceeding a certain value as shown in figure 3.8 (c). The signal that is then collected by the detector consists of a photoemission signal due to photoemission peaks and inelastically scattered electrons, and an Auger signal due to the Auger peak and inelastically scattered Auger electrons above the threshold kinetic energy. Despite the large photoemission derived background observed in this method, the Auger signal will vary with the absorption probability and so summation of the signal at each incident photon energy will allow for the formation of a NEXAFS spectrum.

(c) Total Yield Method

This method utilises the drain current from the sample as a method of obtaining a NEXAFS spectrum. As shown in figure 3.8 (c), the total yield method essentially sums the total emission from the photoemission spectrum, which will contain a photoemission-derived signal and an Auger derived signal at each incident photon energy. By stepping the incident photon energy through the absorption edge a NEXAFS spectrum can be generated.

3.2.2 Experimental Setup

The NEXAFS experiments described in this thesis were carried out on the SX700 beamline at Astrid in Aarhus, Denmark. The experimental station is used primarily for surface science experiments due to the 20-700eV energy range, although this energy range is more useful for bulk analysis than that of the SGM1 beamline. The layout of the chamber is presented in figure 3.9.

The endstation consists of a single mu-metal chamber. A base pressure of 10^{-10} mbar is readily achieved in the analysis chamber after a 24-hour bake of the system. The system is equipped with an Ar^+ gas sputter gun, LEED optics, a mass spectrometer, a gas inlet system and facilities for alkali metal and Barium evaporation. An X-ray tube is used to supplement the synchrotron radiation from ASTRID. The standard sample holder has e-bombardment heating, and can be cooled via a LN_2 flow cryostat. The sample manipulator has x, y, z movements as well as polar and azimuthal rotations.

The system is equipped with two hemi-spherical electron analysers. An angle resolved 50mm mean radius analyser (VG-BLADES), and a fixed 100mm mean radius analyser (VG-CLAM2).

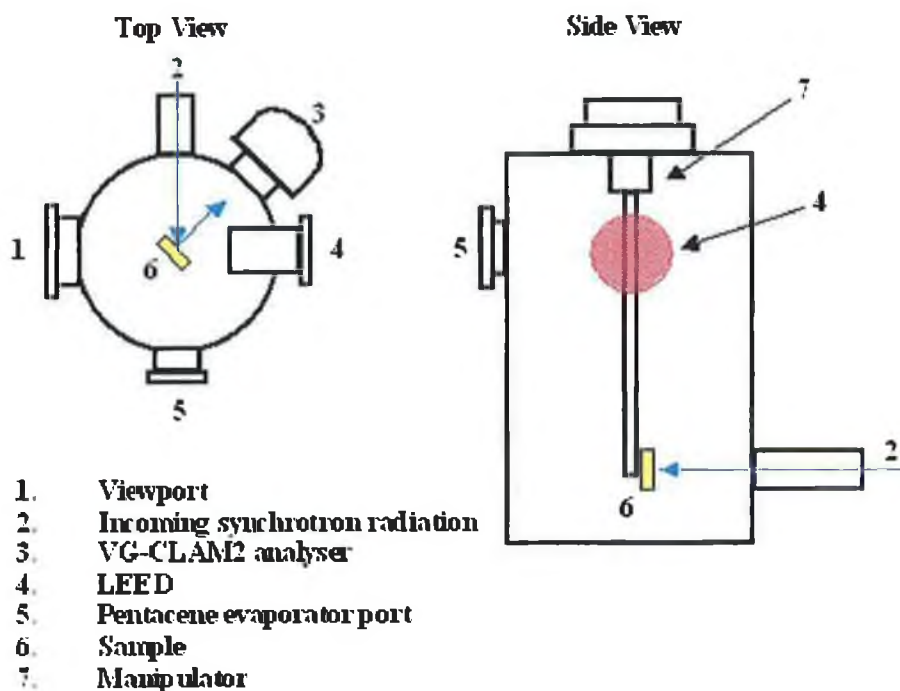


Figure 3.9 Chamber schematic for the SX700 beamline at the Astrid synchrotron used for NEXAFS studies.

3.3 Scanning Tunnelling Microscopy

3.3.1 Experimental Setup

In practice an STM operates by measuring a small tunnel current (~ 0.1 - 10 nA) between two electrodes spaced a few Angstroms apart, with a potential difference (1 mV to ~ 5 V) applied between them. One of the electrodes is the sample under investigation; the other is an atomically sharp tip (usually made of tungsten or a platinum iridium alloy). As discussed in section 2.5.1, the current decays exponentially with an increase in the distance between the two electrodes. At a specific electrode separation within a given distance, it is possible to measure a tunneling current. A topographic image of the sample surface can therefore be obtained by measuring the tunneling current, as the tip is raster scanned across the surface. In the course of the experiments presented here, tungsten and Pt/Ir tips purchased from Omicron were used to acquire atomic scale images of the surfaces under investigation.

3.3.2 Piezo Scanner

Scanning is achieved by using a piezoelectric transducer, which controls the small vertical (z) and lateral (x, y) displacements of the tip. The tip is situated at the top of the piezo tube as shown in figure 3.10. By convention the z -axis is taken as normal to the sample surface and therefore the surface itself is in the xy plane.

The ceramic scanner is manufactured from lead zirconate titanite (PZT), metallized on the outer and inner surfaces and poled in the radial direction⁵. The outside metal coating is sectioned into four quadrants. The extension of a block of piezoelectric material of length L and thickness h if a voltage V is applied across h is given by:

$$\Delta L = \frac{d_{31}VL}{h} \quad (3.34)$$

For commercial piezo-ceramics the d_{31} coefficients lie in the range 1-3 Å/V. Vertical (z) motion can be achieved by applying the same voltage to all four outer electrodes and grounding the inner electrode. Lateral (x or y) motion can be achieved by applying equal and opposite voltages to the two opposite vertical outer electrodes while keeping the other two horizontal electrodes grounded or at constant voltage. In practice, the STM control unit produces four high voltage outputs: $Z-X$, $Z+X$, $Z-Y$ and $Z+Y$. The Z voltage typically ranges from -130 V to $+130$ V and the X and Y voltages range from -135 V to $+135$ V on the Omicron Scala system.

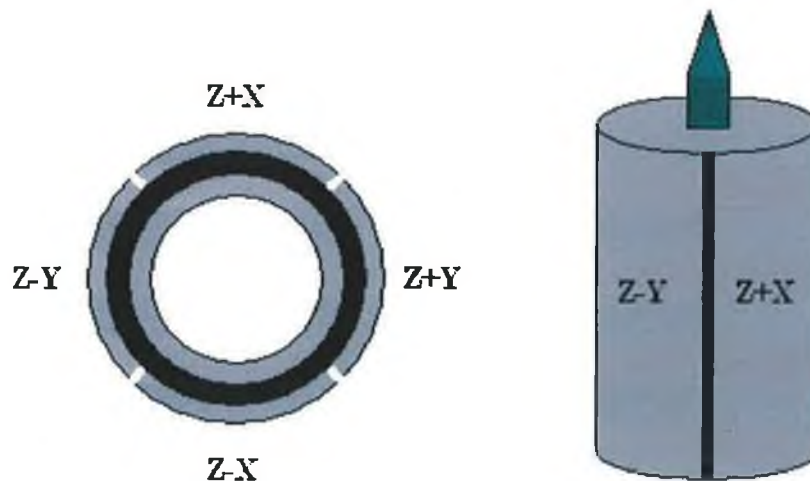


Figure 3.10 Piezo tube scanner, (a) Top View, (b) side view.

3.3.3 Vibrational Isolation System

As mentioned in section 2.5.1 the tunneling current decreases by a factor of 7.75 with a 1Å increase in the tip-sample distance. It is therefore evident that an effective vibration isolation system is one of the most critical elements needed in STM data

acquisition⁶. The typical corrugation amplitude on a metal surface is approximately 0.1-0.5 Å and so disturbances from external vibrations must be kept below 0.01 Å⁷. Two conditions must be fulfilled to achieve low external vibration.

- The STM head should have a high resonance frequency (>1 KHz) i.e. it should be small, light and rigid as possible.
- The STM should be mounted on a vibration isolation system, which has a low resonance frequency (~1 Hz), which effectively damps out vibrations.

Most modern STMs use coiled spring systems⁶ with eddy-current damping⁸, or else viton-metal stack isolators. Spring systems can be designed with resonance frequencies of 1Hz or lower but do not provide much damping. For this reason, eddy-current damping is usually used in conjunction with these systems. The spring system and the eddy current damping system on the Omicron VT-STM is shown in figure 3.11⁹.

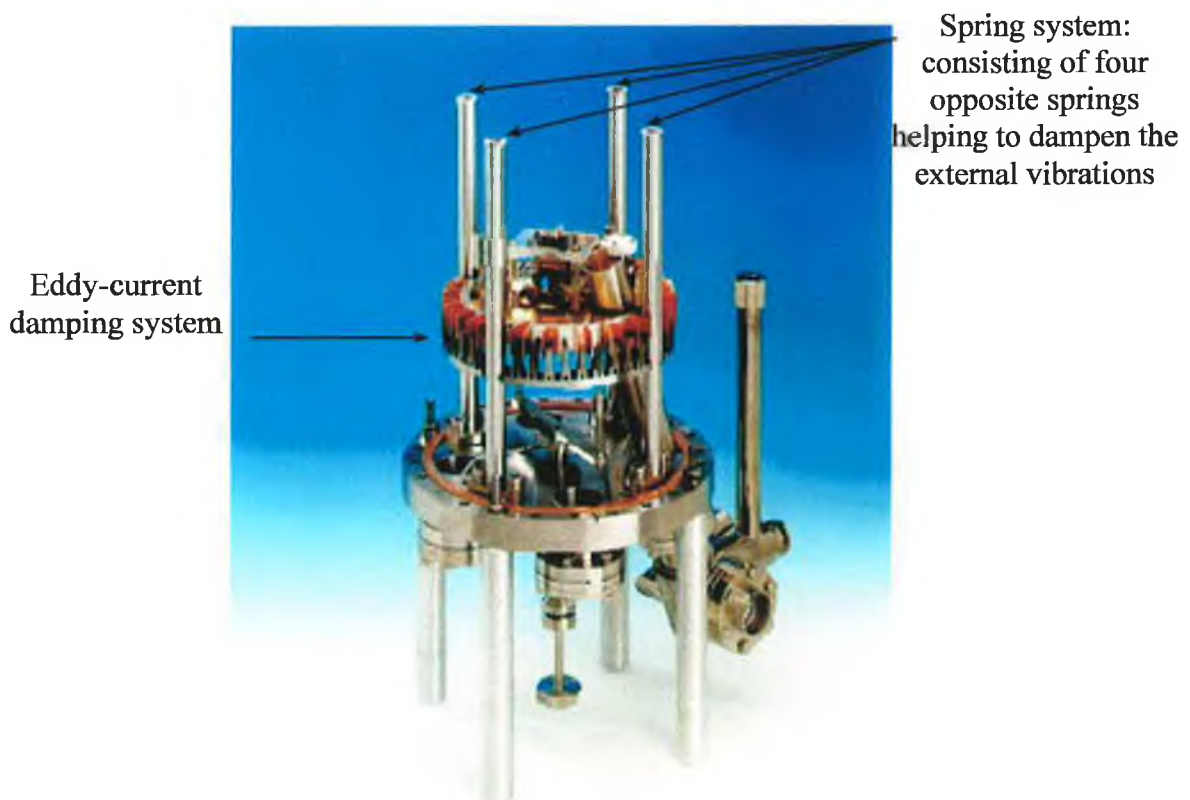


Figure 3.11 Picture of STM showing spring damping system and eddy current damping system⁹.

3.3.4 Scanning Modes

The two modes of operation of the STM are the constant height and constant current modes as shown in figure 3.12. In constant height mode as shown in figure 3.12 (a), the tip traces across the surface with a constant voltage is applied to the z-piezo. The image of the surface is then formed by the variation in the tunnelling current observed with a varying tip-sample distance as discussed in section 3.4.3. This mode of scanning is found to allow for fast data acquisition. However, this scanning mode requires an atomically flat surface to scan, as the absence of a feedback mechanism can cause the tip to crash into the surface if the sample has large variations in height. Since the current drops by a factor of 7.75 with an increase in the tip-surface distance of 1\AA , the tunnelling current amplifier used in this method must have a dynamic input range.

Figure 3.12 (b) shows the experimental setup used for the constant current mode. In this mode the tunnelling current is kept constant by maintaining a constant tip-sample distance by means of a feedback mechanism. By measuring the z-piezo voltage required to maintain a constant tip-sample distance, an image of the surface is formed.

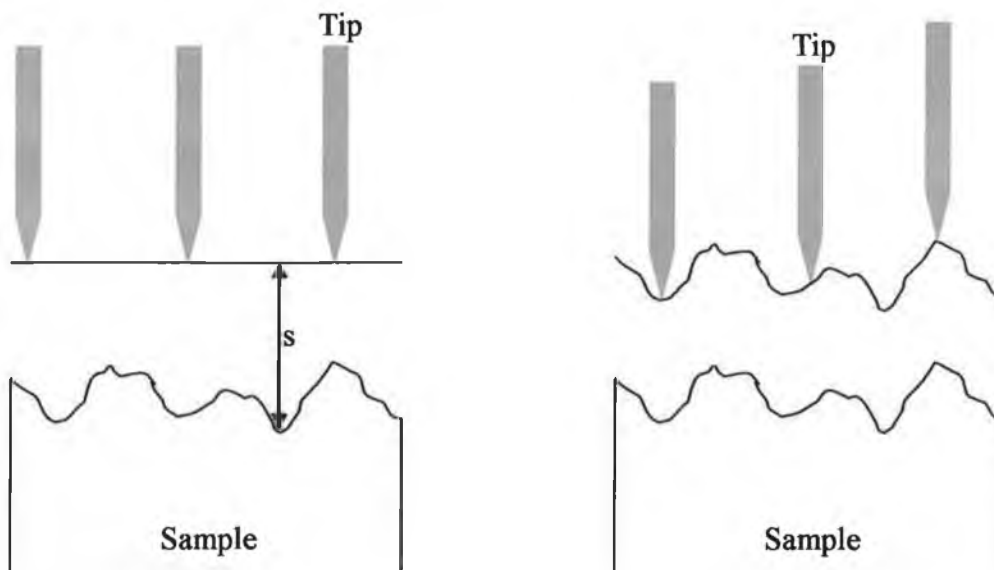


Figure 3.12 Two commonly used modes of STM operation (a) constant height mode, (b) constant current mode.

3.3.5 Feedback Mechanism¹⁰

The tunnel current is first amplified and then converted into a voltage. The distance dependence is then extracted by passing the signal through a logarithmic amplifier and the output signal is compared to a preset value, which corresponds to a desired gap width, s . The difference signal is fed into the z-piezo high voltage amplifier

and the tip is moved towards or away from the surface to bring the gap width (and hence the tunnel current) back to the desired value, i.e. the system operates in negative feedback mode. A topographic image can be attained from the changes in the z-piezo displacement during the scan assuming the barrier height remained constant over the scan area. In the Omicron system, the logarithmic amplifier, the comparator and the high voltage amplifiers shown in figure 3.13 are contained in the STM Scala control unit, which also handles data acquisition and image display.

The main limitation of the constant current mode is the stability of the feedback loop. If the total phase shift of the system exceeds 180° , the feedback becomes positive and the tip begins to oscillate. In practice, the cut off frequency of the feedback loop i.e. the maximum frequency at which it can operate in negative feedback is in the kHz range. Therefore the output of the I-V converter is fed into a low pass filter to suppress the high frequency signals. The scan speed is limited by time delays within the circuit, for example the finite time delays of the piezos, which could cause oscillations. Ideally, the overall gain of the feedback loop should be as large as possible so that the tip accurately follows the contours of the sample surface. However, a compromise value is often chosen to ensure that the gain is less than unity, above the cut off frequency. The cut off frequency must be below the mechanical resonance frequencies of the STM head to prevent feedback instability due to transmitted vibrations.

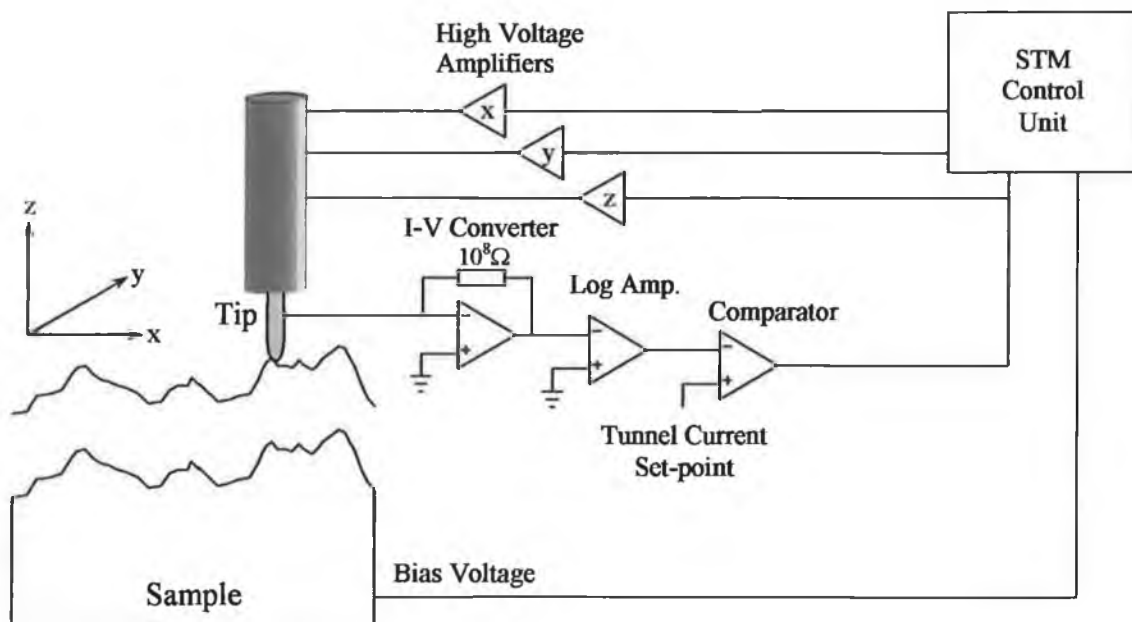


Figure 3.13 Feedback mechanism for constant current mode STM¹⁰.

3.3.6 UHV system

The UHV system consists of two main chambers: the preparation chamber and the analysis chamber with a room temperature STM section. Samples and tips can be loaded through a fast-entry lock attached to the preparation chamber. The layout of the system is shown in figure 3.14(a), (b) and (c)⁹.

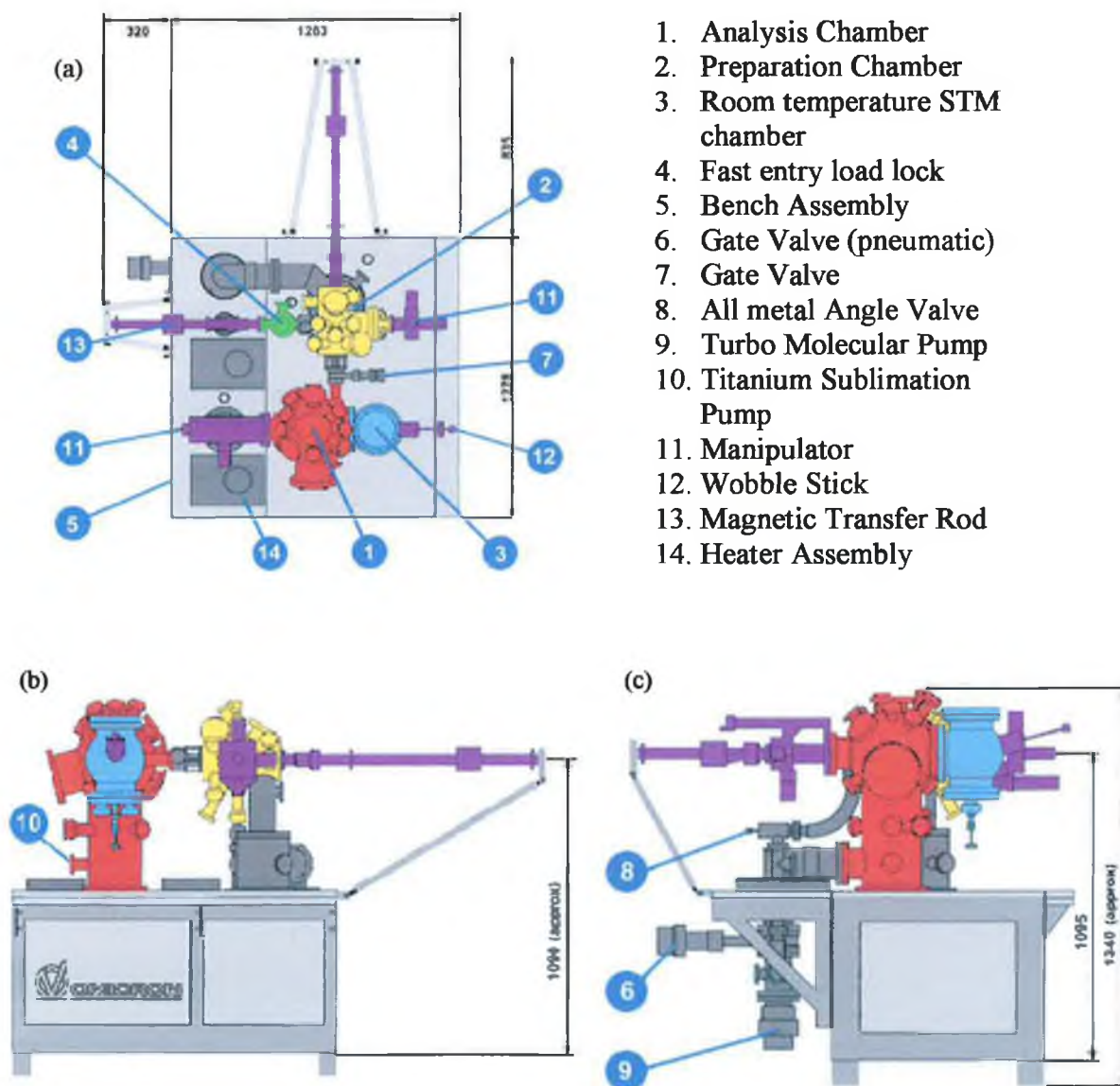


Figure 3.14 Diagram of UHV system showing (a) top, (b) side and (c) end views⁹.

3.4 Low Energy Electron Diffraction

3.4.1 LEED Experimental Setup

LEED experiments in the STM chamber were performed in an ultra high vacuum chamber shown in figure 3.14 equipped with a rear view Omicron Spectaleed system, with an operating base pressure of 1×10^{-10} mbar. The LEED apparatus is shown in figure 3.15 together with a schematic diagram.

The LEED has been fitted with a lanthanum hexaboride filament (LB_6). This filament has good emission characteristics at low power inputs. It yields a higher emission current and lower energy spread than a thoriated tungsten filament. LEED experiments performed in conjunction with NEXAFS experiments on the SX700 beamline at the Astrid synchrotron were carried out using an identical LEED system to that described here. LEED measurements carried out in the course of the photoemission studies in the SGM1 chamber at the Astrid synchrotron were carried out using a tungsten filament in conjunction with the same basic LEED system.

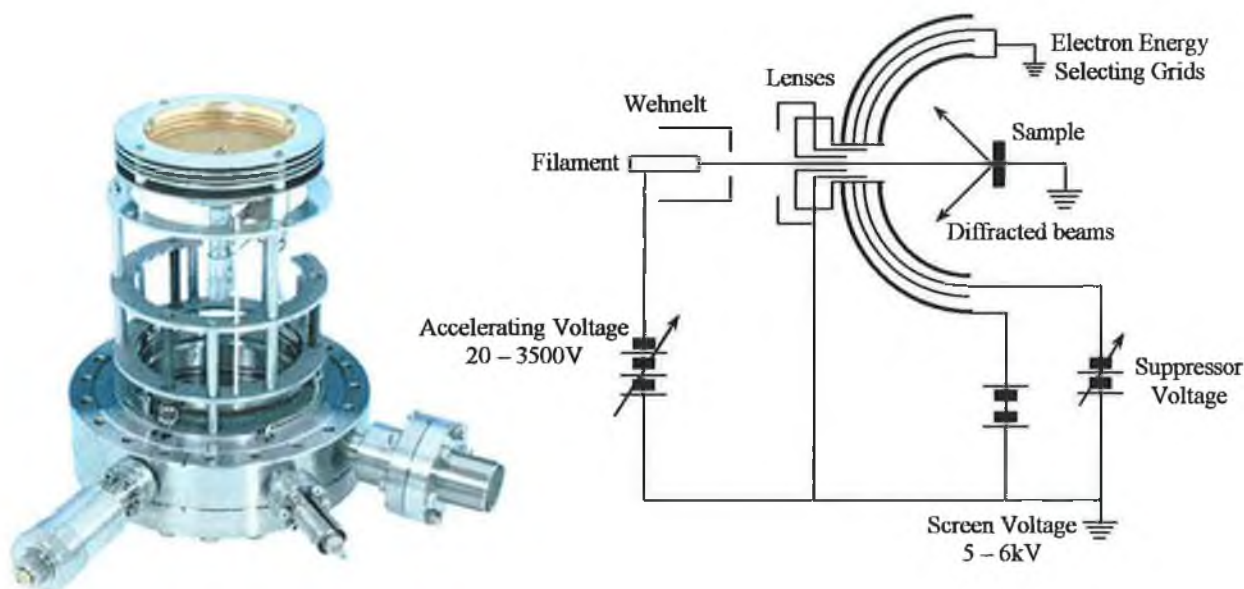


Figure 3.15 Picture⁹ and schematic diagram¹⁰ of LEED system.

The electrons are thermionically emitted by the heated LB_6 filament and collimated by the Wehnelt, which is biased slightly negative with respect to the filament. The lenses are used to focus the electron beam. This beam backscatters from the sample surface, passes through a set of grids, which select only the electrons which are elastically scattered from the surface and are then accelerated to a fluorescent screen. When they strike the screen, they cause the phosphor to glow, revealing the

diffraction pattern. These images are stored at different electron energies with the help of a CCD camera.

3.5 Evaporators

3.5.1 Pentacene Evaporator

The layout of the pentacene evaporator is presented in figure 3.16. The apparatus, purchased from Kurt J. Lesker, is a standard low temperature molecular evaporator consisting of a boron nitride liner resistively heated by tungsten wires. A thermocouple in contact with the base of the liner allows for an accurate measure of the temperature and functions as a feedback mechanism for the evaporator controller, allowing for the accurate setting and maintaining of the temperature to an accuracy of $\pm 0.2\text{K}$, in addition to a controllable temperature ramp rate. The tungsten heating coils are wrapped around the ceramic liner with the inter-coil distance reducing closer to the top of the ceramic. This results in an increased temperature at the top of the ceramic ensuring evaporated pentacene doesn't redeposit to the ceramic once evaporated from the base of the ceramic. A shutter, placed in front of the mouth of the ceramic, is used for more accurate controlling of the deposition rate of the pentacene.

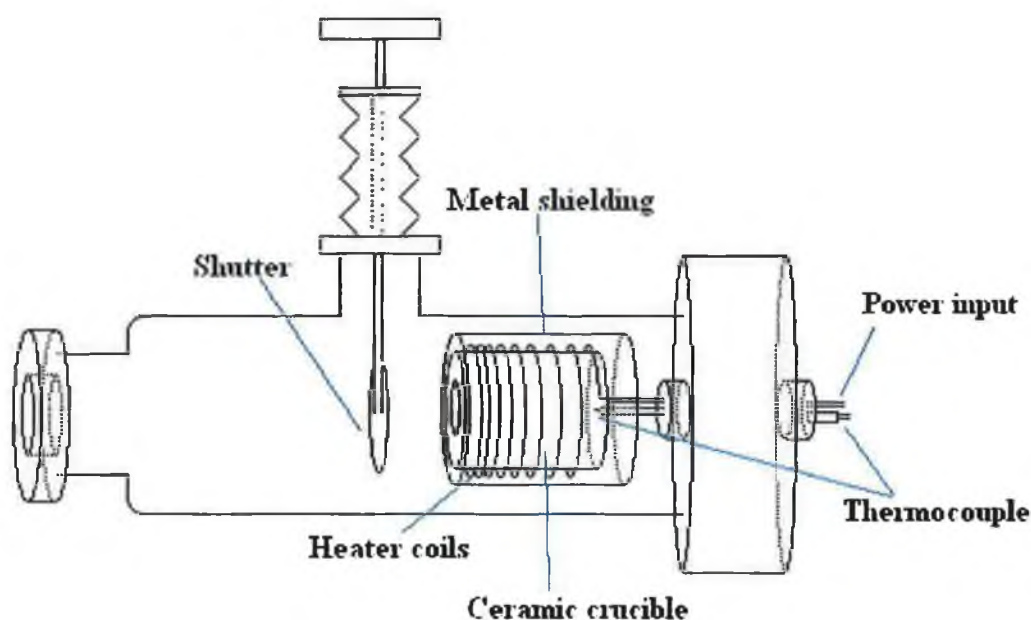


Figure 3.16 Schematic of the pentacene evaporator used for thin molecular film deposition.

Prior to evaporation, the pentacene was degassed using a program that stepped the temperature up from 373K to 418K over a 24-hour period to remove water vapour before use. The pentacene was evaporated at a temperature of 432K, which yielded an approximate deposition rate of 0.15-0.25ML/min, depending on the sticking coefficient of the different substrates.

3.5.2 Sodium Evaporator

The alkali metal evaporator is shown in figure 3.17, and is a simple device consisting of two SAES Na pouches and a UHV titanium sublimation pump feedthrough. The feedthrough was mounted onto a movable bellows so that the sample to evaporator distance could be changed. The two SAES pouches were mounted such that current could be passed through either pouch individually or through both of the pouches for degassing purposes.

The SAES pouches operate by passing a current of 5.5A through them from a constant current source. Just prior to evaporation, a current of 6.0A was briefly passed through the pouches, for the joint purpose of degassing and activating the pouch. Prior to use, the pouches were degassed over a 24-hour period using incremental steps in the current while maintaining UHV conditions in the chamber.

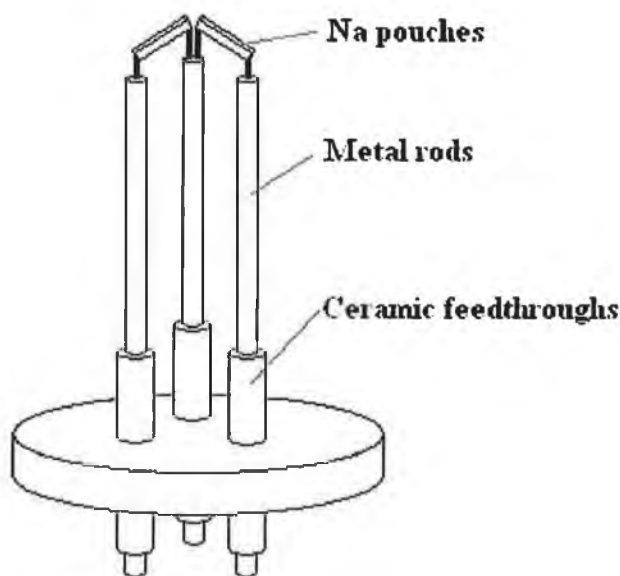


Figure 3.17 Schematic diagram of Na evaporator used in alkali metal doping of molecular films.

3.5.3 Sulphur Evaporator

Figure 3.18 shows a diagram of the sulphur cell used mounted on a knife-edge flange with electric feedthroughs. The sulphur cell consists of a compressed pellet formed by pressing powders of silver (Ag), silver iodide (AgI) and silver sulphide (Ag_2S) together. The pellet is then placed in the glass chimney housing with electrical contact made at both ends of the pellet, through a platinum mesh as the front end, and through the silver powder at the back end. The pellet is heated by passing a current through a tungsten coil wrapped around the glass housing. When the pellet reaches a temperature of approximately 473K, an electrical potential of 200meV exists across the cell. By applying a suitable bias to the cell a constant current ($20\mu\text{A}$) is established by a constant current source. This current is facilitated by the silver iodide acting as an ionic conductor, with Ag^+ ions being transported from the silver sulphide pellet to the back silver electrode resulting in the freeing of sulphur from the silver sulphide. Molecular sulphur is found to effuse from the throat of the chimney due to the local concentration of sulphur at the top of the pellet.

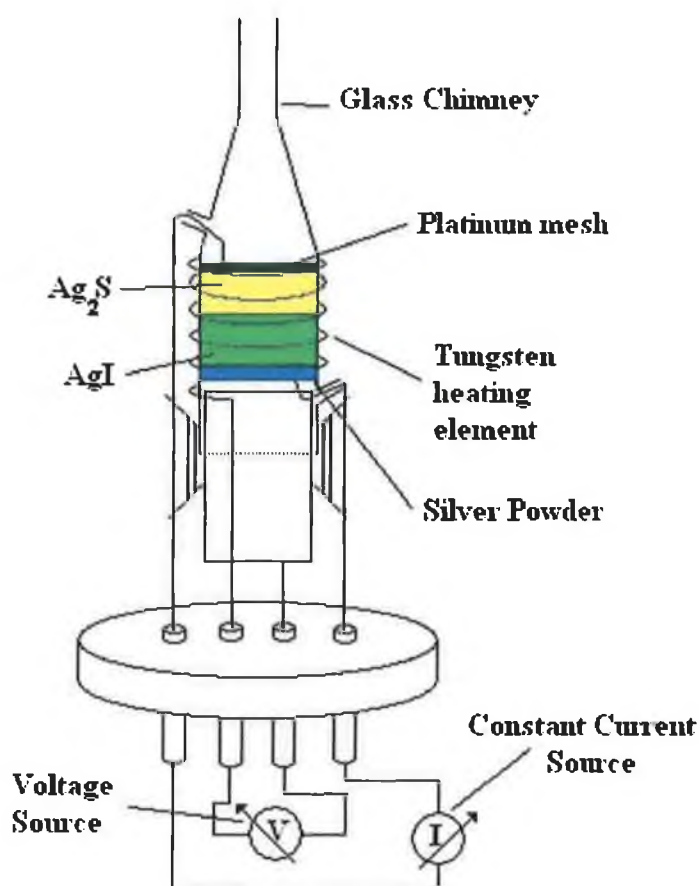


Figure 3.18 Schematic of UHV sulphur evaporator used for the deposition of sulphur interlayers.

3.6 Summary

Section 3.1 introduces the experimental equipment associated with the photoelectron emission studies undertaken in the course of this work. The section begins with a brief history of the emergence of synchrotron radiation sources, and discusses how the radiation is extracted from the accelerated electrons. The section continues by introducing the equipment used to extract useful radiation from the essentially white radiation emitted from the synchrotron source. Additional information is given on the UHV chamber and electron analyser used in the course of this work.

Section 3.2 discusses the modes of detection used in the NEXAFS technique in addition to introducing the UHV chamber used in the course of the NEXAFS experiments. Section 3.3 discusses the different equipment associated with the STM technique, which includes the piezo scanner, vibrational isolation system, the feedback mechanism and the UHV system used in the course of the STM experiments. Additional discussion on the different scanning modes possible in STM is also presented. Section 3.4 details the equipment associated with the LEED technique and section 3.5 describes the operation of the pentacene, Na and S evaporators used in the course of the work presented in chapters 4, 5 and 6.

Chapter 3 References

¹ <http://www.isa.au.dk/astrid/astrid.html>

² J. C. Vickerman, *Surface Analysis – The Principal Techniques*, J. Wiley and Sons, 2002.

³ M. O. Krause, *J. Phys. Chem. Ref. Data*, 8 (1979) 307.

⁴ J. Stöhr, *NEXAFS Spectroscopy*, Springer-Verlag 2003.

⁵ C. J. Chen, *Introduction to Scanning Tunnelling Microscopy*, Oxford University Press, 1993

⁶ G. Binnig, H. Rohrer, *Surf. Sci.* 126 (1983) 236.

⁷ D.W. Pohl, *IBM Journal of Res. Develop.* 30 (1986) 417 – 427.

⁸ K. Nagaya, H. Kojima, *J. Dynam. Syst. Meas. Control*, 106 (1984) 46 – 51.

⁹ www.omicron.de

¹⁰ D. Carty, *RAS and STM Investigations of Pentacene Molecules on Metal and Semiconductor Surfaces*, PhD Thesis, 2004.

Chapter 4 Pentacene on Cu(110)

4.1 Introduction

The study of the bonding interaction between organic molecules and metal surfaces is a subject that has attracted great interest in recent years due to the promising potential that these layers have in the fabrication of various electronic devices, such as organic field effect transistors (OFETs)¹ and optoelectronic devices. Initial studies focussed primarily on the electronic properties of these films², but more recently studies have begun focussing on the quality of these films along with the orientation of the molecules within the films, as these factors have proven to have a large effect on the electronic properties of the films. Studies have concluded that impurities and defects can play a major role in determining the electronic properties of molecular thin films^{3, 4}.

The growth and orientation of molecular thin films depends primarily on the subtle competition between the intermolecular and molecular-substrate interactions, primarily those occurring in the first few monolayers (MLs). It has been shown that in many cases the intermolecular forces, which determine the relative orientation of the molecules in the bulk, are very different to those experienced by molecules bonded to metal surfaces. The interaction between planar molecules and metal surfaces often leads to a planar bonding geometry^{5, 6, 7, 8, 9, 10, 11, 12} in cases where the molecular bonding geometry in the bulk crystal is non-planar^{13, 14, 15}.

In this chapter the growth of pentacene thin films on the Cu(110) metal surface using two different methods of film growth has been investigated using synchrotron photoelectron spectroscopy (PES). An in-depth comparison of the films grown with and without the aid of the annealed monolayer to template the subsequent film growth has been carried out to investigate the differences in the film growth. The application of group theory, introduced in section 2.2, is used in this comparative study to investigate the molecular orientation of the pentacene in the thin films.

4.1.1 Previous studies of the pentacene/Cu(110) interface

Highly ordered pentacene films on Cu(110) have previously been studied using STM^{6, 9}, LEED^{6, 9}, NEXAFS^{5, 7}, x-ray photoelectron spectroscopy (XPS)⁵, He-atom scattering (HAS)⁵, and thermal desorption spectroscopy (TDS)⁵. STM studies indicate that the initial monolayer of pentacene bonds predominantly through its π bonds to the Cu(110) surface, adopting a planar bonding geometry. However, if deposited on a room temperature Cu(110) substrate, the initial monolayer exhibits only short range order

between the molecules, with the long axis of the molecule aligning itself along the $[1\bar{1}0]$ direction of the crystal. Annealing of the monolayer to a temperature of 430K results in the formation of stripes of pentacene along the $[001]$ direction, retaining the same orientation of the molecule with respect to the $[1\bar{1}0]$ direction of the crystal. Figure 4.1 shows the model proposed by Söhnchen et al⁵ for the orientation of the pentacene molecule in the film at different film thicknesses, with three different molecular orientations in evidence at different film thicknesses.

They reported that upon pentacene deposition onto the initial annealed monolayer, the orientation of the molecules in the second layer is found to change, with a tilting of 28° along the short molecular axis being introduced in addition to a 21° rotation of the long molecular axis off the $[1\bar{1}0]$ crystal direction. At higher coverages, a further molecular orientation was discovered similar to the herringbone orientation adopted by the bulk pentacene crystal^{13, 14, 15} with the long molecular axis at 73° to the plane of the surface.

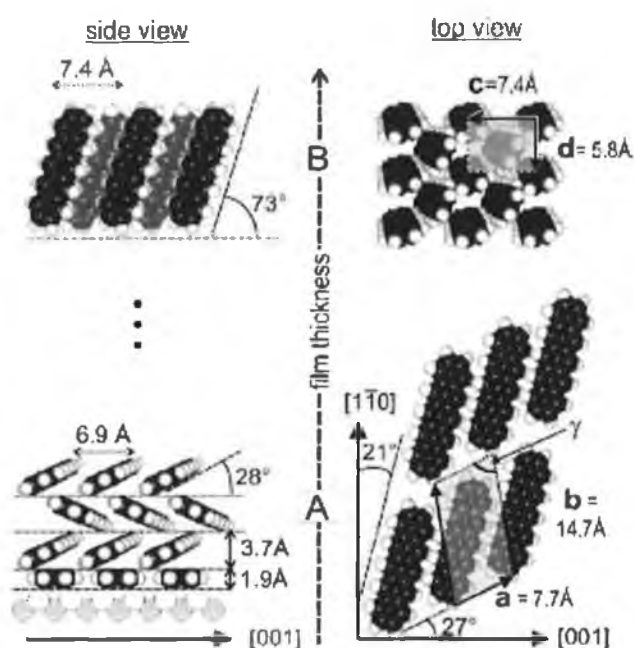


Figure 4.1 Model for pentacene thin films grown on Cu(110) proposed by Söhnchen et al⁵.

4.2 Experimental details

The photoemission experiments were carried out on the SGM1 beamline in ASTRID described in section 2.1.12. The sample was cleaned using repeated cycles of Ar bombardment and sample annealing to 673K by resistive heating of the crystal until

the expected sharp 1×1 LEED pattern for Cu(110) was observed, and no carbon was visible in the photoemission scans. The sample temperature was measured by a thermocouple in contact with the crystal. Due to an offcut in the crystal, the [001] crystal direction was oriented at approximately 30° from the horizontal. The evaporation of pentacene was carried out *in situ*, at pressures of 3×10^{-9} mbar. Pentacene (purchased from Aldrich Chem. Co.) was deposited at 423K using the evaporator described in section 3.5.1. All binding energies are referenced to the Fermi level as measured at each energy. The pentacene was evaporated at normal incidence to the copper surface in a stepwise manner in the preparation chamber, after which the sample was transferred under UHV to the analysis chamber.

4.3 Pentacene on Cu(110) - Untemplated Film Growth

4.3.1 Workfunction analysis

The calculated workfunction for increasing pentacene coverages is presented in figure 4.1. Due to the physical nature of the interface dipole, as discussed in section 2.1.8, it is evident that it should be predominantly completed with the adsorption of the initial monolayer of adsorbate. Therefore extrapolation of the initial linear decrease in the workfunction of the sample to the workfunction of the sample for a thick pentacene film allows for the estimation of an approximate monolayer coverage¹⁶. All coverages are subsequently referenced to the deposition time required for the completion of this monolayer coverage. It should be noted that a change in packing density of the pentacene film as a result of molecular reorientation or the onset of significant island growth in the film will cause the actual film thickness in monolayers to deviate from the estimated thickness. The interface dipole is not fully formed in this case by the completion of the approximate monolayer coverage due to the formation of a bi-layer prior to the completion of the initial monolayer⁶. An additional small contribution to the total interface dipole due to the second and third monolayers¹⁷ is also thought to add to the discrepancy. The total interface dipole formed for a thick pentacene film was found to be approximately 1.0eV, which compares in magnitude with interface dipoles formed between pentacene and other metal substrates¹⁸. For example, pentacene deposited on Au¹⁸ and Au(111)¹² result in calculated interface dipoles of 1.0eV and 0.95eV respectively, while a value of 0.7eV has been calculated for pentacene deposited on Ag¹⁸. In chapter 5 we will see that pentacene deposited on the Au(100) substrate results

in an interface dipole of magnitude 0.9eV. The deposition of pentacene on low workfunction metals such as Sm¹⁹ and Ca¹⁸, with initial workfunction values of 2.7eV and 2.85eV respectively, results in the formation of an interface dipole of smaller magnitude, 0.3eV and 0.4eV respectively, and opposite direction to those formed on high workfunction metal substrates.

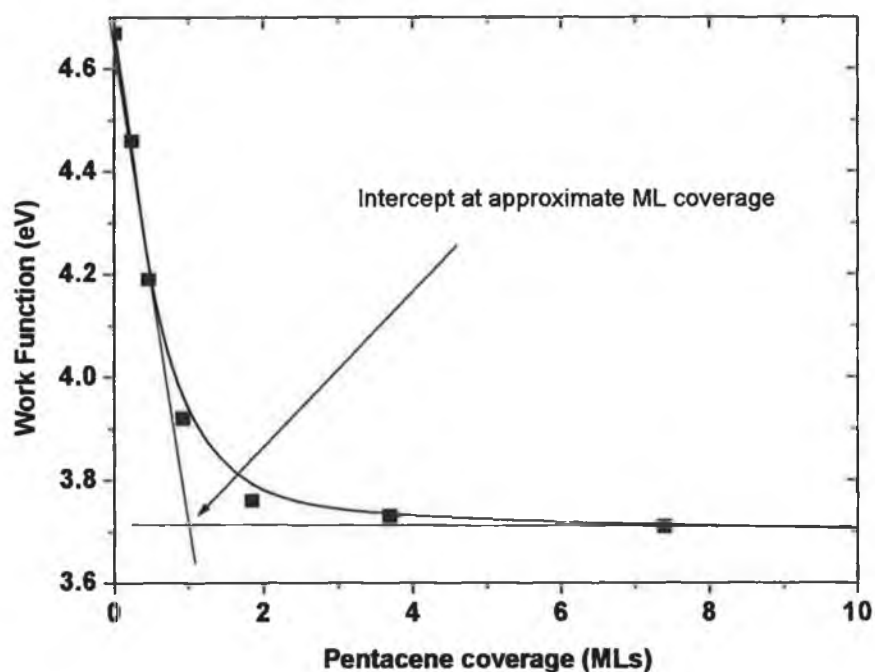


Figure 4.1 Workfunction values with increasing pentacene coverage as calculated from the negatively biased high binding energy cutoff of the valence band.

The calculated interface dipole formed upon the adsorption of pentacene onto the Cu(110) substrate is not however compatible with the model proposed by Watkins et al¹⁸ indicating a linear relationship between the magnitude of the interface dipole formed upon deposition of pentacene on different substrates and the initial workfunction of a given substrate. Watkins' model is based on the idea that the interface dipole formed at a metal/semiconductor interface is due predominantly to chemical bonding at the interface between the metal and the semiconductor²⁰. However, more recent studies by Witte et al²¹, discussed in detail in section 2.1.8, have shown that the predominant contribution to the magnitude of the interface dipole is the repulsion of the surface metal charge by the adsorbate molecular charge. While an additional chemical component to the interface dipole is found in cases where chemical bonding occurs between the adsorbate and the substrate, in general cases it is the charge repulsion derived

component that dominates, and hence the basis of the model proposed by Watkins is inappropriate.

4.3.2 C1s core level analysis

The shape of the C1s feature in figure 4.2 at submonolayer coverages indicates the presence of more than one component in the peak, as indicated by (b) and (c) in the diagram. The separation of these components by approximately 0.5eV indicates the presence of carbon in more than one distinct chemical environment at submonolayer coverages of pentacene. STM images^{6, 9} at these coverages show that the molecules adopt a flat lying molecular orientation with respect to the substrate, exhibiting short range order, indicating the predominance of a single bonding environment despite an absence of long range ordering of the film. Since a second pentacene bonding orientation is not evident, the presence of two carbon components is attributed to differences in the chemical environments of carbon atoms within each individual pentacene molecule. This is evidence of a relatively strong preferential bond between some of the carbon atoms in the pentacene and the Cu(110) substrate and is consistent with previous TDS results⁵, which indicate a strong bond between the initial monolayer of pentacene and the Cu(110) surface.

This evidence of a relatively strong bonding interaction between the pentacene and the Cu(110) substrate is not consistent with the idea of physisorption of the pentacene to the substrate, which is generally observed between metal surfaces and non-functionalised organic molecules, and has been attributed by Söhnchen et al⁵ to a chemisorption of the interfacial pentacene layer. Evidence from the Cu3p peak position in section 4.3.3 would suggest that the component (c), the lower binding energy component of the C1s peak at submonolayer coverages is due to the C atoms chemically bonded to the Cu(110) substrate. This would infer negative charge transfer from the copper substrate to the pentacene molecules of the initial monolayer.

The introduction of a third component, (a), to the C1s lineshape at approximately 285.2eV binding energy for coverages in excess of 1ML is attributed to final state screening effects. Core holes created in the first monolayer by the emission of electrons are screened by the substrate electrons, thereby reducing the binding energy of the C1s electrons in the initial monolayer. This screening effect is not present in the second monolayer resulting in electrons with a higher binding energy than those of the initial monolayer¹⁹. At subsequent higher coverages the peak lineshape becomes more

single component in nature, indicative of a single bonding environment as dictated by the predominance of the molecule-molecule bond and the reduction of the C1s signal originating from the interfacial layer.

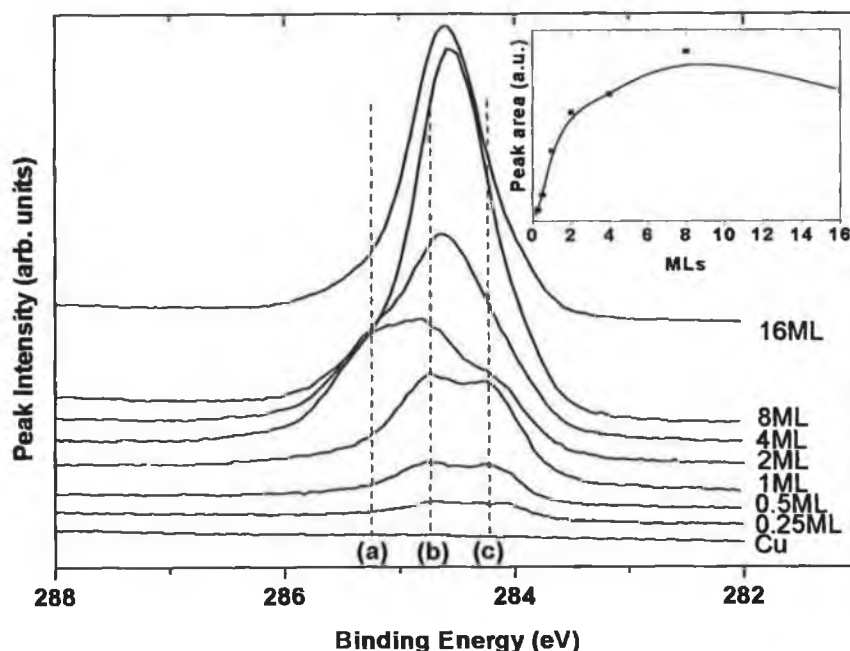


Figure 4.2 C1s core level ($h\nu = 340\text{eV}$) measured during the formation of the pentacene/Cu(110) interface. Inset in the diagram is the calculated peak area for increasing pentacene coverage using a linear fitting background.

The discussion of the C1s lineshape presented here has been carried out by the visual identification of C1s components in the total lineshape. This is due to the complex nature of the C1s lineshape prohibiting any meaningful fitting of the peak. It is visually evident that at submonolayer coverages the peak consists of at least two components, which have been attributed to the chemisorption of the initial monolayer of pentacene to the Cu(110) substrate in the previous discussion. Indeed the peak lineshape can be accurately fitted with two components in the submonolayer regime. However, it is at coverages above a monolayer that the legitimacy of the fitting procedure is in question.

The introduction of a further prominent component at higher binding energy for the 2ML coverage is attributed to substrate screening effects. However the likelihood of an interaction between the initial monolayer of pentacene and the subsequent monolayers of pentacene means that the initial component energy positions cannot be

fixed at their submonolayer positions. Additionally, a greater interaction between either the carbon atoms involved in the bonding process with the Cu(110) substrate or those not involved in the bonding process and the pentacene molecules in the second monolayer could result in a change in the energy separation between the initial monolayer C1s components.

It is obvious that even conceptually the peak lineshape is likely to be quite complex due to the chemisorption of the initial monolayer and the physisorption of subsequent monolayers. The FWHM of the peak never exceeds 2eV and so the fitting of multiple components in the lineshape at coverages higher than a monolayer is likely to be inaccurate as following the energy shifts and changes in intensities of different components within such a narrow peak width is likely to result in errors of large enough magnitude to make the results essentially arbitrary.

The calculated area of the C1s peak, inset in figure 4.2, plots the growth of C1s peak area up until a coverage of 8ML after which it decreases slightly despite an increasing overlayer coverage. Using values for the mean free paths of the C1s photoelectrons of $\lambda_{C1s}=5.2\text{\AA}$ ($E_{kin}=53\text{eV}$) taken from the NIST database²², the total sampling depth of the C1s electrons is found to be approximately 16Å. This is much less than the estimated film thickness of 30.4Å for the 16ML coverage as calculated from the flat bonded monolayer thickness of 1.9Å⁵. The drop in C1s peak area is most likely an artefact of varying film density at different film depths coupled with the overlayer thickness exceeding the sampling depth of the C1s electrons. This apparent reduction in the peak area has also been observed for pentacene deposited on the Au(100) substrate as will be shown in chapter 5.

4.3.3 Cu3p core level analysis

Figure 4.3 shows the reduction in the substrate signal with increasing overlayer coverage. Inset in figure 4.3 are the normalised scans of the Cu3p peak with increasing overlayer coverage from the top to the bottom.

Using values for the mean free paths²² of the Cu3p photoelectrons of $\lambda_{Cu3p}=6.95\text{\AA}$ for the Cu3p line ($E_{kin}=124\text{eV}$), the total sampling depth of the Cu3p electrons is found to be approximately 20.9Å. According to general XPS theory only 5% of the total substrate signal originates from atoms residing outside the sampling depth (taken as three times the IMFP) for a given photoelectron energy. Figure 4.3 indicates that the Cu3p signal for an estimated film thickness of 30.4Å is 14% of the

total signal from the clean Cu(110). This percentage is far in excess of the sub 5% expected for a pentacene thin film of this thickness exhibiting Frank – Van der Mewre type film growth and so is indicative of Stranski – Krastanov growth in the overlayer. This is confirmed by the rapid decrease in the attenuation rate of the Cu3p substrate peak for coverages in excess of 1 ML.

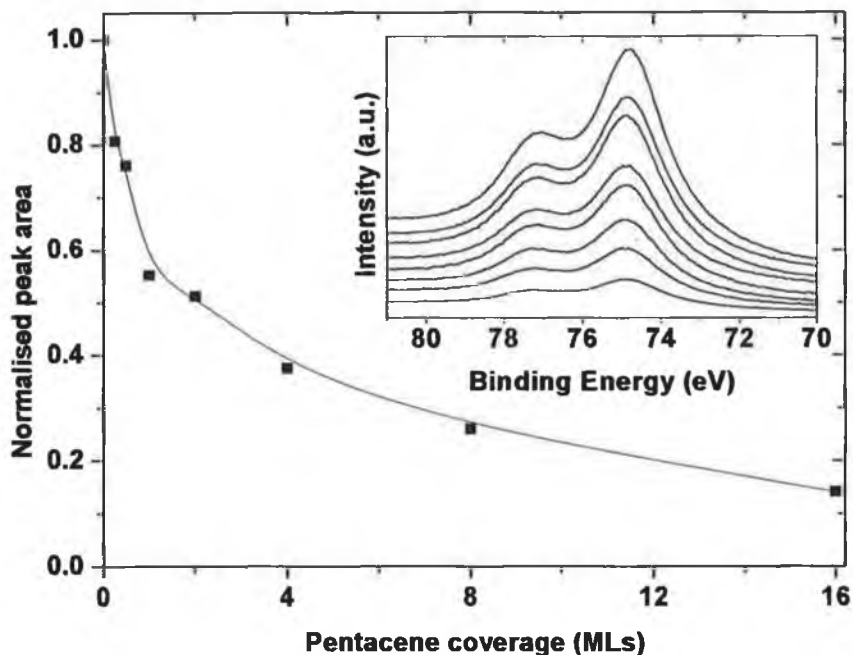


Figure 4.3 Normalised peak area of the Cu3p substrate peak plotted for increasing pentacene coverage. Inset in the graph are the stacked Cu3p spectra ($h\nu = 200\text{eV}$) for clean Cu(110), 0.25ML, 0.5ML, 1ML, 2ML, 4ML, 8ML and 16ML coverages respectively from top to bottom.

This difference in slope of the attenuation at submonolayer coverages and coverages greater than a monolayer is also likely to be affected by the different sticking coefficients experienced by the pentacene molecules in both cases. At submonolayer coverages, the chemisorption of the molecules most likely results in a high sticking coefficient for molecules deposited on the clean Cu(110) substrate. However, at coverages greater than a monolayer, the sticking coefficient is likely to be reduced due to the absence of an intermolecular chemical bond. There should be two distinct sticking coefficients at coverages greater than a monolayer, one for the molecules in the second monolayer coming into contact with the flat bonded molecules of the interfacial layer, and another for the subsequently deposited molecules coming into contact with the tilted pentacene molecules present from the second monolayer of film growth.

Evidence of these two distinct sticking coefficients at coverages greater than a monolayer can be seen in the trend of the Cu3p suppression between the first and second monolayer, which does not fit in with the trend of substrate suppression that follows the completion of the second monolayer.

A shift of 0.1eV to higher binding energy of the Cu3p peak position from the clean Cu(110) substrate to the 1ML pentacene has been observed. Due to the broad nature of the Cu3p peak, a second binding energy shifted component due to the chemisorption of the pentacene to the interfacial copper monolayer was unable to be resolved from the overall peak lineshape. However, the growth of the chemically shifted copper component at higher binding energy coupled with the suppression of the bulk component would result in an overall shift in the measured peak centre to higher binding energy. This shift in the binding energy of the Cu3p peak is therefore evidence of negative charge transfer from the substrate to the pentacene molecule during the chemisorption of the initial monolayer.

4.3.4 Valence band and group theory analysis

The valence band scans at normal emission and s-polarised sample positions are presented in figure 4.4 and figure 4.5. The features in the 2-5eV binding energy region of figure 4.4 and figure 4.5 are attributed to emission from the Cu3d energy level, which occurs in the valence band region of the photoemission spectrum. The features are generally seen to reduce in intensity with increasing pentacene coverage. Closer inspection of the graphs indicates the suppression of features at 2.55eV, 4.1eV and 4.6eV in the normal emission spectra (denoted as S1, S2 and S3), and at 5.35eV (denoted as S4) in the s-polarised spectra. These features are observed to be totally suppressed by the completion of the monolayer coverage indicating that they are surface states related to the substrate that are quenched upon adlayer adsorption. Growth of features at 2.9eV (denoted as I2) in both sample orientations is observed in addition to further growth at 3.55eV (denoted as I1) in the normal emission spectra. The origin of these emissions shall be discussed in more detail later.

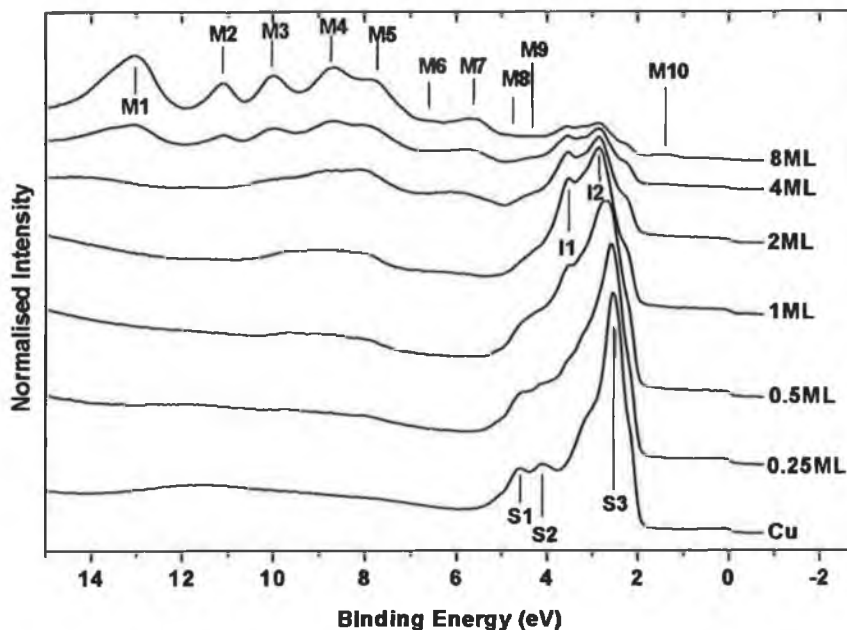


Figure 4.4 Valence band scans ($h\nu = 31\text{eV}$) at normal emission for the stepwise growth of pentacene on Cu(110). Plots present increasing coverages of pentacene on Cu(110). Copper surface states are labelled S1 to S3, molecular orbitals identified for a thick pentacene film are labelled M1 to M10 and interface states are labelled I1 and I2.

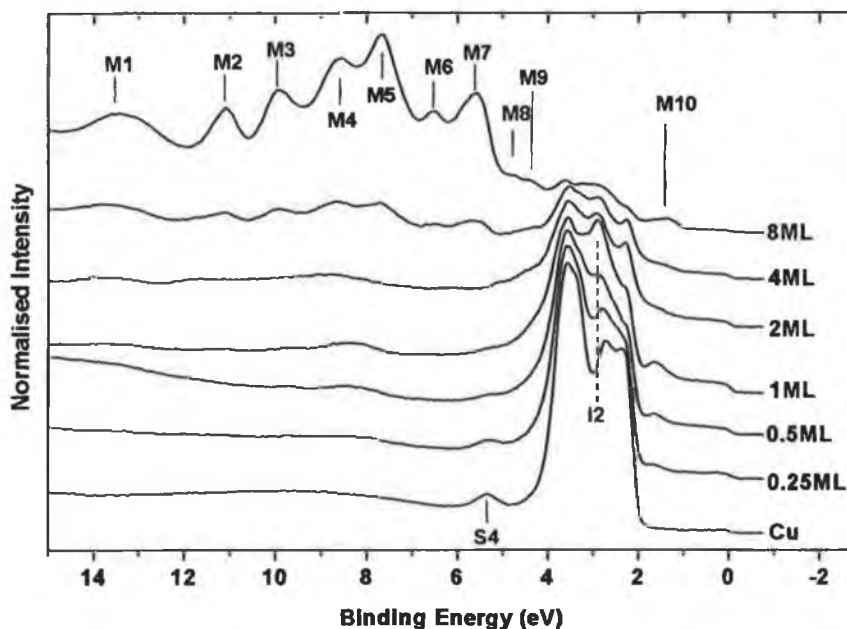


Figure 4.5 Valence band scans ($h\nu = 31\text{eV}$) at the s-polarised sample position for the stepwise growth of pentacene on Cu(110). Plots present increasing coverages of pentacene on Cu(110). S4 denotes the identified copper surface state observed for the s-polarised sample orientation. Molecular orbitals identified for a thick pentacene film are labelled M1 to M10 and an identified interface state is labelled I2.

A broad feature at approximately 8eV binding energy becomes visible at the completion of the monolayer in both sample orientations. This feature is composed of emission from a number of $\pi+\sigma$ hybrid and pure σ derived molecular orbitals, which become more clearly defined at higher pentacene coverages. Due to the large background in the 2-5eV region of the spectra resulting from emission from the Cu3d energy level, the discussion shall centre on the HOMO peak. This feature, which is centred at approximately 1.6eV, is easier to identify than the other π related molecular orbitals, which overlap with the Cu3d emissions. There is little evidence of the HOMO in the normal emission valence band spectra up to the monolayer coverage. In contrast, the s-polarised valence band spectra, presented in figure 4.5, indicate the presence of a strong HOMO feature (M10), centred at 1.6eV binding energy. This feature becomes evident from the initial pentacene coverage of 0.25ML and increases in intensity until the completion of the monolayer coverage. Subsequent coverages show a suppression of the HOMO signal. The presence of the HOMO in the s-polarised VB spectra coupled with its absence from the normal emission spectra is due to the process by which electrons are emitted from molecular orbitals, which is discussed in more detail below.

At high pentacene coverages, features are visible at 2.2eV, 2.75eV and 3.6eV, which are attributed to residual emission from the Cu3d substrate feature. For the 8ML pentacene coverages presented in figure 4.4 and figure 4.5, valence band features derived from molecular orbitals, labelled M1 to M10, are prominent in both the normal emission and s-polarised sample position valence band spectra. Features M1 to M5, which are derived from σ molecular orbitals are evident at 7.7eV, 8.55eV, 9.9eV, 11.1eV and 13.4eV. At 5.65eV and 6.55eV strong emissions, labelled M6 and M7, are observed from $\pi+\sigma$ derived molecular orbitals in the s-polarised VB, while the corresponding emissions are much weaker in the normal emission valence band scans. The identification of π -derived molecular orbital emission is made difficult by the relatively weak intensity of the π -derived emissions and the presence of residual signal from the Cu3d valence band peak in the 2-4eV region of the spectra. However emissions from π -derived molecular orbitals, labelled M8 to M10, are evident at 1.4eV, 4.4eV and 4.8eV.

Figure 4.6 shows the gas phase spectrum of pentacene^{23, 24}. The molecular orbital assignments of the seven lowest binding energy molecular orbitals have been obtained from literature^{24, 25}. There is however a discrepancy in the assignment of symmetry of the π_9 and π_7 molecular orbitals with Clarke et al²⁴ attributing them to

emission from $3b_{3g}$ and $3b_{1u}$ orbitals respectively while Ozaki²⁵ attributes them to emission from $3b_{1g}$ and $3b_{3u}$ orbitals.

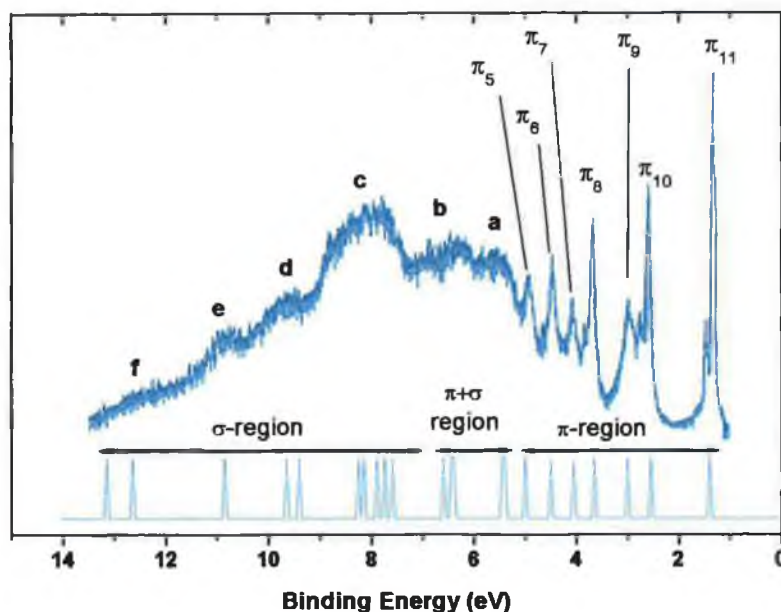


Figure 4.6 Pentacene gas phase spectrum with π molecular orbital assignments^{24, 25}.

The MIINDO3 function in the Hyperchem software package²⁶ was used to simulate the molecular orbital spectrum of the pentacene. A scaling factor of 0.8 was subsequently used to adjust the simulated spectrum so that the π molecular orbital energies were in agreement with those of the gas phase spectrum. The calculated π orbital assignment provided by Hyperchem was found to be in agreement with the molecular assignment provided by Ozaki²⁵. Features a to f in figure 4.6 indicate features in the $\pi+\sigma$ hybrid and pure σ region of the spectrum, which are made up of a number of constituent molecular orbitals. An assignment of the molecular orbitals contributing to features in the $\pi+\sigma$ hybrid and pure σ region of the spectrum is now possible. Table 4.1 indicates the calculated molecular orbital assignment of all the features in the gas phase spectrum shown in figure 4.6. The adsorption of molecules of symmetry D_{2h} onto a substrate can sometimes result in the reduction of the symmetry of the molecule from D_{2h} to C_{2v} with a corresponding reduction in the molecular orbital assignments. The b_{1u} and a_g symmetries are reduced to a_1 , the b_{1g} and a_u symmetries to a_2 , the b_{3u} and b_{2g} symmetries to b_1 , and the b_{3g} and b_{2u} symmetries to b_2 . The reduced symmetries of the molecular orbitals for the C_{2v} molecular symmetry are also presented in table 4.1 for additional analysis.

Feature	Orbital assignment (D_{2h})	Orbital assignment (C_{2v})	Binding Energy
π_{11}	$3b_{2g}$	b_1	1.4eV
π_{10}	$2a_u$	a_2	2.56eV
π_9	$3b_{1g}$	a_2	3.00eV
π_8	$2b_{2g}$	b_1	3.56eV
π_7	$3b_{3u}$	b_1	4.05eV
π_6	$1a_u$	a_2	4.5eV
π_5	$1b_{2g}$	b_1	5.02eV
a	$2b_{1g}$	a_2	5.35eV
	$7b_{3g}$	b_2	5.40eV
b	$7b_{1u}$	a_1	6.38eV
	$6b_{3g}$	b_2	6.45eV
	$2b_{3u}$	b_1	6.58eV
c	$1b_{1g}$	a_2	7.58eV
	$5b_{3g}$	b_2	7.75eV
	$6b_{1u}$	a_1	7.89eV
	$5b_{1u}$	a_1	8.13eV
	$1b_{3u}$	b_1	8.24eV
d	$7a_g$	a_1	9.38eV
	$6b_{2u}$	b_2	9.64eV
e	$4b_{1u}$	a_1	10.86eV
f	$6a_g$	a_1	12.66eV
	$5b_{2u}$	b_2	13.15eV

Table 4.1 Assignment of molecular orbitals to features in the gas phase spectrum of pentacene for both the D_{2h} symmetry of the free molecule and the C_{2v} reduced symmetry of the adsorbed pentacene molecule.

It is evident from table 4.1 that features in the $\pi+\sigma$ hybrid and pure σ region of the spectrum are made up of a number of constituent molecular orbitals of different

inherent symmetry. This makes analysis of these features using the selection rules more difficult, and so analysis will mainly focus on the molecular orbitals in the π region of the spectrum. These features are comprised of single molecular orbitals and are generally well energetically spaced from each other making identification of these features simpler.

A comparison between the gas phase spectrum and the valence band spectra for a thick pentacene coverage is presented in figure 4.7. There is good agreement between the gas phase spectrum and the valence band scans with strong valence band features evident in the $\pi+\sigma$ hybrid and pure σ region of the valence band spectra. Emissions in the valence bands corresponding to features from the gas phase spectrum labelled a to e in figure 4.6 are particularly intense. Emission from features in the π region of the spectra are much weaker in intensity with only a strong emission from the HOMO (π_{11}) in addition to much weaker emission from π_6 and π_5 in evidence. The difficulty in the identification of emission from the other π molecular orbitals arises from their relatively weak emission coupled with the residual intensity from the Cu3d valence band feature in the 2-4eV region of the spectrum.

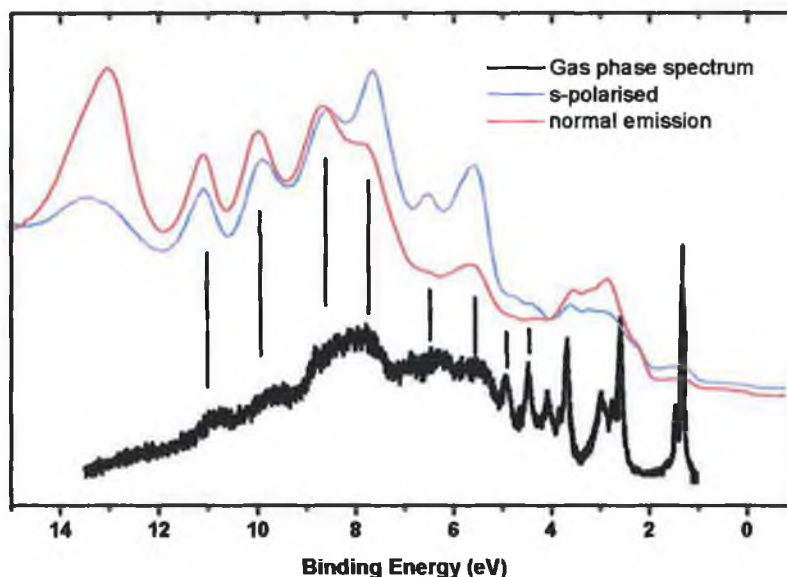


Figure 4.7 Comparison between gas phase spectrum of pentacene from literature and valence band spectra ($h\nu = 31\text{eV}$) of an 8ML coverage of pentacene on Cu(110) for normal emission and s-polarised sample positions.

Figure 4.8 shows a ball and stick model of a pentacene molecule. The x, y and z directions have been defined with respect to the molecule for the subsequent group theory based analysis of emission from molecular orbitals.

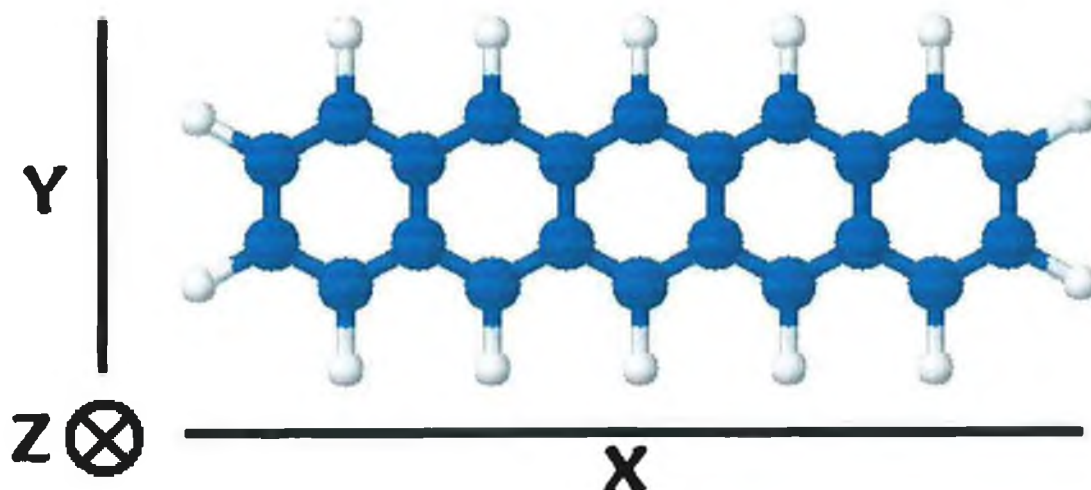


Figure 4.8 Ball and stick model of a pentacene molecule indicating the x , y and z directions with respect to the molecule.

In order to fully interpret the valence band spectra and to investigate the orientation of the molecule on the surface, group theory was applied to the pentacene/Cu(110) interface. Group theory makes extensive use of symmetry conditions in its analysis. In general the more symmetric the molecule, the fewer energy levels it has, and the greater the degeneracies of those levels. Symmetry conditions must be met for transitions between energy levels to occur, for example a molecule might not be able to absorb light of precisely the correct energy to span two energy levels of the molecule if the symmetries of the states involved are not compatible. It is this restriction, which is utilised in the application of group theory analysis. Group theory analysis works by the formation of selection rules that govern which energy transitions are allowed and forbidden. There are two general approaches taken when applying group theory to analysis of the photoemission process. The first approach is often called the “free molecule” approach and assumes that there is no significant distortion of the molecule upon adsorption, and so the D_{2h} symmetry of the free molecule remains intact. The second approach involves the assumption that the symmetry of the molecule is reduced upon adsorption to the substrate due to bonding, with the resultant C_{2v} reduced symmetry found for molecules of D_{2h} symmetry. The selection rules governing the uv-photoemission process from the clean and pentacene covered Cu(110) surface, as a consequence of the symmetry properties of the system will be discussed.

To calculate the basis of the selection rules, it is necessary to have a direct product of the irreducible representations table for the point groups D_{2h} and C_{2v} . These

are necessary to accurately determine the selection rules for the allowed and forbidden transitions.

D_{2h}	A_g	B_{1g}	B_{2g}	B_{3g}	A_u	B_{1u}	B_{2u}	B_{3u}
A_g	A _g	B _{1g}	B _{2g}	B _{3g}	A _u	B _{1u}	B _{2u}	B _{3u}
B_{1g}		A _g	B _{3g}	B _{2g}	B _{1u}	A _u	B _{3u}	B _{2u}
B_{2g}			A _g	B _{1g}	B _{2u}	B _{3u}	A _u	B _{1u}
B_{3g}				A _g	B _{3u}	B _{2u}	B _{1u}	A _u
A_u					A _g	B _{1g}	B _{2g}	B _{3g}
B_{1u}						A _g	B _{3g}	B _{2g}
B_{2u}							A _g	B _{1g}
B_{3u}								A _g

Table 4.2 Direct Products of Representation Table for D_{2h} symmetry.

C_{2v}	A₁	A₂	B₁	B₂
A₁	A ₁	A ₂	B ₁	B ₂
A₂		A ₁	B ₂	B ₁
B₁			A ₁	A ₂
B₂				A ₁

Table 4.3 Direct Products of Representation Table for C_{2v} symmetry.

From the character table for a molecule of symmetry D_{2h} presented in table 2.2, it is found that a light vector polarised along the x-direction of the molecule, as defined in figure 4.8, is attributed B_{3u} symmetry with respect to the molecule. Similarly, light polarised along the y and z directions are attributed B_{2u} and B_{1u} symmetries, respectively.

From the character table for the reduced symmetry C_{2v} presented in table 2.3, it is found that a light vector polarised along the x-direction of the molecule, as defined in figure 4.8, is attributed B₁ symmetry with respect to the molecule. Similarly, light polarised along the y and z directions are attributed B₂ and A₁ symmetries, respectively.

It is useful to consider the outgoing wave in the vacuum as a superposition of spherical harmonics $\langle |L M| \rangle$ centered at an origin on the surface. It is clear that for non-zero photocurrent at the detector, it is necessary for M in equation 2.14 to be non-zero but also that the detector does not lie in a nodal plane of the outgoing wave. For normal

emission the final state must contain $|L 0\rangle$ components (s, p_z , d_z^2 , ...) in order to be detected²⁷. That is, the final state belongs to the totally symmetric representation. This places a restriction on the nature of the initial state, only those initial states which have the same symmetry as a component of the operator can contribute to the detected photoemission signal.

The spherical harmonics for each possible final state for a molecule of symmetry D_{2h} have been obtained from literature and are presented in table 4.4. The ν and μ columns indicate the increment by which the L and M values can be increased for a molecule of symmetry D_{2h} . It is evident that only those transitions that result in a final state of either A_g or B_{1u} should be observed in normal emission. Normal emission is defined as normal to the molecular plane of the pentacene and is therefore in the z-direction with respect to the molecule as defined in figure 4.8. Table 4.5 presents the spherical harmonics for each possible final state for a molecule of symmetry C_{2v} . It is evident that only those transitions that result in a final state of A_1 should be observed in normal emission.

For each given initial state it is now possible, using tables 4.2 and 4.4, to calculate the corresponding final state and spherical harmonics for light vectors polarised along the three different axes of the molecule for the D_{2h} molecular symmetry.

Final State	$\langle L M $	ν	μ
A_g	$ 0 0\rangle_+$	2	2
B_{1g}	$ 2 2\rangle_-$	2	2
B_{2g}	$ 2 1\rangle_-$	2	2
B_{3g}	$ 2 1\rangle_+$	2	2
A_u	$ 3 2\rangle_-$	2	2
B_{1u}	$ 1 0\rangle_+$	2	2
B_{2u}	$ 1 1\rangle_+$	2	2
B_{3u}	$ 1 1\rangle_-$	2	2

Table 4.4 Table showing symmetrized bases for D_{2h} symmetry.

A similar analysis can also be carried out using the information in table 4.3 and table 4.5 to calculate the corresponding final state and spherical harmonics for light vectors polarised along the three different axes of the molecule for the reduced C_{2v} molecular symmetry.

Final State	$\langle L M \rangle$	ν	μ
A_1	$ 0 0\rangle_+$	1	2
A_2	$ 2 2\rangle_-$	1	2
B_1	$ 1 1\rangle_-$	1	2
B_2	$ 1 1\rangle_+$	1	2

Table 4.5 Table of symmetrized bases for C_{2v} symmetry.

Table 4.6 shows the calculated final states and corresponding spherical harmonics for a given initial state using the three different polarisations of incident radiation as operators for molecules of D_{2h} symmetry. It is evident that only those initial states of symmetry B_{2g} and B_{3u} will be observed at normal emission for incident radiation polarised along the x-axis of the molecule. For light polarised along the y-axis of the molecule, only initial states of symmetry B_{3g} and B_{2u} will be evident at normal emission. For light polarised along the z-axis, only initial states of symmetry A_g and B_{1u} will be evident at normal emission.

Initial State	X – polarisation B_{3u}	Y – polarisation B_{2u}	Z – polarisation B_{1u}
A_g	$B_{3u} \rightarrow 11\rangle_-$ $ 31\rangle_-$ $ 33\rangle_-$	$B_{2u} \rightarrow 11\rangle_+$ $ 31\rangle_+$ $ 33\rangle_+$	$B_{1u} \rightarrow 10\rangle$ $ 30\rangle$ $ 32\rangle_+$
B_{1g}	$B_{2u} \rightarrow 11\rangle_+$ $ 31\rangle_+$ $ 33\rangle_+$	$B_{3u} \rightarrow 11\rangle_-$ $ 31\rangle_-$ $ 33\rangle_-$	$A_u \rightarrow 32\rangle_-$
B_{2g}	$B_{1u} \rightarrow 10\rangle$ $ 30\rangle$ $ 32\rangle_+$	$A_u \rightarrow 32\rangle_-$	$B_{3u} \rightarrow 11\rangle_-$ $ 31\rangle_-$ $ 33\rangle_-$
B_{3g}	$A_u \rightarrow 32\rangle_-$	$B_{1u} \rightarrow 10\rangle$ $ 30\rangle$ $ 32\rangle_+$	$B_{2u} \rightarrow 11\rangle_+$ $ 31\rangle_+$ $ 33\rangle_+$
A_u	$B_{3g} \rightarrow 21\rangle_+$	$B_{2g} \rightarrow 21\rangle_-$	$B_{1g} \rightarrow 22\rangle_-$
B_{1u}	$B_{2g} \rightarrow 21\rangle_-$	$B_{3g} \rightarrow 21\rangle_+$	$A_g \rightarrow 00\rangle$ $ 20\rangle$ $ 22\rangle_+$
B_{2u}	$B_{1g} \rightarrow 22\rangle_-$	$A_g \rightarrow 00\rangle$ $ 20\rangle$ $ 22\rangle_+$	$B_{3g} \rightarrow 21\rangle_+$
B_{3u}	$A_g \rightarrow 00\rangle$ $ 20\rangle$ $ 22\rangle_+$	$B_{1g} \rightarrow 22\rangle_-$	$B_{2g} \rightarrow 21\rangle_-$

Table 4.6 Calculated final states and corresponding spherical harmonics for a given initial state for molecules of D_{2h} symmetry.

Table 4.7 shows the calculated final states and corresponding spherical harmonics for a given initial state using the three different polarisations of incident radiation as operators for molecules of C_{2v} symmetry. It is evident that only those initial states of symmetry B_1 will be observed at normal emission for incident radiation polarised along the x-axis of the molecule. For light polarised along the y-axis of the molecule, only initial states of symmetry B_2 will be evident at normal emission and for light polarised along the z-axis, only initial states of symmetry A_1 will be evident at normal emission.

Table 4.8 introduces the application of the formulated selection rule analysis for the valence band orbitals assigned in table 4.1 for both the free molecule approach and the reduced symmetry approach. Molecular orbitals that should be observed under given excitation conditions at normal emission to the molecular plane are assigned a "1" in the corresponding column of the table, while orbitals that should not be observed are assigned "-" in the corresponding column. It is evident that no π -derived molecular orbitals should be visible normal to the molecular plane for light polarised along either the y or z-directions for either the D_{2h} symmetry or the C_{2v} symmetry.

Initial State	X – polarisation B_1	Y – polarisation B_2	Z – polarisation A_1
A_1	$B_1 \rightarrow 11\rangle_-$ $ 21\rangle_-$ $ 31\rangle_-$ $ 33\rangle_-$	$B_2 \rightarrow 11\rangle_+$ $ 21\rangle_+$ $ 31\rangle_+$ $ 33\rangle_+$	$A_1 \rightarrow 00\rangle$ $ 10\rangle$ $ 20\rangle$ $ 30\rangle$ $ 22\rangle_+$ $ 32\rangle_+$
A_2	$B_2 \rightarrow 11\rangle_+$ $ 21\rangle_+$ $ 31\rangle_+$ $ 33\rangle_+$	$B_1 \rightarrow 11\rangle_-$ $ 21\rangle_-$ $ 31\rangle_-$ $ 33\rangle_-$	$A_2 \rightarrow 22\rangle_-$ $ 32\rangle_-$
B_1	$A_1 \rightarrow 00\rangle$ $ 10\rangle$ $ 20\rangle$ $ 30\rangle$ $ 22\rangle_+$ $ 32\rangle_+$	$A_2 \rightarrow 22\rangle_-$ $ 32\rangle_-$	$B_1 \rightarrow 11\rangle_-$ $ 21\rangle_-$ $ 31\rangle_-$ $ 33\rangle_-$
B_2	$A_2 \rightarrow 22\rangle_-$ $ 32\rangle_-$	$A_1 \rightarrow 00\rangle$ $ 10\rangle$ $ 20\rangle$ $ 30\rangle$ $ 22\rangle_+$ $ 32\rangle_+$	$B_2 \rightarrow 11\rangle_+$ $ 21\rangle_+$ $ 31\rangle_+$ $ 33\rangle_+$

Table 4.7 Calculated final states and corresponding spherical harmonics for a given initial state for molecules of C_{2v} symmetry.

Feature	Orbital assignment D_{2h}	Light Vector			Orbital assignment C_{2v}	Light Vector		
		X (B_{3u})	Y (B_{2u})	Z (B_{1u})		X (B_1)	Y (B_2)	Z (A_1)
π_{11}	$3b_{2g}$	1	-	-	b_1	1	-	-
π_{10}	$2a_u$	-	-	-	a_2	-	-	-
π_9	$3b_{1g}$	-	-	-	a_2	-	-	-
π_8	$2b_{2g}$	1	-	-	b_1	1	-	-
π_7	$3b_{3u}$	1	-	-	b_1	1	-	-
π_6	$1a_u$	-	-	-	a_2	-	-	-
π_5	$1b_{2g}$	1	-	-	b_1	1	-	-
a	$2b_{1g}$	-	-	-	a_2	-	-	-
	$7b_{3g}$	-	1	-	b_2	-	1	-
b	$7b_{1u}$	-	-	1	a_1	-	-	1
	$6b_{3g}$	-	1	-	b_2	-	1	-
	$2b_{3u}$	1	-	-	b_1	1	-	-
c	$1b_{1g}$	-	-	-	a_2	-	-	-
	$5b_{3g}$	-	1	-	b_2	-	1	-
	$6b_{1u}$	-	-	1	a_1	-	-	1
	$5b_{1u}$	-	-	1	a_1	-	-	1
	$1b_{3u}$	1	-	-	b_1	1	-	-
d	$7a_g$	-	-	1	a_1	-	-	1
	$6b_{2u}$	-	1	-	b_2	-	1	-
e	$4b_{1u}$	-	-	1	a_1	-	-	1
f	$6a_g$	-	-	1	a_1	-	-	1
	$5b_{2u}$	-	1	-	b_2	-	1	-

Table 4.8 Evaluation of emission from valence band features in normal emission for light polarised along each molecular axis.

From the comparison between the normal emission predictions for both the D_{2h} and C_{2v} molecular symmetries presented in table 4.8, it is evident that identical emission should be evident in the valence band studies at normal emission to the molecular plane, which is the so called “forbidden geometry”. In this manner, the reduction of symmetry from D_{2h} to C_{2v} is an unusual case as the formulation of selection rules for the reduced symmetry case usually results in the prediction of a significantly different spectrum at normal emission.

However while the case for the “forbidden geometry” is found to be identical for both the D_{2h} and C_{2v} symmetries, closer inspection of the spherical harmonics does indicate differences between the two predicted spectra. Take for example the emission from the HOMO, π_{11} , as predicted by both molecular symmetries. Table 4.8 indicates that the HOMO in both cases should only be visible at normal emission when the light vector is polarised along the x-axis of the molecule. The resultant spherical harmonics for the HOMO emission with light polarised along the x-axis for D_{2h} symmetry are $|1,0\rangle$, $|3,0\rangle$ and $|3,2\rangle_+$. For the C_{2v} symmetry investigated, the resultant spherical harmonics are $|0,0\rangle$, $|1,0\rangle$, $|2,0\rangle$, $|3,0\rangle$, $|2,2\rangle_+$ and $|3,2\rangle_+$. If the spherical harmonics are assumed to be independent of each other with little interaction between the different harmonics, a comparison between the observed harmonics is possible. While there is evidently some overlap between the spherical harmonics observed in both cases, the presence of additional components for the C_{2v} symmetry is significant. The $|1,0\rangle$ and $|3,0\rangle$ components are highly directional normal to the molecular plane with emission intensity trailing off rapidly with increase in angle from normal to the molecular plane. The $|2,0\rangle$ component is also found to follow a similar emission pattern. The $|3,2\rangle_+$ is found to have a maximum at mid angles. It is addition of the $|0,0\rangle$ and $|2,2\rangle_+$ components that are of most significance to the angular pattern of electron emission. The $|0,0\rangle$ component has equal emission intensities in all directions and the $|2,2\rangle_+$ component has a node in the plane of the molecule, with the resultant addition of emission in the plane of the molecule that is not predicted for the D_{2h} symmetry. Similar differences are also present in the angular emission distribution for the other orbitals. However since the study is not a comprehensive angle resolved study, we shall concentrate on the predictions made for the “forbidden geometry” of normal emission.

If the experimental setup is now considered, it is evident that the light vector in the s-polarised sample position is parallel to the sample surface, while in the normal emission sample position there are components of the light both parallel and perpendicular to the sample surface.

In the case of the pentacene/Cu(110) experimental system, the plane of the molecule is parallel to the copper surface with the short axis of the molecule lying along the [001] crystal direction⁶, therefore normal to the plane is also normal to the surface of the sample for coverages up to the completion of the initial monolayer.

The experimental setup, with the [001] crystal direction being rotated 30° off the horizontal, and the orientation of the pentacene on the surface as determined by STM studies⁶ resulted in the short axis (y-axis) of the molecule being rotated 30° off the plane of polarisation of the synchrotron light vector. The vector components along each molecular direction can easily be calculated as a function of I , the total intensity of the light vector and are as follows, $I_x=0.41I$, $I_y = 0.71I$, and $I_z=0.57I$. It is therefore evident that the presence of molecular orbitals in normal emission is predominantly dictated by the light vector interaction along the y-axis and z-axis of the molecule. Table 4.7 indicates therefore that there should be no molecular orbitals evident in the valence band spectra at normal emission up to a monolayer coverage of pentacene. The origin of emissions in the $\pi+\sigma$ hybrid and pure σ -derived regions of the spectra are more difficult to analyse because the features in this region of the valence bands are generally made up of a number of different molecular orbitals and therefore less information can be interpreted from the presence or the absence of a feature at normal emission.

In the s-polarised sample position, the component of the light vector along each molecular axes are $I_x=0.5I$, $I_y=0.86I$, and $I_z=0$ (due to the light vector being parallel to the sample surface). However because the analyser is no longer normal to the molecular plane of the pentacene, a similar analysis to that carried out for the pentacene molecular orbitals in normal emission is not possible in this case.

Due to the directional nature of emission from the molecular orbitals as described previously, the suppression of the HOMO derived feature after the completion of the monolayer is an indication of a change in molecular orientation of the pentacene molecules in the second monolayer. This change in molecular orientation after the completion of the initial monolayer is in agreement with the model proposed by Söhnchen et al⁵ for the pentacene thin film grown using an annealed monolayer to

template the growth of the film, where a tilting of the molecule along its short axis occurs after the initial monolayer.

Since it is predicted that π -derived molecular orbitals should not be visible in the normal emission spectra for coverages up to the completion of a monolayer, the features at 2.9eV and 3.55eV observed to grow in intensity up to the monolayer coverage are attributed to the formation of interface states as discussed in section 2.1.6. The assignment of these features as interface states was subsequently confirmed by the fact that doping of the pentacene film, as described in Section 6.3, results in no shift in the position of these features.

4.4 Pentacene on Cu(110) - Templated Film Growth

The annealed monolayer was grown on the substrate by maintaining the substrate temperature at 420K during the deposition of pentacene. This substrate temperature makes the formation of a bilayer thermodynamically unfavourable and so yields highly ordered monolayers of pentacene⁵. The workfunction data indicates a shift in the workfunction by approximately 1.0eV with the formation of the annealed monolayer, which remains constant with subsequent pentacene coverages.

In order to compare the growth of the pentacene film using an annealed monolayer to template the subsequent growth and the pentacene film grown without the use of an annealed monolayer, a coverage calibration is required. Due to the constant flux observed for the pentacene evaporator at a temperature of 423K, subsequent film growth after the formation of the annealed monolayer was calibrated into the units of approximate monolayers as used for the initial experiment. The monolayer coverages in both experiments were then equated on a coverage scale.

4.4.1 C1s core level analysis

Figure 4.9 shows the evolution of the C1s feature with increasing pentacene coverage. A similar trend in the C1s lineshape evolution is observed for the templated film as for the untemplated film. For the monolayer coverage, there are two distinct C1s components evident. Since the pentacene molecules are bonded in a well-ordered film in the annealed monolayer with the molecular planes parallel to the surface⁶ the origin of the multiple components is again attributed to different carbon atoms within each pentacene molecule and is evidence of a relatively strong bond between the pentacene

molecule and the underlying Cu(110) substrate. There is good agreement between the C1s peaks for the monolayer coverages in both pentacene films grown, which show two distinct components present in each peak.

There is however a shift of approximately 0.1eV to lower binding energy for the annealed monolayer coverage in comparison to the unannealed monolayer coverage. Due to the non-uniform layer-by-layer growth exhibited by the stepwise growth of pentacene on Cu(110)⁶, the monolayer coverage in the unannealed film is likely to contain areas of bilayer formation. The shift in the C1s peak position is therefore attributed to polarisation effects by molecules in the second monolayer in the unannealed film. In the subsequent coverages a new component, whose energy shift is attributed to final state screening effects in the initial monolayer, is observed at higher binding energy. The identical evolution of the C1s peaks in both films suggests that the mechanism for film growth is quite similar in both cases.

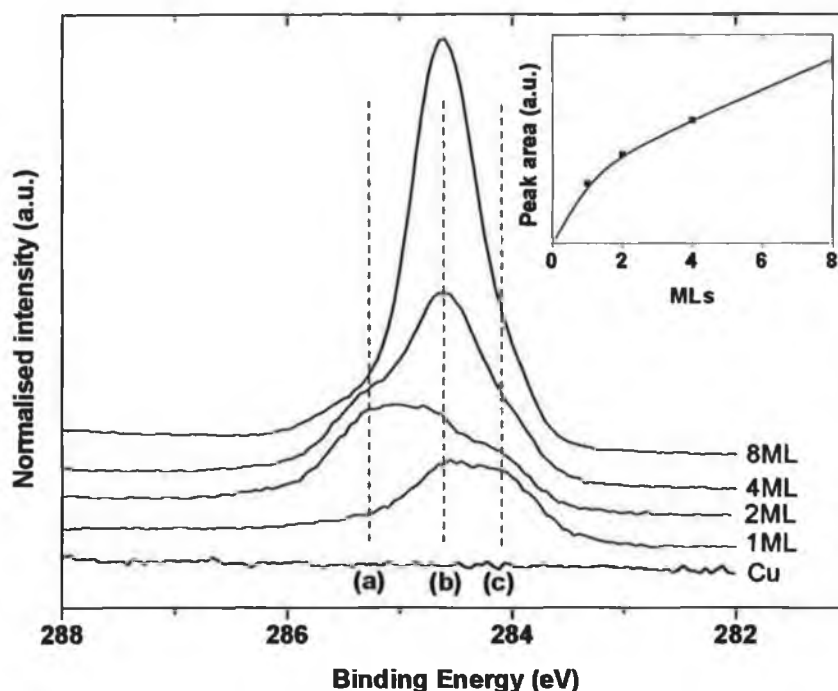


Figure 4.9 C1s core level ($h\nu = 340\text{eV}$) evolution with increasing pentacene coverage. The vertical lines indicate the presence of different components to the lineshape. Inset in the diagram is the calculated peak area for increasing pentacene coverage using a linear fitting background.

The inset in figure 4.9 plots the C1s peak area with increasing pentacene coverage. The plot follows the expected pattern of increasing C1s signal with increasing

pentacene coverage. A reduction in the area at high coverages similar to the growth of the untemplated film is not observed in this case although this decrease in C1s signal was not observed for the 8ML coverage in the initial experiment.

4.4.2 Cu3p core level analysis

Figure 4.10 plots the reduction of the Cu substrate peak with increasing pentacene coverage. The peak areas have been normalised to the peak area of the Cu3p peak for the clean Cu(110) surface. Inset in the graph is the stacked plots of the Cu3p peaks at different coverages in order of increasing pentacene coverage from top to bottom. The peak area of the Cu3p peak decreases to 7% of its original area for a coverage of 8ML. This is much smaller than the 26% and 14% observed respectively for the 8ML and 16ML coverages for an untemplated pentacene film. This indicates that the extent of island growth is much smaller for a pentacene film grown using an annealed monolayer to template the subsequent film growth and so the film is expected to exhibit greater ordering and a more uniform growth mode.

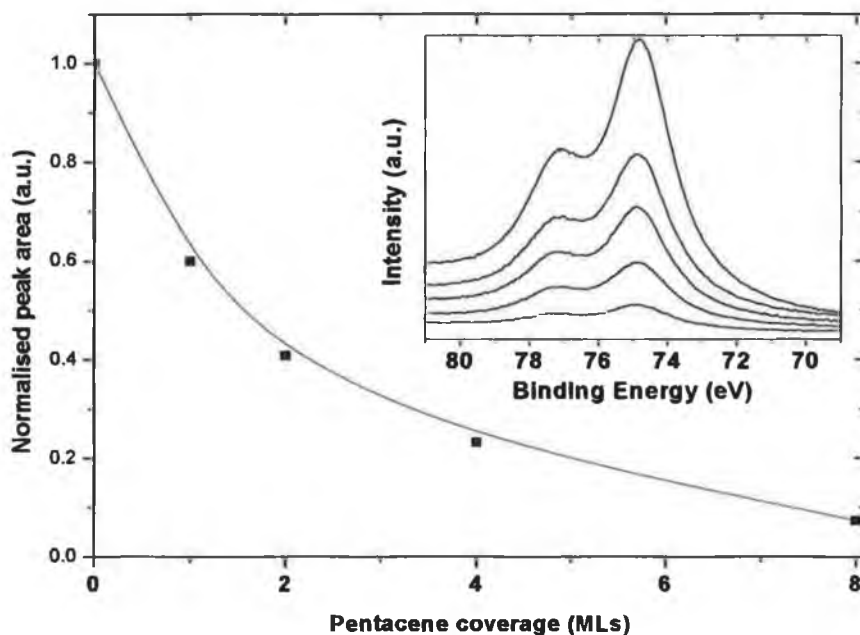


Figure 4.10 Normalised peak area of the Cu3p substrate peak plotted for increasing pentacene coverage. Inset in the graph are the stacked Cu3p spectra ($h\nu = 200\text{eV}$) for clean Cu(110), 1ML, 2ML, 4ML and 8ML coverages respectively from top to bottom.

An apparent shift in the Cu3p peak position of approximately 0.1eV to higher binding energy was observed with the deposition of the annealed monolayer. This was

also observed for the stepwise deposition of pentacene on the Cu(110) substrate described in section 4.3.3, and was attributed to the growth of an unresolved chemically shifted component of the Cu3p peak, coupled with the greater suppression of the clean Cu3p peak, leading to an observed shift in the peak centre. The direction of the shift in the peak centre indicates the growth of a higher binding energy shifted component, which is indicative of negative charge transfer from the substrate to the pentacene.

4.4.3 Valence band analysis

The normal emission valence bands for the templated pentacene film shown in figure 4.11 follow an identical pattern of growth to that of the initial experiment. The only pentacene related feature in evidence at the annealed monolayer coverage is the broad feature in the 8-10eV binding energy range, derived from a number of $\pi+\sigma$ hybrid and pure σ molecular orbitals. This feature resolves into its constituent components at higher pentacene coverages. A comparison between the 8ML coverage for the templated and untemplated films is presented in figure 4.11. There are very few noticeable differences between the two plots apart from the 2-4eV binding energy region of the spectra, where a differing suppression of the Cu3d band by the two pentacene films is observed. The pattern of substrate signal suppression is consistent with that observed for the Cu3p peak suppression shown in figure 4.3 and figure 4.10, in which the substrate suppression is greater for the film grown using an annealed monolayer to template the subsequent film growth.

The s-polarised VB scans presented in figure 4.12 indicate an identical pattern of film growth to that observed for the unannealed monolayer experiment presented in figure 4.5. The HOMO is evident at the monolayer coverage, centred at approximately 1.6eV binding energy and is suppressed by subsequent pentacene coverages indicating a change in orientation of the molecules in the second monolayer with respect to the initial annealed monolayer. As with the normal emission valence band comparison shown in figure 4.11, there is little difference in the valence band scans for the 8ML coverage for the templated film growth and the untemplated film growth for the s-polarised valence band scans as presented in figure 4.12. Due to the takeoff angle of 35° to the analyser for the s-polarised sample position, the differences between the Cu3d bands are less significant than for the normal emission spectra.

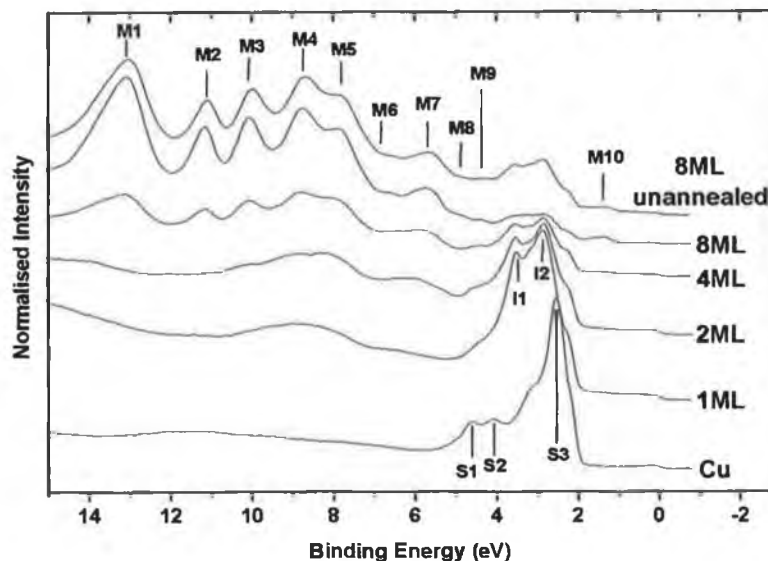


Figure 4.11 Valence band scans ($h\nu = 31\text{eV}$) at normal emission for the templated growth of pentacene on Cu(110). Plots present increasing coverages of pentacene on Cu(110), with the inclusion of the 8ML coverage for the unannealed pentacene film for comparison. Copper surface states are labelled S1 to S3, molecular orbitals identified for a thick pentacene film are labelled M1 to M10 and interface states are labelled I1 and I2.

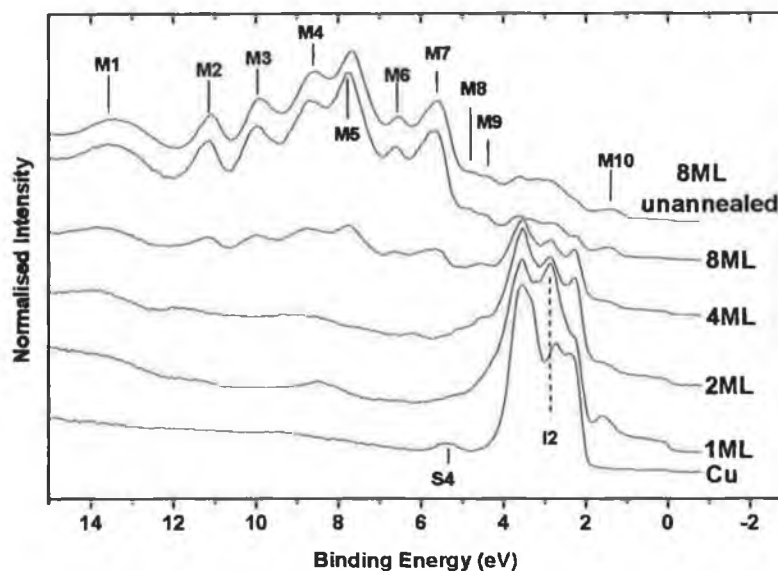


Figure 4.12 Valence band scans ($h\nu = 31\text{eV}$) at the *s*-polarised sample position for the templated growth of pentacene on Cu(110). Plots present increasing coverages of pentacene on Cu(110), with the inclusion of the 8ML coverage for the unannealed pentacene film for comparison. S4 denotes the identified copper surface state observed for the *s*-polarised sample orientation. Molecular orbitals identified for a thick pentacene film are labelled M1 to M10 and an identified interface states is labelled I2.

As mentioned previously, the emission from molecular orbitals is highly directional. The comparison between the valence band spectra in both normal emission and s-polarised sample positions show no differences between the pentacene related valence band features in the two films. Therefore the molecular orientation in the unannealed film is assumed to be similar to that of the templated film and so the molecular orientation is consistent with the model proposed by Söhnchen et al⁵ for the orientation of the molecules in the templated film. The third phase of the pentacene orientation in the film is not thought to be evident in either of the investigated pentacene films as the total film thickness is estimated to be less than 30Å. A pentacene molecule oriented at 73° from the horizontal, as is the case for the third phase of pentacene films grown on Cu(110), would have a height in excess of 13Å making it unlikely that the third phase is in evidence in a film with an estimated thickness of barely twice this value.

4.5 Molecular energy level diagram

In figure 4.13, the molecular energy level diagram is presented for the pentacene/Cu(110) interface. The energy level diagram does not take into account any band bending or polarisation shifts¹² in the film. This is due to the complex nature of the C1s feature prohibiting an accurate measurement of shifts in its position. The figure indicates the photoemission measured values of the interface dipole formed, Δ (1.0eV for the C₂₂H₁₄ interface) as calculated from the shift in the workfunction in figure 4.1. The hole injection gap is calculated from the energy separation between the Fermi level and the low binding energy cutoff of the HOMO derived peak as calculated from the valence band spectra. The hole injection gap was found to be 0.95eV for pentacene deposited on Cu(110). This value was found to be larger than the hole injection gap calculated for pentacene deposited on Au¹⁸ (0.5eV) and Au(111)¹² (0.55eV) but smaller than that found for pentacene deposited on Ag¹⁸ (1.1eV). For pentacene deposited on low workfunction metal substrates the hole injection gap was found to be significantly larger, with calculated values of 1.65eV for pentacene deposited on Ca¹⁸ and 1.8eV for pentacene deposited on Sm¹⁹.

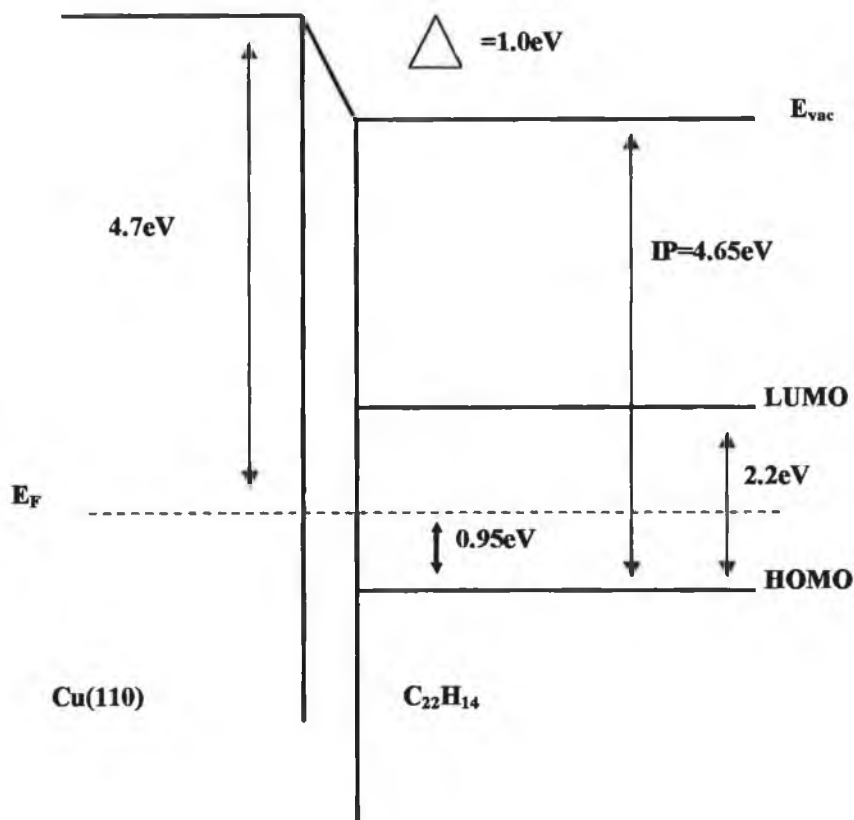


Figure 4.13 Energy level diagram for the pentacene/Cu(110) interface.

The LUMO position has been inferred from the measured charge transport gap²⁸ of 2.2 eV found for pentacene. The ionisation potential was calculated to be 4.65 eV and is found by addition of the workfunction for the thick pentacene film and the hole injection gap. This value for the calculated ionisation potential is smaller than for pentacene deposited on other metal substrates with values of 4.9 eV resulting from the deposition of pentacene on Au, Ag and Ca¹⁸, while values of 5.07 eV and 4.8 eV were obtained for pentacene deposited on Au(111)¹² and Sm¹⁹ respectively. There is no explanation given in literature for these deviations.

4.6 Summary

There is a sufficient body of evidence to suggest that the model proposed by Söhnchen et al⁵ for the growth of a pentacene thin film templated by an annealed monolayer can also be used to describe the growth of a pentacene thin film grown without the use of an annealed monolayer to template the growth. The evolution of the C1s feature in both studies follows an identical pattern inferring that there is a relatively strong bond between a number of carbon atoms in each pentacene molecule in the first

monolayer of pentacene and the underlying Cu(110) substrate. This evidence of a strong bond is contrary to the physisorption usually associated with the bonding of non-functionalised planar organic molecules to metal surfaces and has been attributed to a chemisorption of the initial pentacene layer. This has a large role to play in the flat lying adsorption of the pentacene molecules in the initial monolayer. Without this strong bonding interaction, the molecules in the subsequent monolayers adopt a tilted orientation, mediated by molecule-molecule interaction as opposed to the surface-molecule interaction of the initial monolayer. The evolution of the valence bands at both normal emission and *s*-polarised sample positions follows a similar pattern in both cases indicating an identical molecular orientation for the pentacene molecules in both films.

The formulation of selection rules for the D_{2h} point group, and also for the reduced symmetry C_{2v} point group, allowed for an investigation of the pentacene molecular orientation at low coverages. This selection rules analysis of the pentacene derived valence band features at sub-monolayer coverages indicated that the molecule adopted a flat bonded molecular orientation with respect to the substrate at these coverages, in agreement with the model proposed by Söhnchen et al⁵.

From the suppression of the substrate signal in both experiments, it was evident that a superior film quality could be obtained with the use of an annealed monolayer to template further film growth. This is in agreement with the findings of Söhnchen et al⁵.

Chapter 4 References

-
- ¹ C. D. Dimitrakopoulos and P. R. L. Malenfant, *Adv. Mater.* 14 (2002) 99.
 - ² D. J. Gundlach, Y. Y. Lin, T. N. Jackson, S. F. Nelson, and D. G. Schlom, *IEEE Electron Device Lett.* 18 (1997) 87.
 - ³ N. Karl, *Synth. Met.* 133–134 (2003) 649.
 - ⁴ T. W. Kelley and C. D. Frisbie, *J. Phys. Chem. B* 105 (2001) 4538.
 - ⁵ S. Söhnchen, S. Lukas, G. Witte, *J. Chem. Phys.* 121 (2004) 525.
 - ⁶ S. Lukas, G. Witte, Ch. Woll, *Phys. Rev. Lett.* 88 (2002) 028301.
 - ⁷ S. Lukas, S. Söhnchen, G. Witte, Ch. Woll, *ChemPhysChem.* 5 (2004) 266.
 - ⁸ Ph. Guaino, D. Carty, G. Hughes, O. McDonald, A. A. Cafolla, *Appl. Phys. Lett.* 85 (2004) 2777.
 - ⁹ Q. Chen, A. J. McDowall, N. V. Richardson. *Langmuir* 19 (2003) 10164.

-
- ¹⁰ Y. L. Wang, W. Ji, D. X. Shi, S. X. Du, C. Seidel, Y. G. Ma, H. J. Gao, L. F. Chi and H. Fuchs, *Phys. Rev. B.* 69 (2004) 075408.
- ¹¹ J. H. Kang and X. Y. Zhu, *Appl. Phys. Lett.* 82 (2003) 3248.
- ¹² P. G. Schroeder, C. B. France, J. B. Park and B. A. Parkinson. *J. Appl. Phys.* 91 (2002) 3010.
- ¹³ J. Cornil, J. Ph. Calbert, J. L. Bredas, *J. Am. Chem. Soc.* 123 (2001) 1250.
- ¹⁴ R. G. Endres, C. Y. Fong, L. H. Yang, G. Witte, Ch. Woll, *Comp. Mat. Sci.* 29 (2004) 362.
- ¹⁵ J. E. Northrup, M. L. Tiago and S. G. Louie, *Phys. Rev. B.* 66 (2002) 121404.
- ¹⁶ G. Hill, A. J. Makinen and Z. H. Kafafi, *J. App. Phys* 88 (2000) 889.
- ¹⁷ G. Koller, R. I. R. Blyth, S. A. Sardar, F. P. Netzer and M. G. Ramsey. *App. Phys. Lett* 76 (2000) 927.
- ¹⁸ N. J. Watkins, Li Yan and Yongli Gao. *App. Phys. Lett.* 80 (2002) 4384.
- ¹⁹ J. Ghijssen, R. L. Johnson, A. Elschner and N. Koch. *J. Alloys Compd.* 382 (2004) 179.
- ²⁰ R. T. Tung, *Phys Rev. Lett.* 84 (2000) 6078.
- ²¹ G. Witte, S. Lukas, P. Bagus, Ch. Wöll, *Appl. Phys. Lett.* 87 (2005) 263502.
- ²² The mean free paths were calculated by using the Tanuma, Powell and Penn formula in the program electron inelastic-mean-free-path v.1.1 provided by the National Institute of Standards and Technology, NIST.
- ²³ N. O. Lipari, C. B. Duke, *J. Chem. Phys.* 63 (1975) 1768.
- ²⁴ P. A. Clark, F. Brogli, E. Heilbronner, *Helv. Chim. Acta.* 55 (1972) 1415.
- ²⁵ Hiroyuki Ozaki, *J. Chem. Phys.* 113 (2000) 6361.
- ²⁶ Hyperchem (TM) Professional 7.0, Hypercube Inc., 1115 NW 4th Street, Gainesville, Florida 32601, USA.
- ²⁷ N. V. Richardson, D. R. Lloyd and C. M. Quinn. *J. Electron. Spectrosc. Relat. Phenom.* 15 (1979) 177.
- ²⁸ N. Koch, J. Ghijssen, R. L. Johnson, J. Schwartz, J. J. Pireaux and A. Kahn. *J. Phys. Chem. B.* 106 (2002) 4192.

Chapter 5 Pentacene on Au(100)

5.1 Introduction

The study of new systems is an essential part in the development of a full understanding of all the effects that influence the interaction between organic molecules and various substrates. Naturally, the elemental composition of the substrate plays a large role in the organic-substrate interaction, however the surface topography is also likely to play a significant role. The study of organic molecules deposited on different crystallographic faces of a single crystal metal can give an insight into the effect of surface topography on the growth and ordering of deposited thin organic films.

The growth and orientation of the overlayer molecular thin films depends primarily on the subtle competition between the intermolecular and molecular-substrate interactions, primarily those occurring in the first few monolayers. It has been shown that in many cases, that the intermolecular forces, which determine the relative orientation of the molecules in the bulk crystal, are very different to those experienced by molecules bonded to metal surfaces. The interaction between planar molecules and metal surfaces often leads to a planar or near planar bonding geometry in the initial monolayer^{1, 2, 3, 4, 5, 6, 7, 8} in cases where the molecular bonding geometry in the bulk is non-planar^{9, 10, 11}. For pentacene thin films grown on Cu(110)¹, studies have shown the changeover in molecular orientation within the film from a flat bonded molecular orientation for the initial monolayer to the upright herringbone molecular orientation evident in the molecular crystal^{9, 10, 11}.

There have been numerous studies of pentacene thin films grown on the Au(110)^{4, 12, 13, 14} and Au(111)^{7, 8, 15, 16} substrates using a variety of different techniques, but to date no studies have been carried out of pentacene thin films grown on the Au(100) substrate. These studies suggest a predominantly flat bonded molecular orientation, with a significantly higher degree of ordering observed for monolayer and multilayer pentacene thin films grown on the Au(110) substrate. In this chapter we investigate the growth of pentacene thin films on the Au(100) substrate using synchrotron based PES, NEXAFS techniques in addition to STM and LEED. With the PES study we were able to investigate the electronic interaction between the pentacene and the substrate and measure the magnitude of the interface dipole (ID) formed in addition to investigating the hole injection barrier via the position of the highest occupied molecular orbital (HOMO). NEXAFS studies have been used to investigate the orientation of the pentacene molecules in the thin film and the STM studies allowed the molecular ordering within the film to be investigated. Complimentary LEED studies also allowed an investigation into the ordering of the overlayer pentacene film.

5.2 Experiment

The photoemission experiments were carried out on the SGM1 beamline of the Astrid synchrotron radiation source at the University of Aarhus as described in section 2.1.12. The evaporation of pentacene was carried out in situ, at pressures of 3.0×10^{-9} mbar. Pentacene (purchased from Aldrich Chem. Co.) was evaporated from a resistively heated crucible, maintained at 423K during evaporation. The pentacene was evaporated at normal incidence to the gold surface in a stepwise manner in the preparation chamber, after which the sample was transferred under UHV to the analysis chamber. The sample was cleaned using repeated cycles of Ar bombardment and sample annealing to 673K until the expected sharp ($5 \times n$) LEED pattern for Au(100) was observed and no carbon was visible in the photoemission scans. The sample was heated to 673K by resistive heating of the crystal. The sample temperature was measured using a thermocouple in contact with the crystal. All photoemission scans unless stated were taken at the normal emission sample position shown in section 3.1.3.

The NEXAFS experiments were carried out on the SX-700 beamline of the Astrid synchrotron radiation source at the University of Aarhus as described in section 3.2.2. All NEXAFS measurements were carried out for an energy width of the incident synchrotron radiation of 200meV at the carbon K-edge by using the corresponding exit slit on the monochromator. The NEXAFS data was gathered using a slight variation on the Auger electron yield detection method, by integration of the carbon Auger signal obtained in the 252eV-272eV energy range for a given incident photon energy, after which the photon energy was incrementally changed by 0.1eV, and the process was repeated. The NEXAFS raw data has been normalised using a two-step process. The data was initially divided by the NEXAFS scans taken of the clean Au(100) surface for the corresponding incident angle. A constant was then subtracted so the signal at 280eV incident photon energy was zero. The synchrotron radiation was oriented parallel to the plane of the surface for the s-polarised sample position and was oriented at 70° to the plane of the surface for the p-polarised sample position.

The STM experiments were performed at room temperature using the commercial instrument (Omicron Vakumphysic GmbH) in a UHV system described in section 3.3.6. Electrochemically etched polycrystalline tungsten tips were used. STM images were recorded in constant current mode. The voltage V_s corresponds to the sample bias with respect to the tip. The LEED diffraction patterns were collected with a rear view Omicron SpectraLeed system. All LEED images were recorded at low emission current

to minimise damage to the molecular adsorbate on the sample surface by electron bombardment.

5.3 Photoelectron Emission Spectroscopy Results

5.3.1 Workfunction measurements

The evolution of the workfunction for increasing pentacene coverages is presented in figure 5.1. Since the formation of the interface dipole is predominantly completed with the initial monolayer of adsorbate, extrapolation of the initial linear decrease in the workfunction of the sample to the workfunction of the sample for a thick pentacene coverage allows for the estimation of an approximate monolayer coverage¹⁷. All coverages are subsequently referenced to the deposition time required for the completion of the monolayer coverage. It should be noted that a change in packing density of the pentacene film as a result of molecular reorientation or the onset of significant island growth will cause the actual film thickness in monolayers to deviate from the estimated thickness.

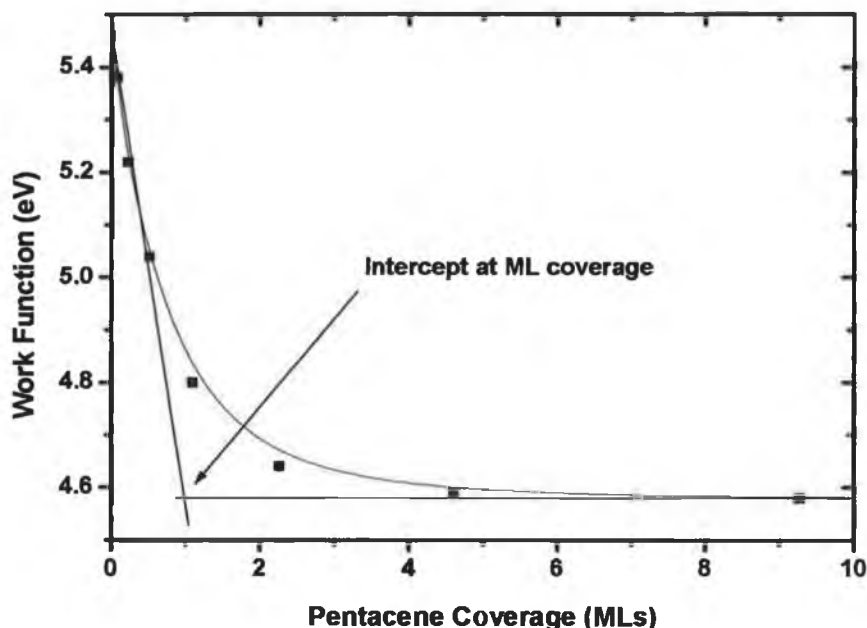


Figure 5.1 Workfunction values with increasing pentacene coverage as calculated from the negatively biased high binding energy cutoff of the valence band.

There are two main effects that result in the interface dipole not being fully formed with the calculated completion of the monolayer coverage. The first is due to the

probable formation of a bilayer prior to the full completion of the monolayer, and a further small contribution is expected due to the second and third monolayers¹⁸. The total interface dipole formed for a thick pentacene film was found to be approximately 0.9eV. This is slightly lower than the calculated interface dipoles formed upon deposition of pentacene on the Au¹⁹, Au(111)⁸ and Au(110)²⁰ substrate, which results in the formation of interface dipoles of magnitude 1.0eV, 0.95eV and 1.21eV respectively.

It is not however compatible with the model proposed by Watkins et al.¹⁹ indicating a linear relationship between the magnitude of the interface dipole formed upon deposition of pentacene on different substrates and the initial workfunction of a given substrate. As discussed in section 4.3.1, the model proposed by Watkins et al is based on the idea that the interface dipole arises primarily due to a chemical bond between the metal and the semiconductor²¹. However, more recent studies by Witte et al²² have shown that the predominant contribution to the observed interface dipole between organic molecules and metal surfaces is a physical repulsion of the surface metal charge by the adsorbate molecular charge, and hence the basis of the model proposed by Watkins is inappropriate.

5.3.2 Au4f_{7/2} core level analysis

Figure 5.2 plots the reduction in the gold substrate signal with increasing overlayer coverage. The inset spectra in figure 5.2 are the normalised scans of the Au4f_{7/2} peak with increasing overlayer coverage. For pure Frank – Van der Merwe growth the substrate signal intensity should drop off exponentially. By taking the natural log of the normalised area of the substrate peak, the growth modes of the overlayer can therefore be examined. A plot of the natural log of the normalised substrate signal, shown in figure 5.3, can be approximated by two straight lines for low and high coverages, which have an intercept point at approximately 3ML. This is indicative of a change in growth mode of the overlayer at a coverage of approximately 3ML, which is apparent from the change in the suppression of the substrate signal at higher coverage. There is also assumed to be an element of island growth involved in the film growth leading to an overall Stranski – Krastanov growth mode for the film. This has been reported for pentacene films grown on other metal substrates¹.

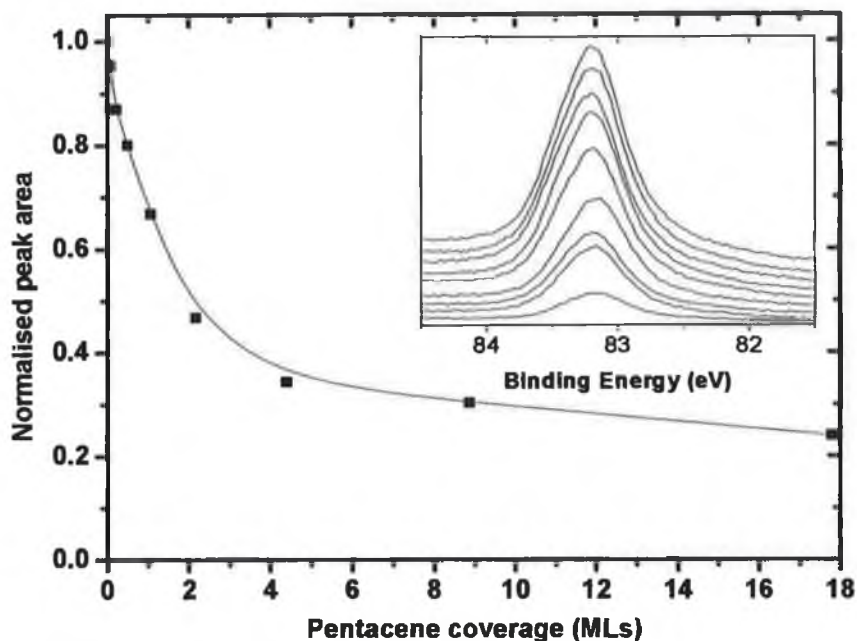


Figure 5.2 Normalised peak area of the $Au4f_{7/2}$ substrate peak ($h\nu = 130\text{eV}$) plotted for increasing pentacene coverage. Inset in the graph are the stacked $Au4f_{7/2}$ peaks with increasing pentacene coverage from top to bottom.

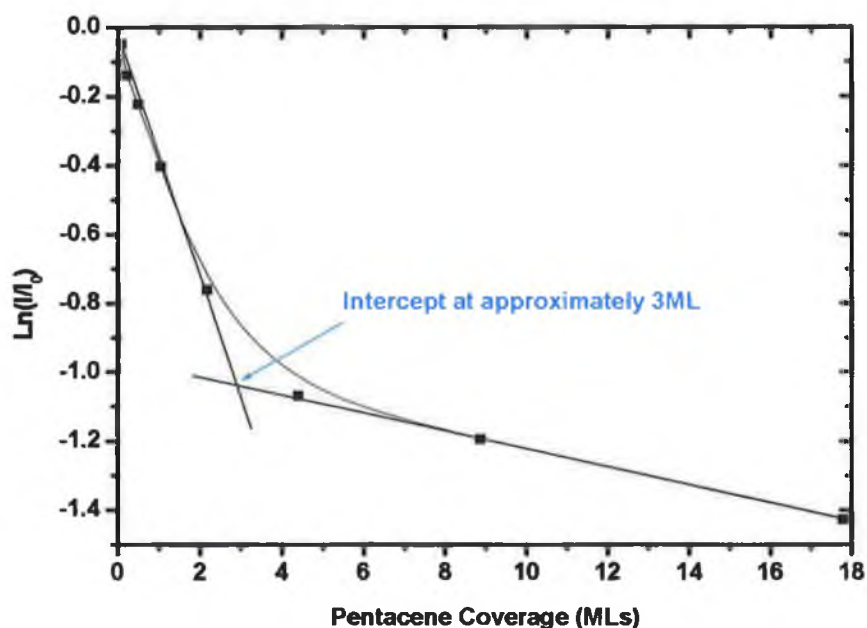


Figure 5.3 Natural log of the normalised $Au4f_{7/2}$ peak area. The plot can be approximated by two straight lines, with an intercept point at approximately 3ML pentacene coverage. The differing slope of the two lines is indicative of a change in overlayer growth.

Using the values for the mean free paths of the Au4f_{7/2} photoelectrons of $\lambda_{\text{Cu3p}}=5\text{\AA}$ ($E_{\text{kin}}=47\text{eV}$) taken from the NIST database²³, the total sampling depth is found to be approximately 15Å. According to general photoemission theory only 5% of the total substrate signal originates from atoms residing outside of the sampling depth for a given photoelectron energy. The monolayer thickness for pentacene bonded in a simple flat molecular orientation is reported to be 1.9Å ML¹. If this monolayer thickness is used to estimate the actual pentacene film thickness for the 18 ML film, it is found to be approximately 33.8Å. Figure 5.2 indicates that the substrate signal for an estimated film thickness of 33.8Å is 24% of the total signal from the clean Au(100). This percentage is far in excess of the sub-5% signal expected for a pentacene thin film of this thickness exhibiting layer-by-layer film growth and so is indicative of Stranski – Krastanov type growth in the overlayer.

5.3.3 C1s core level analysis

It is apparent from the profile of the C1s peak shown in figure 5.4 as a function of coverage, that there is an asymmetry in the lineshape. This asymmetry is most likely due to carbon atoms existing in slightly different chemical environments within each pentacene molecule, due to different bonding interactions with the substrate atoms. The chemisorption of the initial monolayer of pentacene deposited on Cu(110)¹ shown in chapter 4 results in the presence of two distinct components in the C1s spectrum, with a combined FWHM of 1.21eV for a monolayer coverage. The FWHM of the C1s lineshape for the 1.1ML coverage of pentacene shown in figure 5.4 was calculated to be 0.87eV, indicating that the lineshape in this case is a lot more single component in nature. Due to the much smaller FWHM of the C1s peak for pentacene deposited on Au(100), the bond between the pentacene and the substrate is expected to be substantially weaker than the chemisorption exhibited by pentacene bonded to the Cu(110) substrate.

The calculated area of the C1s peak, inset in figure 5.4 plots the increase in the C1s peak area up until a coverage of 8.8ML, after which it decreases slightly despite an increasing overlayer coverage. Using values for the mean free paths of the C1s photoelectrons of $\lambda_{\text{C1s}}=5.2\text{\AA}$ ($E_{\text{kin}}=53\text{eV}$) taken from the NIST database²³, the total sampling depth of the C1s electrons is found to be approximately 16Å. The estimated film thickness of 33.8Å is far in excess of this 16Å sampling depth calculated above. The drop in C1s peak area is most likely an artefact of varying film density at different

film depths coupled with the overlayer thickness exceeding the sampling depth of the C1s electrons. This reduction in the overlayer peak area despite increasing film thickness has also been observed for pentacene deposited on the Cu(110) substrate as shown in section 4.3.2, for an identical experimental setup.

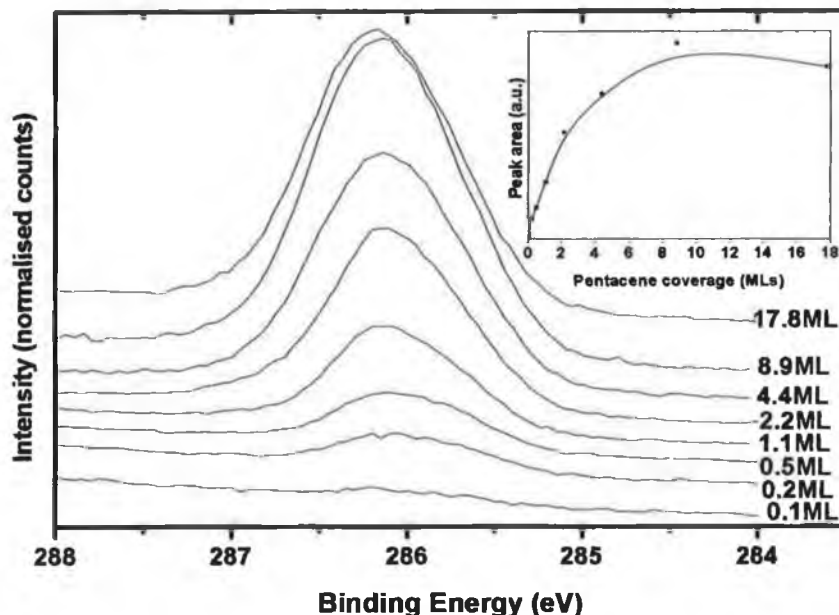


Figure 5.4 C1s core level ($h\nu = 340\text{eV}$) measured during the formation of the pentacene/Au(100) interface. Inset in the diagram is the calculated peak area for increasing pentacene coverage using a linear fitting background.

5.3.4 Valence band and group theory analysis

The valence band spectra at normal emission are shown in figure 5.5. There is little evidence of pentacene related features until the 4.4ML coverage when four well defined molecular orbitals labelled M11, M10, M9 and M8 become evident at 3.2eV, 4.4eV, and 5.0eV binding energy respectively in addition to a number of broader, less well defined features at higher binding energy. Features M11, M10, and M9 are the result of emission from π -derived pentacene molecular orbitals, while M8 and M6 are due to emission from $\pi+\sigma$ hybrid molecular orbitals. The broad features labelled M5 to M1 are due to emission from pure σ -derived molecular orbitals. There are no differences present in the valence band spectra between the 4.4ML and 17.8ML coverages shown in figure 5.6 suggesting that there is little or no change in the film morphology between these two coverages.

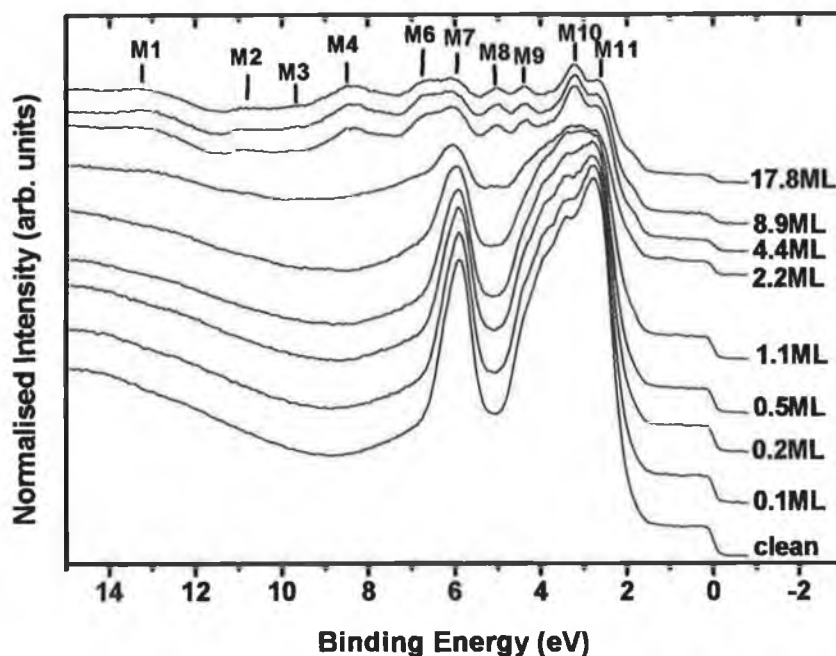


Figure 5.5 Valence band scans ($h\nu = 31\text{eV}$) at normal emission for the stepwise growth of pentacene on Au(100). Molecular orbitals identified for a thick pentacene film are labelled M1 to M11.

The valence band spectra at the s-polarised sample position for different pentacene coverages are presented in figure 5.6. The most obvious difference between the growth of pentacene related valence bands features between the normal emission and the s-polarised sample position is the presence of the HOMO labelled M12, which can be observed centred at approximately 1.0eV binding energy for the 2.2ML coverage in figure 5.6. The HOMO is seen to grow from sub-monolayer coverages and its intensity reaches a maximum for the 2.2ML pentacene coverage. The subsequent coverage of 4.4ML shows a suppression of the HOMO signal. This suppression of the HOMO with the 4.4ML coverage corresponds with the growth of new well defined pentacene related features M11, M10 and M9, in addition to broader pentacene related features M7 to M1 that are also in evidence at high coverages in the normal emission valence band spectra.

As was discussed in chapter 4, the emission from molecular orbitals is a complex process, which is governed by a number of variables. The two main factors that dictate whether a molecular orbital will be visible at a given emission angle, are the process of electron transition from the initial state to a final state, and the emission from the resultant final state. The symmetry of a given molecular orbital coupled with the

symmetry of the incident light vector with respect to the molecule dictates whether a transition from an initial state to a final state is allowed or forbidden. Due to the D_{2h} symmetry of the pentacene molecule, most transitions are allowed, but for molecules with a greater degree of symmetry such as benzene, numerous transitions are forbidden²⁴. The partial wave component of this final state must then be examined in order to predict emission of the electron as a function of angle.

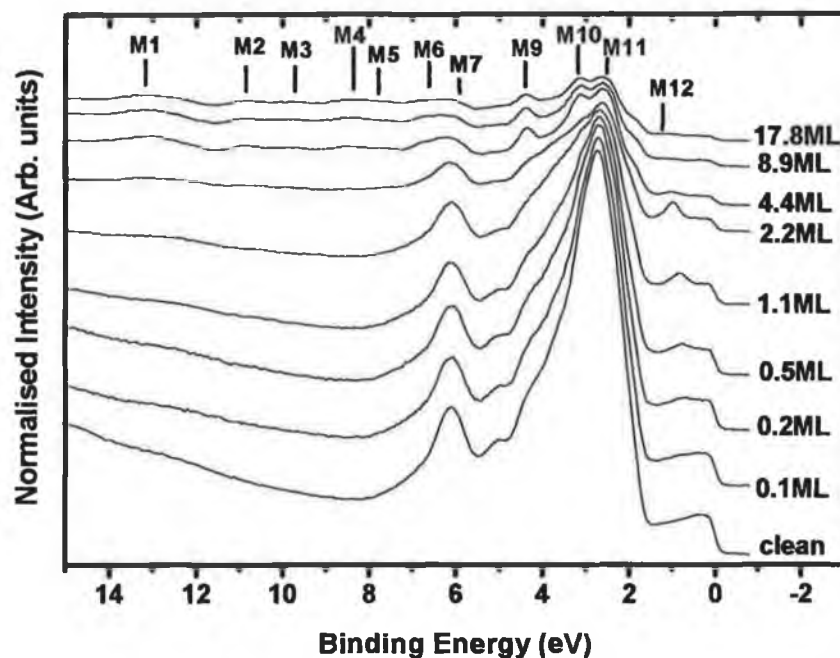


Figure 5.6 Valence band scans ($h\nu = 31\text{eV}$) at the *s*-polarised sample position for the stepwise growth of pentacene on Au(100). Molecular orbitals identified for a thick pentacene film are labelled M1 to M7 and M9 to M12.

A comparison between the valence band spectra for a pentacene coverage of 17.8ML, taken at normal emission and *s*-polarised sample positions, and the gas phase spectrum of pentacene is presented in figure 5.7. It is evident that there is good agreement between the gas phase spectrum and pentacene related features in the $\pi+\sigma$ hybrid and pure σ -region of the valence band spectra. There were however difficulties encountered when trying to attribute valence band features in the π -region of the spectrum to emission from molecular orbitals in the gas-phase spectrum.

Since the HOMO is well energetically separated from the other molecular orbitals in the spectrum, it is good to use this as a starting point for determining which gas phase spectral features result in the features observed in the valence band spectra. The HOMO molecular orbital, π_{11} , shares similar b_{2g} symmetry with the π_8 and π_5

molecular orbitals, and so the emission characteristics of these molecular orbitals should mirror that of the HOMO. The suppression of the HOMO in the s-polarised valence band spectra coincides with the growth of the valence band features M11, M10 and M9. It is therefore evident that these features do not share the molecular symmetry of the HOMO. Since the π_8 and π_5 gas phase molecular orbitals share the same symmetry as the HOMO, it is evident that they cannot correspond to the features M11, M10, M9 and M8, observed in the valence band spectra. Figure 5.7 shows the predicted molecular orbital origin of the features observed in the valence band spectra. The M11 feature has been attributed to π_{10} , the M10 feature to π_9 , the M9 feature to π_6 , and the M8 feature to a $\pi+\sigma$ hybrid band of molecular orbitals.

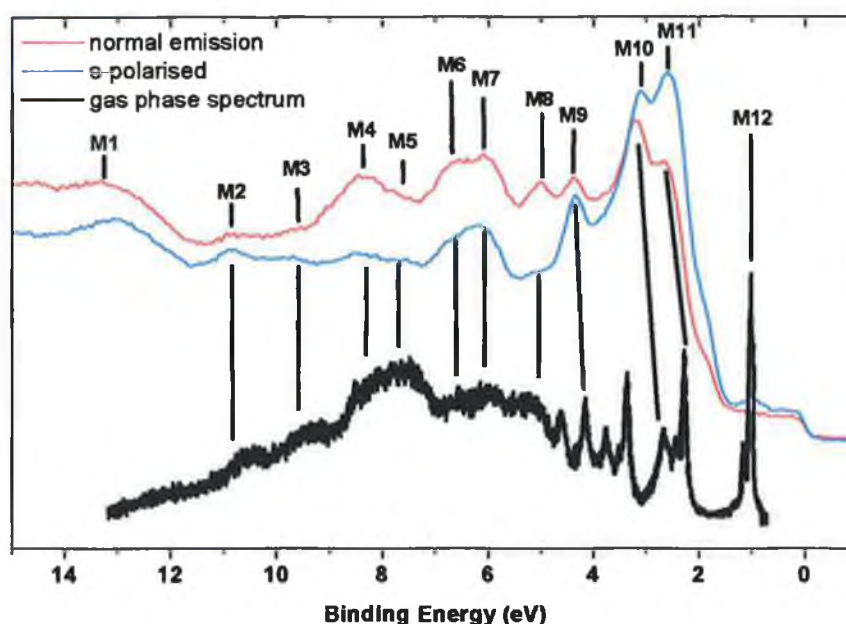


Figure 5.7 Comparison between gas phase spectrum of pentacene from literature and valence band spectra ($h\nu = 31\text{eV}$) of the 17.8ML coverages of pentacene on Au(100) for normal emission and s-polarised sample positions.

The initial sub-3ML valence band spectra will now be analysed using group theory to see if any molecular orientational information can be deduced from the observed molecule derived features in the valence bands.

The NEXAFS data to be presented in section 5.4, and the STM image presented in section 5.5 suggest a predominantly flat bonded molecule at film coverages less than 3ML, and so we will examine the feasibility of this bonding geometry using a group theory derived, selection rules analysis. The formulation of the selection rules for

pentacene on Au(100) follows the same pattern as that presented in section 4.3.4, with the introduction of a slight alteration to the final table.

Due to the quasihexagonal ($5 \times n$) surface reconstruction of the Au(100) substrate exhibiting orthogonal domains, as shown by the LEED data in section 5.5.1, the x-direction and y-direction with respect to the molecule are no longer exclusive. Any given flat bonded molecular orientation resulting in a high degree of light polarised along the x-axis of the molecule in one domain, will result in the same degree of light polarised along the y-axis in the orthogonal domain. Table 4.8, which predicts the observed emission in normal emission for light polarised along the three molecular axes can be therefore simplified to produce table 5.1. In table 5.1 the separate emission predictions for light polarised along the x and y-directions have been replaced by a single "XY" column, which indicates if emission is predicted with light polarised along either the x-axis or the y-axis of the molecule.

Table 5.1 indicates that for a flat bonded molecular orientation emission should be observed in the normal emission valence band for the π_{11} , π_8 , π_7 , and π_5 molecular orbitals. A comparison with the normal emission valence band spectra corresponding to sub-3ML of pentacene however shows virtually no trace of features corresponding to these molecular orbitals in the spectra, except for a very small HOMO derived feature evident in the 2.2ML pentacene coverage.

In contrast, the s-polarised valence band spectrum for the 2.2ML pentacene coverage exhibits a very strong HOMO derived signal at approximately 1.0eV binding energy. It should be noted that there is little evidence in the spectrum of the other molecular orbitals that share the same symmetry properties as the HOMO, despite the fact that emission from these molecular orbitals should exhibit identical behaviour to that of the HOMO. It is not clear why this is the case, as it can be seen using both the D_{2h} and C_{2v} molecular symmetry conditions, that there are a number of other π -derived molecular orbitals that share the same symmetry as the HOMO, and therefore should exhibit similar emission characteristics. Even if the intensity of the emission from the molecular orbitals in the valence band spectra was related to their intensity in the gas-phase spectrum, the π_8 emission should still be sufficiently intense to be observed in the valence band spectrum when the HOMO emission is at its maximum.

Feature	Orbital assignment D_{2h}	Light Vector		Orbital assignment C_{2v}	Light Vector	
		XY ($B_{3u}+B_{2u}$)	Z (B_{1u})		XY (B_1+B_2)	Z (A_1)
π_{11}	$3b_{2g}$	1	-	b_1	1	-
π_{10}	$2a_u$	-	-	a_2	-	-
π_9	$3b_{1g}$	-	-	a_2	-	-
π_8	$2b_{2g}$	1	-	b_1	1	-
π_7	$3b_{3u}$	1	-	b_1	1	-
π_6	$1a_u$	-	-	a_2	-	-
π_5	$1b_{2g}$	1	-	b_1	1	-
a	$2b_{1g}$	-	-	a_2	-	-
	$7b_{3g}$	1	-	b_2	1	-
b	$7b_{1u}$	-	1	a_1	-	1
	$6b_{3g}$	1	-	b_2	1	-
	$2b_{3u}$	1	-	b_1	1	-
c	$1b_{1g}$	-	-	a_2	-	-
	$5b_{3g}$	1	-	b_2	1	-
	$6b_{1u}$	-	1	a_1	-	1
	$5b_{1u}$	-	1	a_1	-	1
	$1b_{3u}$	1	-	b_1	1	-
d	$7a_g$	-	1	a_1	-	1
	$6b_{2u}$	1	-	b_2	1	-
e	$4b_{1u}$	-	1	a_1	-	1
f	$6a_g$	-	1	a_1	-	1
	$5b_{2u}$	1	-	b_2	1	-

Table 5.1 Evaluation of emission from valence band features in normal emission for light polarised along each molecular axis.

For a simple flat bonded molecular orientation the sample orientation has a negligible effect on the components of the light polarised along the x-axis and y-axis of the molecules. If the total intensity of the incident light vector is denoted I, the components along the different molecular axes can be calculated as $I_x=0.53I$, $I_y=0.53I$

and $I_z=0.57I$ for the normal emission sample position, and $I_x=0.65I$, $I_y=0.65I$ and $I_z=0$ for the s-polarised sample position. These intensity values assume that the orthogonal domains present occupy equal surface area on the substrate. Since there is no I_z intensity for the s-polarised sample position, the observation of a strong HOMO signal in the s-polarised sample position, coupled with a weak signal in the normal emission sample position must be the result of the angular emission distribution due to light polarised along the x-axis and y-axis of the molecule.

For the D_{2h} molecular symmetry, the partial wave components of the HOMO are given in table 4.6 as $|10\rangle$, $|30\rangle$, and $|32\rangle_+$ for light polarised along the x-axis of the molecule, and $|32\rangle_-$ for light polarised along the y-axis. For the C_{2v} molecular symmetry, the partial wave components of the HOMO are given in table 4.7 as $|00\rangle$, $|10\rangle$, $|20\rangle$, $|30\rangle$, $|22\rangle_+$, and $|32\rangle_+$ for light polarised along the x-axis of the molecule, and $|22\rangle_-$ and $|32\rangle_-$ for light polarised along the y-axis. While those partial wave components in the form of $|l0\rangle$ should be observed strongest normal to the molecular plane for both molecular symmetries, it is those partial wave components that have a non-zero m number that must be examined in order to investigate why the HOMO derived emission is stronger in the s-polarised valence band spectrum than in the normal emission spectrum.

For D_{2h} molecular symmetry, these partial wave components are $|32\rangle_+$ and $|32\rangle_-$, while for the C_{2v} molecular symmetry, they include the $|22\rangle_+$, $|32\rangle_+$, $|22\rangle_-$, and $|32\rangle_-$ components. The $|22\rangle_+$ and $|22\rangle_-$ components are observed in the plane of the molecule, with emission observed up to medium angles from the molecular plane. Since the emission angle in the s-polarised position is approximately 30° - 35° from the surface normal, a flat bonded molecular orientation should not result in a strong observance of these partial wave components in the s-polarised position. The $|32\rangle_+$ and $|32\rangle_-$ components are not observed either in the plane or normal to the plane of the molecule. They do however exhibit strong emission in an approximate 60° mid-angular range, and so should be strongly observed in the s-polarised sample position for a flat bonded molecule.

While analysis of these non- $|l0\rangle$ partial wave components does allow for an increased HOMO emission observed in the s-polarised position, it still cannot explain the very weak HOMO emission observed at normal emission, where emission from the

$|l0\rangle$ spherical harmonics should be at its strongest. While the selection rules provide us with a framework by which to investigate which molecular orbitals should be visible and at what angles with respect to the plane of the molecule, it is important to note that they provide no information on the relative intensities of the different partial wave components found for each molecular orbital. For example, if the $|32\rangle_+$ and $|32\rangle_-$ partial wave components were found to have a much greater relative intensity with respect to the $|l0\rangle$ components, the observed intensity of the HOMO in the normal emission and s-polarised valence band scans could be accurately explained by the discussion above. However, the assumption that all partial wave components have equal intensity cannot explain why a strong HOMO signal is not observed in the normal emission valence band scan.

It is evident that a more detailed angular resolved study, preferably performed with the use of a movable analyser, or a comprehensive computational study, are needed in order to eliminate the inconsistencies found through the selection rules analysis presented here, and hence to fully investigate the molecular orientation of the pentacene at low coverages. However despite the fact that the selection rules analysis is not conclusive in ascertaining the molecular orientation of the pentacene, valuable information can still be obtained from the valence band studies presented in this chapter.

Since the emission from molecular orbitals is highly directional with respect to the plane of the molecule, the appearance of different molecular orbital peaks with increasing film growth is indicative of a change in orientation of the pentacene molecules in the overlayer film. This change in orientation of the molecules within the film occurs between the 2.2ML and 4.4ML coverages investigated, which is in agreement with the change in overlayer growth mode at approximately 3ML observed from the substrate signal data in figure 5.3.

It should also be noted that there is a 0.3eV shift in the position of the HOMO to higher binding energy between its emergence at a coverage of 0.2ML and its most prominent emission at 2.2ML. This shift in the HOMO position has been previously observed for pentacene deposited on Au²⁵ and has been attributed to polarisation of the molecule by the metal substrate.

Annealing the thick pentacene covered surface to approximately 453K for 10 minutes resulted in the re-emergence of a strong HOMO related signal in the s-polarised spectra. Analysis of substrate and overlayer core level spectra indicated that this

annealing resulted in the desorption of the pentacene multilayers, with an overlayer coverage corresponding to 1-2ML remaining on the gold substrate. This suggests that the molecule-substrate bonding interaction, which dominates at low coverages, is stronger than the intermolecular bonding that dominates in the thick pentacene film.

5.3.5 Molecular energy level diagram

The molecular energy level diagram for the pentacene/Au(100) interface is presented in figure 5.8. The figure indicates the photoemission measured values of the interface dipole formed, Δ (0.88eV of the C₂₂H₁₄ interface), as calculated from the shift in the workfunction indicated in figure 5.1. The hole injection gap was found to be 0.65eV, as calculated from the energy separation between the Fermi level and the low binding energy edge of the HOMO derived peak. This value was found to be slightly larger than the hole injection gap calculated for pentacene deposited on Au¹⁹ (0.5eV) and Au(111)¹⁵ (0.55eV) but smaller than that found for pentacene deposited on Au(110)²⁰ (0.85eV) and Ag¹⁹ (1.1eV). For pentacene deposited on low workfunction metal substrates, the hole injection gap was found to be significantly larger, with calculated values of 1.65eV for pentacene deposited on Ca¹⁹ and 1.8eV for pentacene deposited on Sm²⁶.

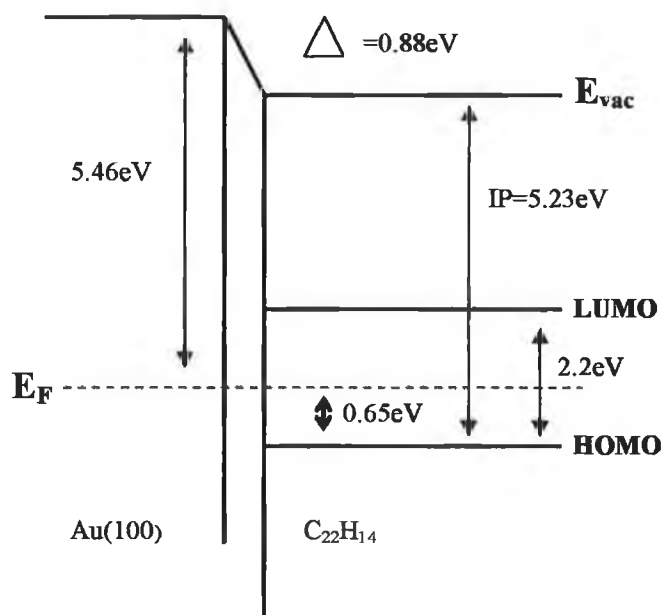


Figure 5.8 Energy level diagram for the pentacene/Au(100) interface.

The lowest unoccupied molecular orbital (LUMO) position has been inferred from the measured charge transport gap²⁶ of 2.2eV found for pentacene. The ionisation potential was calculated to be 5.23eV and is found by addition of the workfunction for the thick pentacene film and the hole injection gap. This value for the calculated ionisation potential is larger than for pentacene deposited on other metal substrates with values of 4.9eV resulting from the deposition of pentacene on Au, Ag and Ca¹⁹, while values of 4.65eV, 5.07eV and 4.8eV were obtained for pentacene deposited on Cu(110)²⁷, Au(111)⁸ and Sm²⁶ respectively.

5.4 NEXAFS results

The NEXAFS data for a 2.1ML coverage of pentacene are shown in figure 5.9 for both the s and p sample positions in addition to a difference spectrum. The 2.1ML coverage corresponds to the first molecular orientation evident in the film from the valence band data discussed in the previous section. High-resolution NEXAFS studies of pentacene on other surfaces^{1, 28} allows for the identification of the π^* derived resonances in the 283eV-288eV region of the spectra and σ^* resonances in the 291eV-300eV region of the spectra. The difference spectrum indicates the prominence of emission in the π^* region of the spectrum at the p-polarised sample position with a prominence of emission in the σ^* region of the spectrum occurring at the s-polarised sample position. In NEXAFS, the probability of population of an unoccupied molecular orbital depends on the cross sectional overlap between the transition dipole moment of the molecular orbital and the plane of polarisation of the incident synchrotron radiation. The transition dipole moment for the π^* resonances in the NEXAFS spectra lies normal to the plane of the molecule²⁹. The prominence of signal from these unoccupied molecular orbitals in the p-polarised NEXAFS data is therefore indicative of a predominantly flat bonded molecular orientation.

The NEXAFS data for a 7.1ML coverage of pentacene is presented in figure 5.10. The 7.1ML coverage corresponds to the second molecular orientation evident in the film at coverages greater than approximately 3ML from the valence band data discussed in the previous section. The overall trend in the s and p spectra is similar to that for the 2.1ML coverage shown in figure 5.9 with the π^* resonance being prominent in the p sample position and the σ^* resonance being prominent in the s sample position. This is again indicative of a predominantly flat bonded molecular orientation with respect to the sample surface.

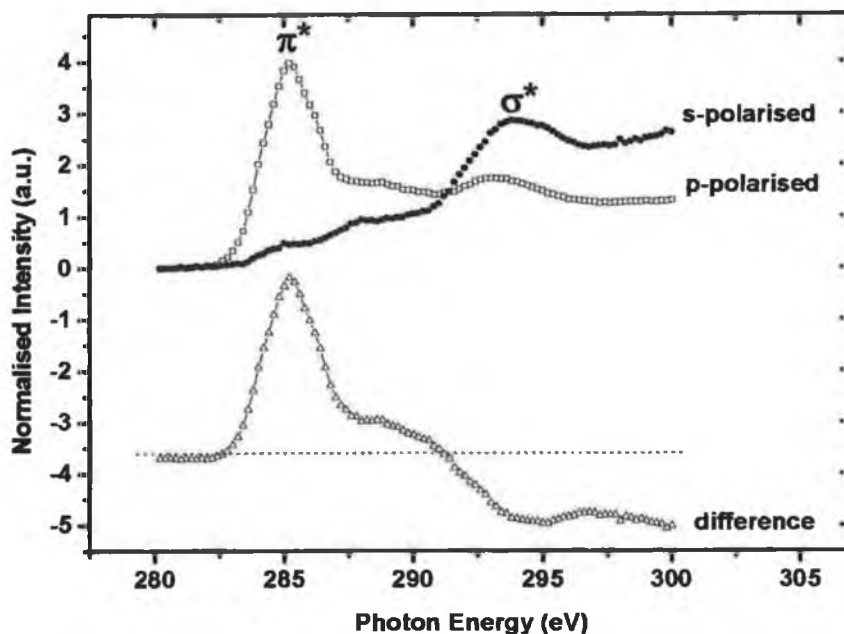


Figure 5.9 NEXAFS spectra for a 2.1 ML coverage of pentacene showing the spectra obtained for s and p sample position in addition to a difference spectrum obtained for p-s.

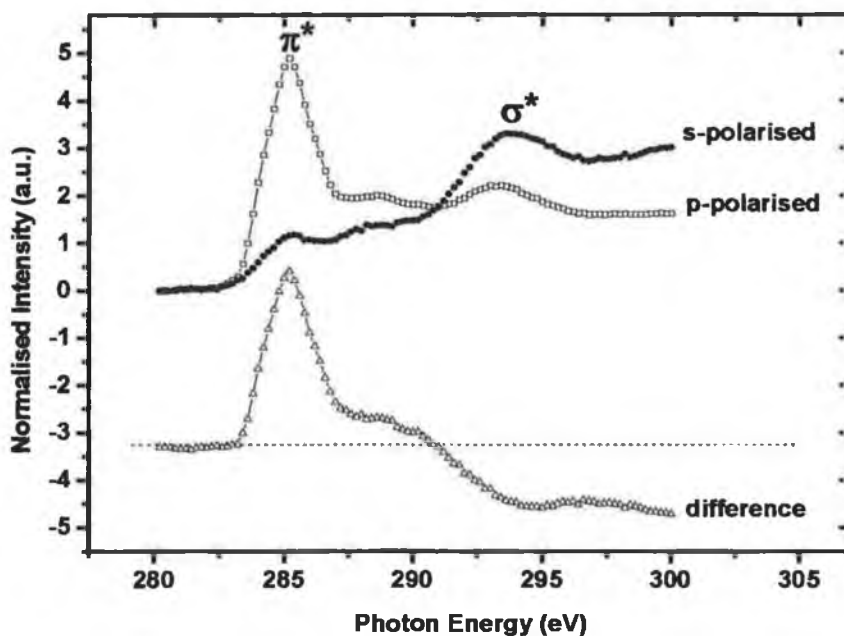


Figure 5.10 NEXAFS spectra for a 7.1 ML coverage of pentacene showing the spectra obtained for s and p sample position in addition to a difference spectrum obtained for p-s.

However, subtle differences in the spectra for the two coverages indicate differences in the molecular orientation at the two coverages investigated here. The greater prominence of the π^* resonance in the s-polarised orientation in figure 5.10 indicates that there is a greater overlap between the E-field of the incident synchrotron radiation and the transition dipole moment for the 7.1ML coverage than for the 2.1ML coverage. This is indicative of a slight tilting of the molecule away from a flat bonding geometry with respect to the sample surface.

In order to further illustrate this point, the orientation of the molecule with respect to the surface was investigated using the models discussed in section 2.3.1. Due to the presence of double domains, oriented at 90° to each other for the Au(100)-(hex) surface reconstruction, equation 2.22 for surfaces exhibiting three fold symmetry or greater was used to simulate the intensity of the π^* molecular orbital with respect to the incident light vector.

The comparison between the experimental and simulated results was carried out in the following manner. It should however be noted that when comparing the simulated and experimentally determined variation in the π^* emission with incident angle, it was found that the minimum in the measured intensity was not found for 90° but for 80° . Since theoretically the minimum should always occur for the E-field of the incident radiation being parallel to the surface plane for molecule tilt angles of less than 45° , it was concluded that the nominal angle 80° was actually the proper 90° position and all plots were adjusted accordingly. This resulted in a shifting of the x-axis in figure 5.11.

- The experimental data at each measured angle was normalised to the maximum intensity obtained for the π^* emission and the data was plotted against the measured angle between the E-field of the synchrotron radiation and the surface normal. It was found that the maximum intensity was observed for the p-polarised sample position i.e. where the angle between the E-field of the incident radiation and the sample normal was found to be 30° after the adjustment of the x-axis by 10° as explained above.
- The varying intensity of the π^* emission with angle was simulated using equation 2.23.
- The simulated spectrum was normalised to the intensity calculated for the 30° angle and the tilt angle was adjusted in a stepwise manner in order to minimise the difference between the simulated spectrum and the experimental data.

Figure 5.11 presents a comparison between the experimentally obtained variation in π^* intensity with angle, and the simulated variation for 3 different tilt angles for the 2.1ML pentacene coverage. By minimisation of the difference between the two, the tilt angle of the pentacene with respect to the surface was calculated to be approximately 21.3° for this coverage. For pentacene deposited on Cu(110)¹, a tilt angle of $27^\circ \pm 5^\circ$ for the initial monolayer of pentacene has been reported. This monolayer however has been shown by STM and helium atom scattering (HAS) analysis to be lying with the molecular plane parallel to the substrate and so an angle of 0° would be theoretically expected for a molecule in such an orientation. The experimentally calculated angle of $27^\circ \pm 5^\circ$ has been attributed to aplanar bending of the molecule due to the interaction between the molecule and the substrate. It is therefore evident that while the calculated tilt angles can be quite precise, there are often external factors other than the orientation of the molecule, which can contribute to this calculated angle. Since these effects are more likely to be located in the interfacial molecular layers, there is a greater error value associated with these angles.

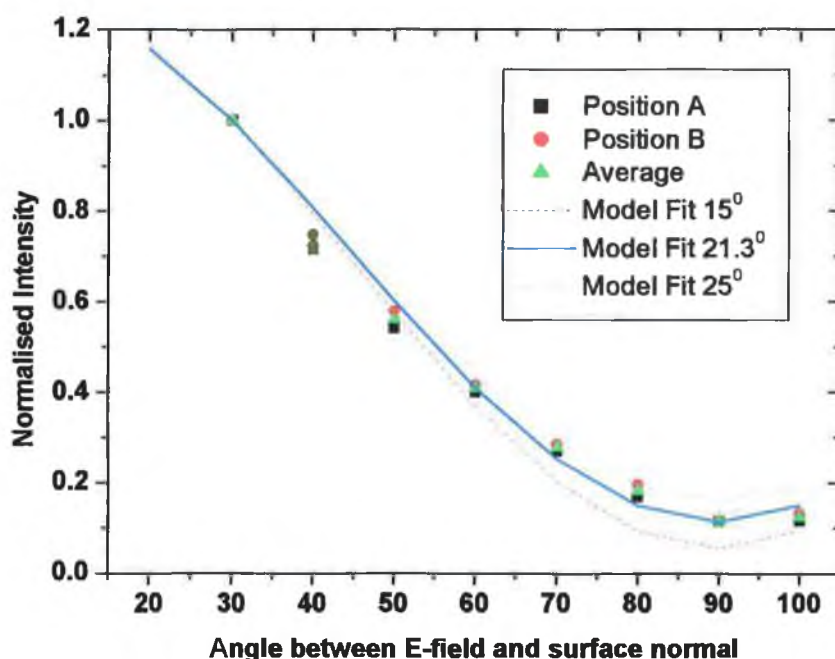


Figure 5.11 Variation in π^* emission intensity with measured angle for the 2.1ML pentacene coverage. The plot shows a comparison between the normalised experimental data and the data simulated using equation 2.23 for tilt angles of 15° , 25° and the best-fit 21.5° .

However the calculated tilt angles can still be helpful as a guideline in examining the orientation of the molecules in molecular films. Figure 5.12 presents the

calculated tilt angle for the pentacene molecule from the NEXAFS data taken at different coverages. This plot illustrates the increasing molecular tilt observed for increasing pentacene film thicknesses with an increase from an average of 18.9° to 29.2° observed between the sub 3ML coverages and thicker pentacene layers. It should be noted that the 12.7ML coverage value was calculated using only the 30° and 100° values shown in figure 5.11 and so is likely to have a much greater error value associated with it that with the other coverages examined.

In the initial two phases of pentacene orientation examined by Söhnchen et al¹ for pentacene on Cu(110) shown in figure 4.1, the calculated tilt angle in going from a planar molecular orientation to a tilted molecular orientation was found to increase from $27^\circ \pm 5^\circ$ to $28^\circ \pm 5^\circ$. It is likely that the aplanar distortions observed for pentacene deposited on Cu(110) are greatly reduced for pentacene deposited on Au(100) due to the reduced molecule-substrate interaction. Indeed ab initio³⁰ studies of pentacene deposited on the unreconstructed (1×1) substrate, show aplanar bending of the C-H bonds of 12.7° , and 7.4° respectively for the centre and end bonds.

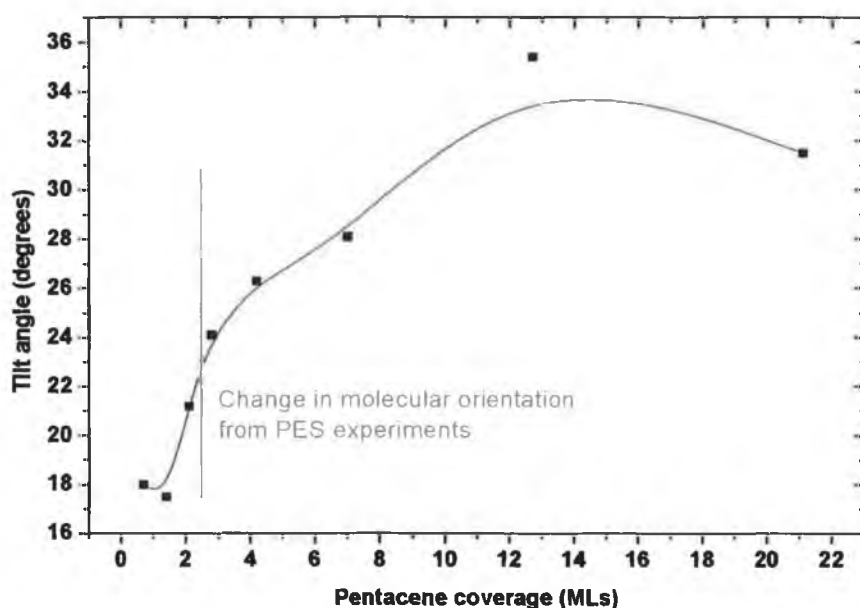


Figure 5.12 Molecular tilt angle as calculated from the NEXAFS spectra obtained at different pentacene coverages.

Since these aplanar distortions are most likely to be surface localised, they result in an increased calculated tilt angle at low pentacene coverages. However, at higher pentacene coverages, the weak intermolecular bonding is unlikely to induce molecular distortions, and so the calculated angles at high coverages are more likely to be an

accurate reflection on the tilt angle of the molecule. The increase in the molecular tilt angle shown in figure 5.12 is therefore likely to represent a significant change in the molecular orientation of the pentacene, and would support similar evidence of a change in molecular orientation presented by the valence band studies discussed in section 5.3.4.

5.5 STM and LEED

5.5.1 Clean Au(100)-(hex)

Figure 5.13 presents an STM image of the clean Au(100)-(hex) substrate exhibiting the surface reconstruction that is commonly denoted as $(5\times 20)^{31}$, but has also been reported in the literature as $(1\times 5)^{32, 33}$, $(5\times 26)^{34}$ and $c(26\times 68)^{35}$. The interatomic spacing along the rows has been found to be approximately $2.82\text{\AA} \pm 0.15\text{\AA}$, taken by averaging over multiple scan windows, which corresponds closely to the predicted in plane spacing given as, $a_p = 4.08/\sqrt{2} = 2.884\text{\AA}$. The most accepted model for the reconstruction assumes that the topmost atomic layer takes an incommensurate, slightly rotated, hexagonal close packed arrangement over the square net of the bulk-terminated substrate³⁴. Similar surface reconstructions have been observed on the (100) surfaces of Pt and Ir, with the origin of the reconstructions attributed to the tendency of the topmost layer to achieve a more compact arrangement³⁶. The unusual reconstruction is specific to these metals, and not the iso-electronic FCC 4d metals, due to the loosely bound electrons of the 5d shell³⁶, which results in a tightly bound 6s shell. Ab-initio calculations³³ have shown that the unreconstructed (1×1) surface presents a d-charge depletion at the first surface layer, assisted and enhanced by hybridisation with the sp orbitals, which results in a relatively high tensile stress. Consequently, the surface would prefer a smaller in-plane lattice constant and a higher in-plane atomic density. The reconstructed surface is found to contain approximately 25% more atoms than a square plane in the bulk. The surface reconstruction is only found in Au, Pt and Ir, because it is only in these metals that the energy gain associated with the increase in surface density is enough to overcome the energy cost of bond rearrangement.

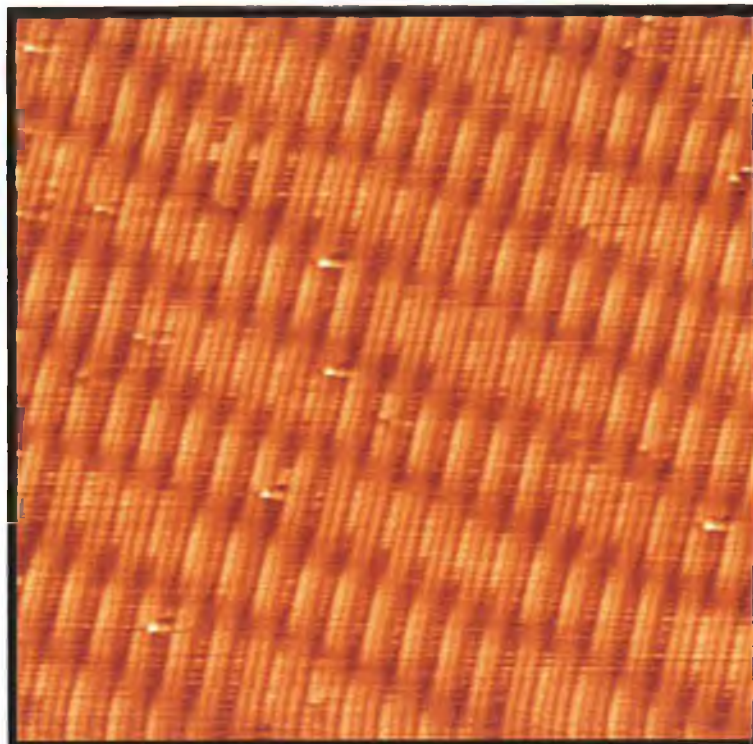


Figure 5.13 STM image of the clean Au(100)-(hex) substrate showing the unusual undulating surface reconstruction. Image parameters: Size = $30 \times 30 \text{nm}^2$, $V_{\text{sample}} = -0.06 \text{V}$, $I_t = 0.8 \text{nA}$.

From figure 5.13, it is evident that there is a distinct corrugation running both along and across the gold rows. A high-resolution image of the gold reconstruction is presented in figure 5.14 (a), showing the distinct (1×5) corrugation is visible across the gold rows, running almost parallel to the $[011]$ direction of the crystal. The quasi-one-dimensional aspect of the reconstruction is the result of Moire fringes coming from the interference between the square substrate and the hexagonal overlayer. A line profile of the $5 \times$ direction is presented in figure 5.14 (b), with a calculated periodicity of $14.82 \text{\AA} \pm 0.37 \text{\AA}$. The undulation in the $5 \times$ direction is due to the packing of six atoms from the hexagonal reconstruction onto five atoms of the underlying square lattice. The resultant ratio of the corrugation across the gold rows to the measured interatomic spacing along the gold rows is therefore calculated as $= 5.25$, and not 5, as expected. This discrepancy is most likely due to different degrees of surface reconstruction compaction along the different crystal directions.

The undulation along the gold rows was found to have a periodicity of $78.61 \text{\AA} \pm 3.07 \text{\AA}$. The ratio of the periodicity along the rows to the interatomic spacing along the rows was found to be ≈ 28 . This differs significantly from the expected value of 20, despite the LEED pattern of the clean substrate, presented in figure 5.15, showing the LEED pattern commonly referred to in literature as $(5 \times 20)^{31}$. A ratio of approximately

5:26 is obtained for the corrugations across and along the gold rows, which is in agreement with previous studies, which found a (5×26) reconstruction on the basis of STM results³⁴. Early STM studies of the surface by Binnig et al³⁷ showed that the n in the observed $(5 \times n)$ reconstruction of the Au(100) surface is sensitive to defect concentration and stresses in the surface.

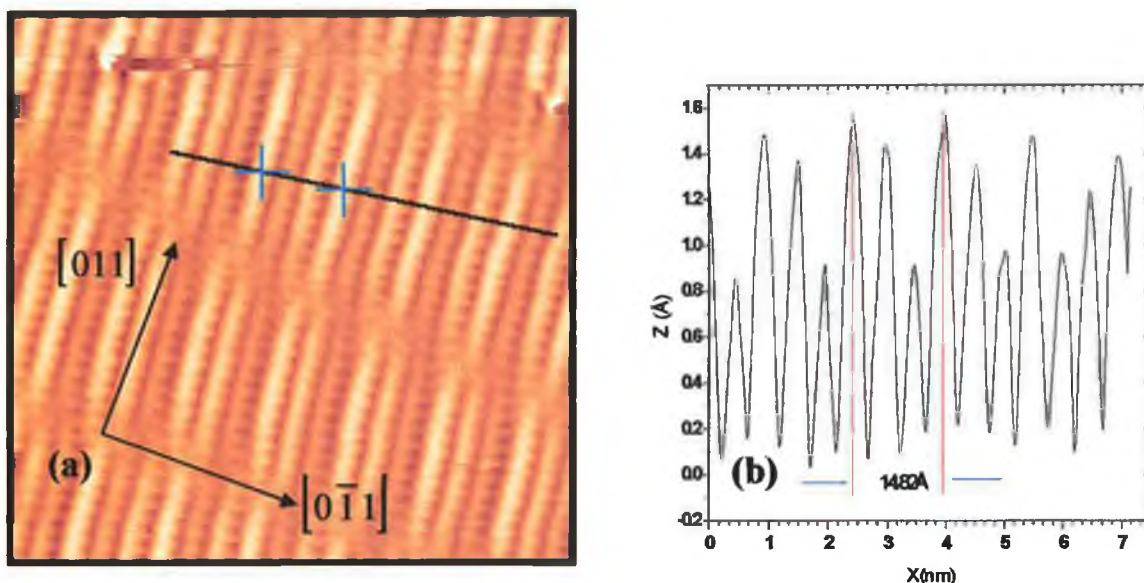


Figure 5.14 (a) Atomic resolution STM image of the hexagonal surface reconstruction of the Au(100) substrate and (b) line profile of single scan in (a) showing row separation of $14.8 \text{ \AA} \pm 0.4 \text{ \AA}$. Image parameters: Size = $10 \times 10 \text{ nm}^2$, $V_{\text{sample}} = 0.07 \text{ V}$, $I_t = 0.8 \text{ nA}$.

A closer inspection of figure 5.14 (a) reveals that the direction of the dislocation along successive gold rows is not perpendicular to the direction of the rows. An angle of $96.5^\circ \pm 1^\circ$ was found between the direction of the rows and the direction of the dislocation along successive rows.

Figure 5.15 (a) shows a LEED image of the clean Au(100)- $(5 \times n)$ substrate. The presence of domains at 90° to each other is evident from the horizontal and vertical rows of spots in the LEED pattern. Figure 5.15 (b) shows a simulated LEEDpat³⁸ image of a (5×26) surface reconstruction, exhibiting domains at 90° to each other. There is good agreement between the observed LEED pattern for the clean Au(100) substrate, and the simulated (5×26) LEED pattern, indicating an n value of 26 for the $(5 \times n)$ surface reconstruction observed for the Au(100) crystal face, as was found with previous STM experiments. Additional spot splitting in the $26 \times$ direction in figure 5.15 (a) indicates the presence of steps on the clean substrate.

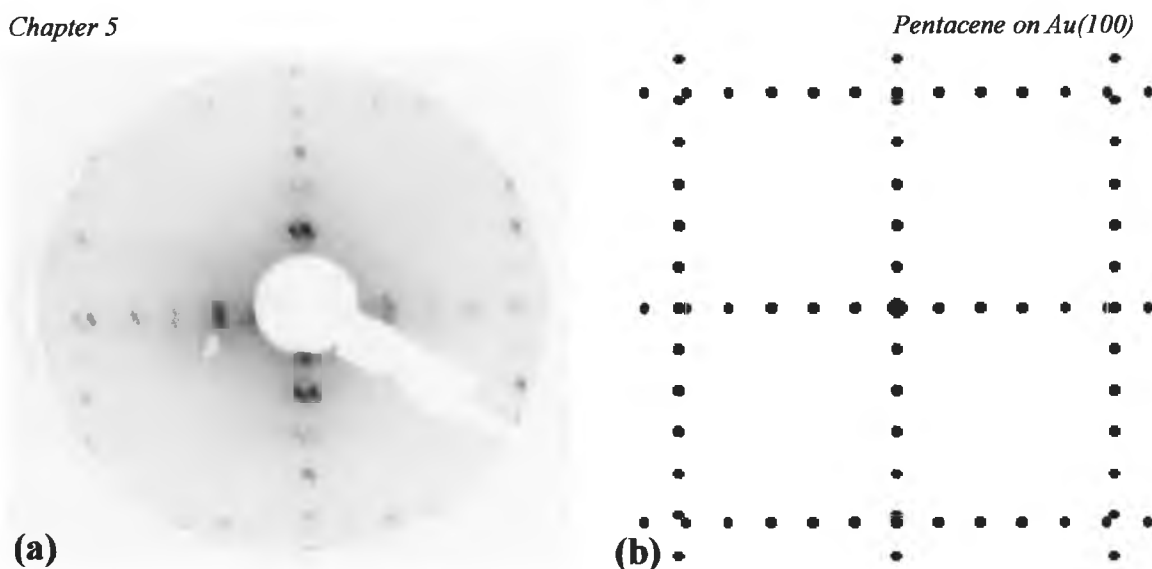


Figure 5.15 (a) LEED image of the clean Au(100) substrate taken at 45eV, exhibiting the quasi-hexagonal (5×26) surface reconstruction, in addition to the presence of orthogonally oriented domains. (b) Simulated LEEDpat³⁸ image of the (5×26) surface reconstruction.

5.5.2 Pentacene on Au(100)

Scanning tunnelling microscopy was used to investigate the extent of molecular ordering present for pentacene molecules deposited on the Au(100) substrate. Figure 5.16 shows an STM image of an approximate monolayer coverage of pentacene deposited at room temperature. The pentacene molecules appear to form long rows in which they align themselves side by side. The direction of these rows is seen to curve under the influence of step edges on the gold substrate or to bend around defects or terminated rows of pentacene. Similar behaviour has been observed for pentacene deposited on Au(111)^{7, 8}. As well as the presence of areas such as in figure 5.16, where many differently oriented pentacene chains coexist, other areas further from step edges were imaged which exhibit a predominant row direction. Preliminary LEED patterns obtained from these pentacene coverages suggest the prominence of a particular row orientation on the substrate.

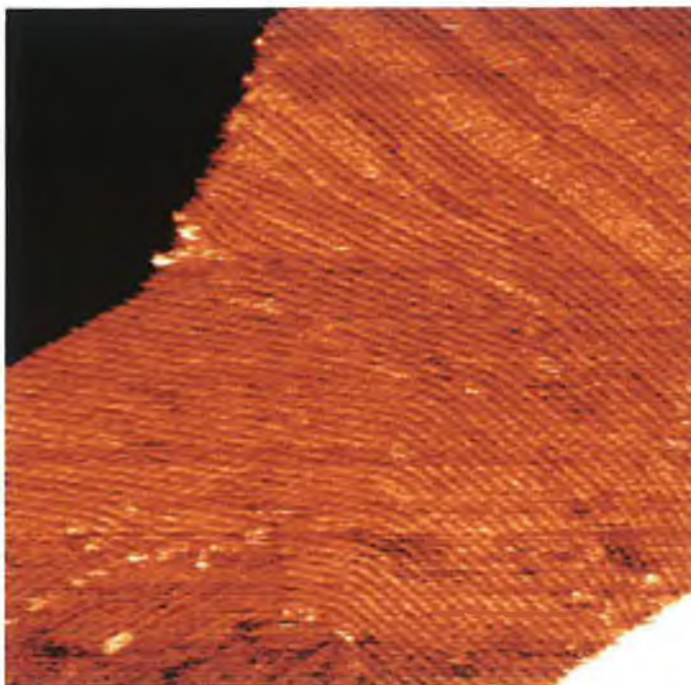


Figure 5.16 STM image of an approximate ML coverage of pentacene on Au(100). The presence of long chains of pentacene molecules can be seen in the image. The dark and light patches in the top left and bottom right corners are due to pentacene on lower and higher Au(100) steps respectively. The height of the upper step has been normalised out of the image in order for better observation of pentacene formations on the central step. Image parameters: Size = $100 \times 100 \text{ nm}^2$, $V_{\text{sample}} = 0.5 \text{ V}$, $I_t = 0.15 \text{ nA}$.

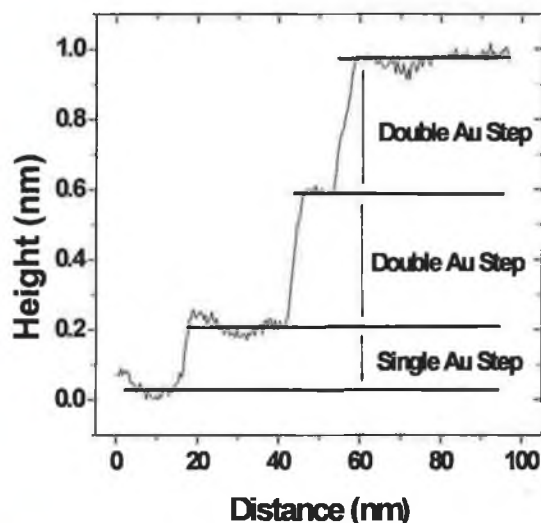
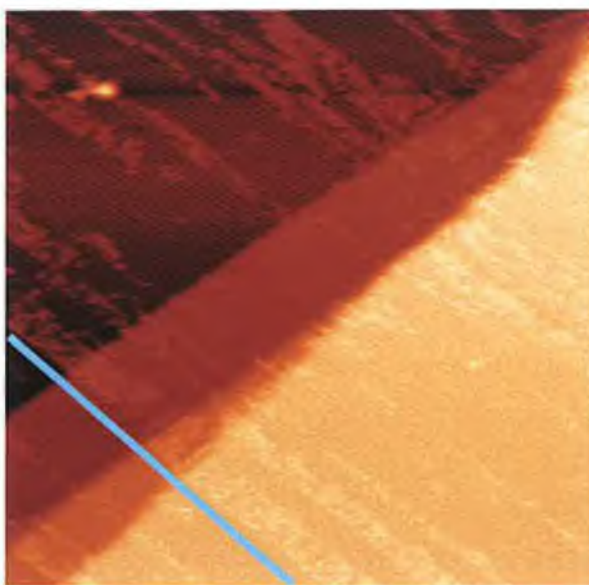


Figure 5.17 (a) STM image of linear rows of pentacene formed across several Au(100) substrate steps. The coverage corresponds to approximately 2ML of pentacene deposited on the substrate at room temperature, with a subsequent annealing of the substrate to 323K for 10 minutes. **(b)** Line profile of Au(100) atomic steps in figure 5.17(a). Image parameters: Size = $150 \times 150 \text{ nm}^2$, $V_{\text{sample}} = 1.2 \text{ V}$, $I_t = 0.4 \text{ nA}$.

Figure 5.17(a) shows an STM image of a large area of pentacene covered Au(100) with the presence of several Au terraces visible. The surface was prepared by the deposition of approximately 2ML of pentacene at room temperature followed by the subsequent annealing of the substrate to 373 ± 20 K. Annealing at this temperature was found to reduce the presence of excess molecules on the surface of the layer, which hindered the acquisition of high-resolution images. The lack of definition on certain sections of the image is attributed to residual excess molecules remaining after the annealing process. The pentacene molecules can be seen to form well-ordered rows across the substrate terraces running from the bottom right to the top left of the image. Despite the presence of several Au(100) step edges, which have been previously observed to influence the directions of the molecular rows in figure 5.16, figure 5.17(a) indicates the presence of a single molecular row direction. The pentacene rows are uniformly spaced with a calculated row spacing of $15.45 \text{ \AA} \pm 0.77 \text{ \AA}$.

There is evidently a high degree of ordering in the film after the anneal, as indicated by the unidirectional pentacene rows over such a large-scale image and across step edges. Indeed the degree of ordering seems to be substantially improved over that of multilayers of pentacene deposited on Au(111)⁷. Annealing of the multilayers in the case of pentacene deposited on Au(111) was observed to improve the ordering of the pentacene film, with single crystal domains ranging from a few nanometres to a few tens of nanometres in evidence. The degree of ordering present in the molecular film shown in figure 5.17 however, is far in excess of single crystal domains of a few tens of nanometres. Such a high degree of ordering of annealed multilayer pentacene films has previously been observed in pentacene films grown on Au(110)⁴, while a high degree of ordering for a monolayer of pentacene has also been achieved with the annealing of a monolayer of pentacene deposited on Cu(110)². A line profile of the step edges shown in figure 5.17(b) indicates a single gold step followed by two double steps going from the lowest to the highest areas on the image. This results in a calculated Au(100) step height of $1.84 \pm 0.14 \text{ \AA}$.

A high-resolution image of the pentacene rows present on the highest Au(100) step from Figure 5.17(a) is shown in figure 5.18, indicating the orientation of the molecules within the individual rows. The pentacene molecules are drawn to scale in the image. The black lines labelled A and B have been used to represent the unit cell lengths along and across the rows respectively. The molecules are thought to lie predominantly flat on the surface at these low coverages as evidenced from the corresponding NEXAFS data for low coverages, which resulted in a calculated tilt angle

of 18.9° at low pentacene coverages. The length of A and B have been calculated as $7.39\text{\AA} \pm 0.4\text{\AA}$ and $15.47\text{\AA} \pm 0.77\text{\AA}$ respectively, with a resultant angle between A and B of $85.5 \pm 2.5^\circ$.

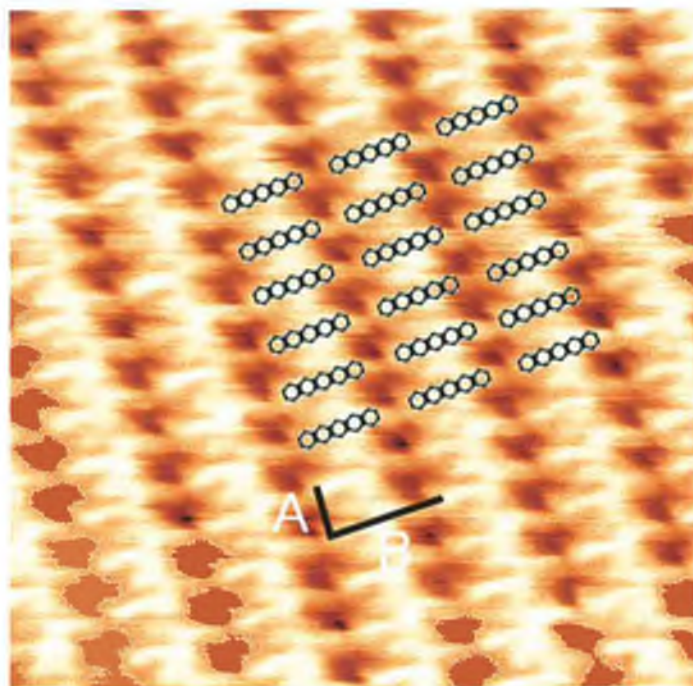


Figure 5.18 High resolution STM image of pentacene molecular lines indicating flat lying pentacene molecules. Values for the unit cell parameters have been calculated from multiple images to be $A = 7.39\text{\AA}$ and $B = 15.47\text{\AA}$ with the resultant angle between A and B = 85.5° . Image parameters: Size = $10 \times 10\text{nm}^2$, $V_{\text{sample}} = 1.2\text{V}$, $I_t = 0.4\text{nA}$.

The molecular packing density was calculated to be approximately 0.88×10^{12} molecules/cm². This falls within the range of values obtained for pentacene deposited on various substrates, with values of 1.19×10^{12} and 1.21×10^{12} molecules/cm² calculated for two close-packed pentacene reconstructions on Au(111)⁸, and values of 0.34×10^{12} and 0.96×10^{12} molecules/cm² obtained for two reconstructions of pentacene on the Ag/Si(111)- $(\sqrt{3} \times \sqrt{3})R30^\circ$ substrate³⁹.

Figure 5.19 shows the LEED patterns obtained for the annealed and unannealed pentacene films on Au(100). Figure 5.19 (a) corresponds to the STM image of the monolayer coverage of pentacene presented in figure 5.16, and figure 5.19(b) corresponds to the STM of the annealed 2ML coverage presented in figure 5.17(a) and figure 5.18. It is evident from the images that identical spots are present in both patterns, indicative of an identical molecular arrangement in both cases. The presence of LEED spots is also an indication of a high degree of ordering in the pentacene films in both cases with a predominant molecular row direction in evidence. No LEED images

were obtainable for either the annealed or unannealed pentacene film above an energy of 25eV.

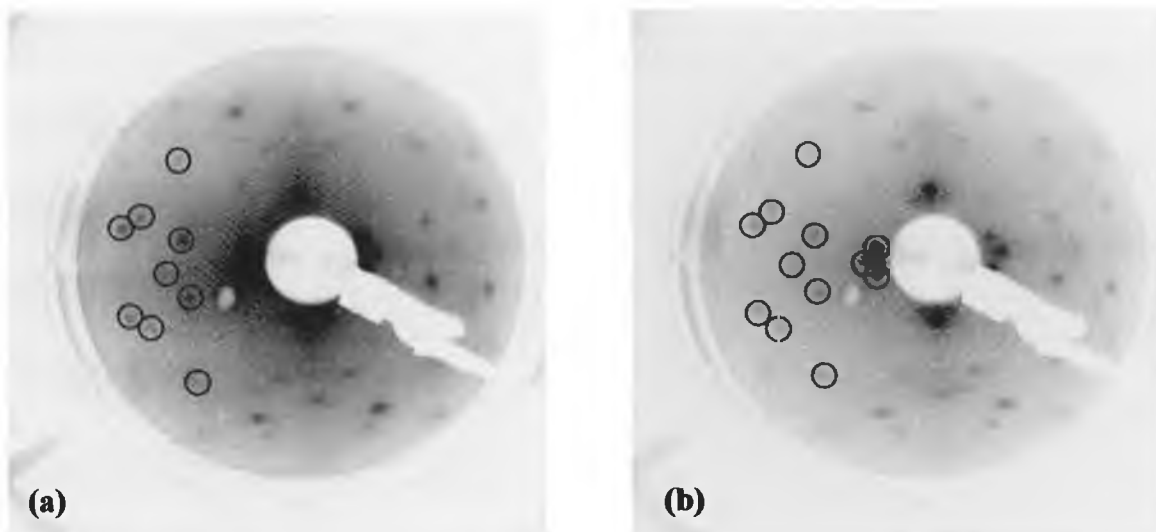


Figure 5.19 LEED images of (a) unannealed pentacene on Au(100)-(hex) taken at 14.7eV (b) annealed pentacene film corresponding to STM images of straight pentacene rows taken at 15.3eV. The spots in one quadrant of each LEED image have been circled for easier identification.

The STM images presented in this section correspond to the sub 3-4ML orientation of pentacene molecules on the substrate. Images of higher coverages of pentacene exhibiting a more tilted bonding geometry with respect to the surface have not been obtained using STM due to loose molecules on the surface making it difficult to image.

It is not evident from the STM or LEED images whether the adsorption of the pentacene on the Au(100) substrate results in a lifting of the hexagonal ($5 \times n$) surface reconstruction. No low coverage STM images showing the molecule and the underlying substrate were obtainable and no LEED images were obtainable above 25eV, making comparison between the LEED of the clean substrate and the adsorbate covered substrate difficult.

The adsorption of copper phthalocyanine⁴⁰, and zinc octaethylporphyrin⁴¹ on Au(100) result in a weak adsorbate-substrate interaction that leaves the surface reconstruction intact. In the case of zinc octaethylporphyrin⁴¹, the molecule has been observed to form different adsorption patterns on the hexagonal ($5 \times n$) surface reconstruction, and on the (1×1) unreconstructed surface. In contrast, strong adsorbate-substrate interactions, as in the case of iodine⁴² and NO⁴³, result in the observed lifting of the hexagonal ($5 \times n$) surface reconstruction.

Ab initio studies³⁰ of pentacene on the unreconstructed (1×1) surface show the molecule adsorbed with its long axis aligned along the [011] axis, centred on an Au bridge site. The study found an optimised unit cell of 6.25Å × 15.30Å for a molecule fixed in a flat bonded geometry, with an angle of 70° between the two cell dimensions. This differs significantly from the experimentally obtained unit cell of 7.39Å × 15.47Å, with an angle of 85.5° between the unit cell vectors. A comparison between the experimentally obtained pentacene unit cell, and both the STM images of the hexagonal (5×n) surface reconstruction, and a model of the unreconstructed (1×1) surface, indicates that the unit cell is not commensurate with either the reconstructed or unreconstructed substrate. However, because the interaction between the pentacene and the Au(100) has been shown to be physisorption in nature, it is likely that the hexagonal (5 × n) surface reconstruction has not been lifted by the pentacene adsorption.

5.6 Summary

PES and NEXAFS measurements indicate the presence of two molecular orientations with respect to the substrate at low and high pentacene coverages with the change in molecular orientation occurring at approximately 3ML coverage. The molecules in the initial three monolayers lie flat or nearly flat on the surface with a slight tilting of the plane of the molecule away from the surface occurring at coverages over 3ML. Similar behaviour has been observed for pentacene deposited on Cu(110)^{1, 3, 27} with the initial monolayer lying flat on the substrate followed by a two alternative tilted molecular orientations at higher coverages. Comparison between the FWHM of the C1s lineshape for a monolayer coverage of pentacene deposited on the Au(100) and Cu(110)²⁷ substrates indicates the presence of a weaker bond between the pentacene and the Au(100) substrate than that of pentacene on Cu(110). It is therefore expected that the initial layer of pentacene is physisorbed on the substrate, as is common for organic molecules deposited on metal substrates.

STM images indicate a high degree of ordering in the pentacene overlayer in the low coverages presented here. The pentacene self-assembles into rows where it adopts a side-by-side geometry with respect to its neighbouring molecules. The unit cell parameters were found to be 7.39Å × 15.47Å, with an angle of 85.5° between the unit cell vectors. This resulted in a packing density of 0.88×10¹² molecules/cm². Step edges have been observed to influence the direction of these molecular rows and to cause defects in the film such as terminating rows.

LEED images indicated that there was a high degree of ordering on both the annealed and unannealed films, with identical LEED patterns observed for both films, despite STM images of the unannealed film exhibiting different pentacene row directions. This indicates that there is a predominant molecular row orientation on the surface for both the annealed and unannealed films, with annealing of the sub 3ML coverage found to improve long range ordering of the film with areas $150\text{nm} \times 150\text{nm}$ exhibiting uniform direction of rows even across several substrate step edges.

Chapter 5 References

- ¹ S. Söhnchen, S. Lukas, and G. Witte, *J. Chem. Phys.* 121 (2004) 525.
- ² S. Lukas, G. Witte, and Ch. Woll, *Phys. Rev. Lett.* 88 (2002) 028301.
- ³ S. Lukas, S. Söhnchen, G. Witte, and Ch. Woll, *ChemPhysChem.* 5 (2004) 266.
- ⁴ Ph. Guaino, D. Carty, G. Hughes, O. McDonald, and A. A. Cafolla, *Appl. Phys. Lett.* 85 (2004) 2777.
- ⁵ Q. Chen, A. J. McDowall, and N. V. Richardson. *Langmuir* 19 (2003) 10164.
- ⁶ Y. L. Wang, W. Ji, D. X. Shi, S. X. Du, C. Seidel, Y. G. Ma, H. J. Gao, L. F. Chi, and H. Fuchs, *Phys. Rev. B.* 69 (2004) 075408.
- ⁷ J. H. Kang, and X. Y. Zhu, *Appl. Phys. Lett.* 82 (2003) 3248.
- ⁸ P. G. Schroeder, C. B. France, J. B. Park, and B. A. Parkinson. *J. Appl. Phys.* 91 (2002) 3010.
- ⁹ J. Cornil, J. Ph. Calbert, and J. L. Bredas, *J. Am. Chem. Soc.* 123 (2001) 1250.
- ¹⁰ R. G. Endres, C. Y. Fong, L. H. Yang, G. Witte, and Ch. Woll, *Comp. Mat. Sci.* 29 (2004) 362.
- ¹¹ J. E. Northrup, M. L. Tiago, and S. G. Louie, *Phys. Rev. B.* 66 (2002) 121404.
- ¹² V. Corradini, C. Menozzi, M. Cavallini, F. Biscarini, M. G. Betti, and C. Mariani, *Surf. Sci.* 532-535 (2003) 249.
- ¹³ C. Menozzi, V. Corradini, M. Cavallini, F. Biscarini, M. G. Betti, and C. Mariani, *Thin Solid Films* 428 (2003) 227.
- ¹⁴ F. Evangelista, A. Ruocco, D. Pasca, C. Baldacchini, M. G. Betti, V. Corradini, C. Mariani, *Surf. Sci.* 566-568 (2004) 79.
- ¹⁵ P. G. Schroeder, C. B. France, J. B. Park, and B. A. Parkinson, *J. Phys. Chem. B* 107 (2003) 2253.
- ¹⁶ T. Suzuki, M. Kurahashi, X. Ju, and Y. Yamauchi. *Appl. Phys. Lett.* 83 (2003) 4342.

- ¹⁷ G. Hill, A. J. Makinen, and Z. H. Kafafi, *J. App. Phys* 82 (2000) 889.
- ¹⁸ G. Koller, R. I. R. Blyth, S. A. Sardar, F. P. Netzer, and M. G. Ramsey, *App. Phys. Lett* 76 (2000) 927.
- ¹⁹ N. J. Watkins, L. Yan, and Y. Gao, *App. Phys. Lett*, 80 (2002) 4384.
- ²⁰ Darren Carty, PhD Thesis, *RAS and STM Investigation of Pentacene Molecules on Metal and Semiconductor Surfaces*, 2004.
- ²¹ R. T. Tung, *Phys Rev. Lett.* 84 (2000) 6078.
- ²² G. Witte, S. Lukas, P. Bagus, Ch. Wöll, *Appl. Phys. Lett.* 87 (2005) 263502.
- ²³ The mean free paths were calculated by using the Tanuma, Powell and Penn formula in the program electron inelastic-mean-free-path v.1.1 provided by the National Institute of Standards and Technology, NIST.
- ²⁴ N. V. Richardson, D. R. Lloyd, and C. M. Quinn. *J. Electron. Spectrosc. Relat. Phenom.* 15 (1979) 177.
- ²⁵ F. Amy, C. Chan and A. Kahn. *Org. Electron.* 6 (2005) 85.
- ²⁶ N. Koch, J. Ghijsen, R. L. Johnson, J. Schwartz, J. J. Pireaux and A. Kahn. *J. Phys. Chem. B.* 106 (2002) 4192.
- ²⁷ O. McDonald, A. A. Cafolla, Zheshen Li, and G. Hughes, *Surf. Sci.* 600 (2006) 1909.
- ²⁸ Y. J. Hsu, W. S. Hu, D. H. Wei, Y. S. Wu and Y. T. Tao. *J. Electron. Spectrosc. Relat. Phenom* 114-117 (2005) 401.
- ²⁹ J. Stohr, *NEXAFS Spectroscopy* (Springer, New York, 1992), Vol. 25.
- ³⁰ K. Lee, J. Yu. *Surf. Sci.* (in press)
- ³¹ D. G. Fedak, N. A. Gjostein, *Surf. Sci.* 8 (1967) 77.
- ³² D. G. Fedak, N. A. Gjostein, *Phys. Rev. Lett.* 16 (1966) 171.
- ³³ V. Fiorentini, M. Scheffler, *Phys. Rev. Lett.* 71 (1993) 1051.
- ³⁴ O. S. Hernán, A. L. Vázquez de Parga, J. M. Gallego, R. Miranda, *Surf. Sci.* 415 (1998) 106–121.
- ³⁵ M. van Hove, R. J. Koestner, P. C. Stair, J. P. Biberian, L. L. Kesmodel, I. Bartos, G. A. Somorjai, *Surf. Sci.* 103 (1981) 189.
- ³⁶ N. Takeuchi, C.T. Chan, K.M. Ho, *Phys. Rev. B* 43 (1991) 14363.
- ³⁷ G. Binnig *et al.*, *Surf. Sci.* 144, (1984) 321.
- ³⁸ LEEDpat 2.0, Made by K. Hermann, Abt. Theorie, Fritz-Haber-Institut, Faradayweg 4-6, D-14195 Berlin (Germany), and M. A. Van Hove MS 2-100, Materials Sciences Division, Lawrence Berkeley National Laboratory, Berkeley, CA 94720 (USA).

-
- ³⁹ Ph. Guaino, A. A. Cafolla, D. Carty, G. Sheerin, G. Hughes. *Surf. Sci.* 540 (2003) 107.
- ⁴⁰ K. Y. Park, A. Miller, K. Klier, R. L. Oplia, J. E. Rowe, *Surf. Sci.* 529 (2003) L285.
- ⁴¹ S. Yoshimoto, Y. Honda, Y. Murata, M. Murata, K. Komatsu, O. Ito, K. Itaya, J. *Phys. Chem. B.* 109 (2005) 8547.
- ⁴² J. Valenzuela-Benavides, M. Herrera-Zaldívar, *Surf. Sci.* 592 (2005) 150.
- ⁴³ E. D. L. Rienks, G. P. van Berkel, J. W. Bakker, B. E. Nieuwenhuys, *Surface Science* 571 (2004) 187–193.

Chapter 6 Organic Film Modification

6.1 Introduction

The growth of organic thin films on metals is a very important study area for the development of future organic based semiconductor devices. There are many favourable qualities sought for these organic/metal systems, such as a high level of ordering in the film, specific electron and hole injection characteristics into the conduction and valence bands respectively, and a high level of conductivity in the film. While the conductivity of the film depends primarily on the organic molecule used, an increased level of ordering in the overlayer has been found to improve the conductivity of the film^{1,2}. It is found that the level of ordering present in the film can be very dependent on the substrate material, and also the surface topography present. For example, highly ordered layers of pentacene have been observed for pentacene deposited on Au(110)³, and to a lesser extent for pentacene grown on the Au(100) substrate, as shown in chapter 5. However on the Au(111)⁴ substrate, pentacene multilayers exhibit a significantly reduced degree of ordering over that found on the (110) and (100) crystallographic faces.

Similarly, the specific hole injection characteristics vary depending on both the substrate and the adsorbate molecule, with a wide range of values found for pentacene deposited on polycrystalline Au⁵ (0.5eV), Au(111)⁶ (0.55eV), Au(100)⁷ (0.65eV), Au(110)⁸ (0.85eV), Cu(110)⁹ (0.95eV), Ag⁵ (1.1eV), and Sm¹⁰ (1.8eV). To date there has been no models proposed that accurately predict the hole injection characteristic observed for different pentacene/metal systems.

For experimental purposes, there is obviously great freedom of choice in the different molecules and substrates that may be chosen in order to obtain certain desirable organic film characteristics, such as a high degree of ordering or certain injection characteristics. However, in the fabrication of molecular based semiconductor devices, the choice of substrate or organic molecule might be limited by external parameters, such as cost, safety concerns, or ease of fabrication. It is therefore essential that methods are developed in order to modify the organic film characteristics, for device optimisation.

In this chapter, two different methods were used to investigate the extent to which overlayer film characteristics could be modified. The first method of overlayer modification involved the use of alkali metal doping to investigate modification of the electron and hole injection characteristics of the molecular film.

Metal doping of organic films has also been found to be one of the most effective ways of controlling the properties these films exhibit. The conductivity of

conjugated polymers¹¹ has been found to increase by many orders of magnitude through the use of doping. In addition to this, dopants have also proved useful in controlling the luminescence and improving the stability^{12, 13, 14, 15} of organic light emitting diodes (OLEDs). Doping has also been used to produce more favourable injection characteristics at organic/metal interfaces by modifying the energy level alignment^{16, 17, 18, 19, 20, 21, 22, 23, 24}. However despite these studies, there are many aspects of the doping process that are not fully understood. In the first part of this study, the controlled deposition of sodium (Na) as an electron donor was investigated in order to dope pentacene films grown on the Cu(110) surface. The effect of the degree of ordering in the overlayer on the doping process was also investigated in this section.

The second method of organic/metal system modification was carried out through the use of interlayers in order to alter the interfacial chemistry of the organic/metal system. The effect of interlayers on the formation of the interface dipole and injection characteristics of different organic/metal systems was investigated in this section. This interface engineering was an attempt to modify the suppression of the metal workfunction, which always accompanied the deposition of pentacene. The Cu(110) substrate was terminated with 0.5ML of oxygen, which resulted in a (2×1) surface reconstruction, prior to the deposition of pentacene. In a comparative study, a pentacene thin film was deposited on a sulphur terminated Au(100) substrate.

6.2 Experiment

The PES experiments were carried out on the SGM1 beamline in ASTRID at the University of Aarhus as described in section 3.13. The cleaning procedure for the Cu(110) and Au(100) crystals has previously been described in sections 4.2 and 5.2 respectively. The evaporation of pentacene was carried out *in situ*, at pressures of 4×10^{-9} mbar using the evaporator described in section 3.5.1. A quartz microbalance was previously used to confirm a constant flux of pentacene when the evaporator was maintained at a temperature of 423K. Na was evaporated from a SAES getter source in the preparation chamber, as described in section 3.5.2. Sulphur was evaporated from the homemade evaporator described in section 3.5.3. The secondary electron cutoff was recorded with the sample biased negatively with respect to the electron spectrometer. The energy position of the cutoff and the highest occupied molecular orbital (HOMO) was determined by linear extrapolation to the background. The workfunction was calculated by subtracting the sample bias from the extrapolation of the position of the

secondary electron cutoff. The vacuum level of the surface was found by the addition of the photon energy to the cutoff energy.

6.3 Alkali metal doping of pentacene films

In this section, the alkali metal doping of two pentacene films grown on Cu(110) is presented. The first pentacene film was grown in a stepwise manner, as described in section 4.3, with a resultant film thickness of approximately 16ML. The second pentacene film was grown using an annealed monolayer to template the further growth of the film. A description of the growth of this film is presented in section 4.4. In this case the estimated film thickness was approximately 8ML. It has been shown in section 4.4, that the degree of ordering present in the templated pentacene film is greater than that present in the stepwise grown film. It has also been established that the molecular orientation in both pentacene films is identical. A comparative study of the doping of the two differently prepared pentacene films allowed for an investigation into the effect of ordering in the overlayer on the doping process.

6.3.1 Na doping of untemplated pentacene film on Cu(110)

Figure 6.1 shows the C1s peak with increasing dopant concentration. The C1s peak is predominantly single component for the 16ML pentacene coverage (top spectrum). The peak is observed to shift to higher binding energy with increasing dopant concentration, while the lineshape of the peak remains relatively unchanged up to the 20 minute Na deposition. The shift to higher binding energy is indicative of negative charge transfer from the metal to the organic semiconductor, as would be expected for alkali metal doping. After the 20-minute deposition the peak lineshape becomes noticeably more asymmetric with the introduction of a low binding energy shoulder on the peak, in addition to a further shift in the C1s peak position. It should be noted that the magnitude of the peak shift observed during the first stage of the doping, up to a 20-minute deposition, was found to be approximately 0.5eV. Beyond this coverage, it becomes more difficult to determine the change in peak position due to Fermi level movements as a second chemically shifted component peak is observed for a 40 minute Na deposition. It should be noted that no shift in the substrate related Cu3p peak was observed during the Na doping of the pentacene film. This suggests an

absence of charging effects in the film, and so legitimises the interpretation of the observed peak shifts as Na doping related shifts.

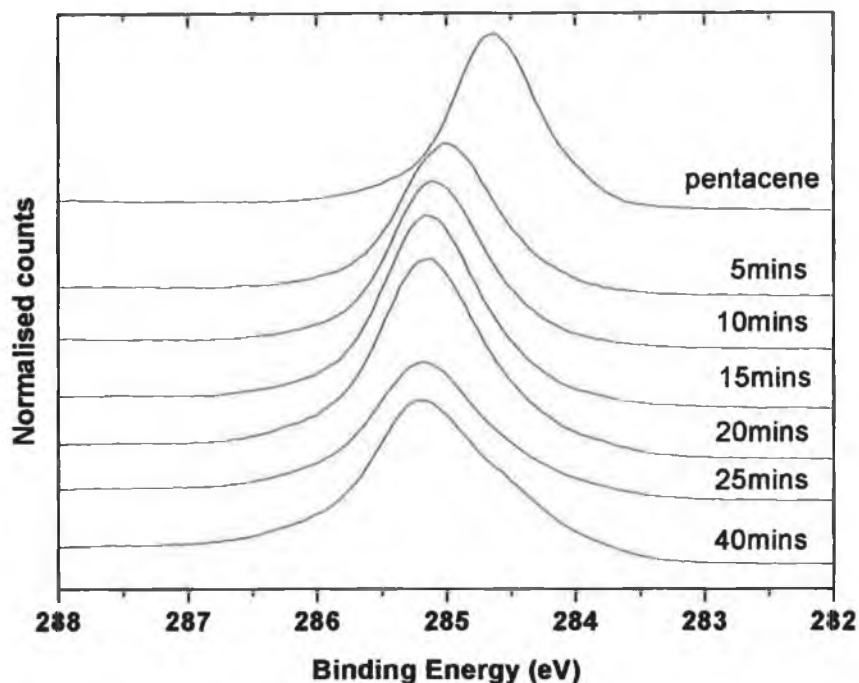


Figure 6.1 Evolution of carbon $1s$ peak ($h\nu = 340\text{eV}$) as a function of increasing dopant concentration in the 16ML untemplated pentacene film.

Figure 6.2 shows the valence band spectra of the unannealed pentacene film with increasing dopant concentration, with a close up of the region adjacent to the Fermi level inset in the graph. Prominent pentacene molecular orbital related features are indicated by **a** to **g** in the diagram. The feature in the 2-4eV region of the graph is due to residual emission from the Cu3d valence band feature. The HOMO is indicated as feature **g** in figure 6.2 and is centred at approximately 1.6eV. The onset of the HOMO is observed at approximately 0.95eV. It is evident that the pentacene related features in the valence band spectra shift to higher binding energy with increasing dopant concentration. However, due to the difficulty in following the shift in the HOMO as it overlaps with the residual Cu3d emission, the shift in the pentacene related features was observed using the other more prominent pentacene related emissions at higher binding energies. The pentacene related features are observed to shift to higher binding energy with increased dopant deposition up until the 20-minute coverage. The lack of change in the lineshape of the pentacene features implies that the pentacene does not undergo significant chemical modification with this initial stage of doping. The observed shift in

the pentacene features in this initial stage of doping is measured to be approximately 0.63eV, which is larger than the observed shift in the C1s position during the corresponding stage of film doping. It should be noted that different pentacene related features in the valence band were observed to shift by different amounts during the doping process by the approximately 0.1eV. The average of these shifts was therefore taken to estimate the magnitude of the HOMO shift. This calculated shift in the HOMO therefore results in a reduction in the electron injection barrier from 1.25eV to 0.62eV, accompanied by a corresponding increase in the hole injection barrier. The pentacene/Cu(110) system has essentially been altered from a p-type system to an n-type system by the doping process.

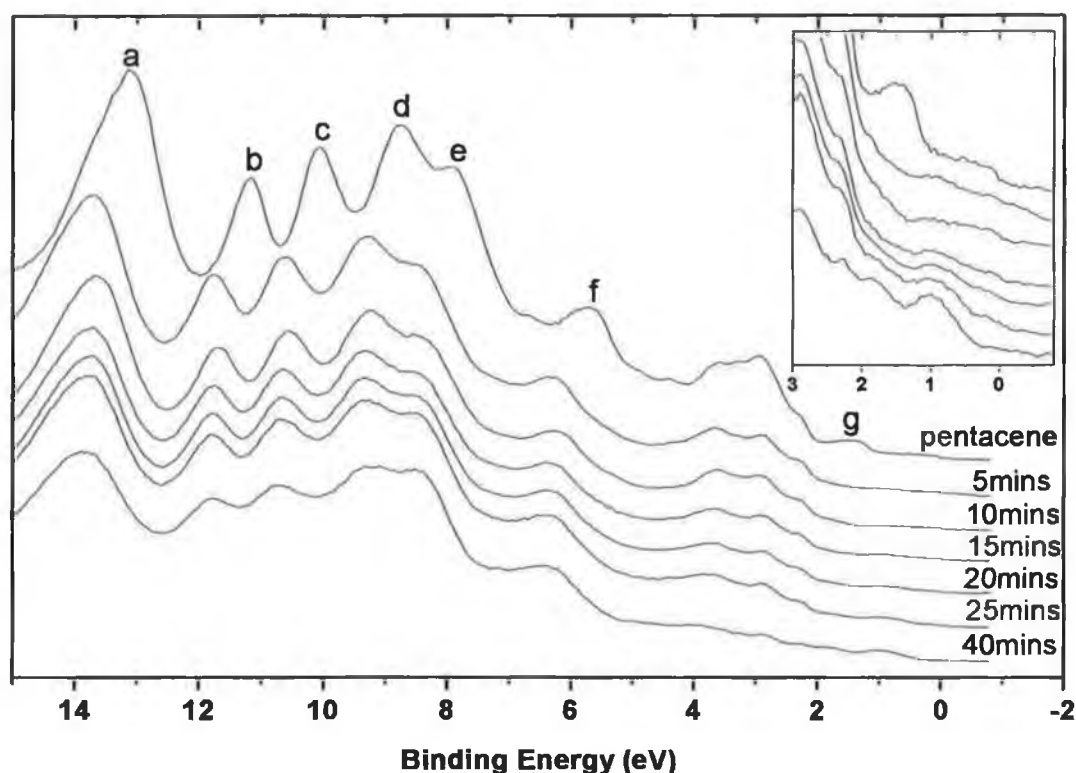


Figure 6.2 Valence band spectra ($h\nu = 31\text{eV}$) for increasing dopant concentration in the 16ML untemplated pentacene film. Inset in the graph is a close up of the valence band region nearest the Fermi level, with increasing dopant concentration from top to bottom.

In the two subsequent depositions there is a further shift to higher binding energy of the pentacene related features, but this is accompanied by a slight modification in the lineshape of the pentacene related valence band features. This is

indicative of the beginning of the second stage of doping observed, which is discussed in more detail later.

The inset in figure 6.2 shows a close up of the region of the valence band near the Fermi level, with increasing Na concentration from top to bottom. As mentioned, the HOMO is observed to shift to higher binding energy with the initial Na deposition and is no longer distinguishable from the residual Cu3d emission. However, a new feature in the region becomes evident from the 15 minute Na coverage, centred at approximately 0.95eV. The growth of this feature is attributed to the formation of a gap state.

The alkali metal doping of organic semiconductors is frequently accompanied by the growth of gap states close to the Fermi level^{19, 20, 25} and has been previously observed for Rb doping of pentacene on W(110)²⁶, although in this case, the gap state was wrongly identified as a LUMO state. The energy separation between the HOMO and the gap state is estimated to be approximately 1.0eV for the Rb doping of pentacene. Difficulty in obtaining a precise measurement for the energy separation was encountered due to the disappearance of the HOMO upon gap state formation. This energy separation is however comparable to that found for the Na doping of pentacene/Cu(110) presented here, with a value of 1.2eV estimated for the HOMO-gap state separation.

Previous studies involving the organic molecule tris (8-hydroxy quinoline) aluminium (Alq), have shown that the deposition of the weakly interacting metal, Ga, results in the diffusion of the metal into the molecular film with time²⁷. However, the deposition of a more reactive metal, Ca, was found to result in a strong interaction between the metal and the Alq surface, with the formation of an interfacial layer resulting in little or no diffusion of the Ca into the molecular film. While the deposition of Na should result in a significant interaction between the dopant and the molecular overlayer, and therefore should in turn result in little Na diffusion into the pentacene film, evidence from the valence band studies suggests the diffusion of the Na throughout the molecular film. Upon deposition of Ca on Alq, significant modification of the molecular orbitals in the valence band region of the PES spectrum was observed, while for the deposition of Ga, there was little modification of the molecular orbitals. The observed modification of the Alq molecular orbitals was attributed to the formation of an interfacial region at the surface of the organic film, due to the strong interaction between the Ca and the Alq, with the formation of metallic Ca on top of the interfacial region at higher coverages. The lack of significant modification of the pentacene

molecular orbitals with initial Na deposition indicates that the Na diffuses into the pentacene film rather than residing on top of the film and subsequently forming a metallic Na layer at higher coverage.

The shift in the workfunction with increasing Na doping is presented in figure 6.3. As with the shift observed in the C1s peak and the pentacene related valence band features presented in figures 6.1 and 6.2 respectively, there is a large shift in the workfunction with the initial doping of the film, which then saturates at the 20 minute Na deposition. This is indicative of the initial stage of doping where negative charge transfer from the Na to the pentacene results in the Fermi level moving up the band gap towards the LUMO. The magnitude of the shift observed in the initial stage of doping was found to be 0.62eV, which is intermediate between the shift observed in the C1s peak (0.5eV) and the pentacene related valence band features (0.63eV).

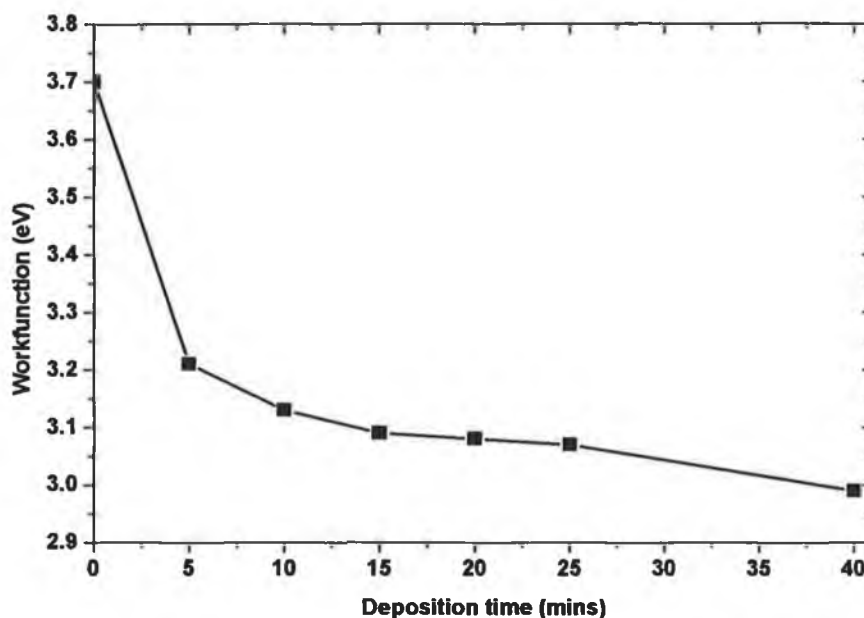


Figure 6.3 Calculated workfunction position ($h\nu = 31\text{eV}$) with increasing Na concentration in the 16ML untemplated pentacene film.

Figure 6.4 introduces the Na2p peak evolution with increasing Na coverage. The lineshape has been fitted with three Lorentzian doublets of intrinsic separation of 0.2-0.3eV, in addition to a Gaussian broadening of 0.2eV to account for instrumental broadening. Due to the small spin-orbit split separation of the Na2p doublet (found to be $0.30\text{eV} \pm 0.05\text{eV}$ during the fitting process), the peak appears to be an asymmetric singlet in figure 6.4. It is evident that there are two main parts to the Na2p peak, a high binding energy section fitted with two components and a low binding energy section

fitted with a single component. An XPS angular study, not shown here, of the 25 minute Na deposition suggested that the low binding energy component was related to sodium located at the pentacene/Cu(110) interface as there is a significant reduction in the intensity of this component relative to the other two components with increasing emission angle. Na deposited on clean Cu(110) resulted in a single peak of binding energy 31.1eV, which corresponds to the binding energy of the low binding energy component. In addition to this, a doping experiment of a significantly thicker pentacene film not presented here resulted in a substantial decrease in the intensity of the lower binding energy component. This was attributed to reduced signal from the pentacene/Cu(110) interface where the lower binding energy component resides due to greater attenuation by the thicker pentacene overlayer.

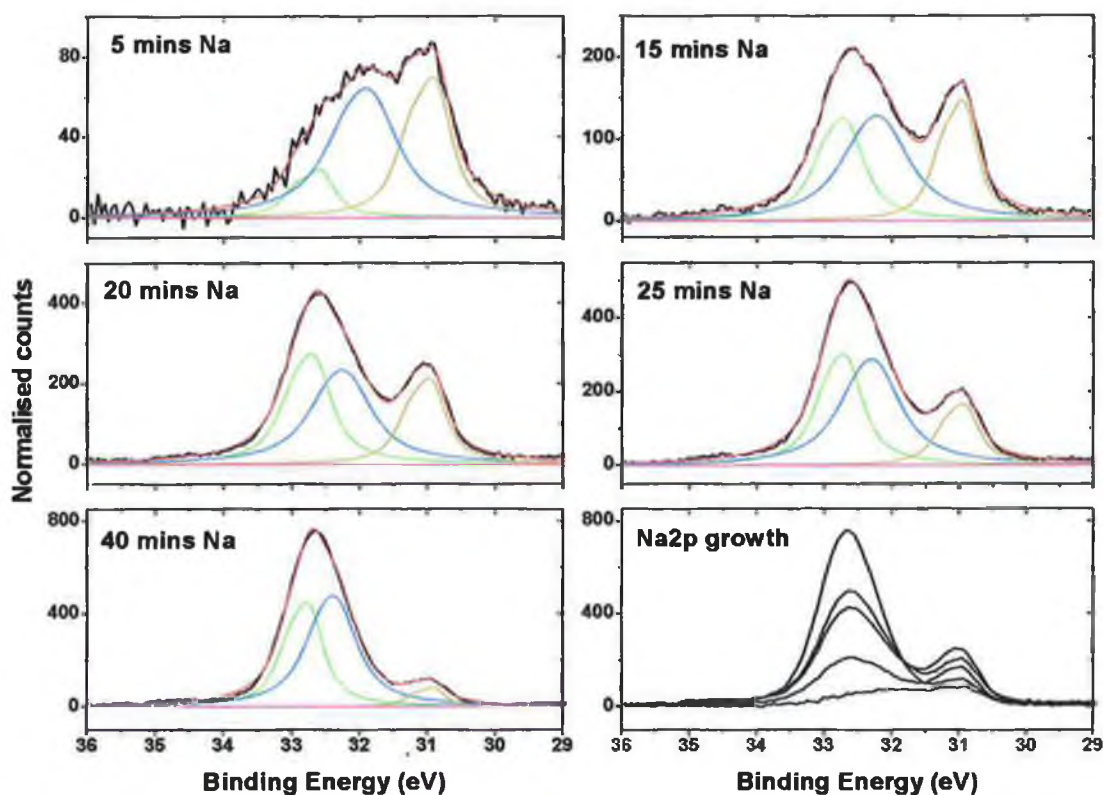


Figure 6.4 *Na₂p* peak ($h\nu = 60\text{eV}$) evolution with increasing dopant concentration in the 16ML untemplated pentacene film. The lower right panel is a composite of the *Na₂p* peaks for the different coverages investigated, showing the relative intensities of the *Na₂p* peaks.

The two higher binding energy components, with a peak separation of $0.46\text{eV} \pm 0.07\text{eV}$, are attributed to emission from Na atoms in different chemical environments within the pentacene film. An angular study, not shown here, indicated a reduction in these components with increasing emission angle, although the reduction in their

intensities was far less than that observed for the low binding energy component. This indicated that both components were due to Na atoms residing within the organic film indicating a diffusion of the atoms within the pentacene film. The angular study revealed no evidence of Na related components residing on top of the organic film.

Figure 6.5 is a summary of the energy shifts observed in the workfunction, the C1s core level peak, and the pentacene related valence band features with increasing Na concentration. It is evident that the shift in the C1s is smaller in magnitude than the shifts observed in the case of the workfunction and the valence band features by approximately 0.1eV in the initial stages of the doping. There is much better agreement between the shift in the workfunction and that observed for the valence band features in the initial stage of doping.

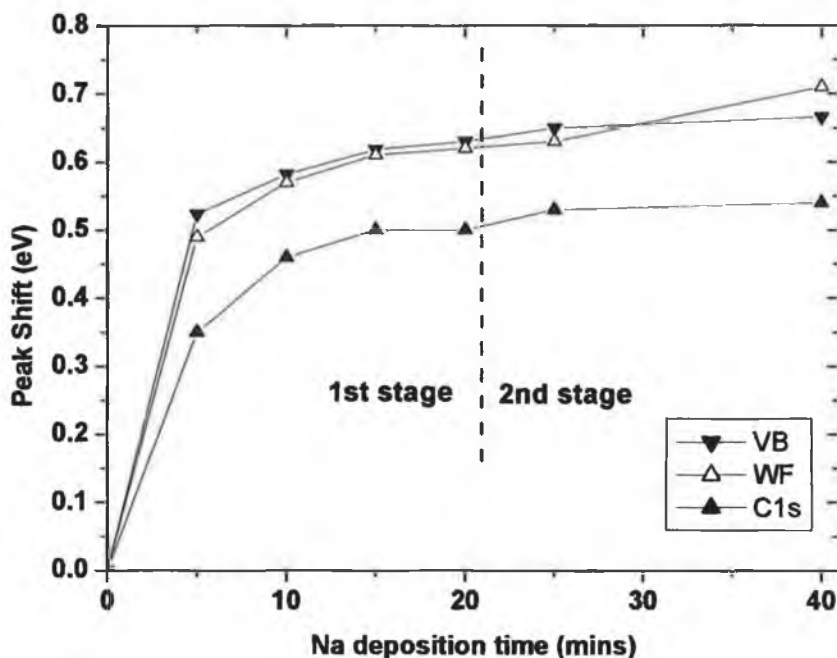


Figure 6.5 Plot of shifts in the pentacene related valence band peaks, the C1s peak and the measured workfunction for increasing Na dopant concentration. The average value of the shift in the valence band peaks was used to indicate the valence band shift, as different features were observed to shift by different amounts.

6.3.2 Na doping of templated pentacene film on Cu(110)

Figure 6.6 plots the evolution of the C1s peak with increasing Na doping of the 8ML pentacene film, grown using an annealed monolayer to template the subsequent film growth, in addition to the 40 minute Na deposition for the unannealed pentacene film for comparison. As observed with doping of the unannealed film, the deposited Na

results in a shift in the C1s peak position to higher binding energy. In the previous section, the lineshape of the C1s peak was observed to remain relatively unchanged in the initial stage of doping, with a change in the lineshape becoming evident in the spectra with the onset of the second stage of the doping. In figure 6.6 the initial stage of the doping can be seen up to a coverage of 14 minutes of Na. For the subsequent high coverage of 74 minutes there is a significant change in the lineshape of the C1s peak. This is manifested in a large broadening of the peak indicating the introduction of several additional components to the lineshape. It is quite likely that this is the result of a significant chemical modification of the pentacene molecules in the film, or the formation of metallic Na on the film surface.

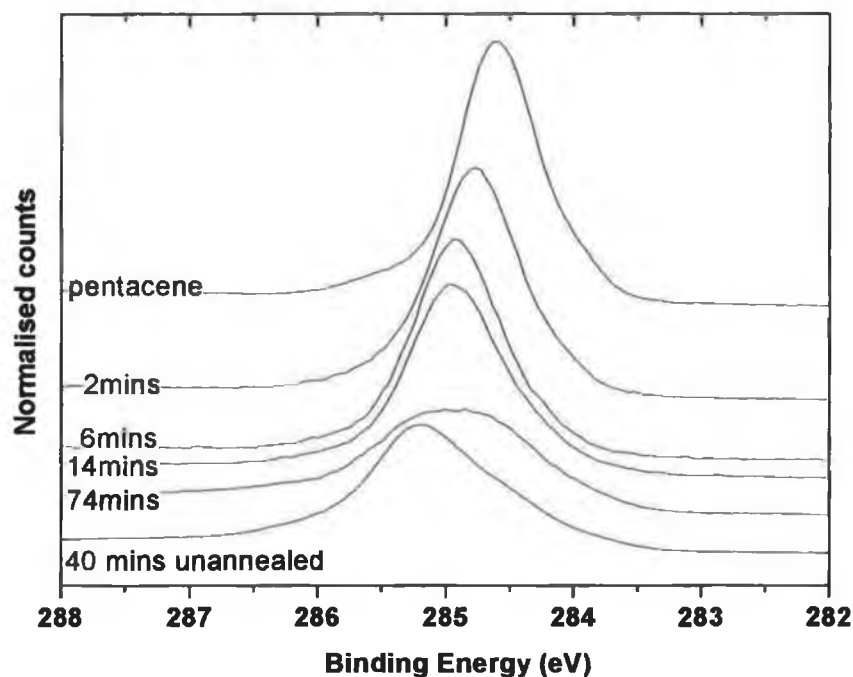


Figure 6.6 Carbon 1s ($h\nu = 340\text{eV}$) evolution with increasing Na concentration for the 8ML templated pentacene film. The 40-minute Na deposition for the unannealed pentacene film is included for comparison.

It should be noted that the magnitude of the shift in the C1s peak observed in the initial stage of the doping is approximately 0.35eV. The shift in the C1s peak in the initial stage of Na doping was found never to exceed the shift observed in the second stage of doping. It is therefore assumed that the position of the C1s peak for 14 minutes Na coverage represents a saturation position in the C1s peak shift for the initial doping stage. Therefore the shift associated with the initial stage of doping of the more ordered

pentacene film is significantly less than the shift associated with the initial stage of doping observed for the film grown in a stepwise fashion, which was found to be 0.5eV. A comparison between the 74 minute Na deposition for the annealed pentacene film, and the 40 minute Na deposition for the unannealed pentacene film indicates that the total shift in the C1s peak position observed for the second phase of doping of the annealed pentacene film is less than that observed for the unannealed pentacene film.

The valence band spectra with increasing Na concentration are presented in figure 6.7, with a close up of the valence band region near the Fermi level inset in the figure. The coverages up to the 14-minute Na coverage show a shifting of the pentacene related valence band features to higher binding energy without a significant alteration in the peak shapes indicating that in this stage of the doping the pentacene molecules do not undergo any significant chemical modification. The average magnitude of the shift in the valence band peaks was found to be 0.38eV between the undoped film and the 14-minute Na deposition. As with the C1s peak, this shift is significantly different from the 0.63eV observed for the doping on the untemplated pentacene film shown in figure 6.2.

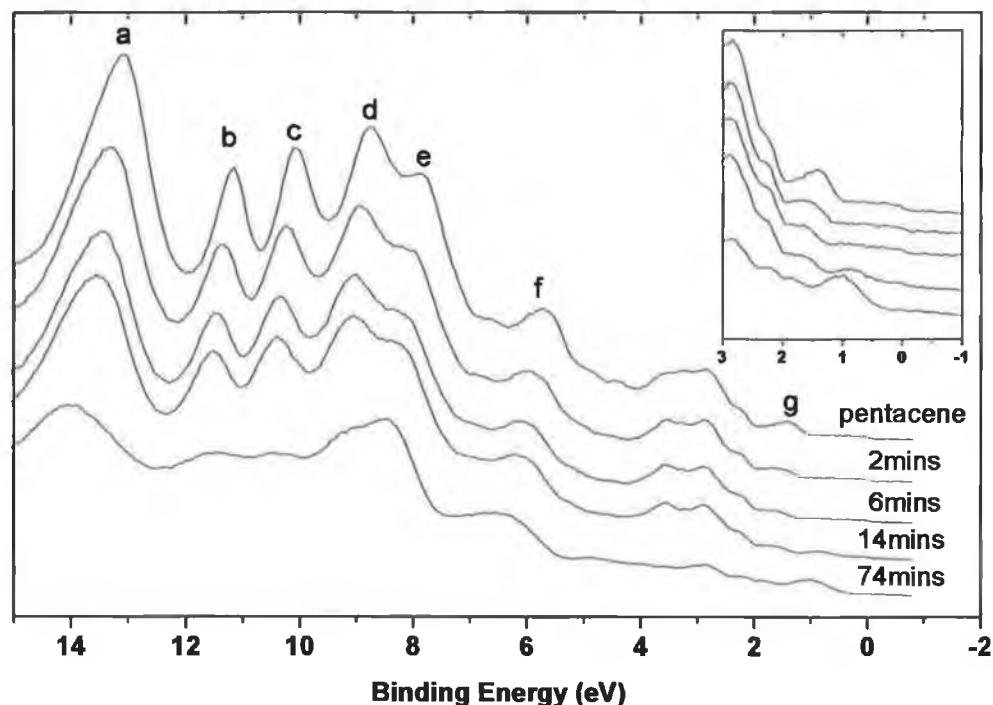


Figure 6.7 Valence band spectra ($h\nu = 31\text{eV}$) for increasing dopant concentration in the 8ML templated pentacene film. Inset in the graph is a close up of the valence band region nearest the Fermi level, with increasing dopant concentration from top to bottom.

The change in the lineshape of the pentacene related features for the 74-minute Na deposition implies a significant chemical modification of the organic overlayer. At this stage, the shift in the position of the pentacene related features in the valence band become more difficult to quantify. This change in lineshape of the pentacene feature is indicative of the second stage of the doping process, in which there is no longer a simple shift in the energy levels of the molecular overlayer. Growth of a gap state, centred at approximately 0.95eV binding energy for the 74 minute Na deposition, as shown in the inset in figure 6.7, accompanies this second stage of doping. A two stage doping process has been observed for the alkali metal doping of copper phthalocyanine^{19, 22} and tris(8-hydroxyquinoline) aluminium^{19, 20}. In the case of these experiments, the second stage of doping occurs after the saturation of the shift in the vacuum level and is accompanied by the growth of gap states in the valence band region between the HOMO and the Fermi level.

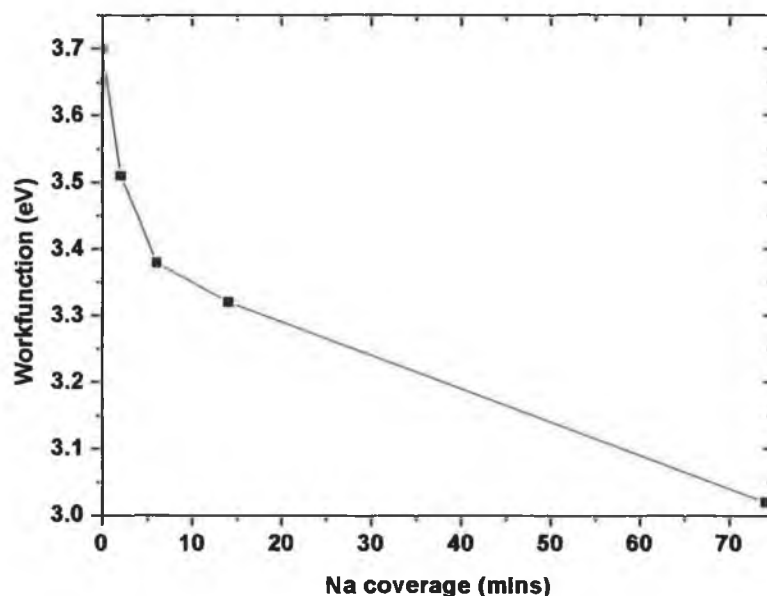


Figure 6.8 Evolution of the workfunction ($h\nu = 31\text{eV}$) with increasing Na concentration.

Figure 6.8 plots the evolution of the workfunction with increasing Na concentration. In the initial stage of the doping process up to 14 minutes of Na deposition, the shift in the workfunction is found to be 0.38eV, which again is significantly less than the 0.62eV observed in the first experiment. In the studies of copper phthalocyanine^{19, 22} and tris(8-hydroxyquinoline) aluminium^{19, 20} in which a two stage doping of the film was observed, there is no further shifts in the workfunction of

the sample after the completion of the initial stage of doping. However in this case a further shift of approximately 0.3eV is observed up to the highest Na concentration investigated, with the workfunction tending towards that of metallic Na.

The fitted Na2p peak for the doping of the 8ML templated pentacene film is shown in figure 6.9. As with figure 6.4 the peak is fitted with three doublet components. The presence of the high binding energy peak attributed to Na at the pentacene/Cu(110) interface is evident in figure 6.9 indicating the diffusion of the Na through the organic film.

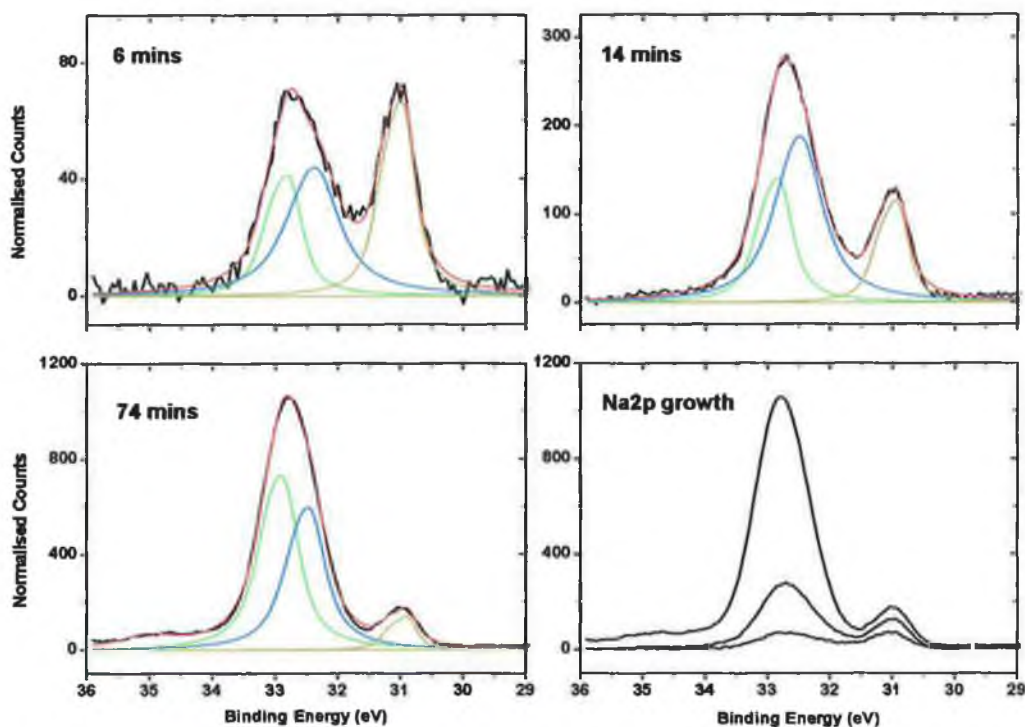


Figure 6.9 Na2p peak ($h\nu = 60\text{eV}$) evolution with increasing dopant concentration in the 8ML templated pentacene film. The lower right panel is a composite of the Na2p peaks for the different coverages investigated, showing the relative intensities of the Na2p peaks.

Figure 6.10 summarises the calculated shifts in the peak positions for the alkali metal doping of the templated pentacene film. As with figure 6.5 it is evident that the magnitude of the shift in the C1s peak position during the doping process is in general smaller than the shift evident in the pentacene valence band peaks and in the workfunction.

In order to examine the differences in the doping of the two pentacene films, we must first look at the differences in the two undoped organic films. Since the molecular orientation of the pentacene is identical in the case of both doped films, as discussed in

chapter 4, the main differences between the two undoped films are the estimated film thicknesses and the degree of ordering in both films. However in a comparative study not shown here, a stepwise grown pentacene film of thickness in excess of 30ML was doped in a similar manner to the two experiments presented. Similar peak shifts to those observed for the 16ML pentacene film were observed for the initial stages of doping of the thicker pentacene film. Since the increased film thickness was not observed to have any significant effects on the doping process, the difference in the magnitude of the peak shifts observed during the initial stage of doping of both the templated and untemplated pentacene films must therefore be attributed to the different degree of ordering present in the two undoped molecular films.

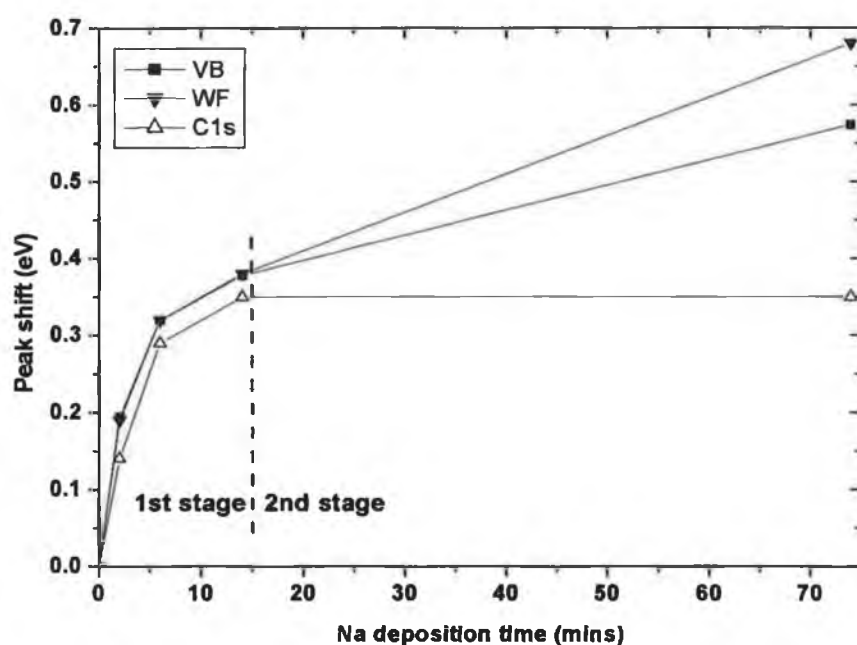


Figure 6.10 Plot of shifts in the pentacene related valence band peaks, the C1s peak and the measured workfunction for increasing Na dopant concentration. The average value of the shift in the valence band peaks was used to indicate the valence band shift, as different features were observed to shift by different amounts.

It is not clear why a higher degree of ordering in the molecular film should influence the doping of the film. The presence of the low binding energy Na2p component in the templated pentacene film indicates that the dopant has diffused through the film down to the pentacene/Cu(110) interface and so the more ordered film does not appear to hinder diffusion of the dopant.

The process by which doping occurs in organic semiconductors has been shown to differ from the conventional doping of crystalline inorganic semiconductors¹⁹. In this

study it was found that the doping of the molecular overlayer resulted in a greater energy level shift than could be explained using the conventional inorganic doping model. This has been partly attributed to the difference in bonding that exists in organic and inorganic semiconductors. Covalent bonding in inorganic semiconductors results in a large electronic wavefunction overlap, which is the basis for forming the Bloch waves and band structure. The prevailing bonding present in organic semiconductors however is Van der Waals²⁸, which results in an electronic structure that remains largely molecular and localised. A larger degree of ordering in the pentacene film should result in a greater overlap of the electronic wavefunction of the molecules in the film than that observed in a less ordered film. This in turn should lead to the doping of the organic semiconductor behaving more like the conventional model for the doping of crystalline inorganic semiconductors, which predicts a reduced Fermi energy shift with doping in comparison to that previously observed for the doping of organic semiconductors¹⁹.

Another possible explanation for the reduced doping observed for the more ordered pentacene film is due to the area integrated nature of the PES technique. The presence of a PES signal from the highly ordered areas of the pentacene film, in addition to a signal from the more disordered areas could lead to the reduced observed movement of the Fermi level up the gap with Na doping for the annealed pentacene film. If the highly ordered areas of the pentacene film are found to inhibit the diffusion of the Na, the extent of doping observed in this area of the film would be reduced over that observed for the more disordered unannealed film. The presence of disordered areas, which allow the thorough diffusion of Na throughout the film, could allow for the observation of the pentacene/Cu(110) interface component of the Na 2p peak. The integration of the signal emitted from the ordered and disordered areas of the film would then result in an overall reduced doping effect in the film. This reduced doping effect should however result in an observed broadening of C1s peak and pentacene molecular orbital related features in the valence band, with the essential introduction of two components, from the ordered and disordered areas of the film respectively. However the shape of the C1s peak and pentacene derived molecular orbital features in the valence band spectra are not observed to change significantly until high dopant concentrations, corresponding to the observed second phase of doping. It is therefore thought to be unlikely that the different peak shifts observed for the first phase doping of the stepwise grown pentacene film, and the templated pentacene film are due to the reduced Na diffusion with a more highly ordered film.

The inconclusive nature of both possible explanations for the reduced doping observed in the more highly ordered pentacene film, suggests that there is much that is still unknown about the doping process, and the role that the organic film itself plays in this process. It is therefore evident that further research is required to fully understand the processes at work here.

6.3.3 Summary

Synchrotron based photoelectron emission spectroscopy (PES) has been used to investigate the energy level shift observed during the Na doping of two pentacene films exhibiting different degrees of ordering of the molecules. The findings indicate that negative charge transfer from the alkali metal to the organic semiconductor result in the Fermi level of the pentacene being modified, essentially from a p-type semiconductor to an n-type semiconductor. The modification of the Fermi level has been observed to occur in two stages. The first stage of doping occurs at low doping concentrations and results in a shift in the Fermi level without any significant modification of the organic film. The second stage of doping occurs at higher doping concentrations. Further shifts in the Fermi level are observed but these are accompanied by significant modification in the pentacene related core level and valence band features, in addition to the growth of gap states between the HOMO and the Fermi level.

The degree of ordering present in the undoped molecular film was observed to play an important role in the doping process. A higher degree of ordering in the molecular film was observed to reduce the extent to which the film could be doped in both stages of doping. The origin of this effect is not yet known and requires further investigation.

6.4 Pentacene deposited on O/Cu(110)-(2×1)

In this section we investigated the effect of an interlayer on the growth of pentacene thin films on the Cu(110) substrate. This was carried out using a half monolayer of oxygen to terminate the Cu(110) substrate prior to the deposition of pentacene.

6.4.1 O/Cu(110)-(2×1)

It is well established in literature^{29, 30, 31, 32, 33, 34, 35} that the Cu(110) (1×1) surface can be terminated with a chemisorbed half monolayer of oxygen, which leads to a (2×1) reconstructed surface.

The oxygen termination was achieved by annealing the copper crystal at 403K for 120 seconds in the SGM1 preparation chamber, while maintaining an oxygen rich environment in the chamber. The chamber was kept at a pressure of 1×10^{-6} mbar by the introduction of O₂, via a leak valve. The surface was then examined with LEED to confirm that the expected sharp (2×1) pattern was obtained, indicating that the desired surface reconstruction had been achieved. In the literature Ozawa²⁹ et al describe the surface as a missing-row reconstructed surface, where every second row of Cu atoms in the topmost layer is missing and the O atoms sit in the long-bridge site, forming linear Cu-O chains. This is easily observed in the ball model shown in figure 6.11. Figure 6.11 (a) shows an overhead view of the clean Cu(110) surface with the (1×1) surface lattice indicated by the black box. The unit cell of the Cu(110) surface is a rectangular lattice with $a = \sqrt{2}b$. The topmost Cu atoms in the diagram are represented by the yellow circles, while the bulk Cu atoms are represented by the red circles.

Figure 6.11 (b) shows an overhead view of the O/Cu(110)-(2×1) surface. The termination of the surface with oxygen gives a (2×1) surface reconstruction with the topmost layer consisting of 0.5 ML of Cu atoms and 0.5 ML of O atoms. The topmost Cu atoms in this picture are represented by the orange circles, while the O atoms are represented by the black circles. In figure 6.11 (c), the side view of the (2×1) oxygen terminated Cu(110) surface shows that the O atoms sit higher on the surface than the surface Cu atoms.

The growth of this (2×1) surface reconstruction starts initially with the formation of the Cu-O-Cu-O chains shown above in figure 6.11 (b), when the substrate is annealed in the presence of O₂. With increasing oxygen coverage, islands grow by the aggregation of the Cu-O-Cu-O chains, giving rise to a local (2×1) reconstruction. By an

oxygen coverage of 0.5 ML, the islands have coalesced and the whole surface is found to be (2×1) reconstructed. There remains a degree of debate over whether the (2×1) reconstruction comes about by the addition of an extra row of copper atoms^{34, 35} or by the removal of a row of copper atoms³⁰.

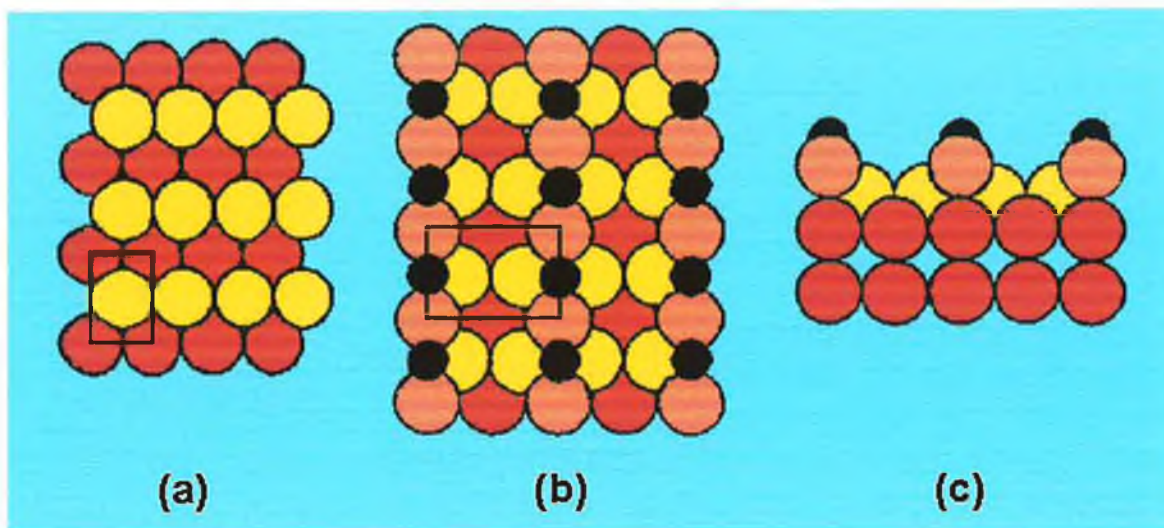


Figure 6.11 (a) Overhead view of the clean Cu(110) substrate showing the (1×1) unit cell²⁹. The topmost row of atoms are shown in yellow with the underlying atoms in red. (b) Overhead view of the oxygen terminated Cu(110) showing the (2×1) surface reconstruction²⁹. The oxygen atoms are shown in black and the topmost Cu atoms are shown in orange. (c) Side view of the oxygen terminated Cu(110) showing the (2×1) surface reconstruction²⁹.

The workfunction of the sample was found to increase from 4.67eV to 4.82eV upon oxygen termination of the surface. This increase in the workfunction is attributed to the electronegative nature of the adsorbed oxygen. The electron affinity of the oxygen atoms results in the pulling of electron density from the surface, therefore increasing the surface dipole component caused by the electron gas spill-out into the vacuum. However, the calculated workfunction values are not in agreement with the literature²⁹ values of 4.5eV and 4.9eV for the clean Cu(110) and O/Cu(110)- (2×1) substrates respectively. The differences in the absolute values of the workfunction and in the calculated change in the workfunction upon oxygen termination of the surface between the literature values and the experimentally measured cannot be accounted for. The presence of the sharp (2×1) LEED pattern, in addition to the absence of contaminants in the PES scans indicate that clean Cu(110) and fully terminated O/Cu(110)- (2×1) were achieved in the course of these experiments.

A comparison between the valence band for the clean Cu(110) substrate and the O/Cu(110)- (2×1) substrate is presented in figure 6.12 for (a) normal emission and (b) s-polarised sample positions. It is evident that the oxygen termination of the Cu(110)

induced new states, labelled A and B in figure 6.12, that are not observed in the spectra for the clean substrate. Feature A corresponds to a broad, relatively intense emission visible in both the normal emission and s-polarised spectra, centred at approximately 6.0eV. Feature B, centred at 1.6eV, is observed as a strong emission in the s-polarised spectra, and as a weak feature in the normal emission spectrum. It is found on the plateau region between the Cu3d valence band feature and the Fermi level. These states have been attributed to bonding and antibonding states³⁶ formed between the O2p states and the Cu3d states.

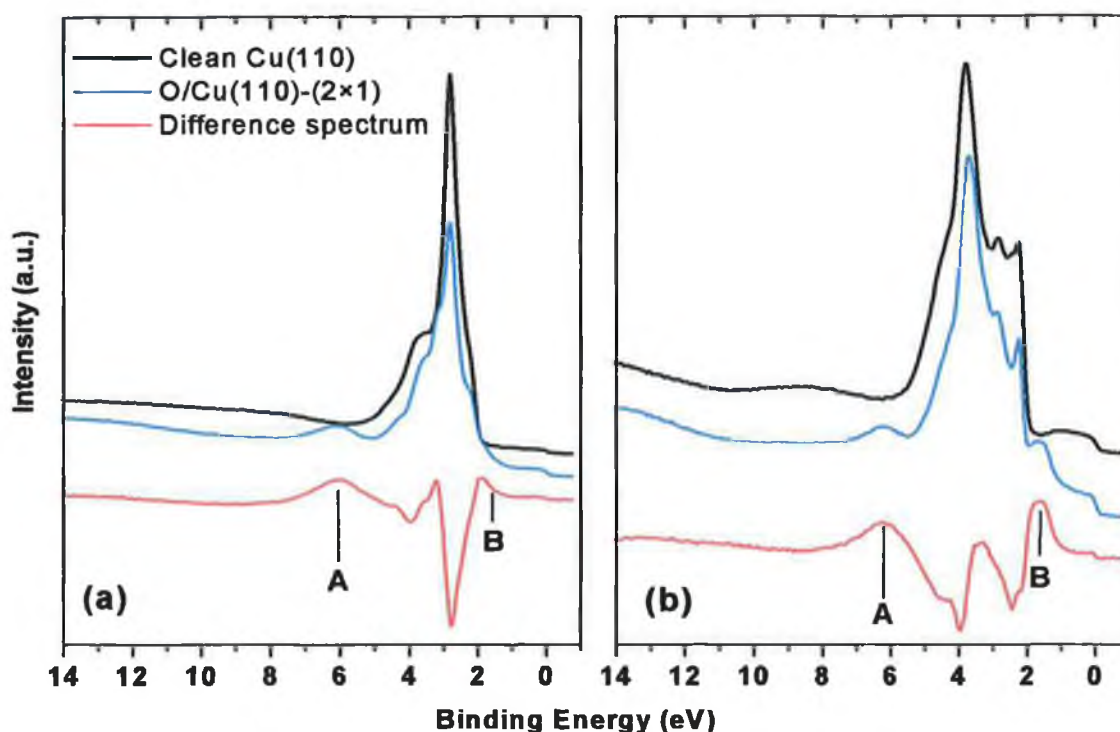


Figure 6.12 (a) Plot showing the normal emission valence band spectra ($h\nu=31\text{eV}$) for the clean Cu(110) substrate, the O/Cu(110)-(2 \times 1) substrate, and a difference spectrum. (b) Plot showing the s-polarised valence band spectra ($h\nu=31\text{eV}$) for the clean Cu(110) substrate, the O/Cu(110)-(2 \times 1) substrate, and a difference spectrum. New features induced by the oxygen termination of the surface are identified as A and B in the diagram.

6.4.2 Workfunction measurements

The evolution of the workfunction for increasing pentacene coverages is presented in figure 6.13. As discussed in chapters 4 and 5, the formation of the interface dipole is predominantly completed with the initial monolayer of adsorbate, therefore extrapolation of the initial linear decrease in the workfunction of the sample to the

workfunction of the sample for a thick pentacene coverage allows for the estimation of an approximate monolayer coverage³⁷. All coverages are subsequently referenced to the deposition time required for the completion of the monolayer coverage. It should be noted that a change in packing density of the pentacene film as a result of molecular reorientation or the onset of significant island growth will cause the actual film thickness in monolayers to deviate from the estimated thickness.

The magnitude of the calculated interface dipole is found to be 0.47eV, which is significantly smaller than that found for the unmodified pentacene/Cu(110) interface (1.0eV) discussed in chapter 4. Ab initio calculations³⁸ have shown, that for a molecule brought into contact with a metal surface, the predominant contribution to the magnitude of the interface dipole is a physical charge repulsion effect, whereby the molecular charge pushes aside the surface metal charge.

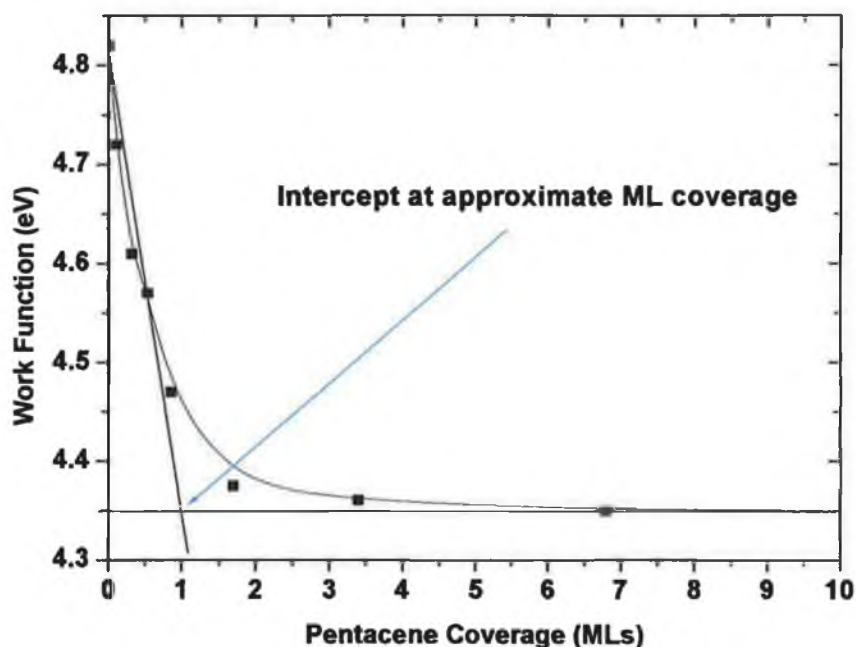


Figure 6.13 Workfunction measurements ($h\nu=31\text{eV}$) for increasing pentacene coverages. A linear extrapolation of the initial decrease in the workfunction allows for the calculation of the approximate monolayer coverage.

In the case of chemisorption of the molecule, there is an additional contribution due to negative charge transfer between the metal and the adsorbate. It has been established in chapter 4 that the initial pentacene monolayer is found to chemisorb to the underlying substrate for the pentacene/Cu(110) system. A contribution by both physical and chemical components to the magnitude of the interface dipole formed is

therefore expected in this case. Adsorbate core level analysis, presented in section 6.4.3, suggests a weak interaction between the pentacene and the substrate for the pentacene/O/Cu(110)-(2×1) system. It is therefore likely that there is no chemical component to the magnitude of the interface dipole formed upon adsorption of pentacene to the O/Cu(110)-(2×1) substrate, and hence the total magnitude of the measured interface dipole is reduced.

It is evident from the workfunction measurements that there is significant modification of the pentacene/Cu(110) system by the introduction of an oxygen interlayer.

6.4.3 C1s core level analysis

The calculated area of the C1s peak with increasing pentacene coverages is presented in figure 6.14. The peak area is observed to rise sharply until the 1.7ML coverage, after which it plateaus. There is a slight reduction in the measured peak area for the 13.8ML coverage. This occurs at a comparable coverage to reductions in the C1s peak area observed for the pentacene/Cu(110) and pentacene/Au(100) systems discussed in chapters 4 and 5 respectively. However, this observed plateau in the measure C1s peak area could be due to the presence of a sticking limit for this experimental system, where additional film growth is limited after the deposition of the initial few monolayers of adsorbate.

The stacked C1s plots for increasing pentacene coverages are shown inset in figure 6.14. The peak lineshape is slightly asymmetrical from the initial evolution of the peak, with a constant FWHM of approximately 0.96eV found for all pentacene coverages. This is smaller than the 1.21eV observed for the chemisorbed initial monolayer of pentacene on Cu(110), and is more comparable with the 0.87eV FWHM measured for the physisorbed monolayer coverage of pentacene on Au(100), discussed in chapter 5. The magnitude of the FWHM measured for the initial chemisorbed monolayer of pentacene on Cu(110) was due to the presence of a chemically shifted carbon component due to the adsorbate-substrate bond. The smaller FWHM magnitude calculated for the pentacene/O/Cu(110)-(2×1) system suggests a weaker bond between the adsorbate and the substrate, and therefore the adsorbate-substrate bond is more likely to be physisorption in nature. Additionally, the constant C1s FWHM for all pentacene coverages suggests that the substrate exhibits little interaction with the pentacene.

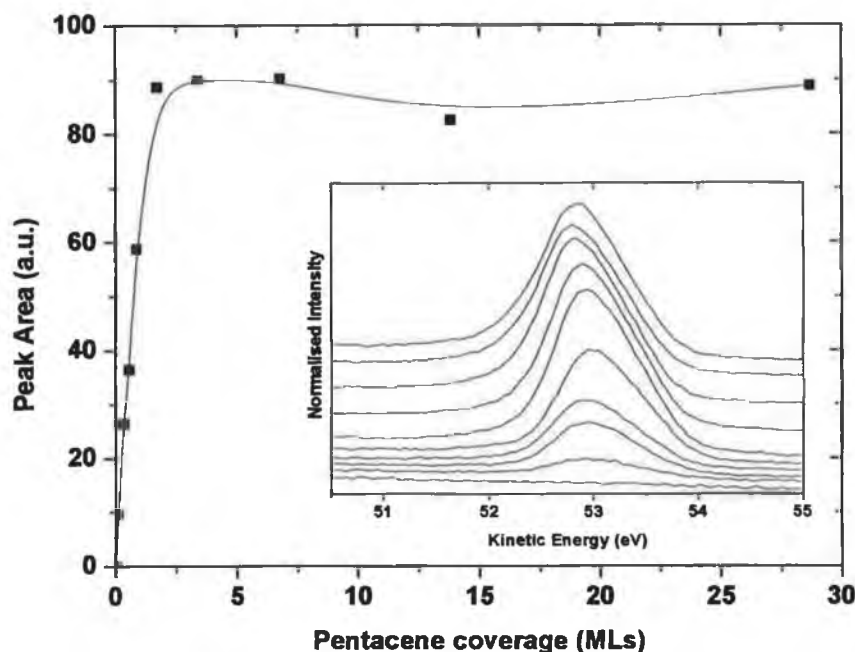


Figure 6.14 Normalised peak area of the C1s pentacene peak plotted for increasing pentacene coverage. Inset in the graph are the stacked C1s spectra ($h\nu = 340\text{eV}$) for O/Cu(110)-(2 \times 1), 0.1ML, 0.3ML, 0.55ML, 0.85ML, 1.7ML, 3.4ML, 6.8ML, 13.8ML and 28.7ML coverages respectively from bottom to top.

As with the workfunction data presented in section 6.4.2, C1s data suggests a significant modification of the pentacene/Cu(110) system by the introduction of an oxygen interlayer. The bonding between the pentacene and the substrate has been altered from a chemisorption like interaction, as observed for the pentacene/Cu(110) system, to a physisorption like interaction.

6.4.4 Substrate signal analysis

Analysis of the reduction in the substrate signal with increasing overlayer thickness was carried out via the Cu3d feature in the valence band region of the PES spectrum. The reduction in the substrate signal is shown in figure 6.15. In section 2.4, the IMFP of an electron travelling through a pentacene was calculated using the program electron inelastic-mean-free-path v.1.1³⁹, with the plot showing the calculated IMFPs for a given electron kinetic energy shown in figure 2.6. However, this program only allowed for the calculation of IMFPs for electrons with kinetic energies greater than 50eV, and so an exact IMFP value for the Cu3d feature electrons (KE \approx 30eV) is not obtainable. A ratio of 1.87 was found between the IMFP for electrons of kinetic energy

124eV and 30eV respectively, calculated using the universal IMFP curve, shown in figure 2.5. If this ratio holds for electrons travelling through a pentacene film, as calculated using the program electron inelastic-mean-free-path v.1.1³⁹, the IMFP for electrons of kinetic energy 30eV can now be estimated at approximately 3.7Å, resulting in a total sampling depth (taken as three times the IMFP) of 10.1Å.

It should be noted that the use of the Cu3d valence band feature as a measure of the decrease in the substrate-derived signal is more complex than the use of a substrate derived core level with higher binding energy. Since the valence band region of the spectrum shows the energy states closest to the Fermi level, and hence those most likely to be involved in bonding, the intensity of the Cu3d substrate feature can be affected by bonding interactions. For example, the growth of molecular orbital derived features, or interface states in this valence band energy range can result in additional measured intensity over that purely due to suppression of the substrate feature with increasing adsorbate coverage. Similarly, the quenching of surface states or a significant chemical bonding between the substrate and adsorbate can result in a greater decrease in the measured intensity of the substrate feature over that purely due to suppression of the substrate feature with increasing adsorbate coverage. Nevertheless, figure 6.15 should still provide some information regarding the overlayer growth mode.

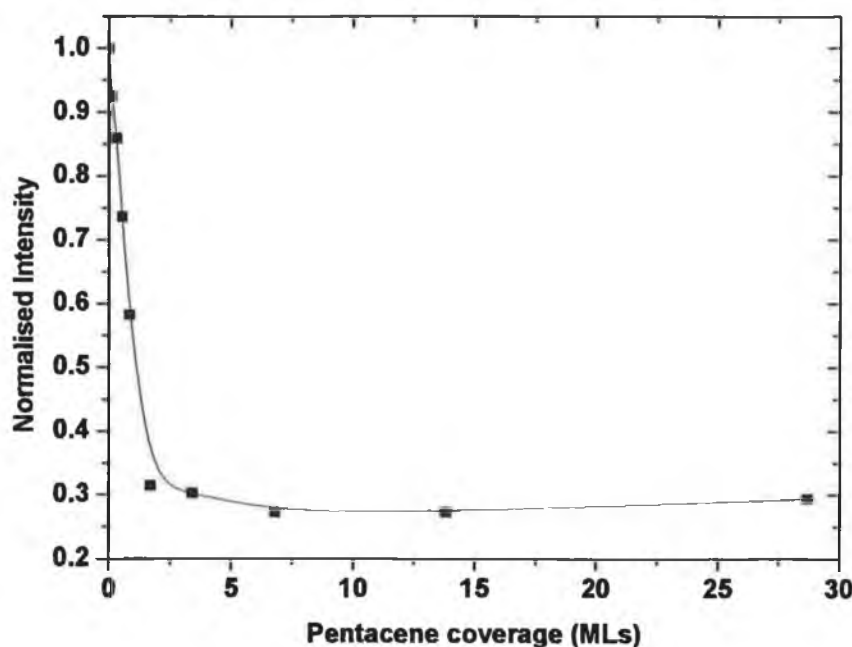


Figure 6.15 Normalised Cu3d peak height ($h\nu=31\text{eV}$) for increasing pentacene coverages.

The substrate intensity is observed to rapidly decrease to approximately 30% of its initial intensity by a coverage of 3.4ML. This decrease occurs over a smaller overlayer thickness range than that observed for the pentacene/Cu(110) and pentacene/Au(100) systems and is attributed to the decreased sampling depth of the Cu3d electrons in this case. The Cu3d peak intensity is observed to drop to 27% of its initial intensity by a pentacene coverage of 6.8ML, after which there is no additionally observed decrease in the substrate signal. This suggests that there is a sticking limit present in the pentacene/O/Cu(110)-(2×1) system after the deposition of the initial few monolayers of adsorbate. This phenomenon has not been observed for either of the two pentacene/metal systems presented so far, and could be an indication of a high degree of disorder in the overlayer film.

6.4.5 Valence band analysis

The normal emission and s-polarised valence band scans for increasing pentacene coverage are presented in figure 6.16 and figure 6.17 respectively. Pentacene related valence band features are identified as M1 to M9 in both figures. The features corresponding identified as M1 to M9 can be found at 13.1eV, 10.8eV, 9.5eV, 9.1eV, 8.2eV, 7.4eV, 5.1eV, 4.5eV and approximately 1.0eV binding energies respectively. The feature denoted as M9 corresponds to the HOMO of the pentacene molecule. While it is difficult to identify the centre of the peak due to the shape of the emission from substrate in that region, the onset of the HOMO can easily be identified at 0.6eV binding energy. This corresponds to a reduction of 0.35eV in the hole injection barrier over that observed for the pentacene/Cu(110) system, which was calculated as 0.95eV in chapter 4.

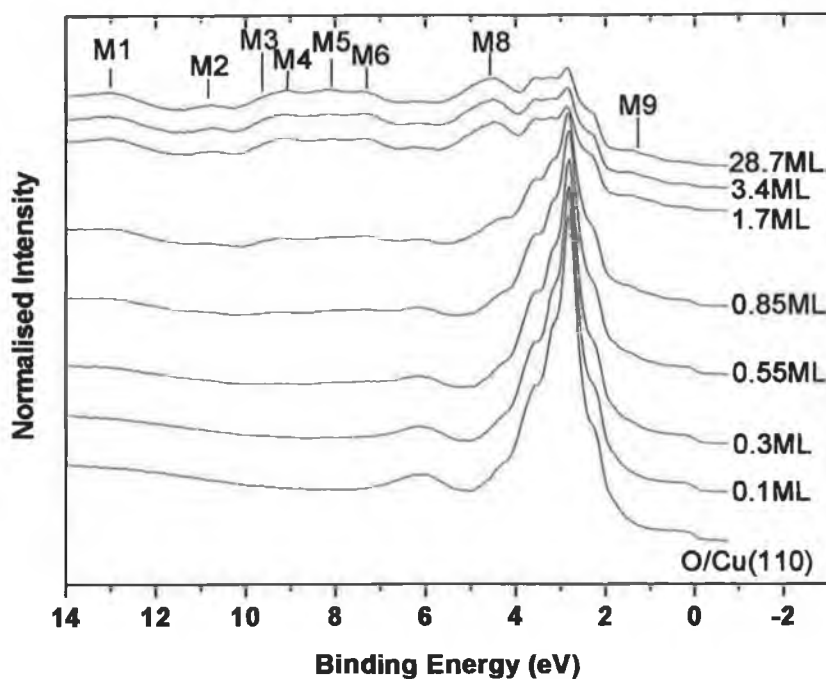


Figure 6.16 Normal emission valence band scans ($h\nu=31\text{eV}$) for increasing pentacene coverages on O/Cu(110)-(2x1). Pentacene related valence band features are identified as M1 to M6, in addition to M8 and M9 on the graph.

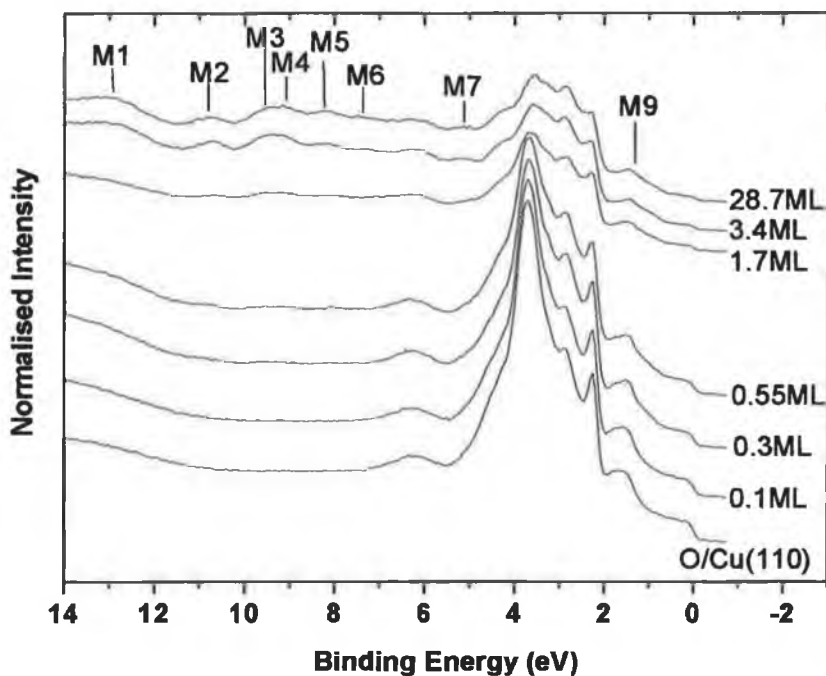


Figure 6.17 S-polarised valence band scans ($h\nu=31\text{eV}$) for increasing pentacene coverages on O/Cu(110)-(2x1). Pentacene related valence band features are identified as M1 to M7, in addition to M9 on the graph.

Figure 6.18 presents a comparison between the normal emission and s-polarised valence band scans for the pentacene/Cu(110) and pentacene/O/Cu(110)-(2×1) systems. The presence of features denoted as S1 and S2 in the spectra for both systems confirms the identification of these features as substrate related features in chapter 4.

It is evident that there is significant modification of the binding energy positions of the σ molecular orbital derived features by the introduction of the oxygen interlayer. Due to the low intensity, and hence difficulty in identification of the features derived from $\pi+\sigma$ hybrid and pure π molecular orbitals, the shift in the binding energy positions of these features has not been plotted in figure 6.18.

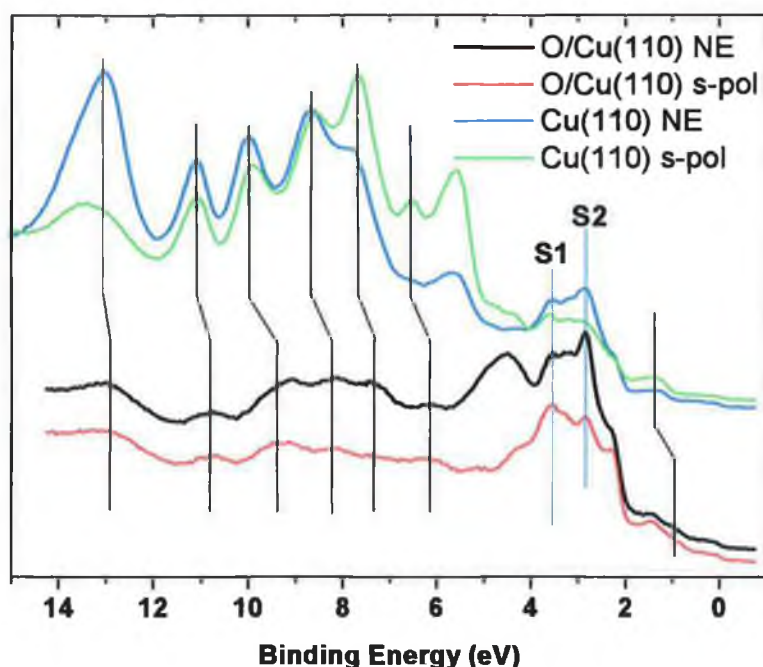


Figure 6.18 Comparison between thick pentacene films (>10ML) grown on the Cu(110) and O/Cu(110)-(2×1) substrate. Features S1 and S2 indicate substrate related features present for both experimental systems.

While the shifts in the molecular orbital derived features indicates altered hole and electron injection characteristics, the different magnitudes of the observed binding energy shifts for different molecular orbitals suggests that the bonding of the molecule to the substrate has been significantly altered for the pentacene/O/Cu(110)-(2×1) system. This is in agreement with the C1s core level data presented in section 6.4.3, which indicated a physisorption like interaction between the pentacene and the

O/Cu(110)-(2×1) substrate, in contrast to the chemisorption like interaction observed for the pentacene/Cu(110) system, as discussed in chapter 4.

While it cannot be unequivocally shown with PES, due to the presence of a component of the substrate signal emanating from deeper in the sample than the initial monolayer, the presence of a strong signal at the Fermi level for the O/Cu(110)-(2×1) system suggests that the surface maintains its metallic character.

6.4.6 Molecular energy level diagram

In figure 6.19 we present the molecular energy level diagram for the pentacene/O/Cu(110)-(2×1) interface. As with the energy level diagrams presented in chapters 4 and 5, the diagram does not take into account any band bending or polarisation shifts in the film. A slight fluctuation ($\pm 0.3\text{eV}$) in the photon energy did not allow for concise binding energy position measurements, upon which estimation of band bending shifts in the film are dependent. The figure indicates the PES measured values of the interface dipole formed, Δ (0.47eV for the $\text{C}_{22}\text{H}_{14}$ interface) as calculated from the shift in the WF in figure 6.13.

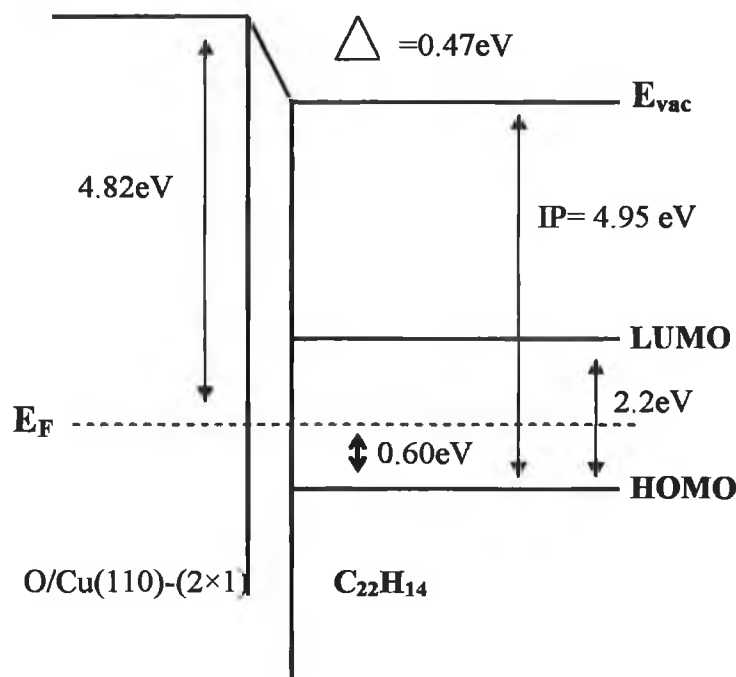


Figure 6.19 Energy level diagram for the pentacene/O/Cu(110)-(2×1) interface.

The hole injection gap is calculated from the energy separation between the Fermi level and the low binding energy cutoff of the HOMO derived peak as calculated

from the valence band spectra. The hole injection gap was found to be 0.60eV for pentacene deposited on O/Cu(110)-(2×1). This value was found to be significantly smaller than the hole injection barrier obtained for the pentacene/Cu(110) system discussed in chapter 4 (0.95eV), but was similar in magnitude to those calculated for pentacene deposited on Au⁵ (0.5eV) and Au(111)⁶ (0.55eV).

The LUMO position has been inferred from the measured charge transport gap¹⁰ of 2.2eV found for pentacene. The ionisation potential was calculated to be 4.95eV and is found by addition of the WF for the thick pentacene film and the hole injection gap. This value for the calculated ionisation potential is similar to that observed for pentacene deposited on other metal substrates, with values of 4.9eV resulting from the deposition of pentacene on Au, Ag and Ca⁵, while values of 4.65eV, 5.07eV and 4.8eV were obtained for pentacene deposited on Cu(110)⁷, Au(111)⁶, and Sm⁴⁰ respectively.

6.4.7 Summary

The termination of the Cu(110)-(1×1) surface with 0.5ML of oxygen, which results in the O/Cu(110)-(2×1) surface, has been found to have a significant effect over the subsequent growth of pentacene thin films, in terms of both chemical and physical properties of the film.

Workfunction, C1s core level, and valence band measurements suggest significant modification of the chemical properties of the adsorbate/substrate interface. The interface dipole, formed upon pentacene adsorption, is observed to reduce to approximately half of the value observed for the pentacene/Cu(110) system, with a resultant value of 0.47eV calculated for the pentacene/O/Cu(110)-(2×1) system.

Additionally, the strength on the bonding between the adsorbed pentacene molecules and the substrate is found to be significantly reduced by the oxygen termination of the Cu(110) substrate, with a physisorption like interaction resulting. This can be seen by the reduction in the C1s feature FWHM from 1.21eV to 0.96eV. The constant C1s FWHM for all pentacene coverages suggests that the substrate exhibits little interaction with the pentacene.

A comparison between the molecular orbitals observed for the pentacene/Cu(110) and pentacene/O/Cu(110)-(2×1) systems shows both a shift in the binding energy positions of the molecular orbitals between the two systems, and also a change in the binding energy positions of some molecular orbitals with respect to the other molecular orbitals. The binding energy shift of the molecular orbitals for the two systems results in a change in the injection characteristics of the pentacene/O/Cu(110)-

(2×1) system, with the magnitude of the hole injection barrier observed to reduce by approximately 0.35eV, to 0.60eV. The difference in the binding energy positions of the molecular orbitals, relative to the other molecular orbitals for the two systems, suggest a significant modification of the pentacene-substrate bonding observed for the two systems.

In addition to the alteration of the chemical properties of the interface, significant alteration of the physical properties of the overlayer film is observed. Substrate peak data suggests the presence of a sticking limit after the deposition of the initial few monolayers of pentacene for the pentacene/O/Cu(110)-(2×1) system

If the assumption that the O/Cu(110)-(2×1) surface retains a metallic character is correct, the use of 0.5ML of oxygen to terminate the Cu(110) substrate allows for a controlled modification of the pentacene/Cu(110) system, changing both the physical and chemical properties of the interface and the deposited pentacene film.

6.5 Pentacene deposited on sulphur terminated Au(100)

In this section a comparative study into the effect of the use of an interlayer on the overlayer molecular properties is presented. A sulphur layer was deposited on the Au(100) substrate, using the homemade sulphur source described in detail in section 3.5.3, and subsequently annealed to 500K prior to the deposition of the pentacene overlayer.

6.5.1 Workfunction analysis

The workfunction for the deposition and anneal of the sulphur layer on Au(100), and the subsequent deposition of pentacene onto the S/Au(100) substrate is presented in figure 6.20. Upon sulphur deposition the workfunction of the substrate is observed to increase, suggesting negative charge transfer from the Au(100) substrate to the adsorbed sulphur. As observed for the adsorption of oxygen to the Cu(110) surface, the electron affinity of the sulphur atoms results in the pulling of electron density from the surface, increasing the surface dipole component caused by the electron gas spill-out into the vacuum, which results in an increased observed workfunction. As before, the subsequent deposition of pentacene results in a suppression of the electron gas spill-out into the vacuum, resulting in the formation of an interface dipole and a corresponding reduction in the measured workfunction.

The magnitude of the interface dipole formed upon pentacene adsorption was found to be 0.86eV, which compares favourably with the magnitude of the interface dipole formed for the pentacene/Au(100), which was found to be 0.88eV in chapter 5. This unaltered interface dipole magnitude is in contrast with the result found for the pentacene/O/Cu(110)-(2×1) system, where the oxygen interlayer was found to substantially decrease the magnitude of the interface dipole formed upon pentacene adsorption.

Annealing of the pentacene covered substrate to 500K was found to completely remove the molecular overlayer, while not disturbing the sulphur termination and resulting in the workfunction returning to 5.37eV. This suggests that the adsorption of pentacene does not remove the adsorbed sulphur from the interfacial region, and that the suppression of the workfunction by the pentacene film is unaffected by the presence of the interlayer.

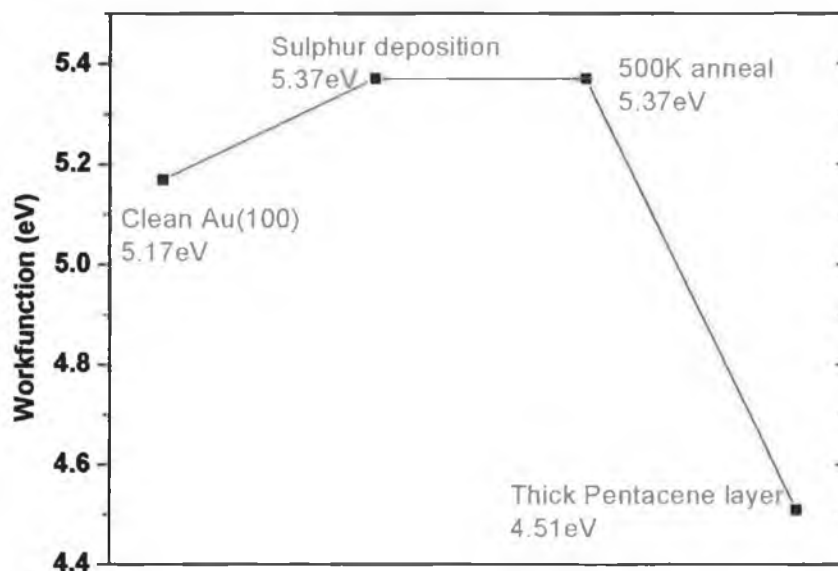


Figure 6.20 Calculated workfunction ($h\nu=31\text{eV}$) for the deposition and anneal of the sulphur interlayer, and the subsequent deposition of pentacene on the S/Au(100) substrate.

6.5.2 Substrate signal analysis

The Au4f_{7/2} peak for the clean Au(100) substrate, sulphur deposition and anneal to 500K, and subsequent pentacene deposition, are shown in figure 6.21. The centre of the peak is observed to shift to lower kinetic energy with the deposition of sulphur, suggesting negative charge transfer from the metal to the sulphur, which is in agreement

with the workfunction data presented in section 6.5.1. Without access to LEED, it is not known whether the deposition of sulphur resulted in a reconstruction of the (5×26) Au(100) surface, or if the sulphur adlayers were ordered on the gold substrate. However, annealing the substrate is more likely to promote an ordered layer of sulphur on the Au(100) substrate, in addition to the desorption of excess sulphur. The anneal of the substrate was observed to cause the Au4f_{7/2} peak position to shift slightly to higher kinetic energy, most likely as a result of the desorption of excess sulphur, and the formation of a more ordered sulphur layer.

A further shift of the peak centre to lower kinetic energy was observed with the deposition of the thick pentacene layer. This suggests further negative charge transfer from the Au(100) substrate, but it is not clear whether the charge is transferred to the sulphur or pentacene adlayers.

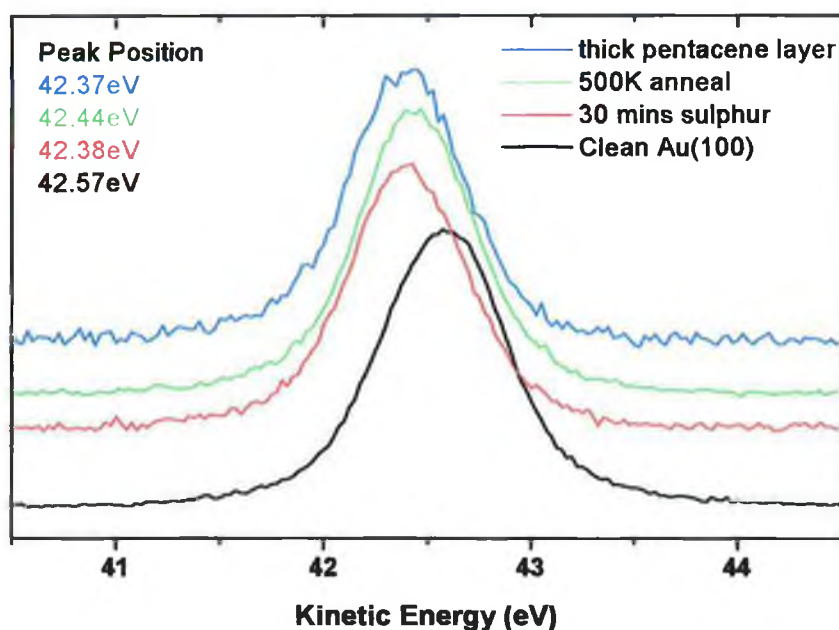


Figure 6.21 Au4f_{7/2} peak ($h\nu=130\text{eV}$) for the clean Au(100) substrate, the sulphur deposition and anneal at 500K, and the subsequent deposition of a thick pentacene overlayer.

The shift in the Au4f_{7/2} substrate peak position was not observed for the pentacene/Au(100) system, in which a weak bond between the pentacene and the Au(100) substrate was observed. It is therefore evident that the sulphur interlayer significantly alters the chemical interaction between the Au(100) substrate and the pentacene overlayer.

6.5.3 Valence band analysis

The normal emission valence band scans ($h\nu=31\text{eV}$) for the clean Au(100) substrate, the sulphur terminated surface and following the deposition of a thick pentacene film are shown in figure 6.22. Four new features, labelled s1 to s4, are observed in the valence band at 6.1eV, 4.95eV, 3.75eV and 2.65eV respectively, upon sulphur deposition. Feature s1 is the most prominent of these new sulphur related features, and is most likely the result of a shift in a large Au5d substrate valence band component that is observed at 5.85eV binding energy for the clean Au(100) substrate. This indicates the presence of a significant interaction between the sulphur and the Au(100) substrate, as suggested by the Au4f_{7/2} core level data presented in section 6.5.2. The feature s2 corresponds to a relatively small feature observed at 4.95eV binding energy in the valence band scans, while s3 and s4 appear as an enhancement of features present in the Au5d valence band emission for the clean Au(100) substrate.

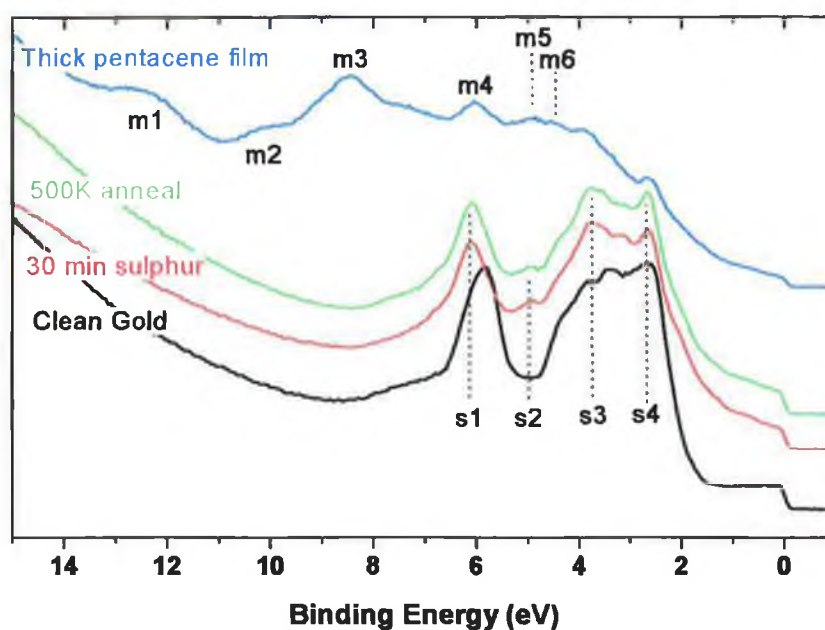


Figure 6.22 Normalised valence band plots ($h\nu=31\text{eV}$) for the clean Au(100) substrate, the sulphur deposition and anneal, and the subsequent deposition of a thick pentacene film. New sulphur related features in the valence bands are labelled s1 to s4, and new pentacene-derived features are labelled m1 to m6.

The deposition of pentacene induces significant changes in the valence band spectra with new features, labelled m1 to m6, observed at 12.5eV, 10.1eV, 8.45eV, 6.0eV, 5.0eV and 4.35eV binding energy, respectively. There is however little evidence of the HOMO, which is generally observed in the 0.5eV – 2.0eV range of the valence

bands. This makes the calculation of the hole injection characteristics for the pentacene/S/Au(100) system more difficult, and less precise. The lack of very strong pentacene molecular orbital derived features in the valence bands suggests that either (a) there is a high level of disorder in the film, or (b) there is a sticking limit present in the film, inhibiting the growth of a thick pentacene film.

The valence band region of the spectrum was also investigated with an incident photon energy of 80eV, providing a greater sampling depth than that found for an incident photon energy of 31eV. Figure 6.23 presents the valence band scans ($h\nu=80\text{eV}$) for the clean Au(100) substrate, the deposited and subsequently annealed sulphur interlayer, and the thick pentacene film grown on the sulphur terminated Au(100) substrate. The clean Au(100) substrate valence band scan shows a large Au5d emission feature in the 2-4eV binding energy range of the spectrum, in addition to two more significant components at approximately 5.95eV and 7.0eV binding energy, labelled B and A, respectively.

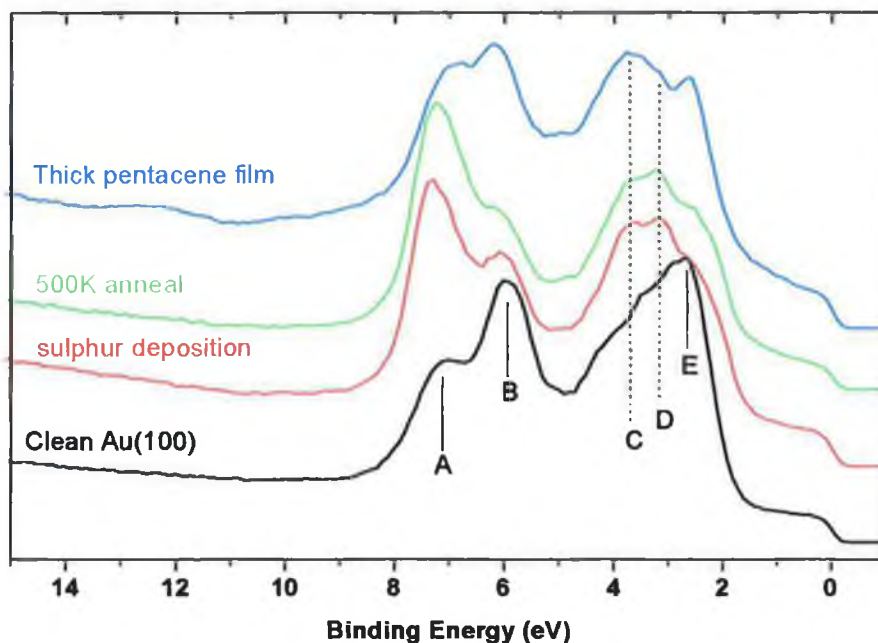


Figure 6.23 Normalised valence band plots ($h\nu=80\text{eV}$) for the clean Au(100) substrate, the sulphur deposition and anneal, and the subsequent deposition of a thick pentacene film. Main features in the valence band spectra are denoted as A to E in the graph.

Upon sulphur deposition, new features, labelled D and C, are observed to grow at 3.15eV and 3.65eV, in addition to a suppression of feature E, located at 2.7eV binding energy in the broad Au5d emission. The substrate components at higher binding energy, labelled B and A were observed to shift slightly to higher binding energy, in

addition to a significant modification of their relative intensities. Subsequent annealing of the sulphur layer is found to further suppress the signal of feature B, now situated at approximately 6.1eV binding energy. These changes to the valence band region of the spectrum indicate significant interaction between the sulphur and the Au(100) substrate, in agreement with workfunction and substrate core level results.

The deposition of a thick pentacene layer induces further changes in the valence band spectra. The sulphur related feature D, observed at 3.15eV binding energy, is suppressed, while the emergence of the feature at 2.7eV is observed. This feature corresponds in energy to feature E for the clean Au(100) valence band spectrum, although the assignment of this feature to a pentacene related π molecular orbitals cannot be fully excluded in this case. However, the lack of additional features relating to molecular orbitals in the rest of the spectrum suggests that this feature is not molecular orbital derived. There is also a significant change in the relative magnitude of the features A and B with the deposition of a thick pentacene film, in addition to a slight energy shift of feature A to lower binding energy.

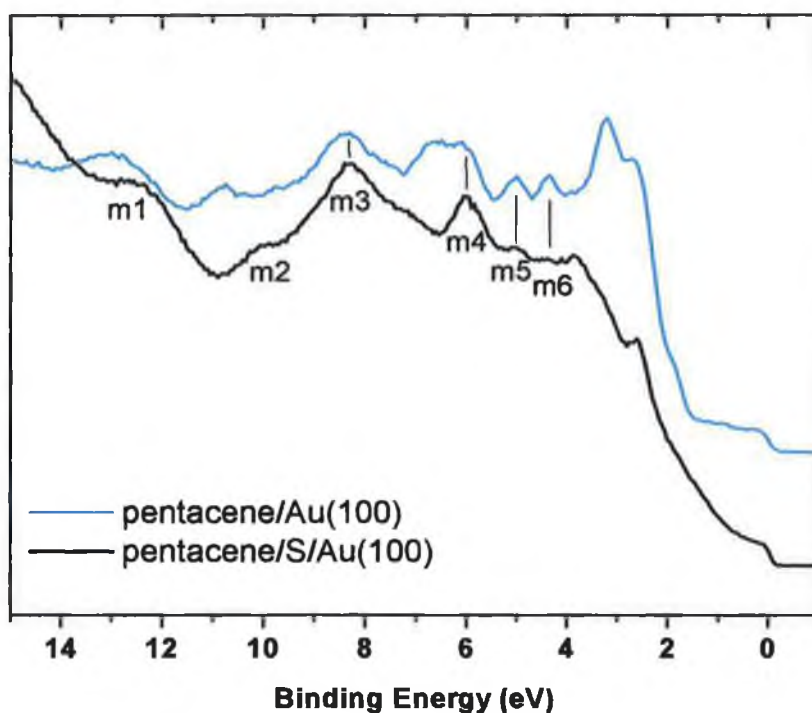


Figure 6.24 Comparison between valence band scans ($h\nu=31\text{eV}$) obtained for thick pentacene films grown on the Au(100) and S/Au(100) substrates. Pentacene molecular orbital related features for the pentacene/S/Au(100) system are denoted as m1 to m6 in the diagram.

As mentioned previously, there is little evidence of pentacene related features for the thick pentacene film shown in figure 6.23. This is due to the increased sampling depth, obtained using an incident photon energy of 80eV, resulting in a much greater substrate related signal. The dwarfing of the pentacene overlayer signal by the substrate related signal does however mean that the valence band scans obtained at 80eV are comprised predominantly of signal from the substrate, allowing an investigation of the substrate interaction with sulphur and pentacene coverage that was not obtainable with the 31eV valence band scans. It is therefore evident that there are significant chemical changes to the substrate with both sulphur and pentacene adsorption.

Due to the absence of a HOMO related signal in the valence band scans, the injection characteristics must be estimated in an alternative way. Figure 6.24 shows a comparison between the thick pentacene films found for the pentacene/Au(100) and pentacene/S/Au(100) systems. Due to the different experimental setups for the two experiments, and the possibility of differently oriented pentacene molecules in both systems, an identical molecular orbital fingerprint would not necessarily be expected for both systems. The pentacene related features for the pentacene/S/Au(100) system retain the m1 to m6 assignments attributed to them in figure 6.22. It is evident from figure 6.24 that there is good agreement between features m3 to m6, and pentacene related features in the pentacene/Au(100) valence band scan. While the m1 and m2 features only roughly correspond with molecular orbital features from the pentacene/Au(100) valence band scan, the agreement between the other features suggests that the hole and electron injection characteristics remain unchanged by the introduction of the sulphur interlayer.

6.5.4 Summary

While significant changes to the pentacene/Cu(110) system were observed by the introduction of an oxygen interlayer, the introduction of a sulphur interlayer to the pentacene/Au(100) system resulted in less significant changes to the overlayer film properties. The magnitude of the interface dipole did not appear to be adversely affected by the introduction of a sulphur interlayer with an interface dipole of 0.86eV observed. Similarly, an estimation of the hole and electron injection characteristics, via a comparison with the valence band scans obtained for the pentacene/Au(100) system, suggests that there is little change to the injection characteristics of the interface by the introduction of the sulphur interlayer.

Annealing of the substrate to 500K was found to remove the pentacene overlayer without removing the sulphur interlayer, suggesting that the adsorption of pentacene does not remove the sulphur from the interfacial region.

While the workfunction and valence band data suggests that the sulphur interlayer does not affect the interface dipole formation, or the hole and electron injection characteristics of the system, the Au4f_{7/2} core level data, and the valence band scans taken with an incident photon energy of 80eV, suggests significant interaction between the sulphur and both the Au(100) substrate and pentacene overlayer. There is significant modification of the substrate related valence band features with both the deposition of the sulphur interlayer, and the pentacene overlayer. Au4f_{7/2} data indicates significant negative charge transfer from the Au(100) substrate to the sulphur upon formation of the sulphur interlayer, with further negative charge transfer to either the sulphur or the pentacene observed upon deposition of the pentacene overlayer.

Chapter 6 References

- ¹ N. Karl, *Synth. Met.* 133–134 (2003) 649.
- ² T. W. Kelley and C. D. Frisbie, *J. Phys. Chem. B* 105 (2001) 4538.
- ³ Ph. Guaino, D. Carty, G. Hughes, O. McDonald, A. A. Cafolla, *Appl. Phys. Lett.* 85 (2004) 2777.
- ⁴ J. H. Kang, and X. Y. Zhu, *Appl. Phys. Lett.* 82 (2003) 3248.
- ⁵ N. J. Watkins, L. Yan, and Y. Gao, *App. Phys. Lett.* 80 (2002) 4384.
- ⁶ P. G. Schroeder, C. B. France, J. B. Park, and B. A. Parkinson. *J. Appl. Phys.* 91 (2002) 3010.
- ⁷ O. McDonald, D. Carty, G. Sheerin, A. A. Cafolla and G. Hughes, *Surf. Sci.* (In Press).
- ⁸ Darren Carty, PhD Thesis, *RAS and STM Investigation of Pentacene Molecules on Metal and Semiconductor Surfaces*, 2004.
- ⁹ O. McDonald, A. A. Cafolla, Zheshen Li, and G. Hughes, *Surf. Sci.* 600 (2006) 1909.
- ¹⁰ N. Koch, J. Ghijsen, R. L. Johnson, J. Schwartz, J. J. Pireaux and A. Kahn. *J. Phys. Chem. B.* 106 (2002) 4192.
- ¹¹ A. J. Heeger, J. R. Schrieffer, W. P. Su, *Rev. Mod. Phys.* 40 (1988) 3439.
- ¹² C.W. Tang, S.A. VanSlyke, C.H. Chen, *J. Appl. Phys.* 65 (1989) 3610.
- ¹³ J. Kido, K. Hongawa, K. Okyama, K. Nagai, *Appl. Phys. Lett.* 64 (1994) 815.

- ¹⁴ A. Yamamori, C. Adachi, T. Koyama, Y. Taniguchi, *Appl. Phys. Lett.* 72 (1998) 2147.
- ¹⁵ H. Fujii, T. Sano, Y. Hamada, K. Shibata, *Macromol. Symp.* 125 (1997) 77.
- ¹⁶ J. Kido, T. Matsumoto, *Appl. Phys. Lett.* 73 (1998) 2866.
- ¹⁷ Y. Yang, A.J. Heeger, *Nature* 372 (1994) 344.
- ¹⁸ J.R. Sheats, H. Antoniadis, M.R. Hueschen, W. Leonard, J. Miller, R. Moon, D. Roitman, A. Stocking, *Science* 273 (1996) 884.
- ¹⁹ Huanjun Ding, Yongli Gao, *Appl. Surf. Sci.* (In press)
- ²⁰ Huanjun Ding, Yongli Gao, *Appl. Phys. Lett.* 86 (2005) 213508.
- ²¹ Kazuyuki Sakamoto, Takanori Wakita, Daiyu Kondo, Ayumi Harasawa, Toyohiko Kinoshita, Wakio Uchida, Atsuo Kasuya, *Surf. Sci.* 499 (2002) 63.
- ²² L. Yan, N. J. Watkins, S. Sorba, Y. Gao, C. W. Tang, *Appl. Phys. Lett.* 79 (2001) 4148.
- ²³ L. H. Tjeng, R. Hesper, A. C. L. Heessels, A. Heeres, H. T. Jonkman, G. A. Sawatzky, *Solid State Commun.* 103 (1997) 31.
- ²⁴ G. H. Fecher, Ch. Grünewald, M. Merkel, Ch. Ostertag, A. Oelsner, G. Schönhense, Th. Jentsch, H. J. Jüpner, *Thin Solid Films*, 303 (1997) 58.
- ²⁵ Kazuyuki Sakamoto, Takanori Wakita, Daiyu Kondo, Ayumi Harasawa, Toyohiko Kinoshita, Wakio Uchida, Atsuo Kasuya, *Surf. Sci.* 499 (2002) 63.
- ²⁶ G. H. Fecher, Ch. Grünewald, M. Merkel, Ch. Ostertag, A. Oelsner, G. Schönhense, Th. Jentsch, H. J. Jüpner, *Thin Solid Films*, 303 (1997) 58.
- ²⁷ M. Probst, R. Haight, *Appl. Phys. Lett.* 70 (1997) 1420.
- ²⁸ E. A. Silinsh, V. Capek, *Organic Molecular Crystal*, AIP Press, New York, 1994.
- ²⁹ R. Ozawa, A Yamane, K. Morikawa, M. Ohwada, K. Suzuki and H. Fukatani, *Surf Sci* 346 (1996) 237.
- ³⁰ U. Dobler, K. Baberschke, D. D. Vvedensky, J. B. Pendry, *Surf. Sci.* 178 (1986) 1679.
- ³¹ S. R. Parkin, H. C. Zeng, M. Y. Zhou, K. A. R. Mitchell, *Phys. Rev. B* 52 (1997) 4748.
- ³² J. Buisset, H. P. Rust, E. K. Schweizer, L. Cramer, A. M. Bradshaw, *Surf. Sci.* 349 (1996) L147.
- ³³ R. Courths, S. Hufner, P. Kemkes, G. Wiesen, *Surf. Sci.* 376 (1997) 43.
- ³⁴ F. Jensen, F. Besenbacher, E. Lagaard, I. Stensgaard, *Phys. Rev. B* 41 (1990) 10233.
- ³⁵ D. J. Coulman, J. Wintterlin, R. Behm, G. Ertl, *Phys. Rev. Lett.* 64 (1990) 1761.

-
- ³⁶ R. Courths, S. Hufner, P. Kempes, G. Wiesen, *Surf. Sci.* 376 (1997) 43.
- ³⁷ G. Hill, A. J. Makinen, and Z. H. Kafafi, *J. App. Phys* 82 (2000) 889.
- ³⁸ G. Witte, S. Lukas, P. Bagus, Ch. Wöll, *Appl. Phys. Lett.* 87 (2005) 263502.
- ³⁹ The mean free paths were calculated by using the Tanuma, Powell and Penn formula in the program electron inelastic-mean-free-path v.1.1 provided by the National Institute of Standards and Technology, NIST.
- ⁴⁰ J. Ghijsen, R. L. Johnson, A. Elschner and N. Koch. *J. Alloys Compd.* 382 (2004) 179.

Chapter 7 Conclusions and Future Work

The purpose of this work was to investigate the properties of pentacene thin films grown on different metal substrates, and to investigate modification of the overlayer film and interface properties of these films using different methods. The main experimental technique used in the course of this work was synchrotron based photoelectron emission spectroscopy (PES), with additional experiments carried out using near edge X-ray absorption fine structure (NEXAFS), scanning tunnelling microscopy (STM) and low energy electron diffraction (LEED).

Chapter 2 introduces the theoretical background behind the techniques used in the course of this work. An in-depth discussion of the origin of the PES signal is introduced, in addition to details regarding the interpretation of spectra, and evolution of changes in the different spectra obtained. The theoretical background behind the formation of the selection rules used in the valence band analysis is also introduced in this section.

This chapter also details the theory behind the NEXAFS technique, including a brief derivation of the formulae associated with investigation of the angular orientation of the molecule. The origin of the surface sensitivity exhibited by both the PES and NEXAFS techniques is subsequently discussed. A brief discussion of the theory behind the STM technique is also included in this chapter, with the use of a quantum mechanical approach to derive equations relating to the tunnelling current observed between two closely spaced surfaces. The theory behind the LEED techniques is dealt with by the introduction of the diffraction theory and reciprocal space.

The equipment associated with the different techniques used in the course of this work is introduced in chapter 3. Since a significant amount of the work was carried out at the Astrid synchrotron radiation source at the University of Aarhus in Denmark, a detailed description of the UHV chambers is included in this section, in addition to a discussion regarding the origin of synchrotron radiation. The equipment associated with the PES and NEXAFS techniques is described, including a discussion of the modes of detection of the NEXAFS technique. Additional discussion is also included in this section regarding the UHV chamber and equipment associated with the STM and LEED techniques. A detailed description of the pentacene, sodium and sulphur evaporators used in the course of this work is introduced in this chapter.

A synchrotron based PES study of the pentacene/Cu(110) system is presented in chapter 4. A comparative study was carried out between pentacene films grown in a stepwise manner, and using an annealed monolayer to template the further growth. Pentacene core level analysis indicates that the initial monolayer of pentacene is

chemisorbed to the substrate, in contrast to the physisorption usually associated with the adsorption of non-functionalised molecules to metals. This is inferred from the presence of two components in the sub-monolayer C1s spectra, indicative of carbon atoms existing in differing chemical environments. Copper core level analysis indicated negative charge transfer from the substrate to the molecule.

Measurement of the shift in the workfunction and the position of the HOMO in the valence band scans allowed for the formulation of a band energy diagram for the pentacene/Cu(110) system. A selection rule analysis of the monolayer coverage of pentacene on Cu(110) suggested a flat bonded molecular orientation, with the growth of new molecular orbitals in the valence bands spectra above this coverage indicative of a change in orientation of subsequent monolayers.

The evolution of the core level and valence band spectra follow similar patterns for the two pentacene films investigated, indicating that a similar growth mode and molecular orientation was present for both pentacene films. A Stranski-Krastanov growth mode was evident for both films, although the degree of ordering present in the pentacene film grown using an annealed monolayer to template further film growth was found to be higher than that of the stepwise grown film.

A study of the pentacene/Au(100) system using PES, NEXAFS, STM and LEED is presented in chapter 5. PES and NEXAFS experiments indicate the presence of two pentacene molecular orientations at low and high pentacene coverages, with a changeover in molecular orientation occurring at approximately three monolayers. NEXAFS results indicate that the molecules in the initial monolayers lie flat or nearly flat on the substrate with the introduction of a tilt in the molecular plane away from the surface at higher coverages. The average NEXAFS derived tilt angle with respect to the surface was found to be 18.9° for low pentacene coverages and 29.2° for coverages above 3ML.

Interpretation of the valence band PES scans using the group theory derived selection rules did not prove as successful as for the pentacene/Cu(110) system. Difficulty in the application of the rules arises due to two main factors. The presence of multiple spherical harmonic components for the calculated final states of the pentacene initial states, results in a complex electron angular emission distribution. This complexity, coupled with the examination of only two sample orientations makes a definitive judgment on the molecular orientation difficult.

PES core level data indicates the presence of a much weaker adsorbate-substrate bond than that observed for the pentacene/Cu(110) system in chapter 4. The pentacene

molecules are found to physisorb to the Au(100) substrate, as is common for the adsorption of non-functionalised molecules on non-reactive metal surfaces.

STM images were obtained of the sub-3ML pentacene coverage, indicating the presence of a high degree of ordering in the overlayer film. The pentacene self-assembles into rows, where it adopts a side-by-side geometry with respect to its neighbouring molecules. Annealing of the pentacene film to approximately 373K was found to improve film quality, without otherwise changing the molecular orientation of the pentacene with regards the substrate. STM images show a more uniform pentacene row direction than that observed for the unannealed film. However, preliminary LEED images of the annealed and unannealed films showed no differences, suggesting that while there is evidently local change in the film ordering with annealing, there is little global change in the overlayer film with annealing. The LEED images of the unannealed film suggest that there is a predominant molecular row direction present, despite the curvature of pentacene rows close to substrate steps, as evidenced from the corresponding STM images. The higher resolution images obtained for the annealed film allowed the calculation of a pentacene unit cell. The unit cell parameters were found to be $7.39\text{\AA} \times 15.47\text{\AA}$, with an angle of 85.5° between the unit cell vectors. The resultant film packing density was found to be 0.88×10^{12} molecules/cm².

While the NEXAFS results presented in this chapter provides adequate information regarding the tilt angle of the molecule, the method in which the NEXAFS experiment was carried out was found to be excessively time consuming. This was mainly due to the acquisition of a PES spectrum of the carbon Auger feature for each incremented incident photon energy. In order to make the data acquisition manageable, a reduction in resolution and scan window size was required, which limited the quality of the results obtained. To obtain higher resolution, and more accurate tilt angle measurements, the use of a different acquisition method, possibly the drain current method should be used. A more comprehensive study of the pentacene/Au(100) system with the STM and LEED techniques could be used to identify the molecular orientation at higher coverages, so that a more complete model of the system at low and high coverages could be presented.

Chapter 6 presented the attempted modification of pentacene film properties via the use of alkali metal doping, and the use of suitable interlayers. For the alkali metal doping experiment, Na was used to dope pentacene films grown on Cu(110). The findings indicate that negative charge transfer from the alkali metal to the organic semiconductor results in the Fermi level of the pentacene being modified, essentially

from a p-type semiconductor to an n-type semiconductor. The doping process was observed to occur in two phases. In the initial doping phase, observed at low dopant concentrations, negative charge transfer from the Na to the pentacene resulted in the Fermi level moving up the gap towards the conduction band of the pentacene, with no significant alteration of the molecular orbitals observed. In the second phase of doping, further shifts in the Fermi level were observed, accompanied by significant modification in the pentacene related core level and valence band features. The growth of gap states between the HOMO and the Fermi level was also observed to accompany this stage of doping.

A comparative study on the Na doping of two pentacene films, exhibiting different levels of molecular ordering in the overlayer film, indicated that the ordering of the molecular film has a strong influence over the extent of doping observed in the initial stage of doping. The origin of this effect is not fully understood at this time, and requires further investigation.

A comparative study on the effect of interlayers on subsequent pentacene thin film growth was carried out via the introduction of oxygen and sulphur interlayers to the Cu(110) and Au(100) substrates, respectively. The oxygen termination of the Cu(110) substrate was found to have a significant effect on the magnitude of the interface dipole formed upon subsequent pentacene deposition, with a reduction in the observed interface dipole from 1.0eV to 0.47eV. In addition to this, the hole injection barrier, calculated from the energy separation between the onset of the HOMO and the Fermi level, was reduced from 0.95eV to 0.6eV by the introduction of an oxygen interlayer. C1s core level data indicated that the bonding between the pentacene and the substrate was significantly reduced in strength by the introduction of the (2×1) oxygen termination of the Cu(110) substrate, most likely resulting in a physisorption-type interaction between the pentacene and the O/Cu(110)-(2×1) substrate. It is therefore evident that the introduction of the oxygen termination of the Cu(110) surface plays a major role in the properties of the subsequently deposited pentacene films, and offers an interesting alternative to the alkali metal doping process for modification of organic film properties.

In contrast to the O/Cu(110)-(2×1) system, the introduction of a sulphur interlayer to the pentacene/Au(100) system does not adversely effect either the magnitude of the interface dipole formed upon molecular adsorption, or the hole and electron injection characteristics of the film. While this suggests that the pentacene molecules might remove the sulphur interlayer upon adsorption, subsequent annealing

of the sample to 500K was found to desorb the pentacene but leave the S/Au(100) substrate intact, showing that this was not the case. Indeed despite the lack of modification of the interface dipole magnitude and injection characteristics of the film, there is evidence of a strong bond between the sulphur and the Au(100) substrate.

It is evident that the study of the effects of interlayers on the properties of subsequently deposited organic films is quite complex. The two interlayers were found to have profoundly different effects on the subsequently deposited pentacene films. It is especially interesting to note that the magnitude of the interface dipole was not altered by the sulphur interlayer, despite the fact that the pentacene molecules are more spatially separated from the Au(100) substrate than for the pentacene/Au(100) system. Using the assumption that the interface dipole is predominantly due to the “cushion effect”, whereby the surface metal charge is repulsed by the adsorbate molecular charge, it is difficult to see how the physical separation of the adsorbate and the metal substrate, via the use of an interlayer, does not effect the subsequently formed interface dipole. Further interlayer study could therefore provide valuable insight into the mechanisms behind the formation of the interface dipole

The PES studies presented in the course of this work have been largely successful in gathering information regarding the bonding in the pentacene/metal systems, in addition to interface dipole formation and hole and electron injection characteristics of the films. While some molecular orientational information has been extracted via the use of the group theory analysis presented in this work, analysis was hindered somewhat by the experimental apparatus used. Analysis of the pentacene molecular orbital emission is generally complicated due to the multiple spherical harmonic partial wave components calculated for each initial state. However, the use of a fixed analyser, as was the case for this body of work, was found to further limit analysis by providing only limited snapshots of the full angle resolved spectrum. The use of a moveable analyser would allow for a full angle resolved PES study to be carried out, which can be used to investigate the molecular orientation in the films to a much greater extent than that achieved here.

For the sulphur and oxygen interlayer studies, further insight into the effects of the respective interlayers could be obtained with better access to the core levels of both the substrate and the interlayer species. For the pentacene/O/Cu(110) system, access to the oxygen core levels was limited by the photon flux at the corresponding photon energy. In addition to this, more accurate calibration of the incident photon energy for the Cu3p and C1s core levels would allow for a fuller investigation of the bonding

between the Cu(110) and the adsorbed oxygen, and also between the subsequently deposited pentacene film and the newly formed O/Cu(110)-(2×1) surface.

Similarly, access to the C1s and sulphur core levels would allow for a fuller understanding of interlayer bonding observed in the pentacene/S/Au(100) system. Supplementary LEED and STM studies could also be used to investigate the ordering of the sulphur adlayer on the Au(100) substrate. The NEXAFS technique could be used in both interlayer studies to ascertain the effect of the respective interlayers on the molecular orientation in the pentacene films in order to gain further insight into the mechanisms at work here.

In the field of 'organic molecular electronics', the work currently being carried out falls broadly into the categories of macroscopic and microscopic studies. The macroscopic studies generally involve the fabrication and analysis of simple molecular based electronic devices, to test their viability for different uses. The microscopic studies on the other hand focus primarily on the fundamental properties of the molecular thin films, and specifically on the interfacial region of the molecular thin film on a variety of substrates. This region is found to have significantly different properties from the bulk films, and extensive understanding of the interaction between substrate and adsorbate is essential if molecular based electronic devices are to be considered as a viable alternative to conventional solid-state semiconductor devices. Study of this interfacial region is best carried out via the study of either different molecules on the same substrate, or via the same molecule deposited on different substrates. These comparative studies can help aid the understanding of the role that both the adsorbate, and the metal substrate play in the interfacial reaction. In addition to this, multi-technique study of these organic/metal systems is essential to build up a full understanding of the interfacial interactions.

The approach taken in the course of this work has been the study of pentacene on different metal substrates, supplemented by work focussed on the modification of the interfacial regions via different methods. For the previously studied pentacene/Cu(110) interface, new techniques have been used to further supplement previous findings, while for the previously unstudied pentacene/Au(100) interface, a multi-technique approach has been used to gain maximum understanding of the new system. The use of the PES technique as a core technique throughout the work has facilitated comparative research into the different systems studied. This approach has been found to be particularly useful for data interpretation.

It is felt that the work contained in chapters 4 and 5 has meaningfully contributed to the literature body of work on the fundamental study of organic thin films on metal surfaces, while the work contained in chapter 6 provided a brief insight into the modification of the properties of these thin films via film doping and the introduction of interlayers.

List of Publications

1. O. McDonald, A. A. Cafolla, Zheshen Li and G. Hughes, "Synchrotron photoemission studies of pentacene films on Cu(110)", *Surface Science*, Volume 600, Issue 9, 1 May 2006, Pages 1909-1916.
2. O. McDonald, A. A. Cafolla, D. Carty, G. Sheerin and G. Hughes, "Photoemission, NEXAFS and STM studies of pentacene thin films on Au(100)", *Surface Science* (*In press*).
3. Ph. Guaino, D. Carty, O. McDonald, G. Hughes and A. A. Cafolla, "Long range order in a multilayer organic film templated by a molecular induced surface reconstruction: Pentacene on Au(110)", *Applied Physics Letters*, Volume 85, Issue 14, 4 October 2004, page 2777-2779.
4. Ph. Guaino, A. A. Cafolla, O. McDonald, D. Carty, G. Sheerin and G. Hughes, "Scanning tunneling spectroscopy of low pentacene coverage on the Ag/Si(111)-($\sqrt{3}\times\sqrt{3}$)R30° surface", *J. of Phys Condensed Matter*, Volume 15, Issue 38, Oct 1 2003, Pages S2693-S2698.
5. G. Hughes, D. Carty, O. McDonald and A. A. Cafolla, "Synchrotron radiation photoemission studies of the pentacene- Ag/Si(111)- $\sqrt{3}\times\sqrt{3}$ interface", *Surface Science*, Volume 580, Issues 1-3, 10 April 2005, Pages 167-172.

List of Tables

Table 2.1 Symmetry elements and symmetry operations.

Table 2.2 Character table for D_{2h} symmetry.

Table 2.3 Character table for C_{2v} symmetry.

Table 4.1 Assignment of molecular orbitals to features in the gas phase spectrum of pentacene for both the D_{2h} symmetry of the free molecule and the C_{2v} reduced symmetry of the adsorbed pentacene molecule.

Table 4.2 Direct Products of Representation Table for D_{2h} symmetry.

Table 4.3 Direct Products of Representation Table for C_{2v} symmetry.

Table 4.4 Table showing symmetrized bases for D_{2h} symmetry.

Table 4.5 Table of symmetrized bases for C_{2v} symmetry.

Table 4.6 Calculated final states and corresponding spherical harmonics for a given initial state for molecules of D_{2h} symmetry.

Table 4.7 Calculated final states and corresponding spherical harmonics for a given initial state for molecules of C_{2v} symmetry.

Table 4.8 Evaluation of emission from valence band features in normal emission for light polarised along each molecular axis.

Table 5.1 Evaluation of emission from valence band features in normal emission for light polarised along each molecular axis.

List of Figures

Figure 2.1 An example of a photoemission process, where an incident photon transfers all its energy to a core level electron.

Figure 2.2 Diagram of pentacene molecule showing all the operations on the molecule.

Figure 2.3 Two-step process that forms the basis for NEXAFS studies. The first step involved excitation of core level electrons into π^* and σ^* unoccupied levels. The core hole left by the excitation process is then filled by a valence electron with the surplus energy resulting in either the emission of (a) an Auger electron or (b) a fluorescent photon.

Figure 2.4 Coordinate system defining the geometry of a π^* vector orbital, denoted by \vec{O} , with respect to the sample surface and the incident synchrotron radiation.

Figure 2.5 Universal Inelastic Mean Free Path versus electron kinetic energy for organics calculated using equation 2.23.

Figure 2.6 Inelastic Mean Free Path versus electron kinetic energy for electrons propagating through a pentacene overlayer.

Figure 2.7 One-dimensional metal-vacuum-metal tunnelling junction. The bias voltage V is assumed to be small ($eV \ll \phi$) and the workfunctions of both electrodes are identical so the vacuum level is effectively the same for both electrodes.

Figure 2.8 Epitaxial Growth Modes: (a) Frank van der Merwe, (b) Stranski-Krastanov; and (c) Volmer Weber.

Figure 2.9 Ewald sphere construction for a cubic lattice. (hkl) are the Miller indices of the point on the Ewald sphere.

Figure 2.10 Two-dimensional Ewald sphere construction.

Figure 3.1 Diagram showing the extraction of synchrotron radiation from accelerated electrons.

Figure 3.2 Schematic diagram of ASTRID Synchrotron.

Figure 3.3 Resolution of the SGM1 monochromator with a typical working setting of the slits at 50 μm .

Figure 3.4 SGM1 monochromater.

Figure 3.5 Chamber schematic for the SGM1 beamline at the Astrid synchrotron used for photoemission studies.

Figure 3.6 Sample positions for valence band photoemission studies.

Figure 3.7 Diagram of SCIENTA electron analyser.

Figure 3.8 Energy level diagram and schematic photoemission spectra at different photon energies for a sample containing atoms with two core levels A and B and a valence band VB.

Figure 3.9 Chamber schematic for the SX700 beamline at the Astrid synchrotron used for NEXAFS studies.

Figure 3.10 Piezo tube scanner, (a) Top View, (b) side view.

Figure 3.11 Picture of STM showing spring damping system and eddy current damping system.

Figure 3.12 Two commonly used modes of STM operation (a) constant height mode, (b) constant current mode.

Figure 3.13 Feedback mechanism for constant current mode STM.

Figure 3.14 Diagram of UHV system showing (a) top, (b) side and (c) end views.

Figure 3.15 Picture and schematic diagram of LEED system.

Figure 3.16 Schematic of the pentacene evaporator used for thin molecular film deposition.

Figure 3.17 Schematic diagram of Na evaporator used in alkali metal doping of molecular films.

Figure 3.18 Schematic of UHV sulphur evaporator used for the deposition of sulphur interlayers.

Figure 4.1 Model for pentacene thin films grown on Cu(110) proposed by Söhnchen et al.

Figure 4.1 Workfunction values with increasing pentacene coverage as calculated from the negatively biased high binding energy cutoff of the valence band.

Figure 4.2 C1s core level ($h\nu = 340\text{eV}$) measured during the formation of the pentacene/Cu(110) interface. Inset in the diagram is the calculated peak area for increasing pentacene coverage using a linear fitting background.

Figure 4.3 Normalised peak area of the Cu3p substrate peak plotted for increasing pentacene coverage. Inset in the graph are the stacked Cu3p spectra ($h\nu = 200\text{eV}$) for clean Cu(110), 0.25ML, 0.5ML, 1ML, 2ML, 4ML, 8ML and 16ML coverages respectively from top to bottom.

Figure 4.4 Valence band scans ($h\nu = 31\text{eV}$) at normal emission for the stepwise growth of pentacene on Cu(110). Plots present increasing coverages of pentacene on Cu(110). Copper surface states are labelled S1 to S3, molecular orbitals identified for a thick pentacene film are labelled M1 to M10 and interface states are labelled I1 and I2.

Figure 4.5 Valence band scans ($h\nu = 31\text{eV}$) at the s-polarised sample position for the stepwise growth of pentacene on Cu(110). Plots present increasing coverages of pentacene on Cu(110). S4 denotes the identified copper surface state observed for the s-polarised sample orientation. Molecular orbitals identified for a thick pentacene film are labelled M1 to M10 and an identified interface states is labelled I2.

Figure 4.6 Pentacene gas phase spectrum with π molecular orbital assignments.

Figure 4.7 Comparison between gas phase spectrum of pentacene from literature and valence band spectra ($h\nu = 31\text{eV}$) of an 8ML coverages of pentacene on Cu(110) for normal emission and s-polarised sample positions.

Figure 4.8 Ball and stick model of a pentacene molecule indicating the x, y and z directions with respect to the molecule.

Figure 4.9 C1s core level ($h\nu = 340\text{eV}$) evolution with increasing pentacene coverage. The vertical lines indicate the presence of different components to the lineshape. Inset in the diagram is the calculated peak area for increasing pentacene coverage using a linear fitting background.

Figure 4.10 Normalised peak area of the Cu3p substrate peak plotted for increasing pentacene coverage. Inset in the graph are the stacked Cu3p spectra ($h\nu = 200\text{eV}$) for clean Cu(110), 1ML, 2ML, 4ML and 8ML coverages respectively from top to bottom.

Figure 4.11 Valence band scans ($h\nu = 31\text{eV}$) at normal emission for the templated growth of pentacene on Cu(110). Plots present increasing coverages of pentacene on Cu(110), with the inclusion of the 8ML coverage for the unannealed pentacene film for comparison. Copper surface states are labelled S1 to S3, molecular orbitals identified for a thick pentacene film are labelled M1 to M10 and interface states are labelled I1 and I2.

Figure 4.12 Valence band scans ($h\nu = 31\text{eV}$) at the s-polarised sample position for the templated growth of pentacene on Cu(110). Plots present increasing coverages of pentacene on Cu(110), with the inclusion of the 8ML coverage for the unannealed pentacene film for comparison. S4 denotes the identified copper surface state observed for the s-polarised sample orientation. Molecular orbitals identified for a thick pentacene film are labelled M1 to M10 and an identified interface states is labelled I2.

Figure 4.13 Energy level diagram for the pentacene/Cu(110) interface.

Figure 5.1 Workfunction values with increasing pentacene coverage as calculated from the negatively biased high binding energy cutoff of the valence band.

Figure 5.2 Normalised peak area of the Au4f_{7/2} substrate peak ($h\nu = 130\text{eV}$) plotted for increasing pentacene coverage. Inset in the graph are the stacked Au4f_{7/2} peaks with increasing pentacene coverage from top to bottom.

Figure 5.3 Natural log of the normalised Au4f_{7/2} peak area. The plot can be approximated by two straight lines, with an intercept point at approximately 3ML pentacene coverage. The differing slope of the two lines is indicative of a change in overlayer growth.

Figure 5.4 C1s core level ($h\nu = 340\text{eV}$) measured during the formation of the pentacene/Au(100) interface. Inset in the diagram is the calculated peak area for increasing pentacene coverage using a linear fitting background.

Figure 5.5 Valence band scans ($h\nu = 31\text{eV}$) at normal emission for the stepwise growth of pentacene on Au(100). Molecular orbitals identified for a thick pentacene film are labelled M1 to M11.

Figure 5.6 Valence band scans ($h\nu = 31\text{eV}$) at the s-polarised sample position for the stepwise growth of pentacene on Au(100). Molecular orbitals identified for a thick pentacene film are labelled M1 to M7 and M9 to M12.

Figure 5.7 Comparison between gas phase spectrum of pentacene from literature and valence band spectra ($h\nu = 31\text{eV}$) of the 17.8ML coverages of pentacene on Au(100) for normal emission and s-polarised sample positions.

Figure 5.8 Energy level diagram for the pentacene/Au(100) interface.

Figure 5.9 NEXAFS spectra for a 2.1ML coverage of pentacene showing the spectra obtained for s and p sample position in addition to a difference spectrum obtained for p-s.

Figure 5.10 NEXAFS spectra for a 7.1ML coverage of pentacene showing the spectra obtained for s and p sample position in addition to a difference spectrum obtained for p-s.

Figure 5.11 Variation in π^* emission intensity with measured angle for the 2.1ML pentacene coverage. The plot shows a comparison between the normalised experimental data and the data simulated using equation 2.23 for tilt angles of 15° , 25° and the best-fit 21.5° .

Figure 5.12 Molecular tilt angle as calculated from the NEXAFS spectra obtained at different pentacene coverages.

Figure 5.13 STM image of the clean Au(100)-(hex) substrate showing the unusual undulating surface reconstruction. Image parameters: Size = $30 \times 30\text{nm}^2$, $V_{\text{sample}} = -0.06\text{V}$, $I_t = 0.8\text{nA}$.

Figure 5.14 (a) Atomic resolution STM image of the hexagonal surface reconstruction of the Au(100) substrate and **(b)** line profile of single scan in (a) showing row separation of $14.8\text{\AA} \pm 0.4\text{\AA}$. Image parameters: Size = $10 \times 10\text{nm}^2$, $V_{\text{sample}} = 0.07\text{V}$, $I_t = 0.8\text{nA}$.

Figure 5.15 (a) LEED image of the clean Au(100) substrate taken at 45eV , exhibiting the quasihexagonal (5×26) surface reconstruction, in addition to the presence of orthogonally oriented domains. **(b)** Simulated LEEDpat image of the (5×26) surface reconstruction.

Figure 5.16 STM image of an approximate ML coverage of pentacene on Au(100). The presence of long chains of pentacene molecules can be seen in the image. The dark and light patches in the top left and bottom right corners are due to pentacene on lower and higher Au(100) steps respectively. The height of the upper step has been normalised out of the image in order for better observation of pentacene formations on the central step. Image parameters: Size = $100 \times 100 \text{nm}^2$, $V_{\text{sample}} = 0.5 \text{V}$, $I_t = 0.15 \text{nA}$

Figure 5.17 (a) STM image of linear rows of pentacene formed across several Au(100) substrate steps. The coverage corresponds to approximately 2ML of pentacene deposited on the substrate at room temperature, with a subsequently annealing of the substrate to 323K for 10 minutes. **(b)** Line profile of Au(100) atomic steps in figure 17(a). Image parameters: Size = $150 \times 150 \text{nm}^2$, $V_{\text{sample}} = 1.2 \text{V}$, $I_t = 0.4 \text{nA}$.

Figure 5.18 High resolution STM image of pentacene molecular lines indicating flat lying pentacene molecules. Values for the unit cell parameters have been calculated from multiple images to be $A = 7.39 \text{\AA}$ and $B = 15.47 \text{\AA}$ with the resultant angle between A and B = 85.5° . Image parameters: Size = $10 \times 10 \text{nm}^2$, $V_{\text{sample}} = 1.2 \text{V}$, $I_t = 0.4 \text{nA}$.

Figure 5.19 LEED images of **(a)** unannealed pentacene on Au(100)-(hex) taken at 14.7eV **(b)** annealed pentacene film corresponding to STM images of straight pentacene rows taken at 15.3eV. The spots in one quadrant of each LEED image have been circled for easier identification.

Figure 6.1 Evolution of carbon 1s peak ($h\nu = 340 \text{eV}$) as a function of increasing dopant concentration in the 16ML untemplated pentacene film.

Figure 6.2 Valence band spectra ($h\nu = 31 \text{eV}$) for increasing dopant concentration in the 16ML untemplated pentacene film. Inset in the graph is a close up of the valence band region nearest the Fermi level, with increasing dopant concentration from top to bottom.

Figure 6.3 Calculated workfunction position ($h\nu = 31 \text{eV}$) with increasing Na concentration in the 16ML untemplated pentacene film.

Figure 6.4 Na2p peak ($h\nu = 60 \text{eV}$) evolution with increasing dopant concentration in the 16ML untemplated pentacene film. The lower right panel is a composite of the Na2p peaks for the different coverages investigated, showing the relative intensities of the Na2p peaks.

Figure 6.5 Plot of shifts in the pentacene related valence band peaks, the C1s peak and the measured workfunction for increasing Na dopant concentration. The average value of the shift in the valence band peaks was used to indicate the valence band shift, as different features were observed to shift by different amounts.

Figure 6.6 Carbon 1s ($h\nu = 340 \text{eV}$) evolution with increasing Na concentration for the 8ML templated pentacene film. The 40-minute Na deposition for the unannealed pentacene film is included for comparison.

Figure 6.7 Valence band spectra ($h\nu = 31 \text{eV}$) for increasing dopant concentration in the 8ML templated pentacene film. Inset in the graph is a close up of the valence band region nearest the Fermi level, with increasing dopant concentration from top to bottom.

Figure 6.8 Evolution of the workfunction ($h\nu = 31\text{eV}$) with increasing Na concentration.

Figure 6.9 Na2p peak ($h\nu = 60\text{eV}$) evolution with increasing dopant concentration in the 8ML templated pentacene film. The lower right panel is a composite of the Na2p peaks for the different coverages investigated, showing the relative intensities of the Na2p peaks.

Figure 6.10 Plot of shifts in the pentacene related valence band peaks, the C1s peak and the measured workfunction for increasing Na dopant concentration. The average value of the shift in the valence band peaks was used to indicate the valence band shift, as different features were observed to shift by different amounts.

Figure 6.11 (a) Overhead view of the clean Cu(110) substrate showing the (1×1) unit cell. The topmost row of atoms are shown in yellow with the underlying atoms in red. **(b)** Overhead view of the oxygen terminated Cu(110) showing the (2×1) surface reconstruction. The oxygen atoms are shown in black and the topmost Cu atoms are shown in orange. **(c)** Side view of the oxygen terminated Cu(110) showing the (2×1) surface reconstruction.

Figure 6.12 (a) Plot showing the normal emission valence band spectra ($h\nu=31\text{eV}$) for the clean Cu(110) substrate, the O/Cu(110)-(2×1) substrate, and a difference spectrum. **(b)** Plot showing the s-polarised valence band spectra ($h\nu = 31\text{eV}$) for the clean Cu(110) substrate, the O/Cu(110)-(2×1) substrate, and a difference spectrum. New features induced by the oxygen termination of the surface are identified as A and B in the diagram.

Figure 6.13 Workfunction measurements ($h\nu=31\text{eV}$) for increasing pentacene coverages. A linear extrapolation of the initial decrease in the workfunction allows for the calculation of the approximate monolayer coverage.

Figure 6.14 Normalised peak area of the C1s pentacene peak plotted for increasing pentacene coverage. Inset in the graph are the stacked C1s spectra ($h\nu = 340\text{eV}$) for O/Cu(110)-(2×1), 0.1ML, 0.3ML, 0.55ML, 0.85ML, 1.7ML, 3.4ML, 6.8ML, 13.8ML and 28.7ML coverages respectively from bottom to top.

Figure 6.15 Normalised Cu3d peak height ($h\nu=31\text{eV}$) for increasing pentacene coverages.

Figure 6.16 Normal emission valence band scans ($h\nu=31\text{eV}$) for increasing pentacene coverages on O/Cu(110)-(2×1). Pentacene related valence band features are identified as M1 to M6, in addition to M8 and M9 on the graph.

Figure 6.17 S-polarised valence band scans ($h\nu=31\text{eV}$) for increasing pentacene coverages on O/Cu(110)-(2×1). Pentacene related valence band features are identified as M1 to M7, in addition to M9 on the graph.

Figure 6.18 Comparison between thick pentacene films grown on the Cu(110) and O/Cu(110)-(2×1) substrate. Features S1 and S2 indicate substrate related features present for both experimental systems.

Figure 6.19 Energy level diagram for the pentacene/O/Cu(110)-(2×1) interface.

Figure 6.20 Calculated workfunction ($h\nu=31\text{eV}$) for the deposition and anneal of the sulphur interlayer, and the subsequent deposition of pentacene on the S/Au(100) substrate.

Figure 6.21 Au $4f_{7/2}$ peak ($h\nu=130\text{eV}$) for the clean Au(100) substrate, the sulphur deposition and anneal at 500K, and the subsequent deposition of a thick pentacene overlayer.

Figure 6.22 Normalised valence band plots ($h\nu=31\text{eV}$) for the clean Au(100) substrate, the sulphur deposition and anneal, and the subsequent deposition of a thick pentacene film. New sulphur related features in the valence bands are labelled s1 to s4, and new pentacene-derived features are labelled m1 to m6.

Figure 6.23 Normalised valence band plots ($h\nu=80\text{eV}$) for the clean Au(100) substrate, the sulphur deposition and anneal, and the subsequent deposition of a thick pentacene film. Main features in the valence band spectra are denoted as A to E in the graph.

Figure 6.24 Comparison between valence band scans ($h\nu=31\text{eV}$) obtained for thick pentacene films grown on the Au(100) and S/Au(100) substrates. Pentacene molecular orbital related features for the pentacene/S/Au(100) system are denoted as m1 to m6 in the diagram.